

Insights into the interfacial chemistry in systems involving magnetic iron oxides

Xining Chen

Department of Chemistry
McGill University, Montreal

April 2022

A thesis submitted to McGill University in partial fulfillment of the requirements of the degree
of Doctor of Philosophy

©Xining Chen 2022

Abstract

This thesis examined the nanoscale interfacial chemistry in different systems involving magnetic iron oxides. Part one of the thesis studies the degradation of carbonyl iron microparticles in hydrocarbon or fluorocarbon magnetorheological smart fluid media after experiencing continual mechanical shear in clutch devices. X-ray photoelectron spectroscopy (XPS) is the technique of choice because it provides depth-resolved profiles of elemental-specific oxidation states of surface and sub-surface species. The combination of XPS with scanning electron microscope (SEM) reveals how the morphological changes of iron particles are related to reactions involving adventitious oxygen and chemical substituents in the host fluid. Such reactions produced a surface layer of iron oxides and iron fluorides encapsulating the particles. The surface layers, accompanied by shear-induced collisions in the clutch environment, lead to nanoscale changes in surface topography and redistributions of surface and sub-surface chemical species.

Part two of the thesis compares carboxylated cellulose nanocrystal (CNC) cryogel porous scaffolds with iron oxide nanoparticle-incorporated cellulose nanocrystal cryogel scaffolds. The cryogel scaffolds are produced using unidirectional freezing processes that employ high and low freezing temperatures, and freeze-thawing. The influence of an applied magnetic field on freezing is also investigated. SEM reveals morphologies of the resulting scaffolds. Pore size distributions are analyzed using the local thickness method. Furthermore, the nanoscopic structure of CNC in the scaffolds is studied using small-angle x-ray scattering (SAXS), and the results are correlated with water sorption data obtained via dynamic water sorption (DVS). It is observed that iron oxide incorporated CNC scaffolds have reduced water sorption. This observation correlates with the increased compactness within nanocrystals containing iron oxide-grafted CNCs.

Part three of the thesis redirects attention to polarized Raman spectroscopy in integrated optical waveguides. The integrated optics technique involved guiding a polarized incoming laser beam into a waveguide through prism coupling. Two waveguide setups are examined. The first setup uses glass waveguides with surface decorations of plasmonic gold-silver core-shell nanoparticles (Au AgNPs) configured as glass optical chemical bench (OCB) sensing elements. We implemented TE-TM polarized guided wave surface-enhanced Raman spectroscopy as a nanoplasmonic waveguide sensor to probe inter-ligand soft-soft interactions between magnetic nanoparticles and nanoplasmonic AuAg NPs.

The second setup is hybrid organic-inorganic sol-gel glass waveguides for investigating induced optical anisotropy inside the waveguide medium. In one experiment, we demonstrated that a polarization-induced refractive index change can be “written” by guiding polarized waves in the hybrid glass medium in the form of a spatially localized self-inscribed waveguide. We examined TE-TM mode conversion by “reading” mode conversion through changes in polarized C-H stretch vibrations of the hybrid glass. We furthered our experiment by “writing” a gyroscopic nanocomposite waveguide comprising magnetite nanoparticles in the host glass. Our attempt to detect non-Faraday effect mode-conversion in the waveguide, although inconclusive at this time, calls for exploration of new theories to describe mode conversion in lossy gyrotropic waveguide media.

Résumé

Cette thèse examine la chimie interfaciale à l'échelle nanométrique dans différents systèmes impliquant des oxydes de fer magnétiques. La première partie de la thèse étudie la dégradation des microparticules de fer carbonyle dans des milieux fluides intelligents magnétorhéologiques d'hydrocarbures ou de fluorocarbures après avoir subi un cisaillement mécanique continu dans des dispositifs d'embrayage. La spectroscopie photoélectronique à rayons X (XPS) est la technique de choix car elle fournit des profils résolus en profondeur des états d'oxydation spécifiques aux éléments des espèces de surface et de sub-surface. La combinaison de la XPS avec le microscope électronique à balayage (MEB) révèle comment les changements morphologiques des particules de fer sont liés aux réactions impliquant l'oxygène fortuit et les substituants chimiques dans le fluide hôte. Ces réactions ont produit une couche superficielle d'oxydes et de fluorures de fer encapsulant les particules. Les couches de surface, accompagnées de collisions induites par le cisaillement dans le milieu d'embrayage, entraînent des changements à l'échelle nanométrique dans la topographie de la surface et des redistributions des espèces chimiques de surface et de sub-surface.

La deuxième partie de la thèse compare les échafaudages poreux de cryogels de nanocristaux de cellulose carboxylés (CNC) avec les échafaudages de cryogels de nanocristaux de cellulose incorporés de nanoparticules d'oxyde de fer. Les échafaudages de cryogel sont produits à l'aide de processus de congélation unidirectionnels qui utilisent des températures de congélation élevées et basses, ainsi que la congélation-décongélation. L'influence d'un champ magnétique appliqué sur la congélation est également étudiée. Le MEB révèle les morphologies des échafaudages obtenus. La distribution de la taille des pores est analysée par la méthode de l'épaisseur locale. De plus, la structure nanoscopique des CNC dans les échafaudages est étudiée

en utilisant la diffusion des rayons X aux petits angles (SAXS), et les résultats sont corrélés avec les données de sorption de l'eau obtenues par sorption dynamique de l'eau (DVS). On observe que les échafaudages CNC incorporés d'oxyde de fer ont une sorption d'eau réduite. Cette observation est en corrélation avec l'augmentation de la compacité des nanocristaux contenant des CNC greffés à l'oxyde de fer.

La troisième partie de la thèse redirige l'attention vers la spectroscopie Raman polarisée dans des guides d'ondes optiques intégrés. La technique de l'optique intégrée consiste à guider un faisceau laser entrant polarisé dans un guide d'ondes par couplage de prismes. Deux configurations de guides d'ondes sont examinées. La première configuration utilise des guides d'ondes en verre avec des décorations de surface de nanoparticules plasmoniques or-argent à cœur-coquille (Au AgNPs) configurées comme des éléments de détection de banc chimique optique (OCB) en verre. Nous avons mis en œuvre la spectroscopie Raman améliorée en surface par ondes guidées polarisées TE-TM comme capteur de guide d'ondes nanoplasmonique pour sonder les interactions douces inter-ligands entre les nanoparticules magnétiques et les nanoparticules AuAg nanoplasmoniques.

La deuxième configuration est constituée de guides d'ondes hybrides organiques-inorganiques en verre sol-gel pour étudier l'anisotropie optique induite à l'intérieur du milieu du guide d'ondes. Dans une expérience, nous avons démontré qu'un changement d'indice de réfraction induit par la polarisation peut être " écrit " en guidant des ondes polarisées dans le milieu de verre hybride sous la forme d'un guide d'ondes auto-inscrit localisé dans l'espace. Nous avons examiné la conversion de mode TE-TM en " lisant " la conversion de mode à travers les changements des vibrations d'étirement C-H polarisées du verre hybride. Nous avons poursuivi notre expérience en " écrivant " un guide d'ondes nanocomposite gyroskopique comprenant des

nanoparticules de magnétite dans le verre hôte. Notre tentative de détection de la conversion de mode par effet non-Faraday dans le guide d'ondes, bien que non concluante pour le moment, appelle à l'exploration de nouvelles théories pour décrire la conversion de mode dans les guides d'ondes gyrotropiques à pertes.

Acknowledgments

I would like to express my sincere gratitude to my supervisor Dr. Mark P. Andrews, for his support, guidance, and devotion throughout my PhD. His enthusiasm for science and endless patience has been an inspiration. I am also indebted to many students, professors, and staff in the Chemistry Department at McGill University for advice and technical assistance. This thesis would be impossible without the help of such intelligent and generous mentors and colleagues.

I wish to thank Dr. Jean-Sébastien Plante for introducing me to the world of magnetorheological fluids (MRF); Dr. Jean-Philippe Lucking Bigué, Anaële Pin, and Alexandre Landry-Blais for performing the MRF aging experiments using their clutch devices and helping me to understand the engineering behind their systems.

I wish to thank Dr. Lihong Shang at the McGill Institute for Advanced Materials (MIAM) for training me on the XPS instrument.

I wish to thank Dr. Hatem Titi at the McGill Chemistry Characterization (MC²) facility for introducing me to an array of x-ray and surface area techniques, including SAXS and DVS, and for his help operating these instruments to collect data; and Petr Fiurasek, also at MC², for training me on UV-Vis spectroscopy.

I wish to thank Dr. S Kelly Sears and Dr. David Liu at the Facility for Electron Microscopy Research (FEMR) for training sessions and technical assistance for SEM and TEM; Weawkamol Leelapornpisit for the operation of Helios SEM.

I wish to thank Dr. Tanya Kanigan and Dr. Jean A. Baldwin, whose work on integrated optics guided me through my optics experiments despite the years between us; and Dr. Mohamed Oubaha from Université de Montpellier for sharing his expertise on sol-gel spin-coating.

I also want to thank all members of the Andrews lab for their accommodation throughout my studies; Chantal at the graduate office for answering my silly questions on rules and policies.

Lastly, I want to thank my mother for continuing to believe in me, and myself for not giving up.

Contribution of Authors

Chapter 2

This chapter is adapted from “Chen, X., Andrews, M.P., Landry-Blais, A., Bigué, J.P.L. and Plante, J.S., 2019. Investigation of shear-induced physical and chemical transformations of Fe microparticles in hydrocarbon-and fluorocarbon-based magnetorheological fluids. *Smart Materials and Structures*, 28(10), p.104001; <https://doi.org/10.1088/1361-665X/ab0b5b0964-1726/>

Xining Chen designed the experiments on characterizing the pristine and expired MRF particles. The magnetorheological fluid (MRF) aging experiments in clutch devices were performed by a team at Université de Sherbrooke led by Dr. Jean-Sébastien Plante and Dr. Jean-Philippe Lucking Bigué. Xining Chen extracted particles from the expired MRFs and did comparison studies on pristine and expired particles using various characterization techniques. Xining Chen also conducted data analysis and manuscript writing. Professor Mark Andrews contributed to project design, data interpretation, and manuscript preparation.

Chapter 3

Xining Chen designed the project, synthesized iron oxide nanoparticle grafted cellulose nanocrystal (MNP-CNC), fabricated cryogel scaffolds using CNC and MNP-CNC materials, performed microscopy characterizations, performed data analysis, and wrote the manuscript. Dr. Hatem Titi performed small-angle x-ray scattering (SAXS) and dynamic water sorption (DVS) on the cryogel scaffolds and helped with proofreading the manuscript. Professor Mark Andrews contributed to project validation and manuscript preparation.

Chapter 4

Xining Chen constructed the integrated optical spectrometer setup and wrote the manuscript. Professor Mark Andrews provided guidance on the instrumental design and contributed to manuscript preparation.

Chapter 5

Xining Chen designed the experiments, carried out the fabrication and characterizations of nanoparticles and waveguides, performed integrated optics-surface enhanced Raman spectroscopy (SERS) on various waveguide samples, analyzed SER data, performed computer simulations, and wrote the manuscript. Weawkamol Leelapornpisit obtained high-resolution SEM data using the Helios SEM instrument. Professor Mark Andrews contributed to project design, data interpretation, and manuscript preparation.

Chapter 6

Xining Chen designed the experiments, fabricated nanoparticles and slab waveguides, performed polarized Raman spectroscopy, and wrote the manuscript. Professor Mark Andrews contributed to project design, data interpretation, and manuscript preparation.

Table of Content

LIST OF FIGURES AND TABLES	XIX
LIST OF ABBREVIATIONS	XXX
CHAPTER 1 INTRODUCTION	1
1.1 Overview of thesis objectives	1
1.2 A brief discussion of iron and iron oxides	1
1.2.1 Overview of iron and iron oxide compounds	1
1.2.2 Types of magnetism	3
1.2.3 Magnetic domains	5
1.2.4 Superparamagnetic nanoparticles	6
1.2.5 Carbonyl iron particles	7
1.2.6 Magnetite nanoparticles	8
1.2 Background literature review for each chapter	10
1.3.1 Iron microparticles in magnetorheological fluids	10
1.3.1.1 Magnetorheological fluids (MRF)	10
1.3.1.2 The role of oxidation of carbonyl iron particles in the degradation of MRFs	13
1.3.2 Carboxylated cellulose nanocrystal cryogel scaffolds	15
1.3.3 Optical chemical bench sensing platforms to study interfaces at the nanoscale	19
1.3.3.1 Literature review of integrated optics waveguide Raman spectroscopy	20
1.3.3.2 Plasmonics and sensing	22
1.3.3.3 Magnetic nanoparticles in optical sensors	24

1.4 Organization of the Thesis	28
1.5 Copyright information	31
1.6 Reference	33
CHAPTER 2 INVESTIGATION OF SHEAR-INDUCED PHYSICAL AND CHEMICAL TRANSFORMATIONS OF Fe MICROPARTICLES IN HYDROCARBON- AND FLUOROCARBON-BASED MAGNETORHEOLOGICAL FLUIDS	42
2.1 Introduction	42
2.1.1 Magnetorheological fluids and their aging problems in applications	43
2.1.2 The Mason number: relating MRF mechanical stress to viscous drag force and magnetic force	44
2.2. Experimental	46
2.2.1 Aging, recovery, and isolation of MR fluid particles	46
2.2.2 SEM and TEM	49
2.2.3 X-ray photoelectron spectroscopy (XPS)	50
2.3. Results and Discussion	50
2.3.1 Aging of particles in hydrocarbon fluids & particle aging in correlation with Mason number	50
2.3.1.1 Particle morphology	50
2.3.1.2 Evidence of carbon catalytic reactions	53
2.3.1.3 Surface oxide composition	55
2.3.1.4 Estimation of oxide thickness and limitation of Ar ⁺ sputtering	59
2.3.2 Particle aging in PFPE-based MR fluids & function of a PFPE-based surfactant additive	62

2.3.2.1 Particle morphology	62
2.3.2.2 Defluorination of PFPE	64
2.3.2.3. Production of iron fluoride	68
2.4 Conclusion	71
2.5 Funding acknowledgment	72
2.6 Copyright information	72
2.7 Supporting materials	73
2.8 References	77
CHAPTER 3 CARBOXYLATED CELLULOSE NANOCRYSTAL CRYOGELS: POROUS MONOLITHS OF CNC AND CNC-MAGNETITE NANOPARTICLES ORIENTED UNDER HYDRODYNAMIC FLOW AND MAGNETIC FIELD	83
3.1 Introduction	83
3.1.1 Cellulose nanocrystals	84
3.1.2 Applications of CNC and magnetite incorporated CNC materials	85
3.1.3 Freeze casting of nanocellulose to make porous scaffolds	86
3.1.4 Design of current experiment	87
3.2 Experimental	88
3.2.1 Cellulose nanocrystalline (CNC) suspension	88
3.2.2 Magnetite nanoparticles decorated cellulose nanocrystalline (CNC-MNP)	88
3.2.3 CNC and CNC-MNP-containing cryogel preparation	89
3.2.4 X-Ray photoelectron spectroscopy (XPS)	91
3.2.5 Scanning electron microscopy (SEM)	91
3.2.6 Quantitative image analysis of macropore sizes using local thickness	91

3.2.7 Small-angle X-ray Scattering (SAXS)	92
3.2.8 Dynamic vapor sorption analysis (DVS)	93
3.3 Results and Discussions	93
3.3.1 CNC and CNC-MNP cryogels	94
3.3.1.1 XPS analysis of as-obtained CNCs and as-synthesized CNC-MNP	94
3.3.2 High and low freezing temperature: Impact on pore morphologies and macropore sizes of CNC and mixed CNC-MNP cryogels	95
3.3.3 Two-step freezing: high-temperature cryogelation followed by low-temperature freezing and the impact of an external magnetic field	100
3.3.4 SMF affects the freezing mechanism	100
3.3.5 Investigating nanoscale structures using SAXS	102
3.3.6 Water vapor sorption study using DVS	104
3.4 Conclusion	107
3.5 Supporting materials	109
3.6 References	120
CHAPTER 4 INTEGRATED OPTICS TECHNIQUES COMBINED WITH SURFACE-ENHANCED RAMAN SPECTROSCOPY	131
4.1 Introduction	131
4.2 Raman scattering	132
4.3 Surface-enhanced Raman spectroscopy (SERS)	133
4.4 Background to guided wave Raman spectroscopy	135
4.5 Waveguide Raman spectroscopy in planar slab waveguides	138
4.6 Integrated optics spectrometer setup	144

4.7 References	150
CHAPTER 5 INTEGRATED OPTICS POLARIZED LIGHT AND EVANESCENT WAVE SURFACE-ENHANCED RAMAN SCATTERING (IO-PEWSERS) TO DETECT LIGAND INTERACTIONS AT NANOPARTICLE SURFACES	154
5.1 Introduction	154
5.1.1 Plasmon waveguide coupled with surface-enhanced Raman spectroscopy for near-field probing of molecules and molecular orientations	155
5.1.2 Design of the present study	157
5.2 Experimental	159
5.2.1 Synthesis of AuAg NPs	159
5.2.2 Hierarchies of assemblies on the waveguide optical chemical bench	160
5.2.2.1 Preparation of the nanoplasmonic OCB by functionalization with AuAg nanoparticles	160
5.2.2.2 Binding of 4MPy or 4ABA molecules onto the nanoplasmonic AuAg waveguide OCB	160
5.2.2.3 Binding of Fe ²⁺ to 4MPy onto the nanoplasmonic AuAg waveguide OCB	161
5.2.2.4 Binding 4ABA functionalized magnetite nanoparticles (MNPs) onto the nanoplasmonic AuAg waveguide OCB	161
5.2.3 X-Ray photoelectron spectroscopy (XPS)	162
5.2.4 Integrated Optics (IO) SERS Spectrometer	162
5.2.5 Scanning Electron Microscopy (SEM)	165
5.2.6 Transmission Electron Microscopy (TEM)	165
5.2.7 Simulation of plasmonic electric field	165

5.3 Results and Discussion	167
5.3.1 OCB overlaid with AuAg nanoparticles- overlayer	167
5.3.2 Binding of 4-Mercaptopyridine (4MPy) on AgAu NP surface	170
5.3.2.1 Assignment of SER spectra	170
5.3.2.2 SER Response of 4MPy to TE and TM Polarization	173
5.3.2.3 Orientation of 4MPy on bimetallic AuAg nanoparticles on the OCB	173
5.3.2.4 Binding of Fe ²⁺ to 4MPy	174
5.3.3 Binding of 4-aminobenzoic acid (4ABA) in comparison to that of 4MPy	176
5.3.3.1 SERS of 4ABA binding to AuAg NPs on the OCB	176
5.3.3.2 Orientation of 4-aminobenzoic acid on nanoplasmonic AuAg on the OCB	178
5.3.3.3 4ABA-functionalized MNPs on nanoplasmonic AuAg on the OCB	180
5.3.3.4 Detection of 4ABA-functionalized MNPs using OCB	182
5.3.4 FDTD simulation of electric fields of AuAg NPs excited by TE/TM polarized light	185
5.4 Conclusion	189
5.5 Supporting materials	191
5.6 References	192
 CHAPTER 6 POLARIZATION MODE CONVERSION IN SOL-GEL DERIVED WAVEGUIDES	 198
6.1 Introduction	198
6.1.1 Background to waveguide polarization state mode conversion and polarized waveguide Raman spectroscopy	198
6.1.2 Polarized Raman Spectroscopy	204
6.1.3 Porto notation	206

6.1.3 Sol-gel derived waveguide and laser-induced anisotropy	207
6.2 Experimental	209
6.2.1 MAPTMS sol-gel	209
6.2.2 Synthesis of magnetite nanoparticles (MNPs)	210
6.2.3 Incorporation of magnetite nanoparticles (MNPs) into the sol	212
6.2.4 Fabrication of sol-gel derived (laser poled) waveguides	212
6.2.5 Applied magnetic field	212
6.2.6 Photographs of the coupling waveguides	213
6.3 Results and Discussion	213
6.3.1 sol-gel derived waveguide with no incorporated MNPs: Sol-gel glass waveguide with isotropic refractive index	213
6.3.2 Sol-gel glass waveguide with polarization induced anisotropy	215
6.3.3 Raman optical “read” in C-H fingerprint region of induced anisotropy in the refractive index of the self-inscribed waveguide	216
6.3.4 MNP doped sol-gel glass waveguide with polarization induced anisotropy	218
6.3.4.1 Problem of optical loss in gyrotropic sol-gel glass waveguides	218
6.3.4.2 Poled gyrotropic MNP sol-gel waveguide	220
6.3.4.3 Polarized Raman spectra after an applied magnetic field orthogonal to the waveguide plane	221
6.3.5 Recommendations for future experiments	226
6.4 Conclusion and Future work	227
6.5 References	230
CHAPTER 7 SUMMARY OF FINDINGS AND SUGGESTIONS FOR FUTURE RESEARCH	233

7.1 Summary of chapters	233
7.2 Contributions to original knowledge	237
7.3 Future directions	239
7.3.1 Conduct targeted studies into factors that affect particle-fluid interfacial chemistry in magnetorheological fluids (MRF) systems	239
7.3.2 Effects of composition designs and fabrication techniques on the physiochemical properties of CNC-based composites	240
7.3.3 Improving the optical chemical bench (OCB) for nanoparticles detection	241
7.3.4 Optical anisotropy induced by magnetic particles and/or applied magnetic field	242
7.4 References	243

List of Figures and Tables

Figure 1.1. (A) A unit cell of the body-centred cubic (bcc) crystal structure for α -iron; the blue circle represents Fe(0). (B) A unit cell of the inverse spinel crystal lattice structure (a) with (b) representing the tetrahedral or "A"-site and (c) representing the octahedral or "B"-sites. In both A-sites and B-sites, O ²⁻ anions (black dot) form the tetrahedral or octahedral structures, while Fe ³⁺ and Fe ²⁺ cations occupy their respective interstitial sites. Figure X(B) is adapted from reference (17), copyright © 2018 John Wiley & Sons, Ltd.....	10
Figure 1.2 Schematic images of MRF particles in dispersion become reversibly aligned after an external magnetic field is applied. Adapted with permission from reference (2) Copyright © 2022 Elsevier B.V.....	12
Figure 1.3 Illustration of the principle of unidirectional freeze casting. An elongated flow field is identified by the blue arrows in the figure. The freezing front decreases in the direction towards the top of the image where CNC particles are evidently randomly oriented. Reprinted with permission from reference (26) Copyright © 2022 American Chemical Society.....	18
Figure 1.4 Basic schematic of the OCB design. On the left, a laser beam is shown to be guided into the OCB, consisting of a waveguide decorated with plasmonic nanostructures. On the right, an enlarged view of the same waveguide is shown. Plasmonic nanoparticles are immobilized onto the surface of the waveguide, serving as sensory elements and binding sites for incoming molecules.....	20
Figure 2.1 Schematic of the clutch durability test bench used for all durability tests in this study.....	47

Figure 2.2 Demonstration of typical torque and viscosity relationship in MR clutch durability tests.....48

Figure 2.3 Control sample of Lord 140 CG MR carbonyl iron microparticles. Particles have not been subjected to shear.....52

Figure 2.4 Sample of Lord 140 CG MR carbonyl iron microparticles. Particles **A** were subjected to low Mn shear, while particles **B** were subjected to high Mn shear. TEM shows residues from the washing of respective particles.....52

Figure 2.5 XPS elemental composition depth profile of control sample of Lord 140 CG MR carbonyl iron microparticles. Particles were not subjected to shear.....54

Figure 2.6 XPS elemental composition depth profile of **(A)** low Mason number sample of carbonyl iron microparticles and **(B)** high Mason number particles.....55

Figure 2.7 XPS oxidation state depth profile for oxygen of **(A)** control sample of carbonyl iron microparticles, **(B)** low Mason number particles, and **(C)** high Mason number particles.....58

Figure 2.8 XPS depth profiles for Fe(O), Fe(II), and Fe(III) species in **(A)** control sample of carbonyl iron microparticles, **(B)** low Mason number particles, and **C** high Mason number particles.....61

Figure 2.9 Control sample PFPE based MR fluid carbonyl iron microparticles. Insert shows aggregates of iron microparticles. Particles have not been subjected to shear.....63

Figure 2.10 Sample of PFPE based MR fluid carbonyl iron microparticles after being subjected to shear. Particles **A** were obtained from fluid with no added surfactant, while particles **B** were obtained from fluid with surfactant added.....64

Figure 2.11 XPS oxidation state depth profiles for carbon species in (A) control sample of carbonyl iron microparticles, (B) aged particles obtained from “no-additive” fluid, and (C) aged particles obtained from “with-additive” fluid. The hydrogen atom is omitted in the labeling of C-F compounds.....66

Figure 2.12 Fluorine, carbon, and oxygen composition profiles for the surfactant additive (Krytox 157 FS) and base oil (Krytox GPL 104) controls. The hydrogen atom is omitted in the labeling of C-F compounds.....67

Figure 2.13 XPS oxidation states depth profiles for fluorine species in (A) aged particles obtained from “no-additive” fluid, and (B) aged particles obtained from “with-additive” fluid. The hydrogen atom is omitted in the labeling of C-F compounds.....69

Figure 2.14 XPS oxidation states depth profiles for iron species in (A) control sample of carbonyl iron microparticles, (B) aged particles obtained from “no-additive” fluid, and (C) aged particles obtained from “with-additive” fluid.....70

Figure S2.1 Thermogravimetric analysis (TGA) was performed on control Lord 140 CG particles and aged particles from the low and high Mason number tests. Samples were incinerated in an argon atmosphere. One can observe that the fluid (hydrocarbon) phase in the aged MR fluids, especially that aged in the high Mn test, has diminished in mass.....73

Figure S2.2 Example of determining the change in the ratio of different oxidation states of an element over-etching depth. The graph on the far left shows one oxidation state profile of oxygen on the surface (unetched) of the control Lord 140 CG particles, while the graph of the far right shows the profile after 350 sec of etching of the same particles. Three such profiles were taken at

each etching time. The areas under the curve for each peak on the three profiles were averaged and plotted against etching time.....74

Figure S2.3 Magnetic moment of control Lord 140 CG particles and aged particles from high and low Mn tests.....75

Figure S2.4 The magnetic moment of control carbonyl iron particles and aged particles from PFPE MR fluids with and without a lubricant additive. Aged particles from the no-additive MR fluid have a notable, although non-substantial, decrease in magnetic saturation.....76

Figure 3.1 Chemical structure of cellulose showing the $\beta(1 \rightarrow 4)$ -glycosidic bond linking two D-glucose units.....84

Table 3.1 Summary of sample names and corresponding freezing conditions.....90-91

Figure 3.2 XPS analysis of (A) CNC as obtained without MNPs, and (B) with MNPs bound to CNC. (C) shows TEM images of the MNP decorated CNCs at two magnifications. The CNC is barely visible as weak contrast against the background.....95

Figure 3.3 SEM images of the 8 cryogel scaffolds investigated in this experiment. Scale bars on the images are each 50 μm98

Figure 3.4 The SEM image (A), inverted binary image achieved by Otsu thresholding (B), local thickness fitting (C), and histogram of the pore diameter distribution against normalized volume fraction (D) of sample "CNC -12 °C". All scale bars on (A) represent 200 μm . The yellow color on B indicates areas of emptiness, and the brown color indicates partitioning formed by the aggregation of CNC. Image analysis for all 8 cryogel scaffolds are summarized in Figure S3.2.....98

Table 3.2 Summary of porosity information on the 8 cryogel scaffolds.....99

Figure 3.5 Small-angle X-ray (SAXS) measurements of (A) CNC and (B) CNC-MNP cryogel scaffolds.....104

Figure 3.6 Relationship between the correlation length obtained by DAB and the DVS equilibrium moisture content (EMC) as indicated by the changes in mass due to water sorption.....107

Scheme S3.1 (A) Top-down schematic diagram of the sample holder with two permanent magnets attached on opposite sides to generate an attractive magnetic field. The grey area is where the CNC and CNC-MNP samples were placed; (B) Schematic diagram of the resulting cryogel scaffold and the removal of one section for analysis. TEM images and subsequent graphical analysis were obtained on the cross-sectional area (grey). In this schematic diagram, the x-axis is the horizontal axis, the y-axis is the vertical axis.....110

Figure S3.1 As-synthesized MNP decorated CNCs under the influence of a bar magnet..... 110

Figure S3.2 Summary of the SEM images and their subsequent processing using the "local thickness" method. Each row is devoted to one of the 8 cryogel scaffold samples, with the name of the sample indicated at the lower-left corner of each row. For each row, (A) shows the SEM image of the cryogel scaffold, (B) shows the inverted binary image achieved by Otsu thresholding, (C) shows the local thickness fitting, and (D) shows the histogram of the pore diameter distribution against normalized volume fraction for each. The scale bars on (A) represent 200 μm . The yellow color in (B) indicates areas of emptiness, and the brown color indicates partitioning formed by the aggregation of CNC.....111-112

Figure S3.3 Fitting of the SAXS curves and corresponding residual graphs for each of 8 cryogel scaffolds. (A) The low end of the SAXS curve ($0.065 - 0.28 \text{ \AA}^{-1}$) was fitted using the mass fractal

model. **(B)** The middle range of the SAXS curve ($0.28 - 1.5 \text{ \AA}^{-1}$) was fitted using the Debye-Anderson-Brumberger (DAB) model.....113-116

Figure S3.4 Cross-section of the CNC $N_{2(l)}$ cryogel scaffold. Structural expansion and contraction of the cryogel scaffold is observed with changing relative humidity in the environment.....117

Figure S3.5 Adsorption isotherms for water vapor at 25°C for each of the cryogel scaffolds. Each adsorption cycle runs between 0 – 98% in actual % partial pressure.....118

Figure S3.6 (A) Percent change in sample mass relative to reference mass versus running time in an adsorption and desorption cycle at 95% relative humidity (approximately between 0 – 98% in actual % partial pressure). **(B)** is a zoom-in view of the turning point from adsorption to desorption, where EMC of the cryogel scaffolds occurs.....119

Figure 4.1 Inelastic Raman scattering versus elastic Rayleigh scattering. S_0 represents the electronic ground state. v_0 , v_1 and v_2 represents the vibrational ground state (0) and level 1 and level 2 of the vibrationally excited states, respectively. Raman scattering can be categorized as Stokes Raman scattering or anti-Stokes Raman scattering, depending on whether the final vibrational state is higher (anti-Stokes) or lower (Stokes) than the initial state.....132

Figure 4.2 Schematics of two types of OCB for integrated optics Raman spectroscopy are explored in the thesis. Waveguide **A** consists of plasmonic nanoparticles chemically bound through the R-group ($-\text{R}-\text{NH}_2$ or $-\text{R}-\text{SH}$) of $(\text{R}'\text{O})_3\text{SiOR}$ species to the surface of the waveguide. As light propagates in the waveguide, the evanescent field localized at the interface activates the SERS effect by exciting plasmonic response of the nanoparticles. Waveguide **B** depicts a sol-gel-type

waveguide supported on a substrate. This waveguide can accommodate different types of dopants to achieve desired optical effects. See text for details.....137

Figure 4.3. Schematics of ray optics as light is coupled by a prism into the core (n_2) of a slab waveguide (**A**). The evanescent field for coupling and the resulting propagating modes must travel with the same phase velocity and (TE/TM) polarization due to restrictions on resonant the eigenmodes (**B**).....139

Figure 4.4 Waveguide coupling assembly. (**A**) reveals the backside of the assembly. The waveguide holder is positioned in a machined aluminum holder mount. The two knurled knobs to adjust the pressure on the pressure bar above the prism (not visible here) are shown. A flat square bar magnet for Chapter 6 experiments is shown attached between the knobs. A Glan-Thompson polarizer is visible as the labeled black rotatable optical component below the holder. (**B**) shows the front (top) view of the waveguide assembly. The prism coupler hypotenuse is visible below the bottom edge of the pressure bar. The bright white dot above the pressure bar is the coupling point of the prism. Emanating from the prism is the guided wave. TM polarization occurs in the z-direction. The TE wave is polarized in the x-y plane along the y-axis. The guided wave is attenuated and does not reach the top end of the glass slab waveguide because of optical loss associated with excitation (resonant absorption) of the surface plasmons from the AuAg core-shell nanoparticles on the waveguide surface (described further in Chapter 5). Raman intensity is collected orthogonal to the slab waveguide along the z-direction, as shown by the yellow-orange arrow of the axis system in panel (**C**). Panel (**C**) is the front view of the waveguide assembly. It faces the slit entrance to the Triax 550 spectrograph. More on this type of waveguide and its application in integrated optics combining Polarized Raman and Evanescent Wave Surface-

Enhanced Raman Scattering (IO-PEWSEERS) is presented in Chapter 5.....143

Figure 4.5 Photographs and schematic of the integrated optics spectroscopy setup. In this setup, light produced at the 532 nm laser source (1) is reflected by a mirror assembly (2) into the beam steering assembly (3). A Glan Thompson polarizer (4) is situated in the beam steering assembly to introduce TE polarization to the incident light. The light is focused by the focusing lens (7) and passes through the half-wave plate (6) for the final adjustment of TE/TM polarizations. The light then reaches the waveguide-prism assembly (5), where it is coupled into the waveguide. Light scattered from the waveguide is collected, collimated, and re-focused by collection lenses 1 (8) and 2(10). A polarization analyzer (9) is placed between the two lenses to remove unwanted polarizations. The focused beam then passes through a depolarizer (11) and a 532 nm notch filter (12) before entering the Triax 550 Raman monochromator through the slit entrance (13).....147-148

Figure 5.1 Hierarchies of assembly of species on a slab waveguide optical chemical bench (OCB). 3-aminopropyl trimethoxysilane grafted to the glass waveguide surface is used as a molecular adhesive to bind AuAg core-shell nanoparticles. This OCB is further modified by binding 4-aminobenzoic acid derivatized magnetite nanoparticles to the plasmonic AuAg nanoparticles (top center diagram). Alternatively, 4-mercaptopyridine is ligated to the AuAg nanoparticles (middle center diagram). The 4MPy ligands can recognize and bind Fe^{2+} ; or 4-aminobenzoic acid can bind to the AuAg nanoparticles (bottom center diagram).....158

Figure 5.2 Schematic of the custom-built IO-SERS setup (top) and the scattering geometry as a laser beam is being guided into the nanoplasmonic OCB (bottom).....164

Figure 5.3 (A) An SEM image showing the sparsely distributed AuAg NPs on a section of the OCB (top) and the positioning of the particles using black discs (bottom). The side length of each square grid is 50 nm. (B) The 3D representation of the OCB structure with sparsely distributed AuAg core-shell nanoparticles mimicking that of the actual OCB calibrated from the SEM experiment.....166

Figure 5.4 (A) Bright-field TEM image of the AuAg NPs; (B) Dark-field TEM images and EDX elemental analysis of Au and Ag components of the AuAg NPs; (C) UV-Vis absorption spectra of AuAg NPs suspended in water and after immobilization on a glass substrate.....169

Figure 5.5 High-resolution SEM image of AuAg NPs immobilized on glass substrate using APTES.....170

Figure 5.6 TE and TM SER spectra of 4MPy molecules adsorbed on AuAg NPs-glass integrated waveguide.....172

Figure 5.7 Guided wave TE polarized SER spectra of 4MPy molecules adsorbed on the AuAg OCB prior to and after different times of exposure to Fe²⁺ solution.....175

Figure 5.8 TE and TM SER spectra of 4ABA molecules adsorbed on the AuAg OCB.....178

Figure 5.9 (A) High-resolution SEM image of 4ABA functionalized MNPS deposited on AuAg NPs immobilized on glass substrate using APTES; (B) Elemental mapping of Fe, Au, and Ag on a surface of 4ABA functionalized MNPS deposited on AuAg NPs integrated waveguide using SEM-EDX; (C) XPS analysis of O1s and N1s spectra of MNPSMNPs prior to and after incubation in 4ABA solution.....182

Figure 5.10 TE and TM SER spectra of 4ABA functionalized MNPS deposited on AuAg NPs-glass integrated waveguide.....185

Figure 5.11 (A) FDTD electric field simulations of AuAg core-shell dimers. The color code on the right indicates the maximum and minimum electric field intensity is corresponding to TE and TM polarization. The vertical axis in each simulation is y, and the horizontal axis is x. The propagation direction is orthogonal to the xy plane. The double-headed arrow (TE) and the arrow-and-dot (TM) indicate the direction of the exciting electric fields. (B) Waveguides streaks from prism coupling of the 532 nm laser polarized TE and TM orientation.....188

Figure S5.1 Raman spectra of crystalline 4ABA using either TE or TM polarized light.....191

Figure 6.1 Raman scattering geometry illustrating Porto notation. Figure adapted from Kanigan Ph.D. thesis (1995) Figure 2.7.....208

Figure 6.2 Iron oxide nanoparticles with oleylamine (A) and APTES (B) capping agents. The MNPs are approximately 9 nm in diameter.....211

Figure 6.3 Right-hand image shows the guided wave Raman spectra in the C-H stretching region of the hybrid organic-inorganic waveguide (no MNPs) for four different acquisitions of polarizations according to the Porto notation. The left-hand image shows the waveguide, input polarization, and analyzer configurations in the laboratory frame of reference. The combinations of input and output analyzer orientations are given according to their corresponding Porto notation. Note how the X(YY)Z spectrum is strongly polarized and that the remaining three spectra are similar, according to predictions from the scattering activities.....214

Figure 6.4 Raman spectrum of the uncured hybrid sol-gel waveguide after the introduction of anisotropy using the technique of TE+TM laser poling. The Raman spectrum is not polarized.....216

Figure 6.5 Polarized waveguide Raman spectra of the CH stretching region of a sol-gel derived waveguide, uncured and TE+TM poled. The Porto notation is indicative of the polarization of each spectrum. The black line shows spectra of the poled waveguide in the absence of MNPs, while the red line shows spectra of the poled waveguide with MNPs. Band position and mode assignment are labeled for the sol-gel waveguide without MNPs (black).....218

Figure 6.6 Photographs of light propagating in sol-gel waveguides. Two versions were taken for each waveguide. The red-tinted photos were taken through the lens of LG12 laser safety glasses, which filter green light that is scattered. It can be observed that doping with MNPs significantly increases the attenuation of green light in the waveguide. The higher the concentration of incorporated MNPs, the higher the attenuation.....219

Figure 6.7 (A) The red line shows the four polarized spectra of the C-H stretching region of the MNP incorporated, uncured and TE+TM poled, sol-gel derived waveguide with an applied magnetic field orthogonal to the waveguide plane. The red spectra are overlaid onto the polarized spectra of the same poled MNP waveguide without an applied magnetic field (black line).....223

Figure 6.7 (B) Distance resolved Raman measurements (along the x-axis) of X(YY)Z focusing on the CH stretching region of the sol-gel derived waveguide, poled, with incorporated MNPs. No external magnetic field was applied for spectra (B-a) and (B-b). An external magnetic field was applied by inserting a bar magnet for spectra (B-c) and (B-d).....224

Figure 6.7 (C) Distance resolved Raman measurements (along the x-axis) of X(YY)Z focusing on the CH stretching region of the sol-gel derived waveguide, poled, without incorporated MNPs. No external magnetic field was applied for spectra (C-a) and (C-b). An external magnetic field was applied by inserting a bar magnet for spectra (C-c) and (C-d).....225

List of Abbreviations

Magnetorheological fluid	MRF
X-ray photoelectron spectroscopy	XPS
Scanning electron microscopy	SEM
Transmission electron microscopy	TEM
Magnetic field	H field
Magnetic induction	B
Carbonyl iron particles	CIP
Mason number	Mn
Critical Mason number	Mn*
Perfluoropolyether	PFPE
Carboxylic acid	COOH
Continuous slippage actuator	CSA
Lifetime dissipated energy	LDE
Chemical vapor deposition	CVD
Device under test	DUT
Cellulose nanofibrils	CNF
Cellulose nanocrystals	CNC
Bacterial nanocellulose	BNC
Small-angle x-ray scattering	SAXS
Dynamic vapor sorption	DVS
Nanoparticles	NPs

Magnetite nanoparticles	MNP
Magnetite nanoparticles decorated cellulose nanocrystalline	CNC-MNP
The Debye-Anderson-Brumberger model	DAB
Static magnetic field	SMF
Equilibrium moisture content	EMC
Surface-enhanced Raman spectroscopy	SERS
Local surface plasmon resonance	LSPR
Surface plasmon polariton	SPP
Optical Chemical Bench	OCB
Transverse electric; s-polarized	TE
Transverse magnetic; p-polarized	TM
Integrated optics	IO
Integrated optics spectroscopy experiments that combine polarized Raman and evanescent wave SERS	IO-PEWSERS
Au-Ag bimetallic nanoparticles with imperfect core-shell structure	AuAg NPs
Finite-difference time-domain	FDTD
Perfectly matched layer	PML
4-Mercaptopyridine	4MPy
4-Aminobenzoic acid	4ABA
3-Aminopropyl trimethoxysilane	APTES
Charge-coupled device	CCD

Chapter 1

Introduction

1.1 Overview of thesis objectives

This thesis focuses on exploring nanoscale interfacial chemistry with different characterization techniques in three different applications of magnetic iron microparticles and magnetite (Fe_3O_4) nanoparticles. Iron-based materials have versatile applications in engineering due to their magnetic, thermal, catalytic, and optical properties. The three applications chosen as background scenarios for interface studies are magnetorheological fluids containing carbonyl iron microparticles, iron oxide nanoparticles on cellulose nanocrystal scaffolds, and iron oxide nanoparticles decorated on a plasmonic optical chemical bench. Instead of exploring fabrication methods to improve material functionalities for a specific application, the studies aim to gain insights into the material interfaces to acquire fundamental knowledge of material behaviours. Each of the three following sections in the introduction chapter offers a brief background on the related concepts and discusses experimental objectives for the application in focus. A general outline of the thesis can be found in the last section of this chapter.

1.2 A brief discussion of iron and iron oxides

1.2.1 Overview of iron and iron oxide compounds

Iron is one of the most abundant elements on Earth. The source of terrestrial iron can be traced to the cosmos.¹ The majority of iron exists in the form of molten metal or alloy in the inner and outer core of the planet.² On the surface of Earth, it exists primarily as various forms of iron oxides. Common examples of these minerals include hematite (Fe_2O_3), magnetite (Fe_3O_4), and goethite (FeOOH).³

Iron is a transition metal with atomic number 26 and electron configuration $[\text{Ar}]3d^64s^2$. According to the Pauli exclusion principle, two electrons in an arbitrary system cannot occupy the same state defined by identical sets of quantum numbers. This means that two electrons in the same orbital must have opposite spins. Electron spin generates magnetic momentum. However, magnetic moments from two electrons in the same orbital with opposite spins cancel out, and no residual magnetic momentum is left.⁴ Of the six electrons in the 3d-shell of iron, five electrons are of $+1/2$ spin quantum number, and one is of $-1/2$. The four unpaired electrons in the 3d orbital of iron lead to spin polarization of the atom with a permanent magnetic moment.

Iron supports a wide range of oxidation states due to the closeness in energies of the 3d and 4s orbitals, of which +2 and +3 are the most common. Despite its permanent magnetic moment, not all forms of iron or iron-based compounds are magnetic. In the following sections, we briefly review several aspects of magnetism relevant to this thesis, followed by a description of the two types of magnetic iron-based particles used in this thesis: "carbonyl" iron particles and magnetite nanoparticles.

1.2.2 Types of magnetism

The origins of magnetism, and ultimately of the magnetic properties of materials, can be traced to contributions from the spin and orbital motions of electrons, the magnetic moments of electrons, and the resulting magnetic moments of atoms and ions. Magnetism is, therefore, essentially a quantum mechanical phenomenon. It depends on the charge and spin of the electron and can be described within the Pauli exclusion principle. Since magnetic monopoles do not exist, the magnetic moments of nuclei and of electrons in atoms and ions correspond to the lowest order of magnetic dipole. Paramagnetism refers to the permanent magnetic moment that arises from unpaired electrons in atoms or molecules. The various types of magnetic behaviour in solids are due to the presence of a well-defined magnetic moment, i.e., paramagnetism, ferromagnetism, antiferromagnetism, and ferrimagnetism. Paramagnetic materials are attracted to a magnetic field by coupling with their magnetic dipole moment.⁵ When an external magnetic field is applied, the spin of the unpaired electrons in each atom can be induced to align parallel to the magnetic field, causing a net attraction. Paramagnets do not retain any magnetization without an externally applied magnetic field because the energy barrier to spin reorientation is on the order of the mean thermal energy. Paramagnetism can exist in materials even when there are interactions between the magnetic moments. As long as these interactions are sufficiently weak, as stated above, no net magnetization occurs, and so the material can be considered paramagnetic. This behaviour occurs, for example, in ferromagnetic materials above their critical temperature and in nanomagnetic materials such as magnetic nanoparticles.

Diamagnetic materials contain only paired electrons. When an external magnetic field is applied, the orbital electrons (as moving charges) experience a counter force known as the Lorentz force. This Lorentz force deflects the path of electrons and produces a current

counterclockwise about the applied magnetic field, which leads to a negative induced magnetic moment.⁶

Magnetic properties manifested by crystalline materials depend on the crystal lattice (space group) and on chemical composition. Magnetic materials are generally classified as ferromagnetic, ferrimagnetic, or antiferromagnetic.

In a crystal lattice, atoms are proximal, meaning interatomic interactions like dipole-dipole and exchange interactions can occur among magnetic atoms and ions.^{5, 6} Interactions among spins determine whether the spins are parallel or antiparallel. In quantum mechanical terms, this exchange interaction is a quantum mechanical phenomenon that can be formulated via the Heisenberg exchange Hamiltonian:^{5, 7, 8}

$$\mathcal{H} = -2JS_i \cdot S_j$$

S_i and S_j are the total spins of the two atoms. J is the exchange constant that governs the orientation of the spins. Parallel spins are favoured when J is positive, while antiparallel spins are favoured when J is negative. Parallel spins lead to ferromagnetism, and antiparallel spins with equal magnitude lead to antiferromagnetism. When the spins are antiparallel with unequal magnitudes, ferrimagnetism occurs.

We should note that the exchange interactions are not only direct, short-range interactions between immediate atoms. Indirect interactions mediated by an intermediate atom such as oxygen can also occur. Double exchange occurs when an electron is exchanged between the same cations of different oxidation states, for example, between the two iron cations in $\text{Fe}^{3+}\text{--O--Fe}^{2+}$ of the magnetite inverse spinel lattice via a symmetry-adapted p-orbital on oxygen.^{8, 9} The lowest energy of such systems corresponds to a parallel alignment of the spins in the two Fe ions,

giving rise to ferromagnetism.⁸ In contrast, superexchanges occur between the same cations of the same oxidation state, such as in $\text{Fe}^{3+}\text{-O-Fe}^{3+}$, and the 180° configuration of the spins favours an antiferromagnetic interaction where the resulting spin pair is antiparallel.^{8, 10}

The alignment of spins through exchange interactions corresponds to the most favourable energy state, meaning the spins remain aligned in the absence of an applied magnetic field^{5, 6} until the Curie point is reached. The Curie point is a critical temperature at which enough thermal energy is supplied to randomize the spin alignment. The spontaneous magnetization diminishes at the Curie point, and the crystal starts to behave like a paramagnet.⁶

1.2.3 Magnetic domains

Magnetic domains are regions within a material in which the spins are aligned in the same direction, thus creating a uniform magnetization. Ferromagnets and ferrimagnets below the Curie point spontaneously organize into many magnetic domains depending on the physical dimensions of the material. Domain formation minimizes magnetostatic energy.¹¹ The magnetization of a magnetic material leads to an external magnetic field. Simultaneously, an internal field called the demagnetizing field is produced in response, opposing the magnetization.¹¹ The larger the demagnetizing field, the larger the magnetostatic energy. To minimize magnetostatic energy, magnetic materials above some critical sizes divide themselves into two or more magnetic domains. These magnetic domains have different directions that compensate for each other, so the net magnetization vanishes. Consequently, the magnetostatic energy becomes zero.

Forming magnetic domains has energy costs. Firstly, most magnetic materials have magnetocrystalline anisotropy, meaning that it is easier for magnetization to occur along one of the crystallographic axes (the easy axis) than the others. The additional energy cost of changing the magnetization of the domain to a less favourable direction is called the magnetocrystalline anisotropy energy.¹¹ Secondly, changing the magnetization of a ferromagnetic or ferrimagnetic crystal produces a spontaneous change in the dimensions of the crystal. However, since the magnetic domains are confined in position by their surroundings, a type of strain called magnetostriction arises from the magnetic interactions.⁶ In addition, the presence of defects such as impurities or dislocations in the crystal lattice can produce internal stress that acts as a barrier to changes in magnetization.¹¹ The energy required to overcome this strain is called magnetoelastic anisotropy energy. The different magnetic domains are separated by domain walls. This is a transitional area where the magnetic spins gradually turn between oppositely magnetized regions, and the system reaches the state of lowest energy.¹¹

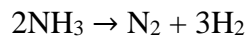
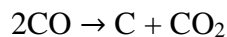
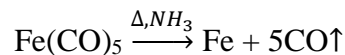
1.2.4 Superparamagnetic nanoparticles

When the size of a ferromagnetic or ferrimagnetic crystal is reduced until multiple domains are no longer supported inside the crystal, it becomes a single-domain particle. All local spins are parallel within these single-domain particles, and the direction of this "macrospin" is determined by an external magnetic field. The behaviour of the spin in single-domain nanoparticles is similar to that of paramagnetic particles, and single-domain nanoparticles are therefore referred to as superparamagnetic. The sizes of superparamagnetic particles depend on the crystal lattice, but they must all be sufficiently small. For example, superparamagnetic magnetite nanoparticles generally have diameters under 17 nm.¹²

Superparamagnetic particles reorient or relax their spin to a new direction to align with the external field via two mechanisms. The first mechanism is Brownian relaxation, which refers to the physical rotation of the particle through diffusion in a carrier liquid. The second mechanism is Néel relaxation, in which the magnetic spin flips between its two opposite directions along the easy axis of magnetization within the particle when thermal energy exceeds the internal magnetic anisotropy energy.⁸

1.2.5 Carbonyl iron particles

Carbonyl iron particles are α -iron microparticles produced from the thermal decomposition of iron pentacarbonyl vapour.¹³ Particle sizes produced by this method range from 0.2 - 8.0 μm . The reaction process is described in the following equations:



Liquid iron pentacarbonyl vaporizes at approximately 103°C and decomposes at 250 – 300°C¹³ with ammonia as a catalyst. The relatively low pressure and temperature in the reaction procedure ensure that α -iron is the only type of iron allotrope that is produced. This allotrope was confirmed by electron diffraction in TEM.¹³ In addition, x-ray crystallographic data suggested that 3 wt.% of impurities exist in the as-produced carbonyl iron particles.¹³ These impurities include a small amount of cementite (Fe_3C), but more importantly, they are loosely bound or trapped carbon, oxygen and nitrogen atoms in the α -iron lattice structure.¹³

α -iron has a body-centred cubic (bcc) crystal structure (Figure 1.1A) and is ferromagnetic below its critical point of 771°C.¹⁴ At around the critical point, thermal excitations of the spin oscillations destroy the long-range magnetic order driving a phase change. Above the critical point, spin fluctuations lead to the formation of short-range magnetic ordering and the turning of the material into paramagnetic.⁵

1.2.6 Magnetite nanoparticles

Magnetite is one of the most common iron oxides with the chemical formula Fe_3O_4 . The lattice structure of magnetite is an inverse spinel, as shown in Figure 1.1B. In the unit cell of the inverse spinel structure, O^{2-} anions form a close-packed face-centred-cubic structure.¹⁵ There are octahedral and tetrahedral interstitial sites within the close-packed structure. Half of the Fe^{3+} cations occupy tetrahedral sites, while the other half, along with Fe^{2+} cations, occupy octahedral sites.¹⁵ The chemical formula of magnetite can, therefore, also be written as $[\text{Fe}^{2+}\text{Fe}^{3+}][\text{Fe}^{3+}]\text{O}_4$.¹⁵

Magnetite appears black because it has more than one oxidation state. A process called intervalence charge transfer occurs when an electron is transferred between two adjacent Fe ions with different oxidation states. This interaction typically results in the absorption of light in the visible and near-IR region and gives magnetite its dark colour. In real-life conditions, however, magnetite nanoparticles are almost always partially oxidized by air and contain surface maghemite, which changes the colour of the nanoparticles from black to brown. Maghemite has the same inverse spinel structure, except that all Fe^{2+} cations have been oxidized to Fe^{3+} .

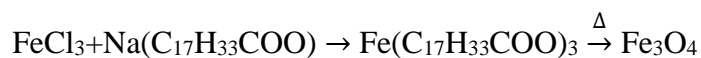
Magnetite is ferrimagnetic by virtue of exchange interactions in its crystal lattice. The Fe^{3+} cations occupying the tetrahedral sites have $3d^5$ configuration and a net magnetic moment of

5 μB .¹⁵ The octahedral sites hold both Fe^{3+} ($3d^5$, 5 μB) and Fe^{2+} ($3d^6$, 4 μB) cations. The Fe^{3+} and Fe^{2+} cations in the octahedral sites aligned ferromagnetically via double exchange interaction, thus having a combined magnetic moment of 9 μB .¹⁵ In contrast, the Fe^{3+} cations in the tetrahedral sites aligned antiferromagnetically to the Fe^{3+} in the octahedral sites via superexchange interaction.¹⁵ A net magnetic moment of 4 μB is produced in each unit cell of magnetite as a result of all spin interactions in the crystal lattice.

Many methodologies have been developed for the synthesis of magnetite nanoparticles¹⁶, the two most common of which are co-precipitation and thermal decomposition. The co-precipitation method precipitates magnetite nanoparticles from an aqueous solution of ferric and ferrous ions. The overall reaction equation for co-precipitation is:



The thermal decomposition method employs organometallic compounds such as iron pentacarbonyl, iron acetylacetonate, and iron oleate.⁸ The magnetite nanoparticles are prepared by the decomposition of the organometallic precursors at high temperatures ($> 300^\circ\text{C}$) in a high-boiling point solvent. The thermal decomposition reaction of iron oleate in octadecene is represented by:⁸



In this thesis, we employed a co-precipitation method to synthesize our magnetite nanoparticles to eliminate surface ligands on the nanoparticles as much as possible. Detailed synthesis is described in the experimental section in Chapter 5.

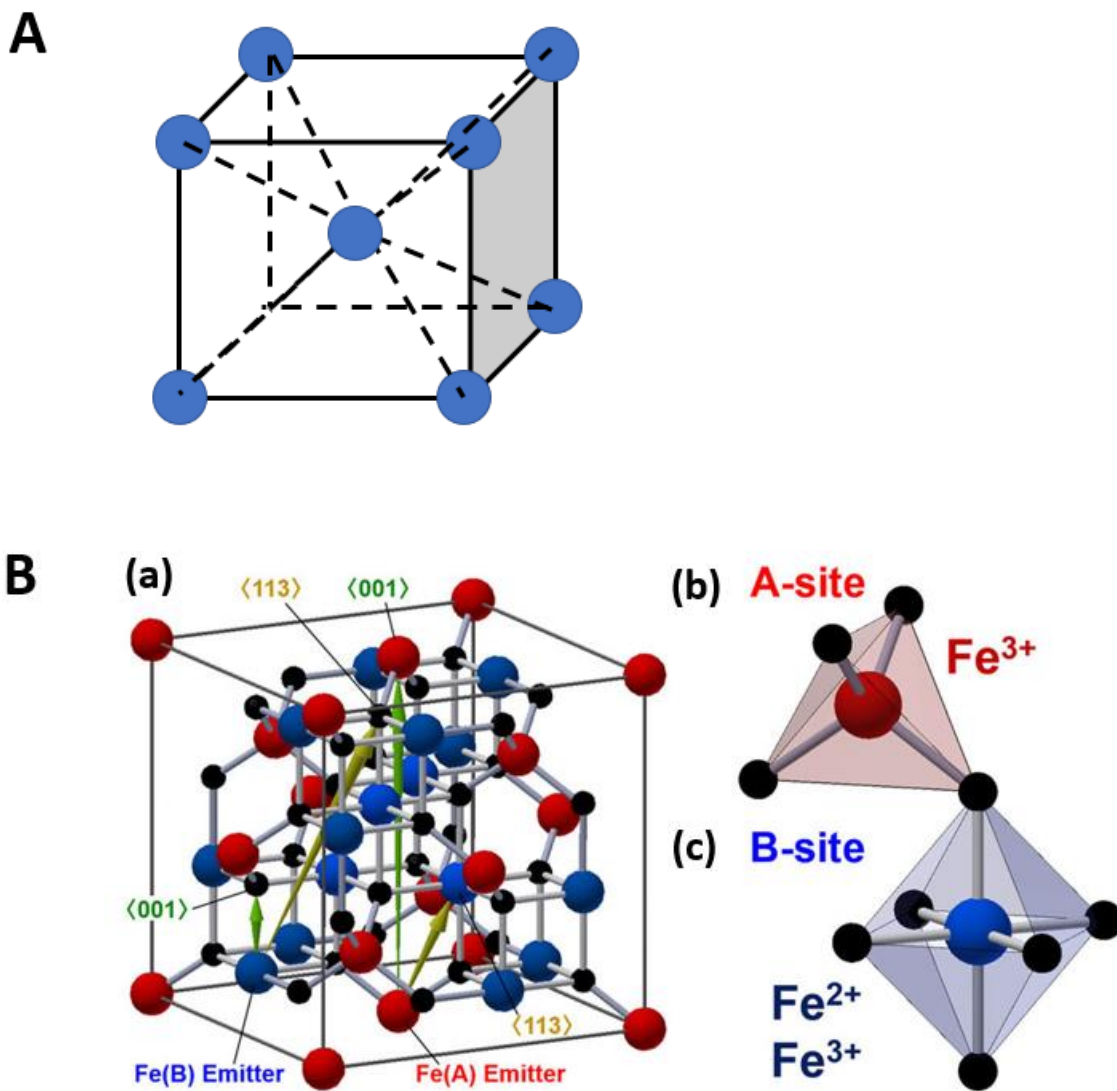


Figure 1.1. (A) A unit cell of the body-centred cubic (bcc) crystal structure for α -iron; the blue circle represents Fe(0). (B) A unit cell of the inverse spinel crystal lattice structure (a) with (b) representing the tetrahedral or "A"-site and (c) representing the octahedral or "B"-sites. In both A-sites and B-sites, O^{2-} anions (black dot) form the tetrahedral or octahedral structures, while Fe^{3+} and Fe^{2+} cations occupy their respective interstitial sites. Figure X(B) is adapted from reference (17), copyright © 2018 John Wiley & Sons, Ltd.

1.3 Background literature review for each chapter

1.3.1 Iron microparticles in magnetorheological fluids

1.3.1.1 Magnetorheological fluids (MRF)

Magnetorheological fluids (MRF) consist of magnetically "soft" microparticles, sized approximately 1 – 10 μm , suspended in carrier fluids like perfluoropolyethers, silicones, or hydrocarbons. The fluids are supplemented with additives, usually surfactants to stabilize the particles against undesirable aggregation and sedimentation by encapsulating them in a sterically repulsive organic shell.¹⁸ MRFs belong to the more general class of "smart materials" due to their ability to adjust rheological properties in response to an external magnetic field.¹⁹ The microparticles in MRFs are multi-domain systems where the magnetic domains are randomly oriented when no magnetic field is applied.^{19, 20} The external magnetic field aligns the dipoles of the magnetic domains along the magnetic field lines.²⁰ As a result, the particles move under the magnetic force to align as chain-like structures.^{19, 20} Figure 1.2 shows the reversible alignment of the microparticles. Columnar alignment of the particles restricts fluid flow in the horizontal (shear) direction between the magnets. Under microprocessor control, the ability to change the yield stress of MR fluids according to the magnetic field enables one to alter structural damping and stiffness coefficients, making the structure "smart" or "intelligent." The yield stress in an MRF is the applied stress that must be exceeded in order to make the structured fluid flow. The apparent viscosity of the MRF can increase by factors of 10^5 - 10^6 or more – within a few milliseconds when the magnetic field is applied.

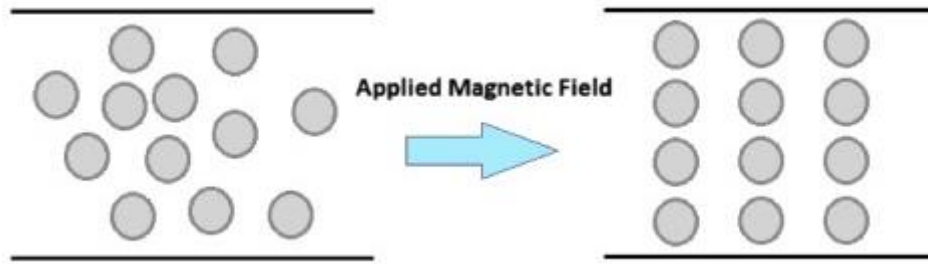


Figure 1.2 Schematic images of MRF particles in dispersion become reversibly aligned after an external magnetic field is applied. Adapted with permission from reference (19) Copyright © 2022 Elsevier B.V.

Below a critical shear stress threshold called the "apparent yield stress," Figure 1.2 suggests that the MRF can be reversibly converted from a liquid state to a semi-solid state.^{19–21} The aligned particle network is disrupted when the shear stress exceeds the apparent yield stress, and the MRF starts to flow.²² The viscosity of the MRF depends on the magnitude and direction of the applied magnetic field as well as the applied shear.^{22, 23}

Because of their magnetically tunable viscosity, MRFs are ideal for applications that require quick, continuous, and reversible rheological changes.²⁰ These applications generally involve interfaces between electrical power input and mechanical power output or replacements of mechanical components, such as dampers, valves, brakes, clutches, actuators, and polishing.^{19,}
²⁴ In recent years, MRFs have also been employed in soft robotic systems.^{25–27}

Despite the wide range of applications of MRFs, the manner by which the fluids age (degrade over time) has drawn attention because the failure modes of MRFs are complex, making the development of predictive models of the useful lifetime of the fluids a difficult task. It turns out that an important feature of how MRFs degrade is related, at least in part, to

nanoscale surface chemistry; hence our interest in probing nanoscale changes at the surface of iron microparticles and how they might be linked to long term performance metrics. The next section gives a brief review of what is currently known about the role of carbonyl iron particles in MRF aging.

1.3.1.2 The role of oxidation of carbonyl iron particles in the degradation of MRFs

To achieve fast switching and desirable rheological properties, it is desirable that the magnetic microparticles exhibit low coercivity and high saturation magnetization. Coercivity refers to the ease with which magnetic domains can be moved (aligned) in a magnetic field. Saturation magnetization refers to the limit beyond which the applied field, H , has maximized domain motion so that the minute magnetic fields within the particles add together to yield a large (saturated) magnetic induction, B . Iron particles are widely preferred for their low coercivity and high magnetic saturation. Saturation magnetization is on the order of 2.1 T at room temperature. The highest purity particles are now obtained by the chemical vapour deposition (CVD) process, where iron pentacarbonyl ($\text{Fe}(\text{CO})_5$) is thermally decomposed. The powders produced by CVD are called "carbonyl iron" particles. Since iron pentacarbonyl can be obtained in high purity, a well-designed CVD process can yield particles with > 99.7% chemical purity. The resulting particles are mesoscale and spherical. Mesoscale iron particles are desirable because they comprise many magnetic domains, raising the saturation magnetization. Spherical particles are desirable because they suppress or eliminate shape anisotropy. High purity particles provide fewer points where domain wall motion can be pinned. Since impurities cause magnetic hardness in iron, they also cause mechanical hardness because dislocation motions are suppressed. Non-abrasive particles are desired for use in MRF-based devices.

It is not surprising that the rheological properties of MRFs depend on particle concentration and density, particle size, shape distribution, properties of the carrier fluid, additives, applied field, temperature, and other factors. The interdependency of all these factors is very complex. A review by Kumar et al. explains some of the challenges.²⁸ Ongoing research attempts to understand the complex interplay of the many factors identified as contributing to MRF aging.¹⁹ Carbonyl iron particles typically occupy 20-40% of the volume in MRFs.²⁹ Not surprisingly, oxidation has been examined as a component of MRF aging. Oxidation begins at the interface, where it can be assisted by adventitious water. The types of iron oxides are varied. They include iron(II) oxide, wüstite (FeO), magnetite (Fe₃O₄), iron(III) oxide (Fe₂O₃), the crystalline polymorphs called alpha phase hematite (α -Fe₂O₃), beta phase β -Fe₂O₃, gamma phase maghemite (γ -Fe₂O₃), and epsilon phase ϵ -Fe₂O₃. These can undergo polymorphic transitions under various conditions.³⁰ Particle-particle collisions can cause spalling of the brittle oxides, leaving debris that can enhance the abrasion of iron microparticle surfaces. Polymorphism among iron oxides can occur at the nanoscale.³⁰ This makes the study of the oxides at carbonyl iron surfaces of fundamental interest beyond applications in MRF formulations and applications. Studies have found that oxidation of the iron particles decreases the overall saturation magnetization of the MRF.^{19,29} In addition, oxidation is associated with increased fluid viscosity when the MRF is at rest.²⁹ It is not certain whether this increase in viscosity is related to shedding fragments from the brittle oxide shell into smaller, non-magnetic particles.³¹

Chapter 2 of this thesis is devoted to gaining nanoscale (surface) insights into the oxidation of carbonyl iron particles submerged in hydrocarbon and fluorocarbon MRF carrier fluids. From a materials perspective, the microparticles in MRFs were subjected to device under test (DUT) conditions in a prototype MRF clutch system designed at the Université de

Sherbrooke. The DUT experiments add relevance and open channels to understanding how surface oxidation might be implicated in MRF aging. In other words, the chapter seeks to fill in some of the knowledge gaps that exist between iron microparticle surface chemistry and real world device performance. Past research has given little attention to the chemical reactions occurring at the particle-fluid interfaces, alongside regular oxidation. We performed X-ray photoelectron spectroscopy (XPS) depth resolution studies to monitor the spatial distribution of iron oxidation states as well as the presence of other chemical species on the surface of pristine and expired carbonyl iron particles.

1.3.2 Carboxylated cellulose nanocrystal cryogel scaffolds

Nanocellulose is a collective term that refers to cellulose nanofibrils (CNF) and nanocrystals (CNC) as well as bacterial nanocellulose (BNC). The present thesis focuses on CNC and its use in making directionally oriented porous scaffolds. CNC is widely produced by the so-called sulfuric acid process. High-temperature hydrolysis and oxidation remove the amorphous components of the raw cellulosic starting material. Simultaneously, the surface of CNC becomes lightly sulfated. The sulfate moieties confer a negative charge onto the nanocrystal. The process has the drawbacks that the sulfate moiety is thermally unstable and that for manufacturing scale-up, the byproducts of the synthesis require capital equipment intensive waste capture and recycling. In view of the worldwide growing commitment to sustainability and Green engineering and chemistry, our group has developed a procedure to make a carboxylated version of CNC. The process uses only dilute hydrogen peroxide and yields waste in the form of very dilute sugars, trace furfurals, and water. The peroxide is fully consumed in the reaction. The resulting CNC is lightly carboxylated, offering a more desirable functional group for chemical

derivatization. CNC is a highly crystalline, needle-like particle with widths ranging from 2 – 20 nm and lengths from around 100 – 300 nm, depending on the cellulose source and synthesis conditions.³² The high surface area of CNC, the abundance of surface hydroxyl groups, and the availability of surface carboxylic acid enable many organic functional group modifications that enhance the appeal of CNC in a host of application domains.³² Applications of CNCs in the biomedical field include drug release systems, scaffolds for tissue engineering, skin replacements for burns and wounds, stent coverings and bone reconstruction nerves, gum and dura mater reconstruction, and blood vessel growth.³² CNC, along with other nano- and micro-cellulose varieties, is known to elicit lesser or non-immunogenic reactions.³³ The notion of "scaffolding" raises the importance of pore distributions in cellulosic structures for tissue engineering. Anticipating our discussion of unidirectional alignment by freezing, alignment of CNC can rather easily be achieved by flow anisotropy induced by air currents and fluid gradients. Isotropic to liquid crystal phase transitions yield chiral nematic left-handed helicoid suspensions or solid films. The diamagnetic response of the CNC rod enhances chiral nematic alignment in strong magnetic fields. This suggests ways of coupling the magnetic field response of CNC to other types of hydrodynamic flow anisotropy to achieve alignment. Flow-induced alignment might then be coupled with strategies to regulate the distribution of pores in CNC-based scaffolds.

Porous materials with interconnected pore structures of well-defined shape, size, and size distribution are highly desired in separation processes. Representative examples include filtration membranes³⁴, catalyst supports³⁵, gas storage devices³⁶, and microfluidic devices³⁷, tissue engineering scaffolds³⁸, and medical implants³⁹. Porous structures may be formed by incorporating a pore generator – a porogen – into a host matrix. A porogen can be a gas, a liquid, or an organic or inorganic solid. In polymers, porogens are incorporated into the fluid or melt

phase, solidified, and then extracted to leave the porous monolith of film. As mentioned above, the scaffold metaphor describes three-dimensional porous structures that are designed to promote live cell-biomaterial substrate interactions, cell adhesion, gas transport and flow of nutrients and regulatory components to promote cell viability, proliferation, and differentiation. Scaffold materials for tissue engineering are discussed in the book edited by Laurencin and Nair.⁴⁰ Cellulose cryogels based on dissolved cellulose recently emerged as an attractive material class for biomedical scaffolding.⁴¹ Cryogels are sponge-like microporous/nanoporous structures produced at sub-zero temperatures, where ice formation occurs throughout the gel medium.⁴¹. During cryogelation, ice acts as the porogen. The resulting scaffolds are collected via freeze-drying.⁴¹

Advances in the use of porous nanocellulose structures from porous gels and films have been discussed by Ferreira et al.⁴² Despite the popularity of nanocellulose for cryogel materials, the subclass of CNC remains a new candidate for this application. The author of this thesis is aware of only two published studies describing CNC-based cryogel scaffolds.^{43,44} The paper by Munier⁴³ is particularly interesting for its emphasis on unidirectional freezing that takes advantage of the known propensity for sulfated CNC rods to self-associate and aligns in water. Unidirectional alignment is conferred on suspensions of nanorods by freezing water suspensions of nanocrystals. Unidirectional freezing refers to the process of freezing an aqueous suspension of CNC to achieve high alignment of the nanorods in the freezing direction. Figure 1.3 from Munier illustrates the principle of unidirectional freeze casting. Plunging a suspension into a cold bath leads to a gradient in the hydrodynamic flow field as the water freezes. Hydrodynamic alignment is locked in once the nanocrystals are oriented. The Munier experiment raises some questions that are explored in Chapter 3 of this thesis: Do carboxylated cellulose nanocrystals

with a lower surface potential than sulfated CNC undergo unidirectional alignment? In view of the diamagnetic response of CNC, can the alignment be assisted by an applied static magnetic field? By binding magnetite nanoparticles to the surface of carboxylated CNC, how does magnetic field-assisted alignment couple with unidirectional freezing to yield oriented magnetite-CNC cryogel monoliths?

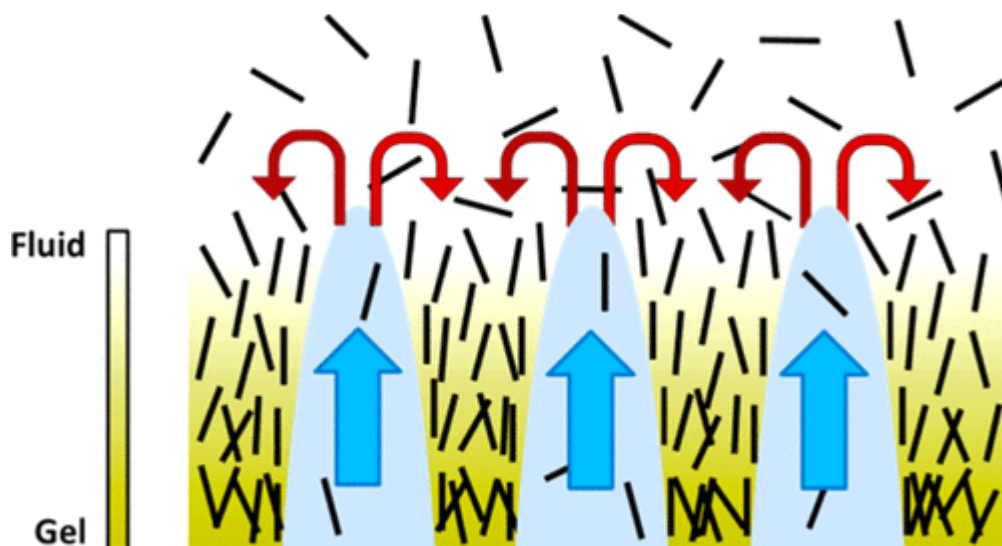


Figure 1.3 Illustration of the principle of unidirectional freeze casting. An elongated flow field is identified by the blue arrows in the figure. The freezing front decreases in the direction towards the top of the image where CNC particles are evidently randomly oriented. Reprinted with permission from reference (43) Copyright © 2022 American Chemical Society.

Chapter 3 of this thesis focuses on new aspects of unidirectional freezing in ice templated CNC cryogels by coupling hydrodynamic flow with the magnetohydrodynamic response of carboxylated cellulose nanocrystals and magnetite nanoparticle-decorated CNC. With scanning electron microscopy (SEM) and small-angle x-ray scattering (SAXS), we trace morphological

details spanning length scales from micrometers to sub-nanometers. Porosity in the anticipatory scaffolds is examined by dynamic water sorption (DVS).

1.3.3 Optical chemical bench sensing platforms to study interfaces at the nanoscale

A persistent challenge to the study of interfaces in nanoscale systems is how to collect information in a non-destructive way over the macro-nano interface. Vibrational spectroscopy, specifically Raman microspectroscopy, has emerged as an enabler, particularly when coupled with the highly localized near-field plasmonic response of coinage metal particles where enhanced local fields at the plasma resonance condition magnify the probability of Raman events. In this section of the Introduction, we provide some background on how methods from the photonics industry can be adapted to build sensing platforms suitable for nanoscale Raman scattering. We describe the sensing platform as an Optical Chemical Bench (OCB). The simplest OCB is a slab waveguide configuration (Figure 1.4) whose surface can be chemically modified to create "recognition elements," effectively tailoring the surface so that the desired nanoscale construct can be spectroscopically probed.

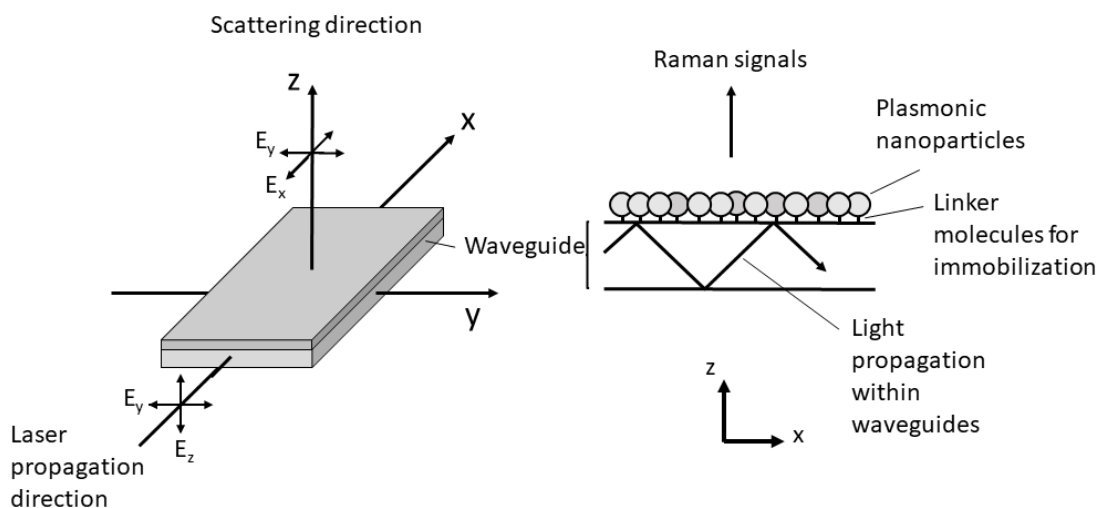


Figure 1.4 Basic schematic of the OCB design. On the left, a laser beam is shown to be guided into the OCB, consisting of a waveguide decorated with plasmonic nanostructures. On the right, an enlarged view of the same waveguide is shown. Plasmonic nanoparticles are immobilized onto the surface of the waveguide, serving as sensory elements and binding sites for incoming molecules.

1.3.3.1 Literature review of integrated optics waveguide Raman spectroscopy

Chapter 4 reviews some salient principles of Raman spectroscopy and integrated optics and offers a detailed description of the integrated waveguide Raman spectroscopy optical setup that was built for this thesis.

Integrated optics refers to the creation of minute passive and active circuits and circuit elements whose function is to conduct light from source to detector (passive guiding) or to achieve lasing or amplification, among other processes (active response). In some ways,

integrated optics is built on the semiconductor electronic chip paradigm where minute (nanoscale) electronic wires are integrated with electronic device architectures like transistors, detectors, and other components. In this paradigm, the electrical wiring on the electronic chip becomes "optical wiring" on the optical chip. In microchip electronics, the wires are passive elements whose role is to move electrons (electron waves) from region to region on the chip real estate. In integrated optics, the "wires" are optical waveguides whose role is to move photons (electromagnetic waves) from region to region on an optical or optoelectronic chip.. The functional operation of the wires can be described in the frame of the electron transport equations (conducting wires) and Maxwell's equations (optical wires), both under suitable boundary conditions.

The seminal paper in integrated optics Raman spectroscopy is the 1974 publication by Dupeyrat and co-workers.⁴⁵ The paper established that the flux of Raman light scattered from the waveguide configuration could experience an increase in the order of 2000 with respect to a traditional Raman backscattering geometry. This emphasizes a singular advantage of the guided wave configuration because spatial confinement of the laser beam in the waveguide results in enhanced optical intensity, meaning that the probability for Raman scattering is significantly increased in a thin film. But it is the boundary conditions on wave propagation where the striking advantage of guided wave Raman spectroscopy becomes manifest. As represented by equation 4.1 in Chapter 4 of this thesis, waveguiding can be described in terms of an eigenvalue equation. Simply put, one can excite what are called discrete transverse magnetic (TM_m) or transverse electric (TE_m) eigenmodes of the waveguide. The subscript "m" enumerates the mode number, which in effect counts the number of nodes in the field amplitude confined to the waveguide. Because of the orthogonality, the eigenmodes TM_m and TE_m , integrated optics Raman allows one

to excite discrete polarization states of the waveguide. Moreover, because the location of the maximum field amplitude of the guided wave depends on the refractive index of the waveguide and its surrounding medium (i.e., the system boundary conditions) and on the mode number and its polarization, one can obtain spatially resolved polarized Raman scattering. In effect, the integrated optics experiment allows one to interrogate the Raman polarizability tensor thanks to its relation to the tensorial character of the waveguide refractive index. In terms of the OCB construct mentioned at the opening of this section, integrated optics position one to obtain detailed information at interfaces, especially when the optical field is enhanced by coupling with plasmonic nanoparticles. We next give an overview of the subject of plasmonics and sensing to frame the research we report in Chapter 5.

1.3.3.2 Plasmonics and sensing

Plasmonics refers to the coupling of light with charges like electrons in nearly-free electron metals and other systems with loosely bound carriers to overcome the diffraction limit and localize light to sub-wavelength dimensions to achieve large field enhancements. Surface plasmons often play a pivotal role in plasmonics. Surface plasmons are described as coherent delocalized electron oscillations excited by resonant electromagnetic field coupling at the interface of materials like metals. Two types of surface plasmon resonance are identified: localized surface plasmon polaritons (LSPRs), and propagating surface plasmon polaritons (SPPs). LSPRs are the coherent oscillation of conduction electrons in nanostructures of sizes smaller than the wavelength of incident light that excites the plasmon.⁴⁶ On the other hand, SPPs are optical waves that travel at the metal-dielectric interface.⁴⁷ Excitation and tuning of the SPPs can be achieved by modifying the angle of incidence of the light and the periodic nanostructuring

of the metallic surface.⁴⁸ In terms of spatial reach, LSPRs are closely bound to the surface of nanostructures, expanding approximately 30 nm and dissipating exponentially into the surrounding medium. In comparison, SPPs penetrate about 10 nm into the metal medium and expand to tens of microns or more into dielectrics.^{47, 49}

Both LSPRs and SPPs are sensitive to changes in the refractive index of the immediate surrounding medium.^{48, 50–52} Probing refractive index changes form the basis for the attenuated total reflectance (ATR) Otto and Kretschmann configurations.^{53, 54} The ATR configuration is one of the most well-studied types of plasmonic sensors.⁵² Outputs of the refractive index plasmonic sensor include variations in wavelength, intensity, phase changes, and polarization of the outgoing light⁴⁷ that can be correlated with the presence of surface adsorbates. Based on the LSPR, SPP, or combinations of both, many variants of plasmonic refractive index sensors have emerged.^{52, 55, 56}

Another well-studied area of plasmonic sensing exploits the enhancement of the Raman effect. This is the Surface-Enhanced Raman Scattering (SERS) effect. Resonant excitation of surface plasmons produces substantial enhancement of electromagnetic field at the surface, which leads to amplification of the otherwise inherently weak Raman signals.⁴⁸ In addition to physically increasing the intensity of the electromagnetic field around the plasmonic substrate, underlying chemical effects also contribute to SERS enhancement. Chemical enhancement may occur when there is charge transfer between adsorbed molecules and the plasmonic surface.^{48, 57} Many different kinds of plasmonic platforms and substrates have been created to increase the efficiency of Raman spectroscopy, and a molecular level of sensitivity has been achieved.^{48, 58, 59}

In keeping with the subject of plasmonic field enhancement, Chapter 5, gives an account of how we recruit core-shell silver-gold plasmonic nanoparticles to achieve the effect. Our study

builds from the method that was first introduced by our research group⁶⁰ before the notion of plasmonic waveguides was popularized beyond the standard ATR Otto or Kretschman configurations, extending non-destructive Raman spectroscopy to the thin-film waveguide regime over much longer length scales than ATR. In this thesis, we configure the OCB as a nanoplasmonic sensing device to provide spectroscopic insight into how surface-bound ligands bind to metal and metal oxide nanoparticles, and how they may be involved in mediating particle-particle interactions that result in interparticle plasmon coupling and interparticle magnetoplasmonic effects. Our OCB merges integrated optics spectroscopy with plasmonics to achieve polarization-specific Raman scattering from 4-mercaptopyridine (4MPy) and 4-aminobenzoic acid (4ABA) as model molecules to calibrate Raman spectroscopic signatures associated with evanescent wave excitations of the plasmonic nanoparticle waveguide. The OCB is also used to probe ligand-mediated interactions between iron oxide nanoparticles and silver-gold core-shell plasmonic nanoparticles. This effort proves that Raman spectroscopy has the potential to provide non-invasive probing of composite nanostructures and give new insights into the various fabrication techniques for plasmonics and magnetoplasmonics today.^{61, 62}

1.3.3.3 Magnetic nanoparticles in optical sensors

Many optical sensing techniques are developed based on the use of magnetic nanoparticles (magnetic NPs). These optical devices commonly employ SERS, chemiluminescence, fluorescence spectroscopy, and surface plasmon resonance for refractive index sensing. In these approaches, magnetic NPs can play the role of catalyst, carrier of analyte for effective enrichment or separation, or as a tool to promote aggregation of magnetic NPs and thus to concentrate analyte for signal enhancement at SPR substrates.^{63, 64} An example of the

latter is the SPR-refractive index sensor introduced by Wang et al. These researchers conjugated magnetic NPs with antibodies to promote analyte binding. The magnetic NP-antibody-analyte was concentrated at an SPR sensor surface by collected particles with an external magnetic field. This procedure greatly enhanced sensing efficiency; the high refractive index of magnetic NPs is believed to have also contributed to the enhancement.⁶⁵ Similarly, conjugating of magnetic NPs and plasmonic nanostructures have been used for SERS readouts. Lai et al. detailed *in situ* and *ex situ* methods to create SERS substrates that contain excitable surface plasmons that are magnetically controllable. The *in situ* method consists of the direct deposition of plasmonic components onto magnetic NPs. The plasmonic component was achieved by reducing metallic ions to make nanoparticles on the surface of magnetic NPs. The *ex-situ* method requires pre-synthesized magnetic NPs and plasmonic nanoparticles that are co-assembled.

In addition to SPR-related sensing, composites of plasmonic materials and magnetic NPs can interact with propagating light under an applied magnetic field to produce what is called the magnetoplasmonic effect. There are two components to the magnetoplasmonic effect: the magneto-optical effect and the response of surface plasmons to the magneto-optic effect. The magneto-optical effect can be described in terms of the Kerr response for a transmission experiment or the Kerr effect for a reflection experiment. The application of a quasi-static magnetic field creates a gyrotropic medium in which left- and right-rotating elliptical polarizations can propagate at different speeds.⁶⁶ Reciprocal magneto-optical-plasmon interactions occur due to spectral overlap of the magneto-optical transition and the plasmon resonance.^{67, 68} As a result, with the help of specifically designed magnetoplasmonic devices, plasmons can be controlled with an applied magnetic field or be used to amplify magneto-optical effects.^{68, 69} This interplay between magneto-optical effects and surface plasmons is also very

sensitive to changes in the refractive index of the surrounding medium, making them useful for refractive index sensing applications.⁷⁰

Elsewhere, it was found that magnetic NP suspensions, commonly known as magnetic fluids, possess tunable refractive indexes depending on external temperature and applied magnetic field.⁷¹ Like the MRFs discussed in Section 1.3.1, magnetic NPs in magnetic fluids will form particle columns aligned with applied magnetic field lines when the magnetic energy overcomes the thermal energy of the particles that superparamagnetic spin states that are otherwise randomized by Brownian motion and low energy barriers between spin up and spin down superparamagnetic states (Neel rotation). As particles align, a magnetoelectric effect can be established. This effect changes the electric susceptibility of the particles, resulting in a change in the refractive index n_{MF} through the relationship, $n_{MF} = \sqrt{\varepsilon} = \sqrt{1 + \chi}$. Here ε is the dielectric constant (tensor) of the magnetic fluid, and χ is the electric susceptibility. The magnetoelectric effect depends on the direction of the magnetic field through the tensorial character of the refractive index.⁷² For an applied field parallel to the propagation direction of light, the refractive index increases with increasing magnetic field, while for an applied field perpendicular to the propagation direction of light, the refractive index decrease with increasing magnetic field.

The response of a propagating optical wave to anisotropy in the refractive index of a medium leads to the well-known phenomenon of birefringence. Birefringence is certainly at play in the magnetoelectric effect described above. This raises the questions for integrated optics Raman: is it possible to interrogate the refractive index tensor in an optical waveguide by polarized Raman spectroscopy and thus to obtain a readout of birefringence that is sedimented in the polarizability, but "read" not as conventional birefringence but as the localized readout of

vibrational modes in the waveguide? Then, if the waveguide is populated in the interior with magnetic NPs, is it possible to use integrated optics polarized Raman spectroscopy to detect TE-TM mode conversion in a gyrotropic waveguide?

Chapter 6 showcases how polarized Raman spectroscopy detects anisotropy in the refractive index of sol-gel derived hybrid organic-inorganic glass waveguide platforms. This optical anisotropy causes TE-TM mode conversion leading to polarization-specific Raman spectra. We borrow a strategy from the photonics literature on optical self-inscription in germanium-doped silica glasses⁷³ to "inscribe" optical anisotropy with a mode and polarization-selected guided wave in the hybrid organic-inorganic glass medium. The waveguide comprises guest methacrylic acid molecules and methylmethacrylate moieties covalently bound to a siloxy network formed by acid-catalyzed crosslinking. Thermal energy from the guided wave induces free radical crosslink formation in the hybrid glass. The crosslinking process raises the local refractive index, which in turn leads to a form of self-focusing of the laser.⁷⁴ Because optical inscription in the hybrid glass can be conducted with polarized light, the possibility exists that anisotropy in the local refractive index can be induced. A measure of the impact of optical anisotropy is the phenomenon of mode conversion. Since the waveguide refractive index goes approximately as $\sqrt{\epsilon_r}$, where ϵ_r is the relative dielectric permittivity, the off-diagonal elements in the ϵ_r tensor of the waveguide material provide coupling, hence a mechanism for conversion, between the two eigen polarization modes in the optical waveguide. In our guided wave Raman experiments, evidence for mode conversion is confirmed from careful spatial imaging of polarization-dependent changes in the C-H stretching modes after launching specific polarization (TE or TM) in the waveguide. Mode conversion in this experiment is manifested in spectral features of C-H stretching region that become contaminated with polarization that is forbidden in

the absence of mode conversion. Having calibrated the mode conversion experiment, we conducted exploratory studies in gyrotropic-like waveguides consisting of magnetic NPs doped in the hybrid glass slab waveguide core. For background, we note the theoretical treatment by Chung and Kim.⁷⁵ These researchers treat the case of mode conversion in a *lossless* (non-absorbing) gyrotropic waveguide medium relevant to guided wave modulators, switches, and phase shifters. The assumption that the waveguide is lossless simplifies the mathematics because the gyrotropic medium can be treated as having a dielectric permittivity tensor that is Hermitian. Regrettably, we find no treatments of gyrotropic media that incorporate optical loss. Magnetite nanoparticles are lossy. They absorb light in the visible domain. Light absorption by magnetic NPs is associated with thermally induced electron delocalization between adjacent Fe^{2+} and Fe^{3+} ions, where the electronic transitions arise from intervalence charge transfer transitions that occur in the visible and out into the near-IR region. Despite the lack of a resolved theoretical framework to understand mode conversion in *lossy* gyrotropic media, we hypothesized that the NPs, under the influence of an external magnetic field, might induce mode conversion. Our intention was to "sense" the intervention of the magnetic medium by "reading out" polarization mode conversion as was done for the case of optical self inscription.

1.4 Organization of the Thesis

This thesis is organized as follows:

Chapter 2 details the nanoscale studies of the surfaces of carbonyl iron microparticles in both hydrocarbon and fluorocarbon MRF fluid hosts after the MRFs have gone through repeated cycles of shear forces in the presence of different applied magnetic fields inside an MRF clutch.

We contrast the worked (aged) MRF particles with pristine particles from MRFs that have not seen service. SEM is used to obtain morphological detail about the particle surface. XPS depth-resolved analysis is performed to reveal the oxidation state of common species such as Fe, O, C, and F and give hints on the identity of the species. The study aims to understand the changes that occur at the particle-fluid interfaces as the particles degrade and expire during the operation of the MRFs.

Chapter 3 carries the theme of hydrodynamic flow, but now includes the superimposed diamagnetic field response of carboxylated cellulose nanocrystals (CNC) and magnetite nanoparticle-grafted CNC. We describe the fabrication of ordered cryogel porous scaffolds by templating the CNC with ice during unidirectional freezing. SEM is used to detail scaffold macroscopic morphology, such as pore size and pore. Pore sizes of different types of scaffolds are quantified and compared. Small Angle X-ray Scattering (SAXS) is performed to reveal structural details of the scaffolds over length scales ranging from ~ 10 nm to sub-nm. Water sorption by the scaffolds is quantified.

Chapter 4 marks a transition in the research on interfaces and matter at the nanoscale with a focus on Raman spectroscopy and how the technique can be deployed to study thin films and interfaces. We introduce the notion of an Optical Chemical Bench (OCB). The OCB is a planar slab waveguide that is co-opted as an autoscopic sensor useful in detecting ligands at the interface of plasmonic and magnetic nanoparticles. This chapter provides background to Raman scattering, surface-enhanced Raman scattering (SERS), and a detailed discussion of integrated optics Raman spectroscopy in planar slab waveguides. We describe the integrated optics spectrometer that was assembled to conduct the experiments that are elaborated in Chapters 5 and 6.

Chapter 5 demonstrates integrated optics spectroscopy experiments that combine polarized Raman and evanescent wave SERS (IO-PEWSERS) to detect ligand molecule binding and how ligands might mediate particle-particle interactions for plasmonics and magnetoplasmonic nanoparticle architectures on the OCB. The chapter starts with the fabrication of SiO₂ slab waveguides with silver-gold core-shell plasmonic nanoparticles sparsely anchored to the top of the OCB. Transmission electron microscopy (TEM), SEM, and X-ray photoelectron spectroscopy are employed to characterize the plasmonic nanoparticles and the OCB. The ability of IO-PEWSERS to probe molecular binding is tested with 4MPy and 4ABA adsorbates. The molecular orientation and mode of adsorption of 4MPy and 4ABA are interrogated by IO-PEWSERS by exciting different waveguide polarizations and coupling the evanescent field of multi-mode waveguide to a nanoplasmonic response. Spectral changes associated with 4MPy pyridine-proton interactions are discussed. The ability of IO-PEWSERS to probe iron oxide nanoparticles functionalized with 4ABA ligands is also examined.

Chapter 6 demonstrates how polarized Raman spectroscopy can detect mode conversion in self-inscribed sol-gel derived hybrid organic-inorganic slab waveguides. Guided wave thermally induced densification self-focuses the propagating laser beam. The densification process causes a local increase in the refractive index of the glass due to C-C bond formation when olefin moieties in the glass undergo crosslinking. Anisotropy in the refractive index of the waveguide can be inscribed. Polarized guided waves are used to interrogate the anisotropic refractive index, which, through the permittivity tensor, induces mode conversion. Evidence of mode conversion is "read" by monitoring C-H stretching vibrations and examining the polarization-dependent Raman spectral profile in the range 2800 – 3000 cm⁻¹. Validation of the mode conversion phenomenon in the "write" "read" guided wave experiments benchmarks a

return to the study of magnetic nanoparticles. Gyrotropic-like waveguides are fabricated in the hybrid sol-gel glass waveguides by incorporating magnetite nanoparticles. The lossy character of magnetite leads to strong attenuation of the propagating waveguide mode. Dilute conditions are found where Raman scattering from C-H vibrations can be imaged for evidence of mode conversion in the absence and presence of an applied magnetic field.

Chapter 7 concludes the thesis with summaries of results and suggestions for future work.

1.5 Copyright permissions

Permission for Figure 1.1B:



Site-sensitive X-ray photoelectron spectroscopy of Fe₃O₄ by photoelectron diffraction

Author: Yusuke Hashimoto, Munetaka Taguchi, Shun Fukami, et al

Publication: Surface & Interface Analysis

Publisher: John Wiley and Sons

Date: Oct 11, 2018

© 2018 John Wiley & Sons, Ltd.

Review Order

Please review the order details and the associated [terms and conditions](#).

No royalties will be charged for this reuse request although you are required to obtain a license and comply with the license terms and conditions. To obtain the license, click the Accept button below.

Licensed Content

Licensed Content Publisher	John Wiley and Sons
Licensed Content Publication	Surface & Interface Analysis
Licensed Content Title	Site-sensitive X-ray photoelectron spectroscopy of Fe ₃ O ₄ by photoelectron diffraction
Licensed Content Author	Yusuke Hashimoto, Munetaka Taguchi, Shun Fukami, et al
Licensed Content Date	Oct 11, 2018
Licensed Content Volume	51

Order Details

Type of use	Dissertation/Thesis
Requestor type	University/Academic
Format	Print and electronic
Portion	Figure/table
Number of figures/tables	1
Will you be translating?	No

Permission for Figure 1.2:



A review on the magnetorheological fluid preparation and stabilization

Author: M. Ashtiani, S.H. Hashemabadi, A. Ghaffari
Publication: Journal of Magnetism and Magnetic Materials
Publisher: Elsevier
Date: 15 January 2015

Copyright © 2014 Elsevier B.V. All rights reserved.

Order Completed

Thank you for your order.

This Agreement between Xining Chen ("You") and Elsevier ("Elsevier") consists of your order details and the terms and conditions provided by Elsevier and Copyright Clearance Center.

License number Reference confirmation email for license number

License date Apr. 16 2022

Licensed Content

Licensed Content Publisher Elsevier
Licensed Content Publication Journal of Magnetism and Magnetic Materials
Licensed Content Title A review on the magnetorheological fluid preparation and stabilization
Licensed Content Author M. Ashtiani, S.H. Hashemabadi, A. Ghaffari
Licensed Content Date 15 January 2015
Licensed Content Volume 374
Licensed Content Issue n/a
Licensed Content Pages 15

Order Details

Type of Use reuse in a thesis/dissertation
Portion figures/tables/illustrations
Number of figures/tables/illustrations 1
Format both print and electronic
Are you the author of this Elsevier article? No
Will you be translating? No

About Your Work

Title Insights into the interfacial chemistry in systems involving magnetic iron oxides
Institution name McGill University
Expected presentation date Aug 2022

Additional Data

Portions Figure 5

Permission for Figure 1.3:



Directional Freezing of Nanocellulose Dispersions Aligns the Rod-Like Particles and Produces Low-Density and Robust Particle Networks

Author: Pierre Munier, Korneliya Gordeyeva, Lennart Bergström, et al
Publication: Biomacromolecules
Publisher: American Chemical Society
Date: May 1, 2016

Copyright © 2016, American Chemical Society

PERMISSION/LICENSE IS GRANTED FOR YOUR ORDER AT NO CHARGE

This type of permission/license, instead of the standard Terms and Conditions, is sent to you because no fee is being charged for your order. Please note the following:

- Permission is granted for your request in both print and electronic formats, and translations.
- If figures and/or tables were requested, they may be adapted or used in part.
- Please print this page for your records and send a copy of it to your publisher/graduate school.
- Appropriate credit for the requested material should be given as follows: "Reprinted (adapted) with permission from (COMPLETE REFERENCE CITATION). Copyright (YEAR) American Chemical Society." Insert appropriate information in place of the capitalized words.
- One-time permission is granted only for the use specified in your RightsLink request. No additional uses are granted (such as derivative works or other editions). For any uses, please submit a new request.

If credit is given to another source for the material you requested from RightsLink, permission must be obtained from that source.

BACK

CLOSE WINDOW

1.6 Reference

1. Maoz, D. and Graur, O., 2017. Star formation, supernovae, iron, and α : Consistent cosmic and galactic histories. *The Astrophysical Journal*, 848(1), p.25.
2. Kong, L.T., Li, J.F., Shi, Q.W., Huang, H.J. and Zhao, K., 2012. Dynamical stability of iron under high-temperature and high-pressure conditions. *EPL (Europhysics Letters)*, 97(5), p.56004.
3. Lu, L. ed., 2015. *Iron ore: mineralogy, processing and environmental sustainability*. Elsevier.
4. Singh, A.K., 2016. Physicochemical, electronic, and mechanical properties of nanoparticles. *Elsevier Academic Press, San Diego*, pp.77-123.
5. Pepperhoff, W. and Acet, M., 2001. *Constitution and Magnetism of Iron and its Alloys*. Springer Science & Business Media, pp. 15-55.
6. McElhinny, M.W. and McFadden, P.L., 1999. *Paleomagnetism: continents and oceans*. Elsevier, pp. 31-37.
7. Heisenberg, W., Mehrkörperproblem und Resonanz in der Quantenmechanik. *Zeitschrift für Physik* 1926, 38 (6), 411-426.
8. Zhong, T. 2020. *Trapping Ferrofluid Patterns: Insights into Hierarchies of Order from Self-Organization of Magnetic Nanoparticles*. Ph.D. thesis. McGill University. Montreal.
9. Zener, C., 1951. Interaction between the d-shells in the transition metals. II. Ferromagnetic compounds of manganese with perovskite structure. *Physical Review*, 82(3), p.403.
10. Anderson, P.W., 1950. Antiferromagnetism. Theory of superexchange interaction. *Physical Review*, 79(2), p.350.

11. McElhinny, M.W. and McFadden, P.L., 1999. *Paleomagnetism: continents and oceans*. Elsevier, pp. 48-74.
12. Lin, C.R., Chiang, R.K., Wang, J.S. and Sung, T.W., 2006. Magnetic properties of monodisperse iron oxide nanoparticles. *Journal of applied physics*, 99(8), p.08N710.
13. Japka, J.E., 1988. Microstructure and properties of carbonyl iron powder. *JOM*, 40(8), pp.18-21.
14. Baker, H., Okamoto, H., 1992. *ASM Handbook, Volume 3: Alloy Phase Diagrams*. ASM International, Cleveland, pp.51, Figure 44.
15. Zhang, Z. and Satpathy, S., 1991. Electron states, magnetism, and the Verwey transition in magnetite. *Physical Review B*, 44(24), p.13319.
16. Niculescu, A.G., Chircov, C. and Grumezescu, A.M., 2021. Magnetite nanoparticles: Synthesis methods—A comparative review. *Methods*.
17. Hashimoto, Y., Taguchi, M., Fukami, S., Momono, H., Matsushita, T., Matsuda, H., Matsui, F. and Daimon, H., 2019. Site-sensitive X-ray photoelectron spectroscopy of Fe₃O₄ by photoelectron diffraction. *Surface and Interface Analysis*, 51(1), pp.115-119.
18. Zhang, P., Kamezaki, M., Otsuki, K., He, Z., Sakamoto, H. and Sugano, S., 2019, July. Development of anti-sedimentation magnetorheological fluids and its implementation to MR damper. In *2019 IEEE/ASME International Conference on Advanced Intelligent Mechatronics (AIM)* (pp. 400-405). IEEE.
19. Ashtiani, M., Hashemabadi, S.H. and Ghaffari, A., 2015. A review on the magnetorheological fluid preparation and stabilization. *Journal of Magnetism and Magnetic Materials*, 374, pp.716-730.

20. López-López, M.T., Kuzhir, P., Lacis, S., Bossis, G., González-Caballero, F. and Durán, J.D., 2006. Magnetorheology for suspensions of solid particles dispersed in ferrofluids. *Journal of Physics: Condensed Matter*, 18(38), p.S2803.
21. Carlson, J.D. and Jolly, M.R., 2000. MR fluid, foam and elastomer devices. *Mechatronics*, 10(4-5), pp.555-569.
22. Premalatha, S.E., Chokkalingam, R. and Mahendran, M., 2012. Magneto mechanical properties of iron based MR fluids. *American Journal of Polymer Science*, 2(4), pp.50-55.
23. Wang, X. and Gordaninejad, F., 2006. Study of magnetorheological fluids at high shear rates. *Rheologica Acta*, 45(6), pp.899-908.
24. Zareie, S. and Zabihollah, A., 2020. The Recent Advances in Magnetorheological Fluids-Based Applications. *Emerging Trends in Mechatronics*, p.129.
25. McDonald, K., Rendos, A., Woodman, S., Brown, K.A. and Ranzani, T., 2020. Magnetorheological Fluid-Based Flow Control for Soft Robots. *Advanced Intelligent Systems*, 2(11), p.2000139.
26. Hua, D., Liu, X., Sun, S., Li, Z., Li, Z. and Li, W., 2021. Precise locomotion controller design for a novel magnetorheological fluid robot based on improved gray wolf optimization algorithm. *Smart Materials and Structures*, 30(2), p.025038.
27. Hartzell, C.M., Choi, Y.T., Wereley, N.M. and Leps, T.J., 2019. Performance of a magnetorheological fluid-based robotic end effector. *Smart Materials and Structures*, 28(3), p.035030.
28. Kumar, J.S., Paul, P.S., Raghunathan, G. and Alex, D.G., 2019. A review of challenges and solutions in the preparation and use of magnetorheological fluids. *International Journal of Mechanical and Materials Engineering*, 14(1), pp.1-18.

29. Wahid, S.A., Ismail, I., Aid, S. and Rahim, M.S.A., 2016, February. Magnetorheological defects and failures: A review. In *IOP Conference Series: Materials Science and Engineering* (Vol. 114, No. 1, p. 012101). IOP Publishing.
30. Machala, L., Tucek, J. and Zboril, R., 2011. Polymorphous transformations of nanometric iron (III) oxide: a review. *Chemistry of Materials*, 23(14), pp.3255-3272.
31. Desrosiers, J.F., Bigué, J.L., Denninger, M., Julió, G., Plante, J.S. and Charron, F., 2013, February. Preliminary investigation of magnetorheological fluid durability in continuous slippage clutch. In *Journal of physics: conference series* (Vol. 412, No. 1, p. 012022). IOP Publishing.
32. Bhat, A.H., Dasan, Y.K., Khan, I., Soleimani, H. and Usmani, A., 2017. Application of nanocrystalline cellulose: Processing and biomedical applications. In *Cellulose-reinforced nanofibre composites* (pp. 215-240). Woodhead Publishing.
33. Oprea, M. and Panaitescu, D.M., 2020. Nanocellulose hybrids with metal oxides nanoparticles for biomedical applications. *Molecules*, 25(18), p.4045.
34. Liu, Z. H., Yi, Y., Gauczinski, J., Xu, H. P., Schonhoff, M., and Zhang, X., 2011, Surface Molecular Imprinted Layer-by-Layer Film Attached to a Porous Membrane for Selective Filtration. *Langmuir*, 27(19), pp. 11806–11812.
35. Sharma, A.C. and Borovik, A.S., 2000. Design, synthesis, and characterization of templated metal sites in porous organic hosts: application to reversible dioxygen binding. *Journal of the American Chemical Society*, 122(37), pp.8946-8955.
36. Lu, W., Yuan, D., Zhao, D., Schilling, C.I., Plietzsch, O., Muller, T., Brase, S., Guenther, J., Blumel, J., Krishna, R. and Li, Z., 2010. Porous polymer networks: synthesis, porosity, and applications in gas storage/separation. *Chemistry of Materials*, 22(21), pp.5964-5972.

37. Simms, H.M., Brotherton, C.M., Good, B.T., Davis, R.H., Anseth, K.S. and Bowman, C.N., 2005. In situ fabrication of macroporous polymer networks within microfluidic devices by living radical photopolymerization and leaching. *Lab on a Chip*, 5(2), pp.151-157.
38. Dhandayuthapani, B., Yoshida, Y., Maekawa, T. and Kumar, D.S., 2011. Polymeric scaffolds in tissue engineering application: a review. *International Journal of Polymer Science*, 2011.
39. Landy, B.C., VanGordon, S.B., McFetridge, P.S., Sikavitsas, V.I. and Jarman-Smith, M., 2013. Mechanical and in vitro investigation of a porous PEEK foam for medical device implants. *Journal of Applied Biomaterials & Functional Materials*, 11(1), pp.35-44.
40. Laurencin, C.T. and Nair, L.S., 2008. *Nanotechnology and tissue engineering: the scaffold*. CRC Press.
41. Tyshkunova, I.V., Poshina, D.N. and Skorik, Y.A., 2022. Cellulose Cryogels as Promising Materials for Biomedical Applications. *International Journal of Molecular Sciences*, 23(4), p.2037.
42. Ferreira, F.V., Otoni, C.G., Kevin, J., Barud, H.S., Lona, L.M., Cranston, E.D. and Rojas, O.J., 2020. Porous nanocellulose gels and foams: Breakthrough status in the development of scaffolds for tissue engineering. *Materials Today*, 37, pp.126-141.
43. Munier, P., Gordeyeva, K., Bergström, L. and Fall, A.B., 2016. Directional freezing of nanocellulose dispersions aligns the rod-like particles and produces low-density and robust particle networks. *Biomacromolecules*, 17(5), pp.1875-1881.
44. Osorio, D.A., Seifried, B., Moquin, P., Grandfield, K. and Cranston, E.D., 2018. Morphology of crosslinked cellulose nanocrystal aerogels: cryo-templating versus pressurized gas expansion processing. *Journal of Materials Science*, 53(13), pp.9842-9860.

45. Levy, Y., Imbert, C., Cipriani, J., Racine, S. and Dupeyrat, R., 1974. Raman scattering of thin films as a waveguide. *Optics Communications*, 11(1), pp.66-69.
46. Kelly, K.L., Coronado, E., Zhao, L.L. and Schatz, G.C., 2003. The optical properties of metal nanoparticles: the influence of size, shape, and dielectric environment. *The Journal of Physical Chemistry B*, 107(3), pp.668-677.
47. Butt, M.A., Khonina, S.N. and Kazanskiy, N.L., 2021. Plasmonics: a necessity in the field of sensing-a review. *Fiber and Integrated Optics*, 40(1), pp.14-47.
48. Cialla, D., März, A., Böhme, R., Theil, F., Weber, K., Schmitt, M. and Popp, J., 2012. Surface-enhanced Raman spectroscopy (SERS): progress and trends. *Analytical and Bioanalytical Chemistry*, 403(1), pp.27-54.
49. Willets, K.A. and Van Duyne, R.P., 2007. Localized surface plasmon resonance spectroscopy and sensing. *Annual Review of Physical Chemistry*, 58, pp.267-297.
50. Mayer, K.M. and Hafner, J.H., 2011. Localized surface plasmon resonance sensors. *Chemical Reviews*, 111(6), pp.3828-3857.
51. Djalalian-Assl, A., 2018. Propagating surface plasmons with an interference envelope and a vision for time crystals. *OSA Continuum*, 1(2), pp.462-476.
52. Lodewijks, K., Ryken, J., Van Roy, W., Borghs, G., Lagae, L. and Van Dorpe, P., 2013. Tuning the Fano resonance between localized and propagating surface plasmon resonances for refractive index sensing applications. *Plasmonics*, 8(3), pp.1379-1385.
53. Kretschmann, E. and Raether, H., 1968. Radiative decay of non radiative surface plasmons excited by light. *Zeitschrift für Naturforschung A*, 23(12), pp.2135-2136.
54. Otto, A., 1968. Excitation of nonradiative surface plasma waves in silver by the method of frustrated total reflection. *Zeitschrift für Physik A Hadrons and Nuclei*, 216(4), pp.398-410.

55. Xu, Y., Bai, P., Zhou, X., Akimov, Y., Png, C.E., Ang, L.K., Knoll, W. and Wu, L., 2019. Optical refractive index sensors with plasmonic and photonic structures: promising and inconvenient truth. *Advanced Optical Materials*, 7(9), p.1801433.
56. Kazanskiy, N.L., Khonina, S.N. and Butt, M.A., 2020. Plasmonic sensors based on Metal-insulator-metal waveguides for refractive index sensing applications: A brief review. *Physica E: Low-dimensional Systems and Nanostructures*, 117, p.113798.
57. Wang, A.X. and Kong, X., 2015. Review of recent progress of plasmonic materials and nanostructures for surface-enhanced Raman scattering. *Materials*, 8(6), pp.3024-3052.
58. Ngo, H.T., Wang, H.N., Fales, A.M. and Vo-Dinh, T., 2016. Plasmonic SERS biosensing nanochips for DNA detection. *Analytical and Bioanalytical Chemistry*, 408(7), pp.1773-1781.
59. Park, S.G., Mun, C., Xiao, X., Braun, A., Kim, S., Giannini, V., Maier, S.A. and Kim, D.H., 2017. Surface energy-controlled SERS substrates for molecular concentration at plasmonic nanogaps. *Advanced Functional Materials*, 27(41), p.1703376.
60. Baldwin, J., Schühler, N., Butler, I.S. and Andrews, M.P., 1996. Integrated optics evanescent wave surface enhanced Raman scattering (IO-EWSERS) of mercaptopyrindines on a planar optical chemical bench: binding of hydrogen and copper ion. *Langmuir*, 12(26), pp.6389-6398.
61. Sohrabi, F. and Hamidi, S.M., 2017. Fabrication methods of plasmonic and magnetoplasmonic crystals: a review. *The European Physical Journal Plus*, 132(1), pp.1-21.

62. Li, C., Li, S., Qu, A., Xu, C., Xu, L. and Kuang, H., 2021. Dimensional Surface-Enhanced Raman Scattering Nanostructures for MicroRNA Profiling. *Small Structures*, 2(7), p.2000150.
63. Rocha-Santos, T.A., 2014. Sensors and biosensors based on magnetic nanoparticles. *TrAC Trends in Analytical Chemistry*, 62, pp.28-36.
64. Lai, H., Xu, F. and Wang, L., 2018. A review of the preparation and application of magnetic nanoparticles for surface-enhanced Raman scattering. *Journal of Materials Science*, 53(12), pp.8677-8698.
65. Wang, Y., Dostalek, J. and Knoll, W., 2011. Magnetic nanoparticle-enhanced biosensor based on grating-coupled surface plasmon resonance. *Analytical Chemistry*, 83(16), pp.6202-6207.
66. Qiu, Z.Q. and Bader, S.D., 2000. Surface magneto-optic Kerr effect. *Review of Scientific Instruments*, 71(3), pp.1243-1255.
67. Jain, P.K., Xiao, Y., Walsworth, R. and Cohen, A.E., 2009. Surface plasmon resonance enhanced magneto-optics (SuPREMO): Faraday rotation enhancement in gold-coated iron oxide nanocrystals. *Nano Letters*, 9(4), pp.1644-1650.
68. Temnov, V.V., Armelles, G., Woggon, U., Guzatov, D., Cebollada, A., Garcia-Martin, A., Garcia-Martin, J.M., Thomay, T., Leitenstorfer, A. and Bratschitsch, R., 2010. Active magneto-plasmonics in hybrid metal-ferromagnet structures. *Nature Photonics*, 4(2), pp.107-111.
69. Maksymov, I.S., 2015. Magneto-plasmonics and resonant interaction of light with dynamic magnetisation in metallic and all-magneto-dielectric nanostructures. *Nanomaterials*, 5(2), pp.577-613.

70. Caballero, B., García-Martín, A. and Cuevas, J.C., 2016. Hybrid magnetoplasmonic crystals boost the performance of nanohole arrays as plasmonic sensors. *Acs Photonics*, 3(2), pp.203-208.
71. Zhao, Y., Wu, D., Lv, R.Q. and Ying, Y., 2014. Tunable characteristics and mechanism analysis of the magnetic fluid refractive index with applied magnetic field. *IEEE Transactions on Magnetics*, 50(8), pp.1-5.
72. Dai, J., Yang, M., Li, X., Liu, H. and Tong, X., 2011. Magnetic field sensor based on magnetic fluid clad etched fiber Bragg grating. *Optical Fiber Technology*, 17(3), pp.210-213.
73. Kamal, A. and Russell, P.S.J., 1994. Physical origins and general dielectric tensor of photoinduced anisotropy in optical fibers and bulk glasses. *JOSA B*, 11(9), pp.1576-1584.
74. Saravanamuttu, K. and Andrews, M.P., 2002. Visible laser self-focusing in hybrid glass planar waveguides. *Optics Letters*, 27(15), pp.1342-1344.
75. Chung, S.K. and Kim, S.S., 1988. An exact wave-optics analysis of optical waveguide with anisotropic and gyrotropic materials. *Journal of Applied Physics*, 63(12), pp.5654-5659.

Chapter 2

Investigation of shear-induced physical and chemical transformations of iron-based microparticles in hydrocarbon- and fluorocarbon-based magnetorheological fluids

2.1 Introduction

This chapter examines the degradation of carbonyl iron microparticles in hydrocarbon and fluorocarbon host fluid environments to better understand the aging of magnetorheological fluids (MRFs). The aim is to uncover the complex chemical changes at the carbonyl iron-fluid interface as the microparticles underwent continual shear loading in a real-life rotary clutch device. X-ray photoelectron spectroscopy (XPS) uncovered the evolving oxidation states of iron, fluorine, oxygen, and carbon on and beneath the surface of MRF particles. Scanning electron microscopy (SEM) revealed how the particles transform from nascent, nearly spherical shape prior to shear to irregular morphology in the clutch mechanisms. The nanoscale changes to surface topography are attributed to collisions among micron-size magnetic iron particles under shear. Transmission electron microscopy (TEM) revealed carbon-rich residues with embedded nanoparticle fragments in aged MRF particle samples, suggesting that MRF particle surfaces may have served as reaction interfaces. These new insights into chemical transformations on and beneath particle surfaces provide a reference for better durability assessment, MRF formulation, and device design in the future.

2.1.1 Magnetorheological fluids and their aging problems in applications

MRFs are magnetic field-responsive ‘smart’ materials consisting of magnetic particles, typically with diameters in the 0.1–10 μm range, suspended in chemically complex carrier fluids. The viscosity of MRFs can be adjusted by varying the strength of an applied magnetic (H) field. In the absence of an H-field (off-state), the fluid exhibits shear thinning behavior. In the on-state, magnetic interactions lead to the alignment of chains of magnetic particles along the magnetic flux lines and orthogonal to fluid flow. The particle chains resist fluid motion only until critical shear stress is reached, beyond which fluid motion can occur.^{1–3} The on-off process is reversible in millisecond time scales, making MR fluids one of the fastest electromechanical interfaces.^{1,3} The ability to fine-tune viscosity makes MRFs of interest in clutch and damper devices such as robotics and vehicle-control applications.^{1,4,5}

Durability is a critical issue in the application of magnetorheological fluid technology.⁴ The change in fluid properties is especially important in devices where the fluid is continually stressed under high loads.⁵ Past MR fluid durability studies often focused on testing certain MR fluids in devices, monitoring only changes in device performance and changes in macroscopic properties of the fluid. For example, Wang et al. studied the performance of a liquid-cooled clutch and found that in-use-thickening and particle oxidation cause an irreversible decline in performance.⁶ For damping application, Utami et al. noticed oxidation, deformation, and deposition of particles, which resulted in the reduction of viscosity and damping force.⁴ These results confirmed the findings of many previous studies, which observed failure modes such as oxidation of constituent iron particles, the subsequent breakdown of the oxide layer, mechanical abrasion of the iron particles, particle-fluid separation, loss of MR fluid carrier matrix due to leakage, and decomposition of the carrier fluid matrix during the aging of MR fluids.^{5,7–9}

Although many possible failure modes have been proposed, few studies have examined the interfacial chemistry between the particles and the fluid phase to determine the chemical factors that lead to the failure of the MR fluid.^{9, 10} The connection between device performance and MR fluid physical and chemical state is not well understood. Research that advances our understanding of the physical and chemical processes that occur at interfaces in MR fluids is therefore important to inform the design, formulation, and application of MR fluids. Indeed, nanoscale physical and chemical transformations at interfaces can significantly impact MRF macroscale engineering performance.

The present study provides a systematic investigation of the connection between MR fluid failure modes and the corresponding chemical and physical changes at magnetic particle surfaces and in MR fluids. SEM, TEM, and XPS provide insight into the surface morphological and chemical changes of carbonyl iron particles (CIP) in control and aged MR fluids obtained from either hydrocarbon-based or fluorocarbon-based MRFs.

2.1.2 The Mason number: relating MRF mechanical stress to viscous drag force and magnetic force

Two separate sets of durability experiments were performed with a drum-type clutch device. The first set of durability experiments was performed with hydrocarbon-based Lord 140 CG fluid. To explore the influence of operating conditions on MR fluids, two aging tests were done, each with a different Mason number. The Mason number (Mn) connects the two components of mechanical stress affecting the particles in MRFs: viscous drag force and magnetic force. These forces govern particle-particle interactions that give rise to microstructures in the fluid.¹¹ As shown

in Equation 2.1, the ratio of particle magnetic polarization forces F_0 to viscous forces F_H resulting from fluid shearing yields the Mason number:¹¹⁻¹⁴

$$M_n = \frac{F_H}{F_0} = 144 \frac{\eta_c \dot{\gamma}}{\mu_0 M^2} = \frac{8\eta_c \dot{\gamma}}{\mu_0 \mu_{cr} \beta^2 H^2} \quad (2.1)$$

$\dot{\gamma}$ is the magnitude of the shear rate tensor, η_c is the carrier fluid viscosity, μ_0 is the permeability of free space, μ_r is the relative permeability of the carrier fluid, M is the magnetization.^{11, 12} This expression assumes that the particles are spheres of radius σ . It is known that the Mason number correlates with the formation of microstructures in MR fluids. These arise from very strong particle-particle dipole interactions in the presence of the H-field. These interactions may result in the formation of networks of particles and/or agglomerates throughout the suspension that affects the shear response.^{1, 11}

The critical Mason number (M_n^*) is useful to frame the response of the MRF. It is defined:

$$\eta/\eta_\infty = 1 + (M_n/M_n^*)^{-1} \quad (2.2)$$

where η_∞ is the field-independent high-shear viscosity, and η is the shear viscosity.¹² The critical Mason number indicates the point at which hydrodynamic forces and magnetic forces reach a balance.^{11, 12} Below the critical Mason number, magnetic forces dominate MR fluid response, and particles tend to align into chains.^{13, 15} For example, magnetic particle chain length in microstructures decreases with increasing Mason number.¹³ Above the critical Mason number, hydrodynamic forces dominate, and particles instead form short chains, small clusters or sheets, which are easier to disperse.^{13, 15} Different types of microstructures formed during shear may affect the performance of the MR fluid as well as aging of particles.

The second set of durability experiments was performed with a custom perfluoropolyether (PFPE)-based fluid. Here the focus was on the reactivity of the fluorocarbon systems at fixed Mn. Choice of the PFPE was motivated by the well-known chemical inertness of fluorocarbons. The strong C-F bond makes fluorocarbons resistant to chemical reactions.¹⁶ In addition, the PFPE based ferrofluid is stable to acids, alkali, and high-temperature environments.¹⁷ The two aging tests described in this set focused on two formulations: one contained only a PFPE carrier fluid, while the other contained a fluorocarbon additive lubricant oil with PFPE carrier fluid. The additive contains carboxylic acid functional groups capable of binding (chelating) to the surface of microparticles. Despite the alleged chemical inertness of fluorocarbons, we show below that they can indeed react with the guest CIP species, leading to the formation of iron fluorides.^{18, 19}

2.2 Experimental

2.2.1 Aging, recovery, and isolation of MR fluid particles

Lord 140 CG MR fluid and a fluorocarbon host MR fluid were used to examine the effects due to abrasion by shear in a rotary clutch device. The Lord 140 CG fluid is a commercial hydrocarbon product with a high (40%) volume of microparticles. The formulation of the fluid is proprietary, but it is known to have a dynamic viscosity of 0.00987 Pa-s.¹⁴ The yield stress of the Lord MR fluid reaches ~ 60 kPa at about 200 kAmp/m in an applied magnetic field.²⁰

Two types of fluorocarbon MR fluid were formulated.²¹ A surfactant-containing version contained 40 % by volume of carbonyl iron particles (BASF Inc. CC grade) + 57 % by volume of base fluid (Krytox GPL 104) + 3 % volume of surfactant additive (Krytox 157 FS). Krytox GPL 104 is a perfluoropolyether oil with a dynamic viscosity of 0.06 Pa-s. Krytox 157 FS is a

poly(hexafluoropropylene oxide) with terminal carboxylic acid (COOH) functionalities. A surfactant-free version contained 40 % by volume of carbonyl iron particles + 60 % by volume of base fluid (Krytox GPL 104). The particles were prepared in a glove box filled with inert gas. The components were weighed, combined, and mixed thoroughly.

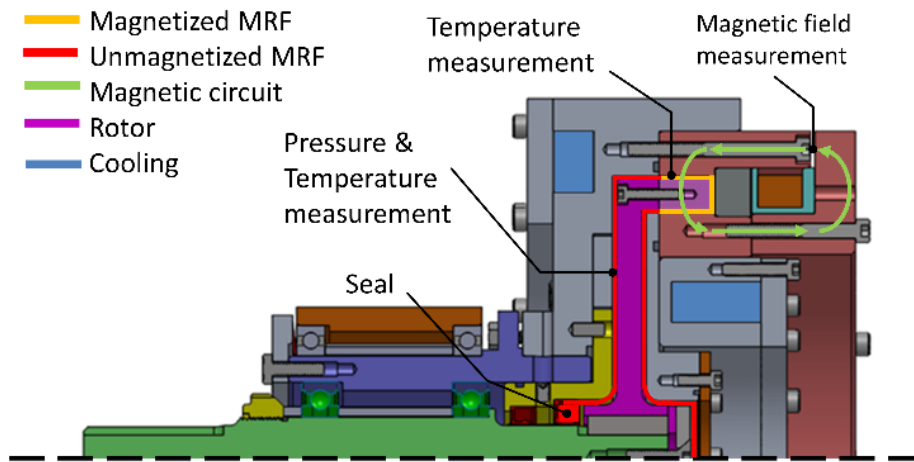


Figure 2.1 Schematic of the clutch durability test bench used for all durability tests in this study.

Durability tests on these fluids were performed using a drum-type MR clutch device in a continuous slippage actuator (CSA) system (Figure 2.1). The rotor (in green and purple) creates shear stress in the MR fluid at the stator interface (yellow). Torque is modulated up to ~40 Nm by increasing the H-field at this interface, which can go up to about 200 kA/m. A water-cooling jacket is installed within the clutch to maintain a constant operating temperature. In each of the tests, 50 mL of MR fluid was injected into the clutch. The clutch is operated at a constant velocity input, and the magnetic field is controlled in a closed-loop to achieve a constant torque output, thus giving a constant power dissipated within the MR fluid. The MR fluid was recirculated to ensure fluid homogeneity.

To assess the state of the MR fluid, the open-loop response of the clutch was measured at 1-hour intervals during the durability tests. Once the open-loop torque dropped below 80% of its initial value, the MR fluid was considered expired. For the Lord 140CG sample, this typically coincided with a sharp increase in the measured apparent viscosity and an increase in the closed-loop current required to achieve a given torque output (Figure 2.2). Fluid in the shear gap was collected for analysis. Samples were compared against controls that had not been submitted to shear.

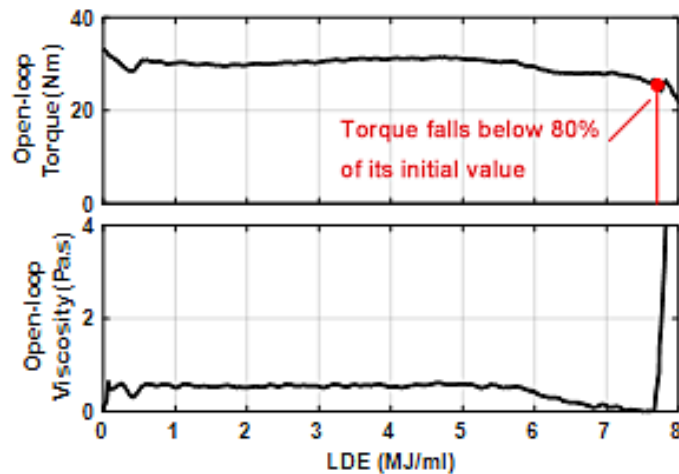


Figure 2.2 Demonstration of typical torque and viscosity relationship in MR clutch durability tests.

The hydrocarbon aging test was performed with Lord 140 CG fluid. A high Mason number trial used an input torque of 5 Nm resulting in a Mason number of 0.1017. A low Mason number trial was characterized by an input torque of 20 Nm and a Mason number of 0.0153. Both tested Mason numbers were below the critical Mason number. The lifetime dissipated energy (LDE) for

the Lord hydrocarbon MRF samples are as follows: 8.1 MJ/mL (low Mn) and 12.2 MJ/mL (high Mn).

The fluorocarbon MRF aging tests were performed with fluorocarbon MRF described above. A constant input torque of 20 Nm was applied in these cases. The Mason number for this test series was fixed at 0.43. The LDE for the fluorocarbon fluids are as follows: 5.5 MJ/mL (no additive) and 12.5 MJ/mL (with additive).

Control samples and aged samples were washed with solvent to remove the carrier fluid prior to analysis by XPS and SEM. Hydrocarbon based Lord 140 CG MR fluids were washed with ACS grade hexane, while PFPE based MR fluids were rinsed with DuPont Vertrel XF specialty fluid (2,3-dihydrodecafluoropentane). For each wash, solvent 10 times in volume was added to the MR fluid, and the mixture was shaken with a vortex mixer for 5 minutes. The particles were then separated with a magnet, and the liquid phase was collected to be dried in a vacuum for TEM. The washing for each sample continued until the liquid phase became clear. Dry state CIP powder was used as received.

2.2.2 SEM and TEM

The morphology of the particles derived from the control and aged particles was examined by SEM (field emission FEI Inspect F-50 FE-SEM at 5 KeV). All aged particles that were washed with solvent yielded a dark, insoluble oily residue that coated the surface of the particles. There was no such residue on the control samples. Residues isolated from the aged particles were dried under vacuum and examined by TEM (Philips CM200 200 kV unit equipped with an AMT XR40B CCD camera).

2.2.3 X-ray photoelectron spectroscopy (XPS)

XPS was performed with a Thermo Scientific K-Alpha XPS (Al-K α 1486.6 eV). All samples were mounted on conductive copper tape. The XPS vacuum chamber was maintained at $<2 \times 10^{-7}$ mbar. The x-ray beam was directed at an incident angle of 60° from normal (30° from the horizontal plane of the sample) with a focal spot size of 400 μm . A flood gun was used alongside the x-ray gun to suppress peak shifting. A monoenergetic Ar⁺ ion beam of 3000.0 eV with a current of 4.13 μA was used to erode the particle sample for depth profiling. The ion beam impinged at an angle of 58° from normal (32° from the horizontal plane of the sample) and was projected onto an area of 2 mm \times 1 mm, some five times the x-ray beam size. Changes in oxidation state as a function of depth in MR fluid particles were profiled by XPS. Fe(2p), C(1s), and O(1s) spectra were collected for hydrocarbon-based MR fluid particles, while F(1s) spectra were collected for PFPE-based MR fluid particles. The peak fitting was made by Voigt shape functions to account for the energy resolution of the instrument and chemical disorder (Gaussian part) and the lifetime width of the photoionization process (Lorentzian part).

2.3. Results and Discussion

2.3.1 Aging of particles in hydrocarbon fluids & particle aging in correlation with Mason number

2.3.1.1 Particle morphology

The Lord 140 CG MR fluid control sample contains a bimodal distribution of polydisperse particles. SEM analysis (Figure 2.3) reveals that many particles show necking, and there is evidence of widespread decoration of the larger particles by smaller species. Particles are aggregated into colonies throughout the sample (Figure 2.3 insert). All particles show a somewhat

roughened surface texture. Larger particles have diameters ranging from 2 to 5 μm , while the smaller particle distribution consists of objects $\leq 1 \mu\text{m}$. Overall, the microparticle population deviated significantly from the ideal of uniform spheres. The effects of particle shape and aggregation on MR fluid performance were not examined in this study.

Nevertheless, since magnetic particles dispersed in an MR fluid are forced into close contact by the applied H-field, particle shape may determine the field-induced structure of the particle dispersion at rest, the break-up of aggregates, frictional forces, and dissipation mechanisms under shear.

Non-spherical particles will exhibit a smaller demagnetization factor in their long direction. Aged particles from low Mn and high Mn tests have different modes of surface coarsening (Figure 2.4). Aged particles from the high Mn test exhibit a more uniformly coarsened surface, while their low Mn test counterparts have many nanoscale protrusions on particle surfaces.

Insoluble residues were found and collected from the washing of the aged particles (Figure 2.4 insert). The residues contain additional clues about what transpires at the surfaces of the microparticles in the high and low Mn tests. TEM images of residue from the low Mn test revealed an untextured carbon-rich matrix (by XPS) with embedded $\sim 1 \text{ nm}$ diameter particles. By contrast, the residue from the high Mn test contained no nanoparticles. The production of visible spalling residue in the form of nanoparticles suggests more abrasive conditions associated with the low Mn runs. These observations are in line with the lower LDE observed for low mason number.²² This observation is consistent with the findings of Sherman et al. and Melle et al., who argue that MR fluids will form easier-to-disperse, small particle clusters at higher Mn.^{13, 15}

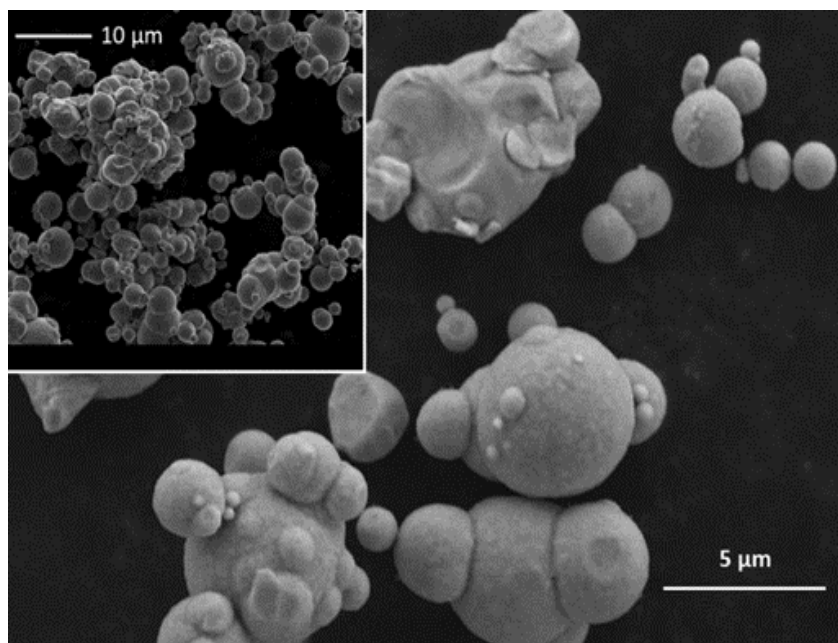


Figure 2.3 Control sample of Lord 140 CG MR carbonyl iron microparticles. Particles have not been subjected to shear.

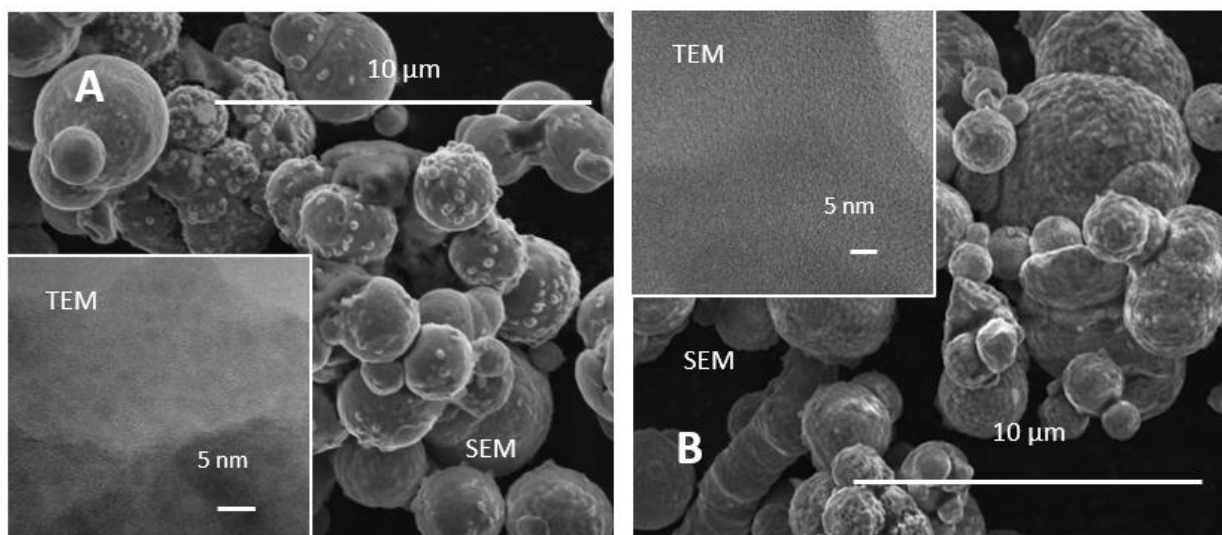


Figure 2.4 Sample of Lord 140 CG MR carbonyl iron microparticles. Particles **A** were subjected to low Mn shear, while particles **B** were subjected to high Mn shear. TEM shows residues from the washing of respective particles.

2.3.1.2 Evidence of carbon catalytic reactions

XPS and XPS depth profiling were used to identify surface and sub-surface elements and their oxidation states. The elemental composition of all particles is shown in Figures 2.5 and 2.6. Note that each curve represents the total amount of the specified element, regardless of oxidation state. The surface of the control sample is enriched in carbon and oxygen. In fact, the iron particles are very well coated. The sample was subsequently eroded with Ar^+ projectiles (beyond $t = 0$). As expected, the iron content rose rapidly as the projectiles ablated the surface. Aged particles contained higher oxygen and carbon contents in general compared to pristine particles. The elevated carbon and oxygen concentrations, especially around the surface, suggest reaction and even diffusion and incorporation of these elements into the metallic iron-based particles.^{23, 24} A majority of the carbon (depth profile not shown) shows binding energy of 284.78 eV, typical of sp^3 hybridized carbon (C-C or C-H bonds). Small amounts of carbon with binding energies of 286.5 eV and 288.5 eV are found. They are associated with carbon bonded to oxygen in C-O and O-C=O bonds from the hydrocarbon base fluid. Trace amounts of carbidic C-Fe at 283.3 eV are also identified.²⁵ The latter is believed to have been deposited during the decomposition of $\text{Fe}(\text{CO})_5$ to make carbonyl iron.

Evidently, primary sources of carbon are the surfactants stabilizing the particles and the host hydrocarbon-based carrier fluid. As can be seen, comparing Figures 2.5 and 2.6, the high and low Mn samples have a more gradual decline in carbon content over time (increasing erosion) than the control sample. The low Mn sample contains more carbon on the surfaces than the high Mn sample, suggesting that the more abrasive environment of the low Mn sample leads to more extensive organic coating due to greater breakdown of the host fluid and surfactant.

Fresh fracture surfaces caused by collisions among particles and spalling of surface carbon and oxides will expose iron atoms and coordinatively unsaturated iron oxides that, even at the nanoscale, are well-known to be catalytically active for C-C and C-H bond activation.^{26, 27} The untextured residues found on aged particles are high molecular weight species, likely produced from this process. During the durability tests, considerable outgassing from the MR fluid chamber was observed. Thermogravimetric analysis of the aged and control hydrocarbon MR fluids (Figure S2.1) also showed that aged fluids, especially the fluid from the high Mn test, which sustained longer operation, contain higher weight percentages of solid. The outgassing and the decrease in mass of the fluid phase are evidence of transformations in the MRF.

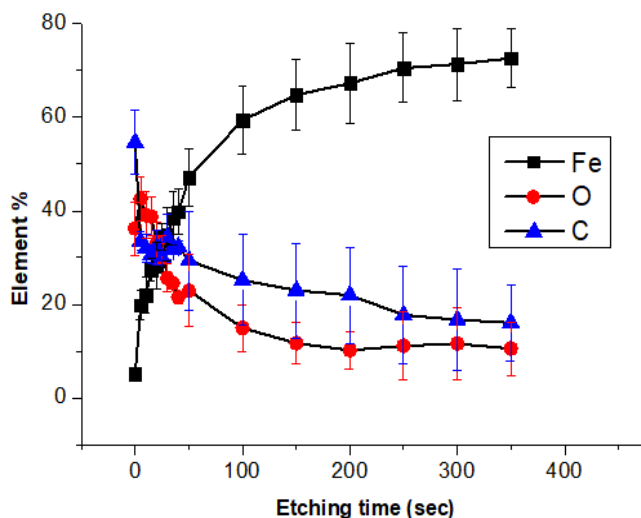


Figure 2.5 XPS elemental composition depth profile of control sample of Lord 140 CG MR carbonyl iron microparticles. Particles were not subjected to shear.

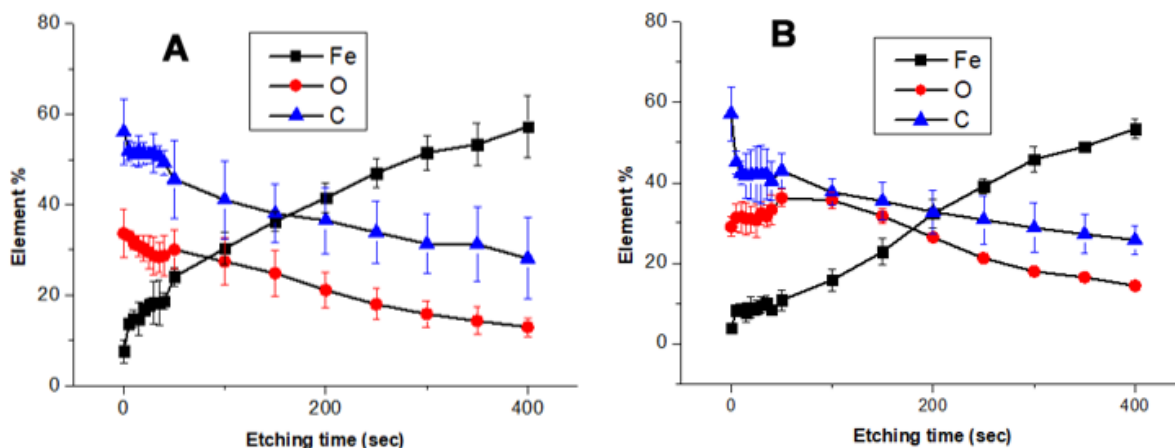


Figure 2.6 XPS elemental composition depth profile of (A) low Mason number sample of carbonyl iron microparticles and (B) high Mason number particles.

2.3.1.3 Surface oxide composition

close examination of the depth profile curves in Figures 2.5 and 2.6 gives further insight into iron oxide formation on the particle surface. Turning first to Fe, observe the steep and parabolic rise in Fe content in Figure 2.5 for the control sample. Ar⁺ erosion of the Fe particles in the high and low Mn regimes is accompanied by a more gradual rise in the iron content compared with the control. The high Mn sample shows persistent oxidation over a greater etching period than the control and low Mn samples.

The depth profile of O(1s) (Figure 2.7) indicates the oxidation states of iron oxides in control and aged particles. The “% oxidation state” was calculated by dividing the area under the curve of a given peak at specific binding energy by the total area under the curve (see Figure S2.2 for detail). Each data point is the average of three measurements. The main oxygen peak in the control (Figure 2.7A) corresponds to oxygen bound in the lattice to Fe (Fe-O lattice bonds, O_{lattice}).

An overlapping peak centered at 531.3 eV ($O_{\text{adsorbed/defect}}$) is not assigned with certainty: it may be due to chemisorbed oxygen²⁸ and/or oxygen in defect sites,²⁹ $O_{\text{adsorbed/defect}}$. Although it can be argued that the peak may be due to hydroxide, a common intermediate species in the oxidation of iron in the presence of moisture,³⁰ this is considered unlikely given the hydrophobic environment. Finally, a peak associated with bonding between oxygen and carbon (O-C) is located at ~533 eV. This signal is likely associated with surfactant on the particles. Regardless of the precise origin of the 531.3 band, there are marked changes in the distribution of oxygen environments on comparing the control sample with the aged samples. This is evident from Figure 2.7 where the $O_{\text{adsorbed/defect}}$ content increases markedly in both the low and high Mason number samples, compared with the O_{lattice} and O-C contributions. The implication is that the aged particles become enriched in oxides of iron.

It is not straightforward to assign the oxidation states of Fe with precision in these samples. Different oxidation states of Fe have overlapping binding energies, making it difficult to employ multi-peak fitting techniques commonly used for accurate iron oxide species determination. The problem was simplified by fitting three oxidation states in each Fe(2p) spectrum for the species, Fe(0), Fe(II), and Fe(III). The peak assignments are based on those of Lin³⁰ and Yamashita:³¹ Lin et al. assign the Fe(II) and Fe(III) sites in Fe_3O_4 (magnetite) ($2p_{3/2}$ state) at 709.7 eV and 711.1 eV, respectively.²⁸ Yamashita et al. locate the Fe(III) $2p_{3/2}$ peak for Fe_2O_3 at 711.0 eV, the Fe(II) $2p_{3/2}$ peak for $Fe_{1-y}O$ at 709.5 eV, and the overlapping Fe(II) and Fe(III) $2p_{3/2}$ peak for Fe_3O_4 to be at 710.6 eV.³¹ Figure 2.8 collects the results of depth profile analysis of Fe(0), Fe(II), Fe(III) fractions from the different microparticle samples. Particles from the control and aged samples follow a similar pattern in the evolution of oxidized iron species. Prior to etching, the surface of particles from all samples contains a high percentage of Fe(III) species. Immediately after etching, the

concentration of Fe(III) species decreases sharply, while the concentration of Fe(II) species increases to approximately 70%, before declining. There is only a trace amount of Fe(0) at the surface. The concentration of Fe(0) increases rapidly, plateauing at about 85%. The small percentage of Fe(II) and Fe(III) species at long etching times is likely an artifact of the nonuniform samples and not the result of deep penetration of oxygen to the core of the particles.

The oxide layer is the thinnest in particles from the control. Aged particles from the high Mn test have the thickest oxide layer. Fe(II) is the major component found in the oxide layers, while Fe(III) species have elevated concentrations on the surface. On the surface of high Mn particles, Fe(III) species reached a 2:3 ratio when compared with the Fe(II) species. The elevated Fe(III) presence on the surface, as well as the line shape of the Fe(2P) spectrum (not shown), both suggest the presence of Fe₃O₄. These experiments do not rule out contributions from Fe(III) originating from maghemite or hematite (Fe₂O₃). Underneath the surface, a majority of the oxide layer appears to be composed of Fe(II), indicating the presence of FeO.

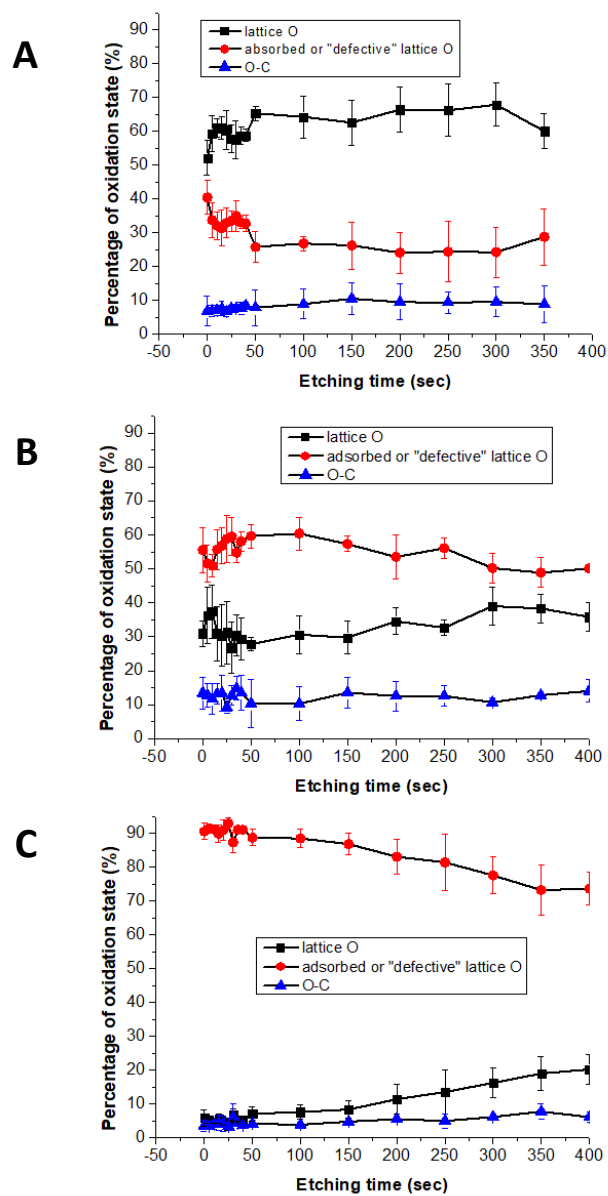


Figure 2.7 XPS oxidation state depth profile for oxygen of (A) control sample of carbonyl iron microparticles, (B) low Mason number particles, and (C) high Mason number particles.

2.3.1.4 Estimation of oxide thickness and limitation of Ar⁺ sputtering

In order to better estimate the thickness of iron oxide layers in the particles, the sputter rate and chemical changes due to sputtering must be evaluated. The sputter yield, defined as the number of atoms removed per Ar⁺ ion, is described by Equation 2.3:³²

$$S = \frac{1000ez\rho Nn}{JM} \quad (2.3)$$

here e = charge, z = etch rate, ρ = density of the oxide, N = Avogadro's number, n = number of atoms per molecule, M = molecular weight and J = ion beam flux density (current/contact area).³² Substituting the instrumental parameters of this experiment into the results obtained by Viehhaus et al., the sputter rate of relevant iron oxide species is calculated: 0.40 nm s⁻¹ for Fe₂O₃, 0.51 nm s⁻¹ for Fe₃O₄, and 0.39 nm s⁻¹ for FeO.³² These compare well with the results from other sources, where the sputter rate of Fe₂O₃ was calculated to be 0.38 nm s⁻¹,³³ and that of Fe₃O₄ was calculated to be 0.49 nm s⁻¹.³² The sputtering rate of metallic Fe is estimated to be lower than that of FeO using published sputter yield data.³⁴

One must interpret the curves in Figure 2.8 judiciously since lighter elements like oxygen tend to be sputtered preferentially in iron oxides, with a concomitant reduction in the oxidation state of iron. For example, Suzuki *et al.* found after 300 s of Ar⁺ sputtering (3 KeV), that Fe(III) at a surface of Fe₂O₃ was partially reduced to Fe(II), such that the surface manifested the characteristics of magnetite by XPS.³⁵ This was established for Fe₂O₃ (hematite and maghemite) and Fe₃O₄ (magnetite).^{36, 37} Overall then, preferential sputtering can result in underestimation of the thickness of an oxide layer³⁵ and complicate quantitative calculation of the quantities of Fe in different oxidations states.

Nevertheless, the quantity of Fe(II) caused by preferential sputtering and detected at the early stages of etching is likely to be small for the following reasons. It is noted that XPS spectra acquired prior to etching indicated that the most oxidized portion of the particles – the surface – contained Fe_3O_4 instead of Fe_2O_3 as a major species. A past study by Mauvernay et al. has demonstrated that substantially higher Ar^+ sputtering power is needed to convert the surface of a Fe_3O_4 substrate into a Fe_{1-x}O film.³⁸ It is more difficult to reduce Fe(II) by Ar^+ sputtering than Fe(III).³⁸⁻⁴⁰ The short Ar^+ sputtering time in our experiments is insufficient to convert much Fe(III) to FeO, or even to Fe(0).

Combining sputter rate analysis (Equation 2.2) with the etching times (Figure 2.8), we calculate the thickness of the oxide layer to be about 20 nm for particles from the control 140 CG fluid, and ~ 60 – 75 nm for particles from aged fluids. These oxide layers are thin compared to the volume of the particles, thus unlikely to significantly decrease the saturation magnetization. This was confirmed by SQUID measurements (Figure S2.3). The hysteresis curves for the aged particles from the high Mn test nearly overlap those of the control 140 CG particles. Those from the low Mn test show slightly lower magnetic saturation.

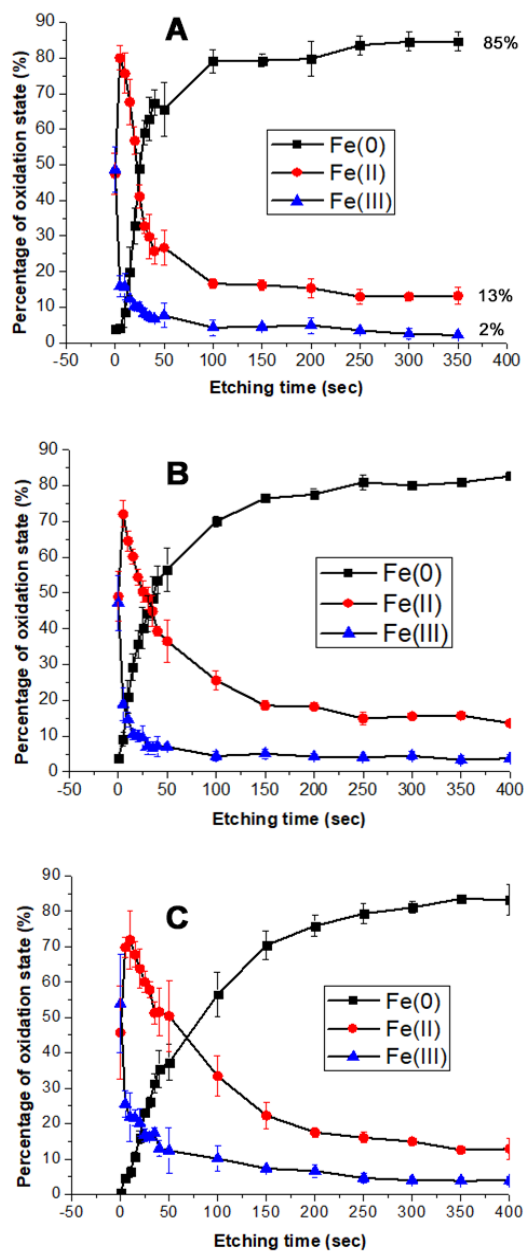


Figure 2.8 XPS depth profiles for Fe(O), Fe(II), and Fe(III) species in (A) control sample of carbonyl iron microparticles, (B) low Mason number particles, and C high Mason number particles.

2.3.2 Particle aging in PFPE-based MR fluids & function of a PFPE-based surfactant additive

2.3.2.1 Particle morphology

Similar to control particles used in the hydrocarbon-based fluid, the CIP used in the PFPE-based MR fluids are polydisperse with bimodal size distribution. Figure 2.9 reveals particles 2–5 μm in diameter coexist with smaller particles with diameters below 1 μm . The particles are approximately spherical and exhibit a small amount of surface roughness. In addition, aggregation of large particles, decoration of large particles with smaller particles, as well as iron microrods are found. There is evidence of necking among particles, likely an effect of the manufacturing process.

After aging, SEM images of both ‘with-additive’ and ‘no-additive’ washed particles show coarsened surfaces (Figure 2.10). Of the two samples, aged particles from the ‘no-additive’ fluid show different qualities of surface roughness.

The ‘no-additive’ sample (Figure 2.10A) contains particles with surface coarsening and dense aggregates of nanoscale protrusions. The ‘with-additive’ sample (Figure 2.10B) also contains nanoscale protrusions, but these are less coarse than those from the ‘no-additive’ sample. The residues from washing the two types of MRF reveal additional information. Nanoparticles are generated from the larger MRF particles during the aging process. Images of nanoparticles in the host matrix are shown as inserts in Figures 2.10A and 2.10B. The sample with no added Surfactant shows large numbers of embedded nanoparticles with diameters on the order of 8 nm. In contrast, residues from the ‘with-additive’ sample show comparatively fewer particles and smaller sizes, about 5 nm in diameter. Notably, more nanoparticles were found in the residues from the fluorocarbon aged samples than were found in the residues from both high and low Mn

hydrocarbon aged samples. As discussed below, this difference can be attributed to the formation of brittle metal fluorides.

Nanoparticle production can impact MR fluid properties: past studies have found that replacing 0.5% of the mass of carbonyl iron with the same mass of nano-sized ferrite particles leads to a doubling of the MR fluid off-state viscosity.⁷ The continual production of submicron particles during shear may play a significant role in the expiration of MR fluids.

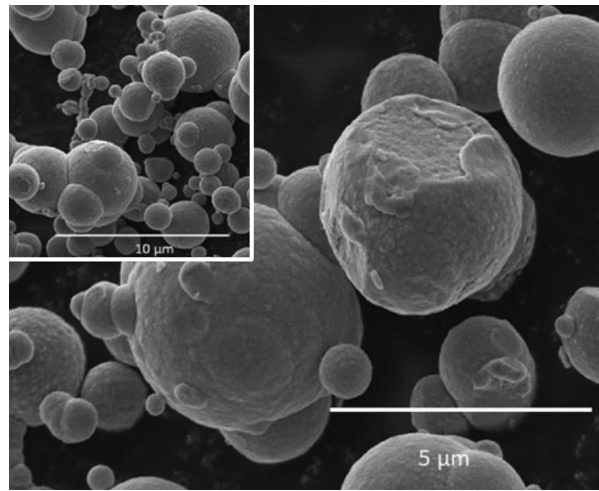


Figure 2.9 Control sample PFPE based MR fluid carbonyl iron microparticles. Insert shows aggregates of iron microparticles. Particles have not been subjected to shear.

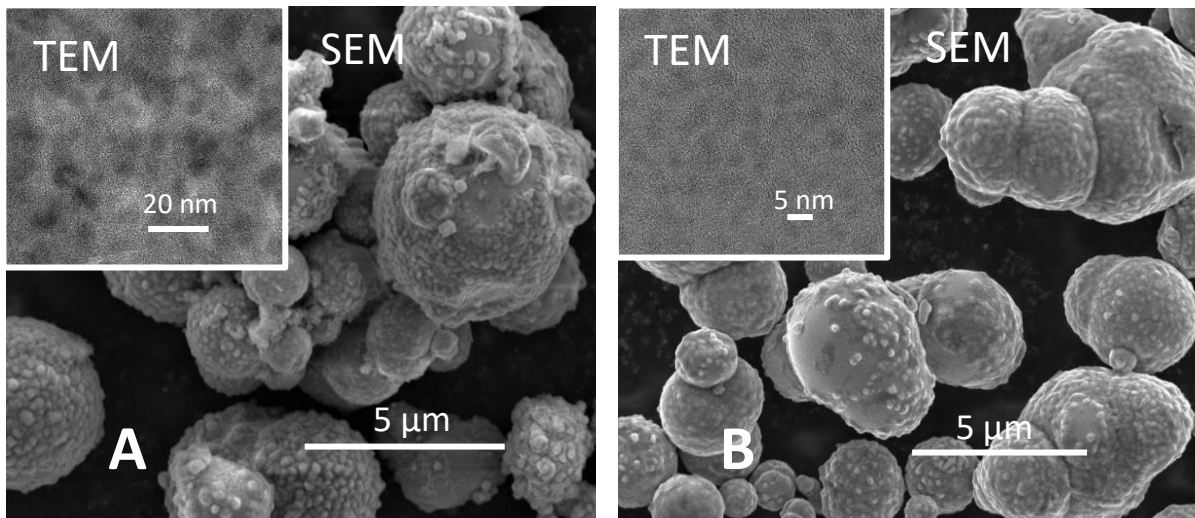


Figure 2.10 Sample of PFPE based MR fluid carbonyl iron microparticles after being subjected to shear. Particles **A** were obtained from fluid with no added surfactant, while particles **B** were obtained from fluid with surfactant added.

2.3.2.2 Defluorination of PFPE

The carbon depth profile (Figure 2.11) reveals that pristine particles are rich in carbon from the manufacturing process. A majority of the detected carbon species are sp³ hybridized carbon (C–H or C–C) at 284.8 eV. A peak evolves at 283.3 eV as the erosion process moves more towards the core. The 283.3 eV band is associated with a carbidic C–Fe bond (Figure 2.11).²⁵ The pristine particles are coated with a thin layer of iron oxide, likely with Fe₂O₃ on the surface and Fe₃O₄ in the near subsurface.²⁸ Fe(0) emerged as the dominant oxidation state after approximately 30 s of etching, corresponding to an estimated thickness of about 20 nm or less.

While the pristine particle samples contain no F, both of the aged particle samples incorporate fluorine to different extents. The incorporation of fluorine into iron particles is the result of the decomposition of fluorinated ethers by ferrous species. This is thought to proceed via

a two-step mechanism.^{18, 19} The first step is rate-determining defluorination, where iron serves as the reducing agent to activate and break the C–F bond of the fluorocarbon. The second step is the thermodynamically driven formation of iron fluorides.^{18, 19} The newly formed iron fluorides behave as Lewis acids that can catalyze the further decomposition of fluorinated ethers.^{18, 19, 41, 42} It has been argued that the initial iron fluorides accept electron density from oxygen on the perfluoropolyether chain, weakening the O–CF₂ bonds and breaking the O–C bond with concomitant production of a fluorocarbon and an oxide radical.^{41, 42} The oxide radical can cause further unzipping of the fluorocarbon chain.⁴²

Evidence of the defluorination reactions can be seen in the carbon profiles (Figure 2.11). Newly formed species with binding energies corresponding to C–F–C, C–C–F, and various carbonyl groups are found on the surface of aged ‘no-additive’ particles. These species do not originate from either the base oil (Figure 2.12) or the particles themselves and must be created during the in-use thickening process. The ratio between the original species in the base oil (CF₂O/CF₃ and CF₂) and the newly formed fluorine-poor species continues to decrease with etching time. This shows that perfluoropolyethers close to the iron surface are consumed by defluorination. A similar observation is made for particles from aged ‘with-additive’ fluid. Although the fluorine-poor species formed as a result of defluorination could not be differentiated from those that originated from the additive, the portion contributed by the additive is small due to the small quantity of additive in the exclusively fluorine-rich base oil. Moreover, the ratio between fluorine-rich and fluorine-poor species is lower on the surface of particles extracted from the aged ‘with-additive’ fluid compared to that of the pristine additive oil, demonstrating that defluorination has taken place.

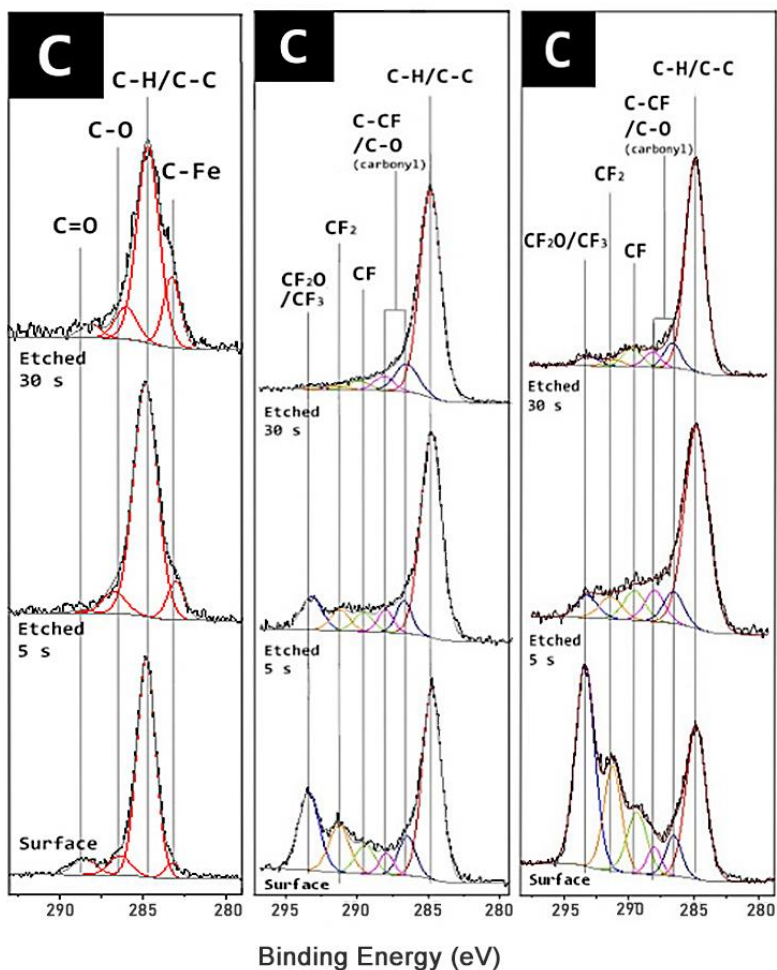


Figure 2.11 XPS oxidation state depth profiles for carbon species in (A) control sample of carbonyl iron microparticles, (B) aged particles obtained from “no-additive” fluid, and (C) aged particles obtained from “with-additive” fluid. The hydrogen atom is omitted in the labeling of C-F compounds.

It is worth noting that aged particles from the ‘with additive’ fluid have elevated $\text{CF}_2\text{O}/\text{CF}_3$ levels and a higher fluorine-rich to fluorine-poor species ratio on the surface than their counterparts from the ‘no-additive’ fluid. This indicates a lower extent of defluorination. Because the surfactant additive forms a protective layer on the surface of particles, the iron/ferrous surface of the particles

has reduced access to fluorine-rich species in its surroundings to initiate the defluorination reaction, thus limiting the formation of iron fluoride species.

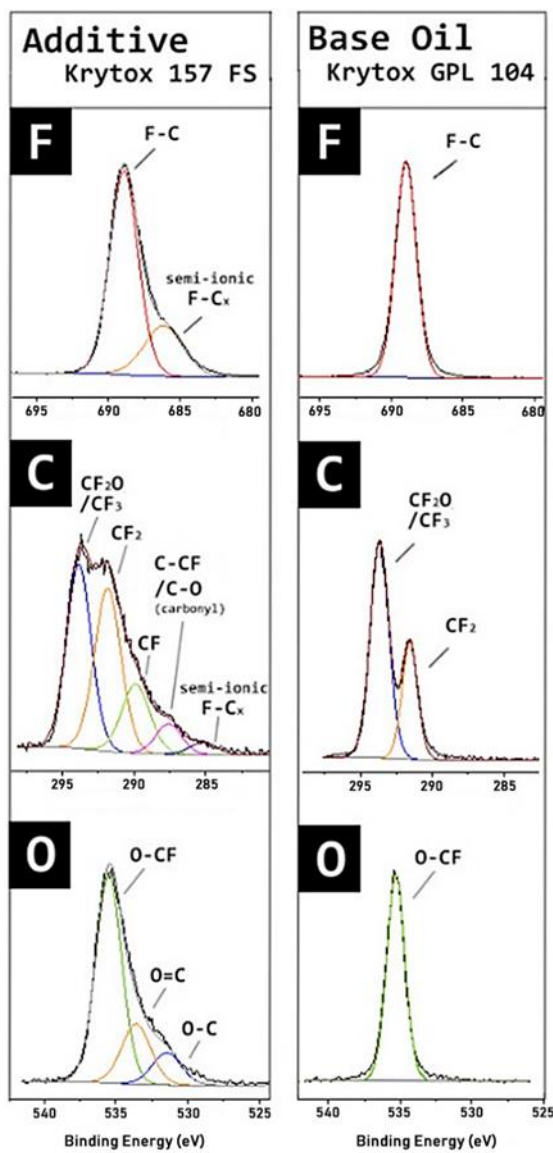


Figure 2.12 Fluorine, carbon, and oxygen composition profiles for the surfactant additive (Krytox 157 FS) and base oil (Krytox GPL 104) controls. The hydrogen atom is omitted in the labeling of C-F compounds.

2.3.2.3. Production of iron fluoride

The percentage of F in aged particles from the ‘no-additive’ fluid was found to be close to 40% at the surface, declining gradually to about 25% after 600 s of etching. For particles from the aged ‘with additive’ fluid, the fluorine content sharply decreased from 40% prior to etching to 25% after etching for only 5 s, then followed a slow trend of decline until the fluorine content reached 7% after 600 s of etching. A majority of the detected fluorine on the surface involves F–C bonds rather than F–Fe bonds (Figure 2.13). This indicates that most of the surface fluorine species are adsorbed fluorocarbon. However, the F–C/F–Fe ratio decreases rapidly on probing the core of the particles; clear peaks due to F–Fe are visible at 285.5 eV after 600 s of etching. Accurate estimation of etching rate was not made due to the lack of referencing data. Minor preferential sputtering has been observed with iron fluorides at 3 keV Ar⁺ bombardment, suggesting that the actual extent of iron fluoride formation might be slightly higher than observed.⁴³

The iron oxidation state profiles (Figure 2.14) confirm the presence of iron fluoride and identify it as primarily FeF₂.^{28, 44} FeF₂ is the kinetically favored iron fluoride product, having been observed as the only iron fluoride to form at 265°C from a study of fluorination of 304 stainless steel.⁴⁵ Our results suggest that generation of FeF₂ may be responsible for the production of nanoparticles in aged fluorocarbon samples. Iron fluorides are known to be brittle, adhering poorly to iron, thus spalling easily.⁴⁶ FeF₂ is a weak anisotropic antiferromagnet. Long term production during clutch operation is expected to reduce the overall magnetic remanence of the particles. The magnetic saturation of aged particles is decreased relative to the control particles in the PFPE test (Figure S2.4). Over the lifetime of the experiment, the decrease in magnetization is nevertheless relatively small.

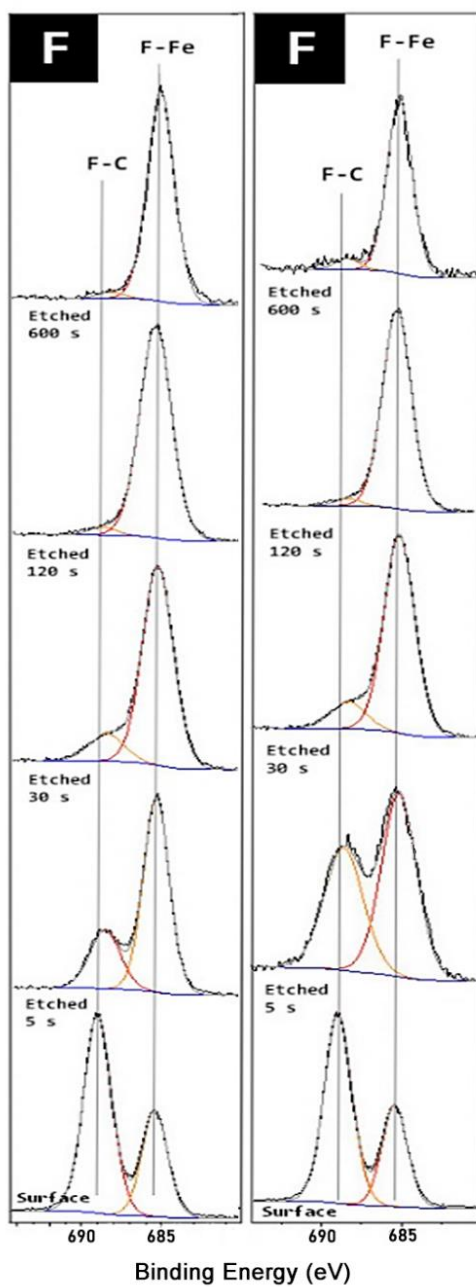


Figure 2.13 XPS oxidation states depth profiles for fluorine species in (A) aged particles obtained from “no-additive” fluid, and (B) aged particles obtained from “with-additive” fluid. The hydrogen atoms are omitted in the labeling of C-F compounds.

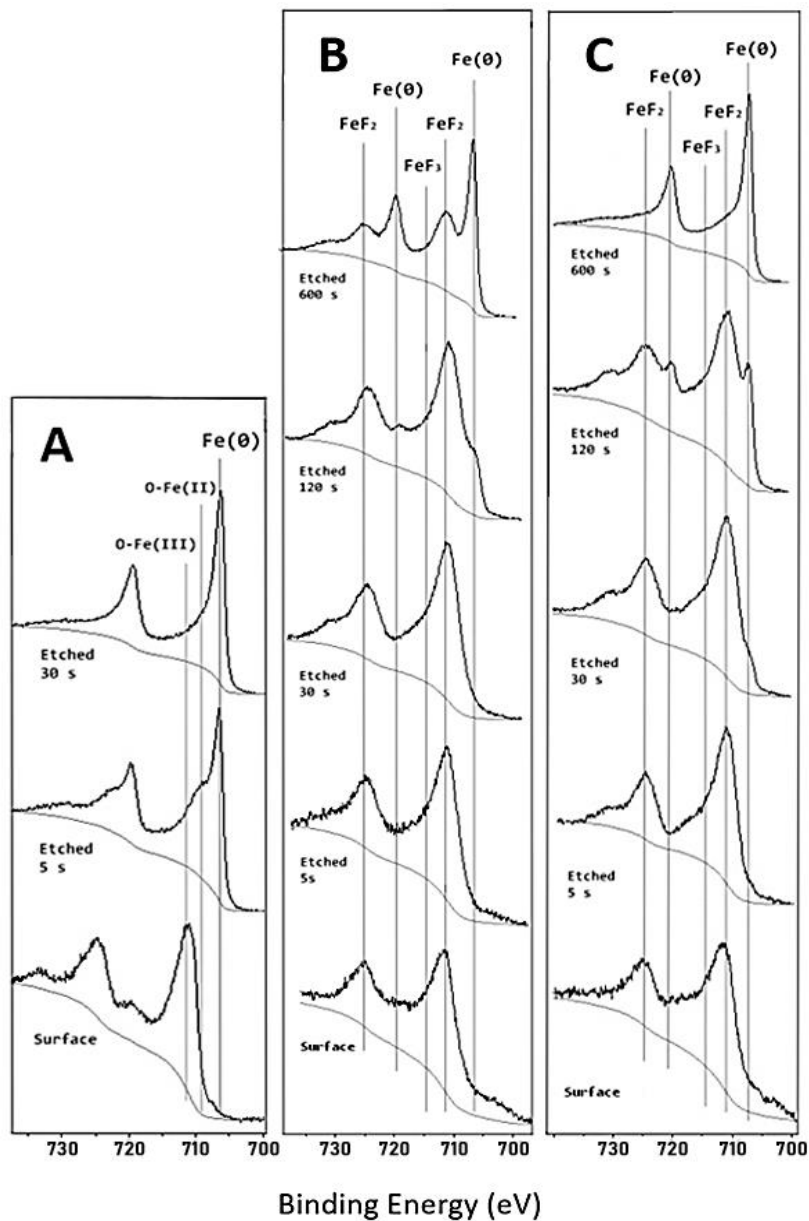


Figure 2.14 XPS oxidation states depth profiles for iron species in (A) control sample of carbonyl iron microparticles, (B) aged particles obtained from “no-additive” fluid, and (C) aged particles obtained from “with-additive” fluid.

2.4 Conclusion

This study has shown that collisions among micron-size magnetic iron particles under shear can result in nanoscale changes to surface topography. Moreover, it has shown that shear-induced collisions can lead to redistributions among different oxidation state species on the surface and near sub-surface regions of the particles. The redistributions among oxidation states and chemical species are the result of interfacial reactions that can involve adventitious oxygen, catalysis, and other energetic processes that can act on either or both, the host fluid medium and additives introduced to stabilize the MRF. The interfacial chemistry is complex, inviting studies that couple macroscale processes (shear events in a clutch mechanism) with nanoscale inquiries into the effects of such processes. This study has examined physical and chemical changes to magnetic particles in two classes of MRF. A hydrocarbon-based commercial fluid Lord 140 CG was subjected to constant shear. A detailed analysis by XPS and XPS depth profiling revealed a diversity of iron species and oxidation states. Iron oxide layers and surface coarsening were found on aged particles in both high and low Mason number regimes. Oxide layers were shown to be relatively thin and on the order of nanometers. There is only a minor impact on the magnetic properties, as revealed by magnetization studies. In addition, evidence of nanoparticle spalling was observed in the low Mn test. A PFPE-based MR fluid was also studied. It was found that the host fluorocarbon and fluorocarbon additive are not immune to chemical reactions during clutch operation. Defluorination of PFPE produces iron fluorides on particle surfaces. FeF_2 is the main product formed in this process. Since FeF_2 is a brittle compound, an FeF_2 layer is likely to fragment to yield nanoparticles. These may be catalytically active and accelerate fluorocarbon decomposition. Over the duration of the experiment, the impact of FeF_2 production on the magnetic properties of

the fluid was determined to be small. The fluorocarbon surfactant appeared to increase the stability of the iron particle interface against conversion to iron fluorides.

2.5 Funding acknowledgment

This research was supported by the CRIAQ Project ENV-709 and NSERC grant CRDPJ 471265 – 14.

2.6 Copyright information

This is the Accepted Manuscript version of an article accepted for publication in [Smart Materials and Structures] IOP Publishing Ltd is not responsible for any errors or omissions in this version of the manuscript or any version derived from it. The Version of Record is available online at [<https://doi.org/10.1088/1361-665X/ab0b5b0964-1726/>]

2.7 Supporting materials

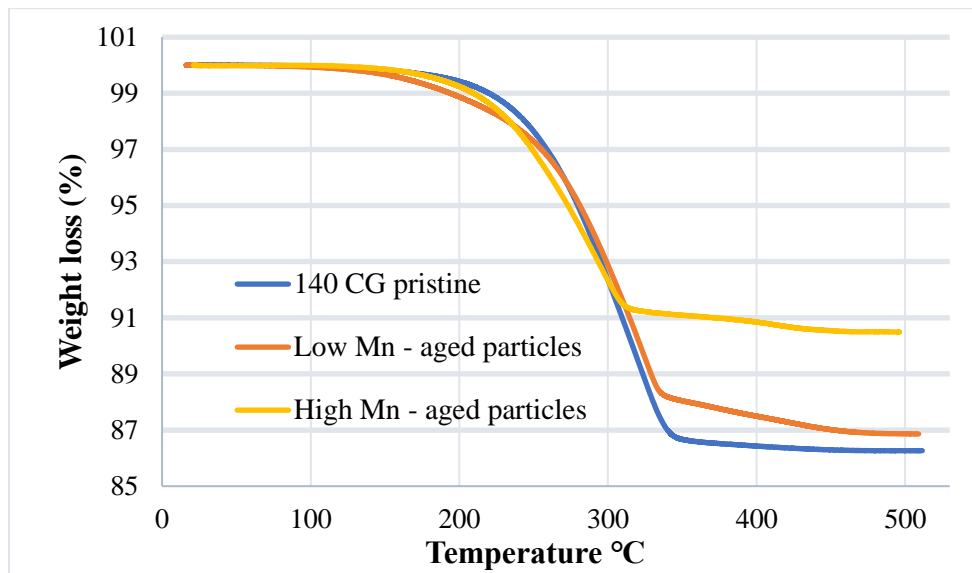


Figure S2.1 Thermogravimetric analysis (TGA) was performed on control Lord 140 CG particles and aged particles from the low and high Mason number tests. Samples were incinerated in an argon atmosphere. One can observe that the fluid (hydrocarbon) phase in the aged MR fluids, especially that aged in the high Mn test, has diminished in mass.

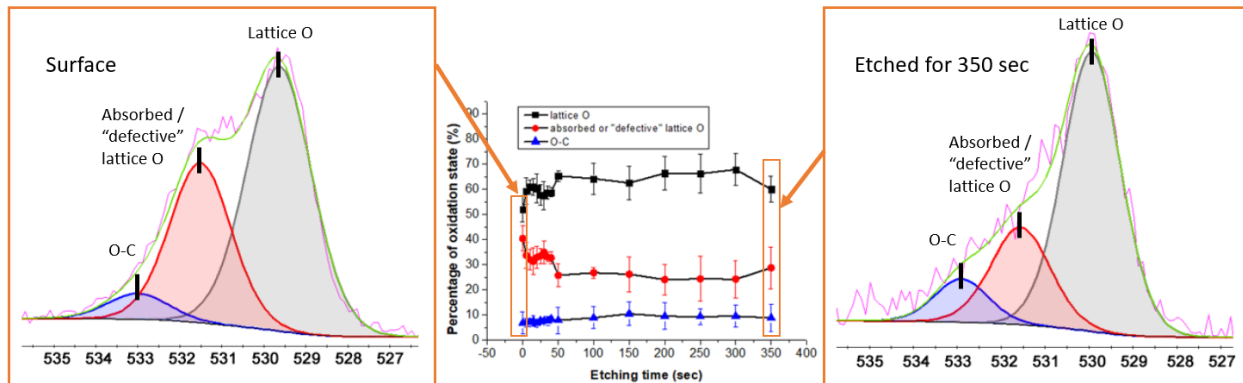
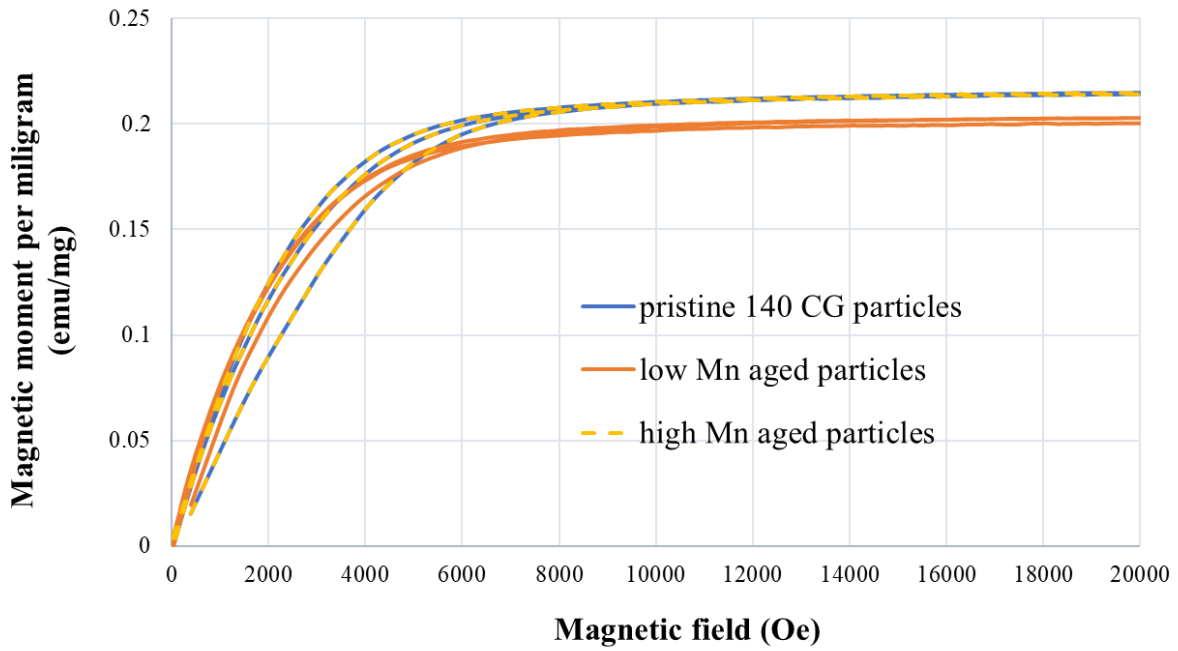
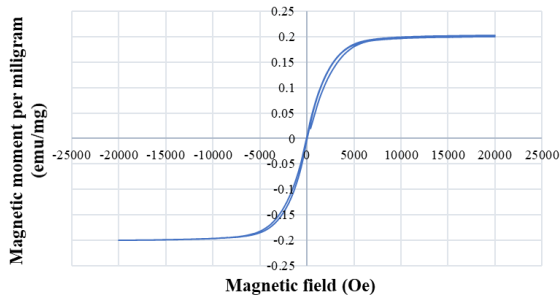


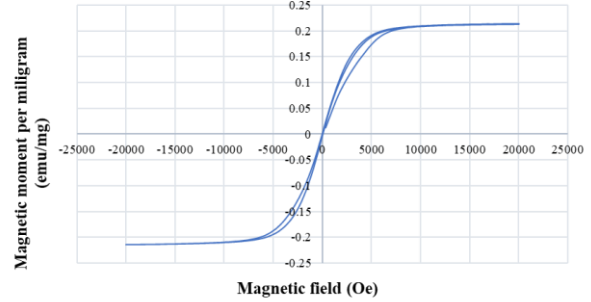
Figure S2.2 Example of determining the change in the ratio of different oxidation states of an element over-etching depth. The graph on the far left shows one oxidation state profile of oxygen on the surface (unetched) of the control Lord 140 CG particles, while the graph of the far right shows the profile after 350 sec of etching of the same particles. Three such profiles were taken at each etching time. The areas under the curve for each peak on the three profiles were averaged and plotted against etching time.



Low Mn - aged particles



High Mn - aged particles



Lord 140 CG - control particles

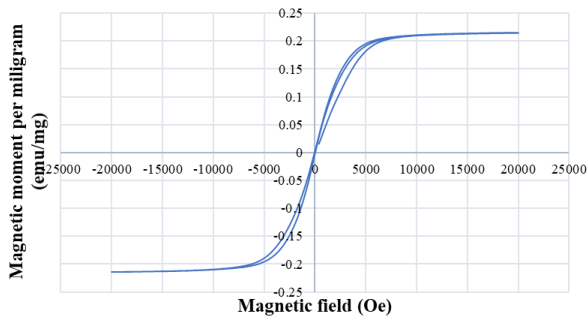


Figure S2.3 Magnetic moment of control Lord 140 CG particles and aged particles from high and low Mn tests.

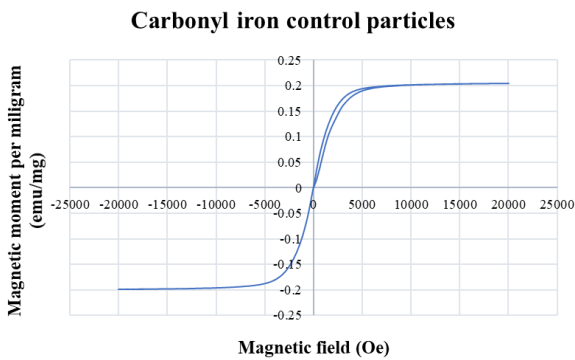
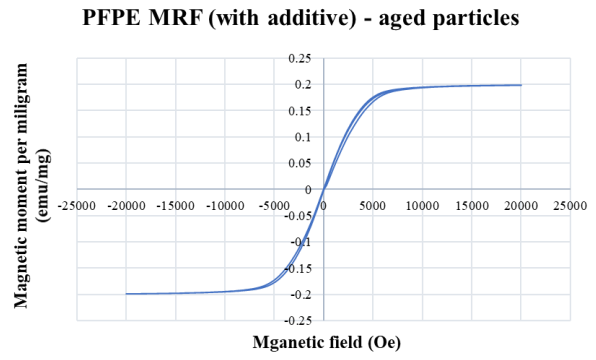
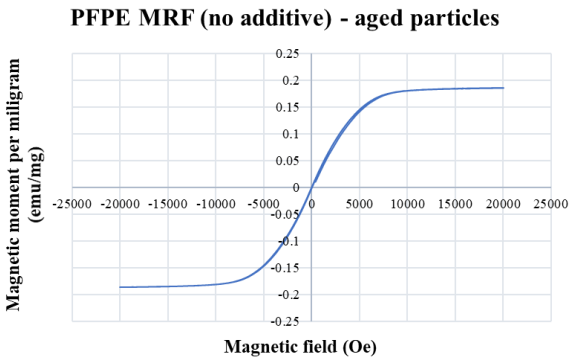
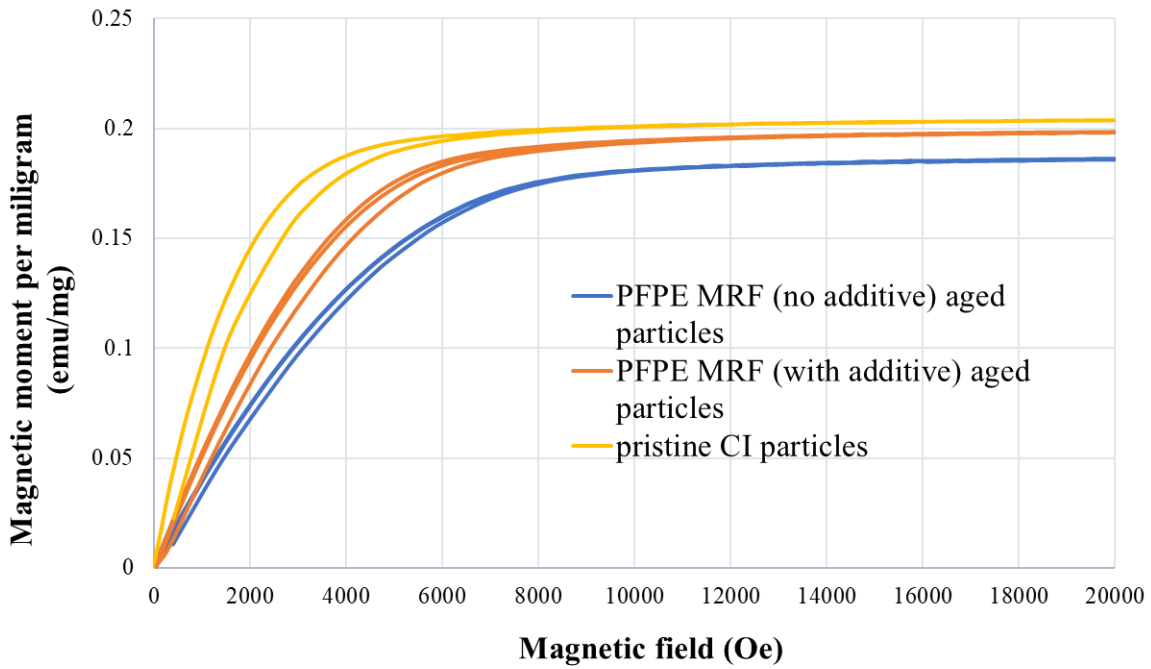


Figure S2.4 The magnetic moment of control carbonyl iron particles and aged particles from PFPE MR fluids with and without a lubricant additive. Aged particles from the no-additive MR fluid have a notable, although non-substantial, decrease in magnetic saturation.

2.8 References

1. Ashtiani, M., Hashemabadi, S.H. and Ghaffari, A., 2015. A review on the magnetorheological fluid preparation and stabilization. *Journal of magnetism and Magnetic Materials*, 374, pp.716-730.
2. Premalatha, S.E., Chokkalingam, R. and Mahendran, M., 2012. Magneto mechanical properties of iron based MR fluids. *Am. J. Polym. Sci*, 2(4), pp.50-55.
3. Spaggiari, A., 2013. Properties and applications of Magnetorheological fluids. *Frattura ed Integrità Strutturale*, 7(23), pp.48-61.
4. Utami, D., Mazlan, S.A., Imaduddin, F., Nordin, N.A., Bahiuddin, I., Aziz, A., Aishah, S., Mohamad, N. and Choi, S.B., 2018. Material characterization of a magnetorheological fluid subjected to long-term operation in damper. *Materials*, 11(11), p.2195.
5. Desrosiers, J.F., Bigué, J.L., Denninger, M., Julió, G., Plante, J.S. and Charron, F., 2013, February. Preliminary investigation of magnetorheological fluid durability in continuous slippage clutch. In *Journal of physics: conference series* (Vol. 412, No. 1, p. 012022). IOP Publishing.
6. Wang, D., Zi, B., Zeng, Y., Xie, F. and Hou, Y., 2015. An investigation of thermal characteristics of a liquid-cooled magnetorheological fluid-based clutch. *Smart Materials and Structures*, 24(5), p.055020.
7. Carlson, J.D., 2002. What makes a good MR fluid?. In *Electrorheological Fluids and Magnetorheological Suspensions* (pp. 63-69).
8. Smith, A.L., Ulicny, J.C. and Kennedy, L.C., 2007. Magnetorheological fluid fan drive for trucks. *Journal of Intelligent Material Systems and Structures*, 18(12), pp.1131-1136.

9. Ulicny, J.C., Balogh, M.P., Potter, N.M. and Waldo, R.A., 2007. Magnetorheological fluid durability test—Iron analysis. *Materials science and engineering: A*, 443(1-2), pp.16-24.
10. Ulicny, J.C., Hayden, C.A., Hanley, P.M. and Eckel, D.F., 2007. Magnetorheological fluid durability test—organics analysis. *Materials Science and Engineering: A*, 464(1-2), pp.269-273.
11. Sherman, S.G., Becnel, A.C. and Wereley, N.M., 2015. Relating Mason number to Bingham number in magnetorheological fluids. *Journal of Magnetism and Magnetic Materials*, 380, pp.98-104.
12. Berli, C.L. and de Vicente, J., 2012. A structural viscosity model for magnetorheology. *Applied Physics Letters*, 101(2), p.021903.
13. Sherman, S.G. and Wereley, N.M., 2014. Performance of magnetorheological fluids beyond the chain based shear limit. *Journal of Applied Physics*, 115(17), p.17B523.
14. Becnel, A.C. and Wereley, N.M., 2017. Using Mason number to predict MR damper performance from limited test data. *AIP Advances*, 7(5), p.056725.
15. Melle, S., Calderón, O.G., Rubio, M.A. and Fuller, G.G., 2003. Microstructure evolution in magnetorheological suspensions governed by Mason number. *Physical Review E*, 68(4), p.041503.
16. Tatlow, J. C. 1984. The stabilities of organic fluorine compounds. *Journal of Fluorine Chemistry*, 25(1), pp. 99-110.
17. Cui, H. and Li, D., 2018. Preparation and property research of perfluoropolyether oil-based ferrofluid. *Journal of Superconductivity and Novel Magnetism*, 31(11), pp.3607-3624.
18. Napier, M.E. and Stair, P.C., 1991. Perfluoroalkylether reactions on iron and oxygen covered iron surfaces studied using x-ray photoelectron spectroscopy and secondary ion

- mass spectrometry. *Journal of Vacuum Science & Technology A: Vacuum, Surfaces, and Films*, 9(3), pp.649-652.
19. Napier, M.E. and Stair, P.C., 1992. Decomposition pathway for model fluorinated ethers on the clean iron surface. *Journal of Vacuum Science & Technology A: Vacuum, Surfaces, and Films*, 10(4), pp.2704-2708.
 20. Lord corporation. 2015. LORD TECHNICAL DATA. Available from: <http://www.lordmrstore.com/lord-mr-products/mrf-140cg-magneto-rheological-fluid>
 21. Hreinsson E, 2011. Durability of a magnetorheological fluid in a prosthetic knee joint (Doctoral dissertation).
 22. Bigué, J.P.L., Landry-Blais, A., Pin, A., Pilon, R., Plante, J.S., Chen, X. and Andrews, M., 2019. On the relation between the Mason number and the durability of MR fluids. *Smart Materials and Structures*, 28(9), p.094003.
 23. Livshits, L. S., 1959. Migration of carbon in alpha iron and solubility of carbon in ferrite *Metal Science and Heat Treatment*, 1, pp. 15-18.
 24. Kusmanov, S.A., Belkin, P.N., D'yakov, I.G., Zhiron, A.V., Mukhacheva, T.L. and Naumov, A.R., 2014. Influence of oxide layer on carbon diffusion during anode plasma electrolytic carburizing. *Protection of Metals and Physical Chemistry of Surfaces*, 50(2), pp.223-229.
 25. Furlan, A., Jansson, U., Lu, J., Hultman, L. and Magnuson, M., 2015. Structure and bonding in amorphous iron carbide thin films. *Journal of Physics: Condensed Matter*, 27(4), p.045002.

26. Torres Galvis, H.M., Bitter, J.H., Davidian, T., Ruitenbeek, M., Dugulan, A.I. and de Jong, K.P., 2012. Iron particle size effects for direct production of lower olefins from synthesis gas. *Journal of the American Chemical Society*, 134(39), pp.16207-16215.
27. Bauer, I. and Knölker, H.J., 2015. Iron catalysis in organic synthesis. *Chemical Reviews*, 115(9), pp.3170-3387.
28. Grosvenor, A.P., Kobe, B.A. and McIntyre, N.S., 2004. Examination of the oxidation of iron by oxygen using X-ray photoelectron spectroscopy and QUASESTM. *Surface science*, 565(2-3), pp.151-162.
29. Biesinger, M.C., Lau, L.W., Gerson, A.R. and Smart, R.S.C., 2010. Resolving surface chemical states in XPS analysis of first row transition metals, oxides and hydroxides: Sc, Ti, V, Cu and Zn. *Applied surface science*, 257(3), pp.887-898.
30. Lin, T.C., Seshadri, G. and Kelber, J.A., 1997. A consistent method for quantitative XPS peak analysis of thin oxide films on clean polycrystalline iron surfaces. *Applied Surface Science*, 119(1-2), pp.83-92.
31. Yamashita, T. and Hayes, P., 2008. Analysis of XPS spectra of Fe²⁺ and Fe³⁺ ions in oxide materials. *Applied surface science*, 254(8), pp.2441-2449.
32. Viefhaus, H., Hennesen, K., Lucas, M., Müller-Lorenz, E.M. and Grabke, H.J., 1994. Ion sputter rates and yields for iron-, chromium-and aluminium oxide layers. *Surface and interface analysis*, 21(9), pp.665-672.
33. Tapping, R.L., Davidson, R.D., Jackman, T.E. and Davies, J.A., 1988. Effect of analytical method on thickness measurements of thin oxide films. *Surface and interface analysis*, 11(8), pp.441-446.

34. Ullevig, D.M. and Evans, J.F., 1982. Sputtering yields of electrochemically deposited metal and metal oxide thin films. *Journal of Vacuum Science and Technology*, 20(3), pp.379-382.
35. Suzuki, S., Sugiyama, K. and Waseda, Y., 2002. Changes in the chemical state and composition of the surface of iron oxides due to argon ion sputtering. *Journal of Surface Analysis*, 9(3), pp.455-458.
36. McIntyre, N.S. and Zetaruk, D.G., 1977. X-ray photoelectron spectroscopic studies of iron oxides. *Analytical Chemistry*, 49(11), pp.1521-1529.
37. Fondell, M., Gorgoi, M., Boman, M. and Lindblad, A., 2018. Surface modification of iron oxides by ion bombardment—Comparing depth profiling by HAXPES and Ar ion sputtering. *Journal of Electron Spectroscopy and Related Phenomena*, 224, pp.23-26.
38. Mauvernay, B., Presmanes, L., Capdeville, S., De Resende, V.G., De Grave, E., Bonningue, C. and Tailhades, P., 2007. Elaboration and characterization of Fe_{1-x}O thin films sputter deposited from magnetite target. *Thin Solid Films*, 515(16), pp.6532-6536.
39. Matsuda, Y., Yamaguchi, K., Suenaga, K., Yamagata, Y., Honda, C., Maeda, M., Yamamura, Y., Muraoka, K. and Akazaki, M., 1988. Measurement of preferential sputtering of iron-oxides using laser fluorescence spectroscopy. *Japanese journal of applied physics*, 27(11A), p.L2022.
40. Steinberger, R., Walter, J., Greunz, T., Duchoslav, J., Arndt, M., Molodtsov, S., Meyer, D.C. and Stifter, D., 2015. XPS study of the effects of long-term Ar⁺ ion and Ar cluster sputtering on the chemical degradation of hydrozincite and iron oxide. *Corrosion Science*, 99, pp.66-75.

41. John, P.J. and Liang, J., 1994. Initial metal fluoride formation at metal/fluorocarbon interfaces. *Journal of Vacuum Science & Technology A: Vacuum, Surfaces, and Films*, 12(1), pp.199-203.
42. Liu, J., Stirniman, M.J. and Gui, J., 2003. Catalytic decomposition of perfluoropolyether lubricants. *IEEE transactions on magnetics*, 39(2), pp.749-753.
43. Sina, M., Thorpe, R., Rangan, S., Pereira, N., Bartynski, R.A., Amatucci, G.G. and Cosandey, F., 2015. Investigation of SEI layer formation in conversion iron fluoride cathodes by combined STEM/EELS and XPS. *The Journal of Physical Chemistry C*, 119(18), pp.9762-9773.
44. Carlo, S.R., Wagner, A.J. and Fairbrother, D.H., 2000. Iron metalization of fluorinated organic films: A combined X-ray photoelectron spectroscopy and atomic force microscopy study. *The Journal of Physical Chemistry B*, 104(28), pp.6633-6641.
45. Miki, N., Maeno, M., Maruhashi, K., Nakagawa, Y. and Ohmi, T., 1990. Fluorine passivation of metal surface for self-cleaning semiconductor equipment. *IEEE Transactions on Semiconductor Manufacturing*, 3(1), pp.1-11.
46. Daniel, P.L. and Rapp, R.A., 1976. Halogen corrosion of metals. In *Advances in corrosion science and technology* (pp. 55-172). Springer, Boston, MA.

Chapter 3

Carboxylated cellulose nanocrystal cryogels: porous monoliths of CNC and CNC-magnetite nanoparticles oriented under hydrodynamic flow and magnetic field

3.1 Introduction

This chapter describes the fabrication and characterization of oriented porous cryogel scaffold monoliths from carboxylated cellulose nanocrystals (CNC) and CNC nanocomposites comprising bound magnetite nanoparticles. Impetus for the research comes in part from the medical field where nanoscale cellulose, including CNC and cellulose nanofibers, are under development for use in tissue engineering. The study is also motivated by the larger field of research into self-assembling and self-organizing matter. Under certain conditions, water suspensions of sulfated and carboxylated CNC will undergo an isotropic to chiral nematic phase transition. This is a nonlocal event that can be assisted by applying a magnetic field that interacts with the diamagnetic susceptibility of the nanocrystals. The magnetic field promotes the uniaxial alignment of the helicoid axes of the chiral nematic phase. Evaporation of water in the presence of the field to make solid films and monoliths locks in the chirality. CNC will also align under shear in hydrodynamic flow. Recent research by Munier et al. has shown that unidirectional freezing of sulfated CNC in water underflow can yield somewhat ordered monoliths of CNC with different pore size distributions.¹ From a medical applications perspective, these monoliths may have potential as tissue scaffolds. Our experiments focus on fabricating carboxylated CNC-based

cryogel scaffolds from aqueous suspensions at different freezing temperatures, under different modes of freezing, and by freezing with or without the influence of an applied static magnetic field. In these experiments, water acts as a porogen. We examined the resulting cryogel scaffolds by scanning electron microscopy (SEM) and processed the images quantitatively to extract porosity. Our findings showed that the pore morphologies of the carboxylated CNC-based cryogel scaffolds depend in complex ways on the conditions under which freezing takes place. Small-angle x-ray scattering (SAXS) was performed to obtain nanoscale structural information, while dynamic vapor sorption (DVS) was performed to obtain specific surface area and equilibrium moisture content.

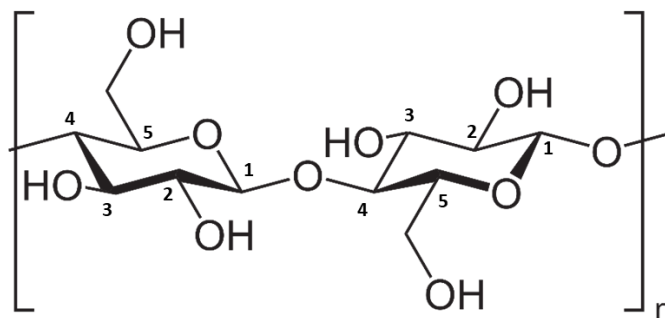


Figure 3.1 Chemical structure of cellulose showing the $\beta(1 \rightarrow 4)$ -glycosidic bond linking two D-glucose units.

3.1.1 Cellulose nanocrystals

Cellulose is a biopolymer consisting of repeating β -D-anhydroglucopyranose units and can be produced from many sources such as plants and bacteria (Figure 3.1).² Nanocellulose is a general term that encompasses cellulose nanofibers (CNF), cellulose nanocrystals (CNC) and bacterial nanocellulose (BNC). Cellulose nanocrystals (CNCs) are made from cellulose by selectively degrading the cellulose disordered and amorphous regions using strong acids and

oxidizers.² Carboxylated CNC used in our studies was obtained by oxidation with dilute hydrogen peroxide of dissolving pulp from black spruce. CNC exhibits high crystallinity, robust mechanical strength, and unusual optical anisotropy in scattering left circularly polarized light.^{2, 3} CNC also retains many advantages shared amongst other cellulose materials, such as low cytotoxicity.^{2, 4} Much research interest has been focused on utilizing the unique properties of CNC to develop novel CNC-based materials with advanced functionality.

3.1.2 Applications of CNC and magnetite incorporated CNC materials

There is a strong incentive to make porous materials from CNC for use in applications as diverse as supercapacitors and sensors,⁵ thermal insulators,⁶ adsorbents,⁷ host matrices to support catalysts,⁸ drug loading and release systems,^{9, 10} hosts for cell culture,¹¹ and supporting scaffolds for tissue engineering.^{12–15} Incorporating magnetite nanoparticles (MNP) into the nanocellulose networks helps expand the applications and better realize some existing functionalities.¹⁶ For example, magnetite nanoparticle-CNC nanocomposites have been demonstrated as contrast agents for magnetic resonance imaging.¹⁷ MNP-CNC composites have been used as adsorbents for metal ions such as Hg(II) and Sb(III).^{18, 19} Magnetite (Fe_3O_4) can be attracted to a magnetic field to ease separations and recovery of contaminants. Polymer-coated MNPs have been grafted onto scaffolds made with CNC or bacterial nanocellulose (BNC) for biomedical applications. BNC appears to have higher intrinsic crystallinity and purity than plant-based CNCs due in part to the complete lack of lignin and hemicellulose.¹⁴ Nevertheless, high purity CNC can be obtained by carefully controlling the reaction and purification conditions. In one application, the combination of coated MNPs in CNC scaffolds is found to simulate the architecture and biomechanical behavior of animal tendons and provides magneto-mechanical stimulation for cell regeneration.²⁰ Elsewhere,

coated MNPs in BNC scaffolds have been applied to the surface of stents to orient magnetized endothelial cells for the reconstruction of tunica media tissue.²¹

3.1.3 Freeze casting of nanocellulose to make porous scaffolds

Freeze casting is a common method for making porous materials such as various types of colloidal gels. In freeze casting, solidification of the solvent induces a physical separation of nanocellulose from the suspending medium. Crystals of the frozen solvent serve as sacrificing templates, allowing physical or chemical crosslinking of nanocellulose around the crystals. The frozen crystals are then removed by sublimation methods like freeze-drying and supercritical drying, revealing scaffolds of nanoparticle networks with an interconnected porous structure.^{14, 15}

It is known that freezing temperature, solvent type, freezing mode, and the physiochemical properties of the colloidal nanoparticles are important factors governing the structure of the porous product.¹⁵ Numerous experiments have looked into the freeze casting of cellulose nanofibrils (CNFs) which have long and flexible fibril chains allowing for entanglements.^{22 – 25} Similar research on CNCs is relatively scarce,^{1, 26} and no work has been done to examine the freeze casting of MNP-decorated CNC scaffolds.

Furthermore, the majority of nanocellulose cryogel studies have focused on investigating morphologies and mechanical properties. For example, water sorption greatly impacts materials' mechanical properties and stability and can affect their applicability in the biomedical fields.^{27 – 32} There has been some water sorption study of cellulose-based materials such as MCCs, CNFs, and CNCs.^{33 – 36} However, to the best of our knowledge, the water sorption properties of CNC cryogels,

especially in connection with explorations of nanoscale structural features, have not been investigated.

3.1.4 Design of current experiment

Our experiments described below aim to provide a reference for the freeze casting fabrication of cryogel scaffolds using CNCs and MNP decorated CNCs. Three freezing modes are tested: one-step low temperature freezing at -196 °C, one-step high temperature freezing at -12 °C, and two-step freezing by a freeze-thaw cryogelation cycle at high temperature, followed by freezing at low temperature. The two-step freezing aims to investigate how a change in freezing pattern affects pore structures. In addition, inspired by the debates on the effects of static magnetic fields (SMF) on freezing,^{37–47} an SMF was applied in the cryogelation step to examine possible changes to the final pore structures.

Non-invasive analyses were carried out to probe structural insights of the cryogels from macroscale to nanoscale. Image analysis using a "local thickness" algorithm was performed on SEM images of the cryogel scaffolds to obtain accurate estimates of minimum macropore sizes. Small-angle x-ray scattering (SAXS) was performed to characterize nanoscale structures such as the aggregation of CNCs and the arrangement of polymers within the CNC crystals. SAXS experimentally determines the x-ray scattering intensity $I(q)$ as a function of the scattering vector q , i.e., $I(q) \propto q^{-\tau}$, where τ is the scattering exponent. It was found that the polydispersity of particles in a cluster can affect the scattering exponent due to their self-similarity.⁶⁴ This self-similarity can be deterministic in nature, where an intrinsic pattern repeats itself under a transformation scale, or it can be a statistical similarity, which is the case for most structures in

practice.⁶⁴ As a result of the self-similar property, regions where the scattering intensity $I(q)$ decays as a power law can be described using the ideas of fractal distributions.^{51, 64, 65} Other models that depend on the decay of $I(q)$ as a power law also apply. For example, the Debye, Anderson and Brumberger (DAB) model interprets a cluster system as a periodic lattice with equal distance between particles (or phases), with the assumption that the particles have smooth interfaces and the cluster exhibit $I(q) \propto q^{-4}$ behaviour.⁵² In addition, dynamic vapour sorption (DVS) was performed to obtain specific surface area and equilibrium moisture content. By relating the analyses done by SEM-local thickness, SAXS, and DVS, we aim to improve our understanding of the structural properties of CNC-based cryogels as renewable, biocompatible, and biodegradable porous materials.

3.2 Experimental

3.2.1 Cellulose nanocrystalline (CNC) suspension

The CNC suspension used in this experiment was a carboxylated entity obtained from Anomera Inc. The CNC was used without further purification. This suspension has a solid concentration of 3.8 %wt in water.

3.2.2 Magnetite nanoparticles decorated cellulose nanocrystalline (CNC-MNP)

Cellulose nanocrystals decorated with MNPs were synthesized *in situ* with a co-precipitation method based on the work of Hassan et al.¹⁹ Briefly, 20 mL of the CNC suspension was thoroughly mixed in 100 mL of MiliQ water(18.2 MOhm), first by stirring, then by sonication

(Sonics Vibra-cell VCX130 probe sonicator), until the cellulose crystals were fully dispersed. The CNC suspension was degassed under vacuum several times before flushing with argon. An argon atmosphere was maintained for the duration of the synthesis.

A separate 10 mL aqueous solution containing 1.0 mmol of ferrous chloride ($\text{FeCl}_2 \cdot 4\text{H}_2\text{O}$; Sigma Aldrich) and two equivalent of ferric chloride ($\text{FeCl}_3 \cdot 6\text{H}_2\text{O}$; Sigma Aldrich) was prepared and was slowly injected into the stirred CNC suspension. Addition of the Fe-based solution induced agglomeration in the reaction mixture, but this agglomeration was eventually dispersed after continual mixing. After thorough mixing, the mixture exhibited an orange color. It was then heated to 70 °C for 1 hour.

A 1:10 diluted aqueous NH_3OH solution was used to coprecipitate the iron oxide. The NH_3OH solution was injected into the reaction mixture in small quantities under vigorous stirring. The reaction was completed when the mixture turned black. The mixture was stirred for 15 min more before the heat was removed. Once cooled to room temperature, the product was collected by a magnet. The product was washed many times using DI water until the wash reached a pH of 7. Excess water was removed by centrifuge at 500 rpm.

3.2.3 CNC and CNC-MNP-containing cryogel preparation

The as-obtained CNC suspension exhibited a gel-like texture, while the as-synthesized MNP decorated CNCs showed a wet sand-like consistency. CNC cryogels were prepared directly with the as-obtained CNC suspension. MNP-incorporated CNC cryogels were made from a mixture of 20 % v/v of the as-synthesized MNP decorated CNCs (CNC-MNP) and 80 % v/v of as-

obtained CNC suspension to achieve gelation similar to that of the CNC suspension. The mixed CNC-MNP suspension has a solid concentration of 3.9 %wt in water.

"High-temperature" freezing of the suspension was performed in a freezer (-12 °C), while "low-temperature" freezing was achieved by submerging the suspension in liquid nitrogen (-196 °C). Two-step freezing was conducted by first freezing the sample at -12 °C for 8 hours, allowing the sample to thaw, then re-freezing the sample at liquid nitrogen temperature. Each sample consisted of 2 mL of CNC or mixed CNC-MNP suspension placed in a 6-dram vial. Each sample was placed in a holder during the freezing experiments. Two pieces of permanent NdFeB bar magnets (type BX8X84 1.5" x 1.5" x 0.25" thick nickel plated; K&J Magnet Inc) were attached to the sample holder to create an external magnetic field, as shown in Scheme S3.1A. After freezing, the frozen samples were freeze-dried in a lyophilizer (Labconco FreeZone 2.5L benchtop freeze dryer) for 48 hr. Specific freezing conditions for each of the cryogel samples are detailed in Table 3.1.

Table 3.1 Summary of sample names and corresponding freezing conditions

Name	Magnetic field applied	Freezing temperature and duration
CNC -12°C	-	-12°C for 12 hr
CNC N _{2(l)}	-	-196°C for 40 min
CNC 8 hr	-	-12°C for 8 hr, thawed for 2 hr, then -196°C for 40 min
CNC 8 hr; H field applied	85 mT	-12°C for 8 hr, thawed for 2 hr, then -196°C for 40 min
CNC-MNP -12°C	-	-12°C for 12 hr
CNC-MNP N _{2(l)}	-	-196°C for 40 min

CNC-MNP 8 hr	-	-12°C for 8 hr, thawed for 2 hr, then -196°C for 40 min
CNC-MNP 8 hr; H field applied	85 mT	-12°C for 8 hr, thawed for 2 hr, then -196°C for 40 min

3.2.4 X-Ray photoelectron spectroscopy (XPS)

XPS was performed using Thermo Scientific $K\alpha$ X-Ray Photoelectron Spectroscopy. The X-ray source employed in this experiment was an Al- $K\alpha$ X-ray of 1486.6 eV. The X-ray beam was directed at an incident angle of 60° from normal (30° from the horizontal plane of the sample) with a focal spot size of 400 μm . A flood gun was used alongside the X-ray gun to suppress peak shifting caused by sample charging due to insufficient conductivity.

Before XPS analysis, as-obtained CNC and as-synthesized CNC-MNP were dried in a vacuum. Dried and crushed samples were then mounted onto conductive copper tape to avoid elemental contamination. The XPS vacuum chamber was maintained at $<2 \times 10^{-7}$ mbar throughout the experiments.

3.2.5 Scanning electron microscopy (SEM)

Qualitative images of the cryogel scaffold structures were taken with FEI Quanta 450 Environmental Scanning Electron Microscope (FE-ESEM). The scaffolds were coated with a 4 nm layer of platinum to increase conductivity before conducting SEM.

3.2.6 Quantitative image analysis of macropore sizes using local thickness

Quantitative image analysis of macropore sizes was performed using the local thickness functionality in the python library "PoreSpy".⁴⁸ The "local thickness" of a 2D or 3D pore structure is measured using a superseding spheres algorithm to quantify the maximum diameter of a sphere that would fit in the pore space. This algorithm disregards the pore shape while only focusing on the minor axis of the pore. As a result, local thickness gives an accurate estimate of the lower bound of the pore sizes.^{49, 50}

In PoreSpy, local thickness data are described in voxels, which correlate with the partial volume occupied by spheres of a certain size. The diameter of the spheres was changed from voxels to micrometers by multiplying the voxel length in micrometers for each image being analyzed. The voxel length in micrometers was obtained using ImageJ. Prior to calculating local thickness, each SEM image underwent inverse Otsu thresholding to transform the image from greyscale to binary. A summary of the local thickness analysis for the 8 cryogel scaffolds can be found in Figure S3.2.

3.2.7 Small-angle X-ray Scattering (SAXS)

SAXS measurements were conducted on a SAXSpoint 2.0 (Anton Paar, Austria) equipped with a CuK α radiation source (wavelength, $\lambda = 1.54 \text{ \AA}$), using a detector of Eiger R 1M (Horizontal). The sample-to-detector distance was maintained at 574 mm. The cryogel scaffolds were placed in a special solid holder. The obtained SAXS profiles were corrected and shown as a function of the scattering vector ($q = (4\pi/\lambda) \sin\theta$, where θ is the scattering angle in degrees and q in nm^{-1}). The SAXS curves contain the scattering pattern produced by elastic scattering of X-rays as they travel through the material at angles in the $0.1\text{--}10^\circ$ range. The maximum SAXS q range

obtained in this experiment was $0.066 - 5.5 \text{ \AA}^{-1}$. Each SAXS curve was fitted using a combination of the surface fractal model and the Debye-Anderson-Brumberger (DAB) model, both available in the analysis program SasView. The fractal model, constructed based on the work of Mildner et al., compared the non-integral power-law density correlation function of a SAXS curve to the theoretical predictions of the form of the scattering expected from fractal clusters.⁵¹ On the other hand, the DAB model calculates the correlation function based on scattering from a randomly distributed, two-phase system.⁵² The DAB model is well suited for approximating spacing between smooth surface domains of fully random shape, size, and distribution. Definitions of the two models employed in this experiment are elaborated in Supporting material.

3.2.8 *Dynamic vapor sorption analysis (DVS)*

Dynamic vapor sorption analysis (DVS) was performed using Surface Measurement Systems. The experiment was conducted based on a full cycle sorption desorption method. The sorption cycle starts from 0RH% to 98RH% sorption with an increment of 5RH% followed by desorption to 0RH%, in which the temperature was kept constant at 25 °C during the measurements. The sample was allowed to equilibrate for a period of one hour between steps. DVS provides a gravimetric measurement of how quickly and how much water is absorbed by each of the cryogel scaffolds. In addition, DVS provides "Brunauer, Emmett and Teller" (BET) specific surface area data. DVS-BET was calculated using gravimetric measurements obtained during water vapor adsorption at ambient pressure and temperature (298 K).

3.3 Results and Discussions

3.3.1 CNC and CNC-MNP cryogels

3.3.1.1 XPS analysis of as-obtained CNCs and as-synthesized CNC-MNP

The highest intensity peak (286.8 eV) in the C1s spectrum of CNC (Figure 3.2A) is assigned to C-O and C=O bonds, with the C-O bond being typical for the cellulose molecules composed of glucose rings. The peak at 288.4 eV indicated the presence of carboxylate groups.⁵³ The O1s spectrum has a major peak at 533.1 eV and a minor peak at 531.8 eV. The former is assigned to O-C, reaffirming the abundance of ether and hydroxyl groups in cellulose. The latter peak is assigned to ketones.^{53, 54}

The growth of iron oxide (magnetite) nanoparticles on the CNC produced no discernable change in the carbon and oxygen-binding energies, as indicated in Figure 3.2B. The most notable change in the spectral features is the addition of a broad peak centered at 530.4 eV in the O1s spectrum. We assign this peak to Fe-O bonds of iron oxide. The Fe-C2p spectrum confirms the presence of iron. TEM images of the MNP-decorated CNCs are shown in Figure 3.2C. Magnetite nanoparticles 3 – 12 nm in diameter are visible on the surface of CNC particles that have assembled end-to-end and aggregated side-by-side. No MNPs were observed free in the surrounding regions away from the CNC. This observation is consistent with the nucleation and growth of magnetite nanoparticles on the CNC. MNPs in this size range are superparamagnetic, meaning that the hybrid CNC/MNP system aligns in an external magnetic field. (See Figure S3.1).

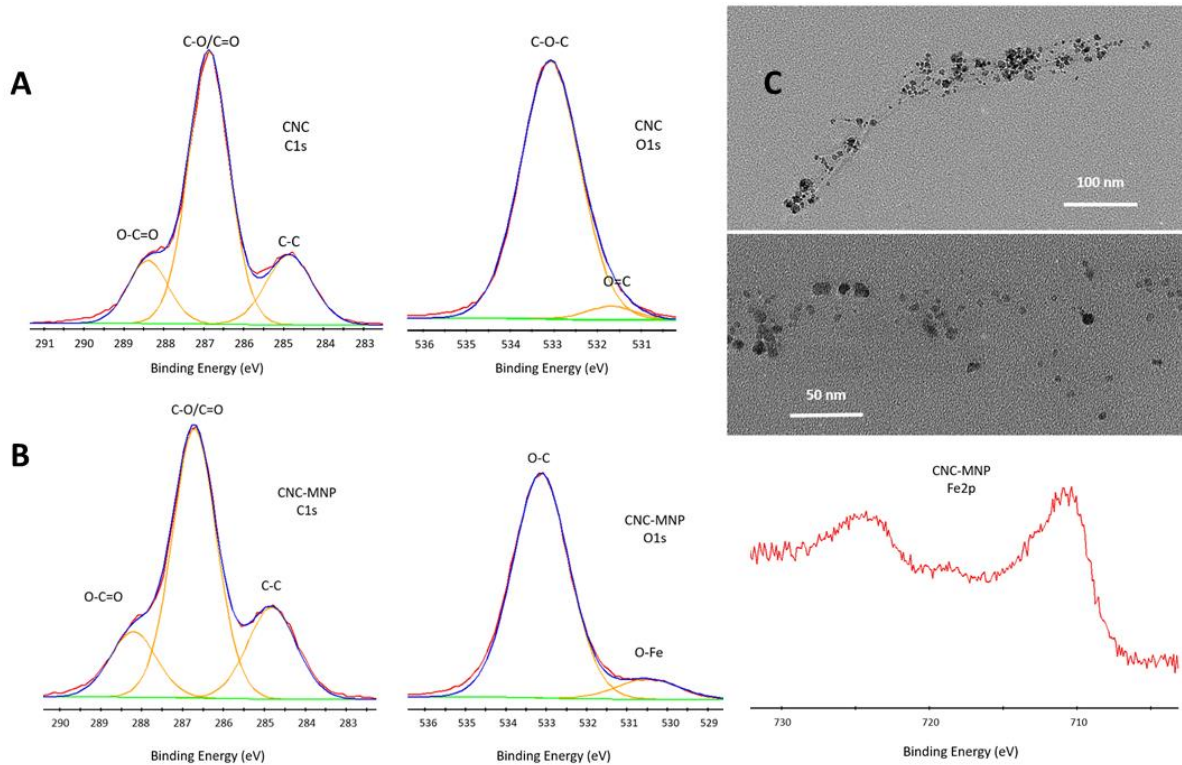


Figure 3.2 XPS analysis of (A) CNC as obtained without MNPs, and (B) with MNPs bound to CNC. (C) shows TEM images of the MNP decorated CNCs at two magnifications. The CNC is barely visible as weak contrast against the background.

3.3.2 High and low freezing temperature: Impact on pore morphologies and macropore sizes of CNC and mixed CNC-MNP cryogels

Figure 3.3 shows SEM images of the various microporous structures obtained under the different freezing conditions that are organized in Table 3.1. The most prominent morphological change is observed between the cryogel scaffold frozen at $-12\text{ }^{\circ}\text{C}$ when compared with that frozen rapidly in liquid nitrogen. The slow freezing process associated with high-temperature freezing

resulted in polydisperse pore structures with large pore sizes (Figure 3.3A, C), while rapid, low-temperature freezing produced closely aligned and layered structures and smaller pore sizes (Figure 3.3B, D). A sample macropore size calculation of CNC cryogel scaffold frozen at -12 °C using the local thickness method is shown in Figure 3.4.

The distinctive morphological differences between cryogel scaffolds produced by high- and low-temperature freezing can be explained by the effects of temperature on ice nucleation. Studies on ice nucleation and crystal growth have found that lower freezing temperatures lead to a higher degree of supercooling.⁵⁵ A higher degree of supercooling means a greater number of ice crystals are nucleated and more water is instantly frozen.^{55, 56} As a result, fewer but larger ice crystals are expected when the freezing temperature is high, and numerous but smaller ice crystals are expected when the freezing temperature is low.^{55, 56}

Ice crystal formation creates porous structures when foreign particles are present in the freezing suspension. In our case, CNCs are rejected by the moving solidification front and are concentrated and entrapped between the ice crystals.^{56 – 59}

The ordered layering of elongated pores produced by low-temperature freezing is very similar to that produced by directional freezing in other studies.^{1, 57, 60} In those studies, directional freezing was achieved by slowly lowering the sample into liquid nitrogen, creating a temperature gradient within the suspension, where the direction of freezing was guided from the cold end to the warm end along the vertical axis. Although directional freezing was not carried out in this experiment, alignment of the pores with tilted horizontal orientation was observed (Figure S3.4), and the cryogel scaffold exhibited radial symmetry around the center axis. This tilted horizontal ordering was likely produced by the temperature gradient created as the suspension cooled from the outer edge of the container towards the center. Vertically aligned pores were not observed. A

possible explanation is the large contact surface at the bottom resulted in a small vertical temperature gradient. Furthermore, the growth of ice crystals could be affected by the inter-particle interactions and arrangements of the CNCs.¹ The CNCs are known to exhibit nematic ordering at high enough concentrations where layers of aligned CNCs are arranged.³ This arrangement could serve as an initial template to assist with the growth of lamellar ice sheets in between nematic planes. Unlike low-temperature freezing, high-temperature freezing produced rounded pore structures in scaffolds, indicating aggregated CNCs around individual unoriented ice crystals.^{57, 58}

The introduction of CNC-MNPs appeared to decrease the smoothness of the scaffold, with clusters of entangled fibers visible around the edges. This observation suggested an inhomogeneous distribution of CNC-MNPs within the CNC suspension. The cause of this inhomogeneity could be the aggregation of the uncoated MNPs, as observed in a previous ferrogel study.⁶¹ The effect of MNP-induced surface roughness is the most pronounced in high-temperature freezing (Figure 3.3C; CNC-MNP -12 °C). While pure CNC formed leaf-like scaffolds at high freezing temperatures (Figure 3.3A; CNC -12 °C), CNC-MNP formed sponge-like scaffolds with smaller pore sizes (Table 2) under the same conditions. The smaller pore sizes are an indication that the presence of MNPs induces changes to the formation of ice crystals. For example, MNPs are known to be highly effective ice nucleation sites.⁶² Furthermore, the MNP-induced surface roughness may have allowed CNC aggregates to better adapt to the shapes of unoriented ice crystals.

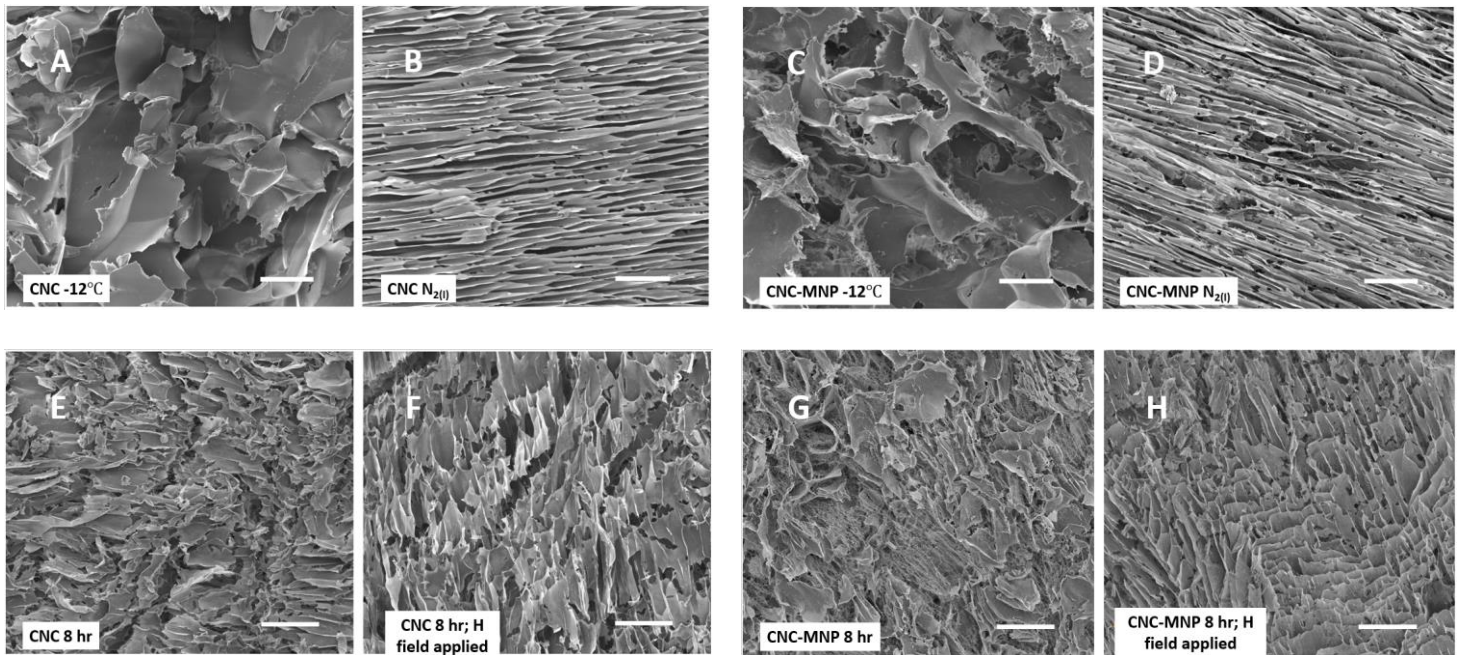


Figure 3.3 SEM images of the 8 cryogel scaffolds investigated in this experiment. Scale bars on the images are each 50 μm .

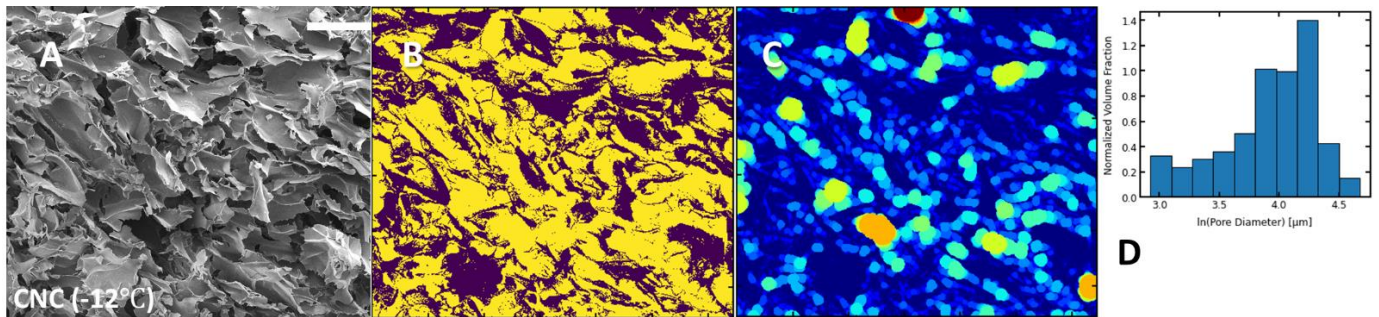


Figure 3.4 The SEM image (A), inverted binary image achieved by Otsu thresholding (B), local thickness fitting (C), and histogram of the pore diameter distribution against normalized volume fraction (D) of sample "CNC -12 °C". All scale bars on (A) represent 200 μm . The yellow color on B indicates areas of emptiness, and the brown color indicates partitioning formed by the aggregation of CNC. Image analysis for all 8 cryogel scaffolds are summarized in Figure S3.2.

Table 3.2 Summary of porosity information on the 8 cryogel scaffolds

name	Most frequent fraction Of diameter (μm)	2 nd most frequent fraction Of diameter (μm)	Total range of diameter (μm)	Surface fractal dimension ($q = 0.065 - 0.28 \text{ \AA}^{-1}$)	Correlation length (\AA) calculated by DAB model ($q = 0.28 - 1.5 \text{ \AA}^{-1}$)	DVS BET (m^2/g) ¹
CNC -12°C	75.5-63.4	53.2-44.7	18.6-107.1	2.00 ± 0.06	5.77 ± 0.61	141.9
CNC N _{2(l)}	11.1-9.5	9.5-8.1	4.4-20.7	2.00 ± 0.06	6.64 ± 0.64	144.2
CNC 8 hr	17.2-15.1	15.1-13.2	7.8-29.3	2.00 ± 0.06	6.61 ± 0.65	144.6
CNC 8 hr; H field applied	16.1-14.2	14.2-12.4	7.3-27.3	2.00 ± 0.06	5.83 ± 0.61	142.0
CNC-MNP -12°C	38.2-32.0	54.8-45.8	13.1-78.4	2.12 ± 0.06	2.54 ± 0.25	132.2
CNC-MNP N _{2(l)}	11.1-9.9	8.8-7.8	5.4-18.1	2.05 ± 0.06	2.80 ± 0.30	134.6
CNC-MNP 8 hr	18.1-15.7	11.9-10.4	7.8-31.6	2.07 ± 0.07	2.88 ± 0.31	130.5
CNC-MNP 8 hr; H field applied	11.8-10.3	13.5-11.8	6.9-26.5	2.11 ± 0.06	3.08 ± 0.33	135.1

¹The calculation of the BET is based on water as absorbent

3.3.3 Two-step freezing: high-temperature cryogelation followed by low-temperature freezing and the impact of an external magnetic field

Figure 3.3E-H shows the SEM images of CNC and CNC-MNP cryogel scaffolds made with two-step freezing to produce elongated pores with larger diameters. It was found that the additional cryogelation step increased the pore sizes of CNC scaffolds compared to the scaffolds made with N_{2(l)} freezing alone (Table 2). The cryogelation step introduced an aggregated network of CNCs, most likely caused by van de Waals forces and hydrogen bonding, which inhibited the redispersion of CNCs even after thawing.⁵⁹ This network served as a template for ice crystal growth during the follow-up low-temperature freezing step. CNC cryogel scaffolds that underwent this two-step freezing process showed mixed morphology characteristics of high and low temperature freezing as they possess somewhat elongated pore shapes and enlarged diameters (Figure 3.3E, 2F, Table 2). The effects of an applied SMF were also examined. The CNC-MNP cryogel made with an applied SMF during two-step freezing (Figure 3.3F) showed an increase in pore alignment over its counterpart made without an SMF (Figure 3.3E). The CNC-MNP cryogel made without an applied SMF (Figure 3.3G) consisted largely of unoriented pores surrounded by aggregated CNC-MNP sheets and exposed fibres. In comparison, the CNC-MNP cryogel made with an applied SMF (Figure 3.3H) exhibited more elongated pores (Figure 3.3D).

3.3.4 Potential SMF effects on the freezing mechanism

Liquid water freezes when water molecules come together to form clusters of 5–7 membered rings through hydrogen bonding.⁶³ Although water molecule clusters are normally short-lived, longer-lasting hydrogen bonds are formed when water enters the supercooling state.

Ice nucleation occurs when enough long-lived hydrogen bonds appear simultaneously at the same location.⁶³

Much research effort was devoted to investigating whether SMF can affect hydrogen bonding and hence be used to manipulate freezing,^{37–44} although results are ambiguous and likely depend on experimental conditions. While some studies found an SMF to increase the number of hydrogen bonds,^{37, 41} others found the SMF to weaken or distort hydrogen bonding,^{38–40, 42} as well as showing tendency to prolong the supercooling state of saltwater.^{43, 44}

Despite ongoing debates on the effects of an SMF on hydrogen bonding and freezing, an SMF has been demonstrated to impact the freezing of meat and fruit.^{45–47} It was observed that an applied SMF lowers the ice nucleation temperature in pork and beef^{45, 46} and reduces the ice crystal sizes in cherries.⁴⁷ The reduction in ice nucleation temperature and ice crystal sizes were attributed to a weakening of the hydrogen bonds due to the alignment and thermal motions of the water molecules under the SMF.^{40, 45–47}

The apparent difference between CNC-MNP 2-step freezing cryogel made with and without an applied SMF may be explained by these mechanisms. That is, the presence of the SMF may have disrupted the formation of ice crystals during the high temperature freezing step, reducing the aggregation of CNCs in the intercrystalline space between ice crystals. The resulting hydrogels thaw without retaining strong cryogelation networks. The stronger the cryogelation networks, the more structural restrictions they impose.⁵⁹ Weak cryogelation networks led to the formation of cryogel scaffolds with increased lamellar pore characteristics after low-temperature freezing.

3.3.5 Investigating nanoscale structures using SAXS

SAXS curves for CNC and CNC-MNP cryogel scaffolds is shown in Figure 3.5A and B, respectively. The x-axis of the SAXS curves is the scattering vector q , which relates to a length scale by $\frac{2\pi}{q}$.^{64 - 66} The SAXS data therefore reveals nanoscale insights 9.7 nm and under, corresponding to the low end of the current data set of 0.065 \AA^{-1} . Two q ranges of interest were examined. The first q range of interest of $0.065 - 0.28 \text{ \AA}^{-1}$ represents size range of $9.7 - 2.2 \text{ nm}$. In this size range, the slope of the scattering curve of all CNC and CNC-MNP cryogel scaffolds displayed approximate q^{-4} power law behaviour, indicating highly aggregated structures.⁶⁶ This aggregated structure likely corresponds to the aggregated CNC sheets making up the walls of the porous scaffolds, as indicated in Figure 3.4. As the measured scattering exponent for our samples is approximately 4, the samples fall into the surface fractal realm and are fitted using the surface fractal model.^{64, 65} The surface fractal dimension for each of the cryogel scaffolds is shown in Table 3.2. Cryogels made with CNC only all have a surface fractal dimension of 2, indicative of smooth surfaces and confirms our SEM observations. CNC-MNP cryogel scaffolds have slightly higher surface fractal dimension compared to the CNC scaffolds, suggesting that the surfaces are somewhat roughened due to the incorporation of MNPs; however, this difference is not significant.

The second q range of interest is at $0.28 - 1.5 \text{ \AA}^{-1}$, corresponding to a size range of $2.2 - 0.4 \text{ nm}$, respectively. The SAXS curves of CNC-MNP cryogel scaffolds differ from those of CNC cryogel scaffolds by showing a bump at this q range. This q range of interest, at length scales of individual CNC crystals or smaller,² was fitted using the DAB model (Figure S3.3B). The DAB model examines the average spacing between regions of two phases, namely the correlation length.⁵² The DAB fitting assumes a divided two-phase system with smooth interfaces. This makes

it a good model to probe the spacing between hard segmental units.⁶⁷ DAB is, therefore, the model of choice to investigate the structural changes induced by the *in situ* synthesis and deposition of MNPs onto the CNC surfaces. In a size range of 2.2 – 0.4 nm, the structures in focus are the cellulose polymers that bundle together to form one cellulose nanocrystal. The correlation length shows the amount of empty spacing between the polymers within the bundle.

Correlation lengths calculated using DAB revealed that deposition of MNPs onto CNC surfaces reduces the spacing between CNC polymers within a bundle (Table 3.2). The average correlation length for CNC-MNP cryogel scaffolds is 2.8 Å, while for CNC cryogel scaffolds, the value is 6.2 Å. This difference in average correlation lengths suggested that deposition of MNPs on CNC surfaces changes the arrangement of cellulose polymers within a cellulose nanocrystal. CNCs that underwent in-situ synthesis of magnetite nanoparticles seem to be more "compact", that is, having less spacing between polymers inside their nanocrystals.

Research on the CNC-MNP hybrid system found that introducing metal cations, such as Fe²⁺ and Fe³⁺ during the in-situ synthesis of magnetite on CNCs, can induce phase separation in CNC aqueous suspensions.¹⁶ The separation is due to electrostatic interactions between the negative surface groups on CNCs, such as the carboxylate groups found in our CNC samples, and the metal cations. The electrostatic interactions also induce irreversible aggregation of the CNCs, especially when large quantities of cations are added.¹⁶ Our DAB data shows that encountering cations can also result in cellulose polymers inside the nanocrystals being more tightly packed. This increased compactness of the CNC-MNP fibres could affect the surface area and adsorption properties.

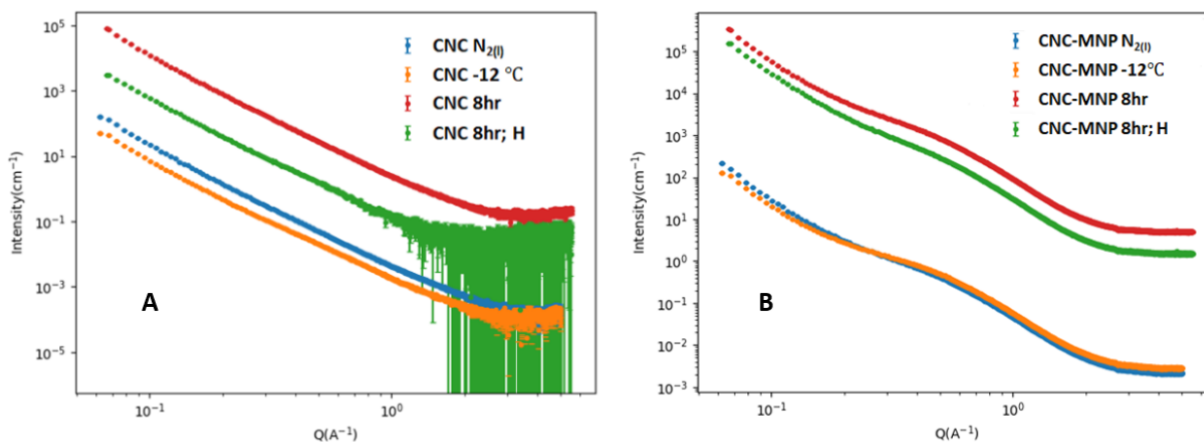


Figure 3.5 Small-angle X-ray (SAXS) measurements of (A) CNC and (B) CNC-MNP cryogel scaffolds.

3.3.6 Water vapor sorption study using DVS

The cryogel scaffolds expand with increasing water uptake and contract as moisture is removed (Figure S3.4). The adsorption isotherm for each cryogel scaffold is shown in Figure S3.5, and the calculated BET surface areas are listed in Table 3.2. The water vapour adsorption/desorption isotherms for different CNC cryogels are all type IV(a) isotherms with H2(b) hysteresis loops according to IUPAC classification.⁶⁸ Type IV(a) isotherms with H2(b) hysteresis loops correspond to mesoporous adsorbents with monolayer-multilayer adsorption and possible pore condensation.⁶⁸

The percent change in sample mass by adsorption and desorption of water vapor over time (Figure S3.6) reveals the equilibrium moisture content (EMC) and the sorption kinetics pattern of the cryogel scaffolds. Despite the difference in compositions (CNC vs. CNC-MNP) and pore structures, the cryogel scaffolds show similar adsorption kinetics. The EMC for different cryogel

samples falls within the range of 17.6% – 20.0%. CNC cryogel scaffolds show slightly higher EMC than CNC-MNP cryogel scaffolds, as shown in Figure 3.6.

Water sorption is greatly affected by the crystallinity of the material.^{34 – 36, 69 – 71} For crystalline solids, water adsorbs on the surface as monolayers and multilayers, while for amorphous solids, water sorption takes place in both adsorption on surfaces and absorption into the bulk fibril material.^{33, 34, 71, 72} Amorphous solids, therefore, can take up much more water than crystalline solids.^{70 – 72}

It was found that water penetrates pore structures and causes swelling, likely due to interactions with hydroxyl groups at the interface.^{35, 36, 73} The swelling, in turn, opens new sites for water sorption, including increasing the accessibility to micropores under 2 nm in size.^{36, 73, 74} The increased EMC for cryogel scaffolds with higher DAB-correlation lengths demonstrated in this experiment suggests micropores (< 2nm in size) exist in the cryogel samples.

The effects of crystallinity and structural swelling are visible in the hysteresis of water sorption. The lower the degree of cellulose crystallinity, the broader the hysteresis^{35, 36} The broad hysteresis is due to delayed desorption attributed to the slow breaking of hydrogen bonds at the interface, difficulty evacuating different pore sizes, and structural deformations.^{35, 36, 73} The hysteresis curves of water sorption for all cryogel scaffolds examined in this experiment are comparable to those identified elsewhere for CNCs with low amorphous content.³⁶

Nitrogen sorption BET at 77K is a common method to investigate the surface area of materials. BET produces reliable results for materials with meso- and macropores.⁷⁵ However, studies have found that N₂ sorption can be unreliable for determining the surface area of materials with small pores. In one study, Schlumberger et al. found the N₂ sorption can overestimate surface

area due to interactions with surface groups and the filling up of micropores.⁷⁵ On the contrary, in another study using Stöber silica spheres, Farrando-Pérez et al. found N₂ to have limited accessibility to micropores, likely due to kinetic barriers to N₂ molecules at 77K, which leads to underestimation of surface area for structures with very high microporosity, especially when the micropores have restricted ("ink-bottle") entrances.^{73, 74} In a previous study on microcrystalline cellulose, Kocherbitov et al. also proposed that N₂ adsorbs on the surface of cellulose particles, while studies have shown that water sorption occurs on both the surface and the gaps between nano-sized components inside the particles.⁶⁹

N₂ is known to have limited interfacial interaction with hydroxyl groups which avoid the problem of overestimating the area of surfaces where hydroxyl groups are numerous,³⁵ however, this may contribute to an unreliable surface area estimation using N₂. On the other hand, adsorbed water multilayers were found to have higher thickness compared to adsorbed nitrogen multilayers. Water sorption also led to more efficient pore network filling.^{33, 35, 76} Water sorption can build up to 3 – 6 layers on a crystal surface.⁷¹ In a study using Stöber silica spheres, it was estimated about 4 layers of water can adsorb on the surfaces at 25°C and $p/p_0 = 0.89$.^{73, 74}

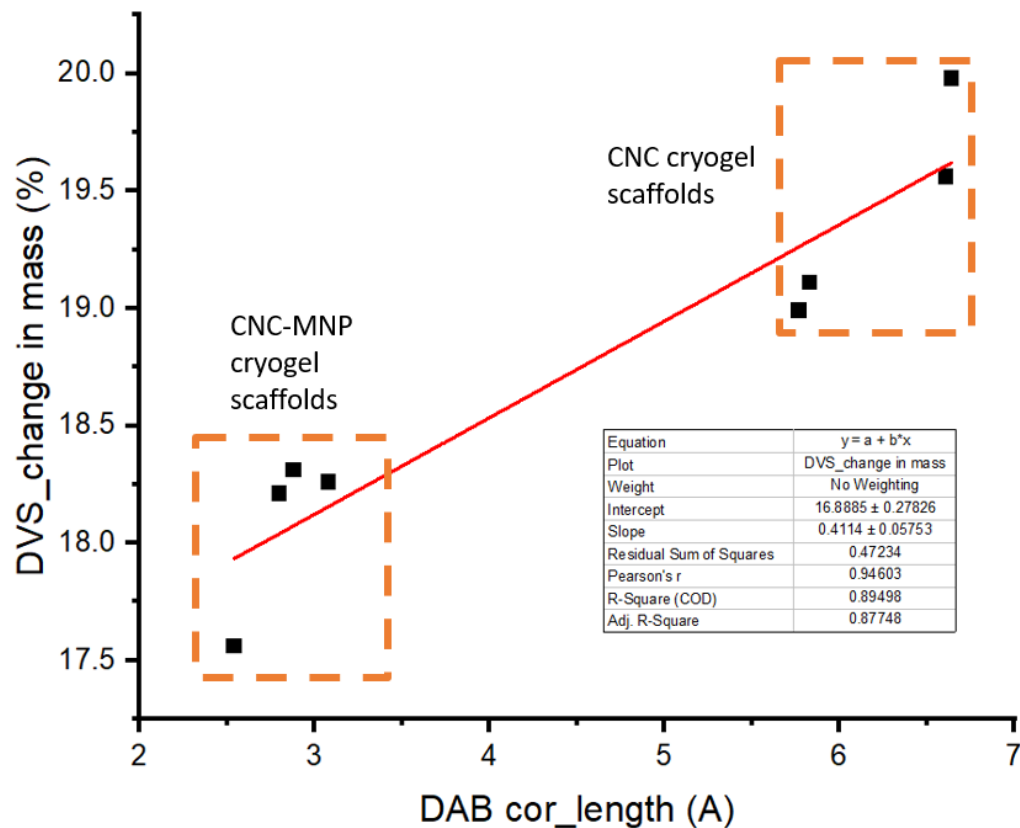


Figure 3.6 Relationship between the correlation length obtained by DAB and the DVS equilibrium moisture content (EMC) as indicated by the changes in mass due to water sorption.

3.4 Conclusion

Incorporation of MNP decorated CNCs, the co-precipitation of MNPs onto CNC surfaces, freezing temperature, freezing mode, and an applied SMF all affected pore morphology in CNC cryogel scaffolds. High freezing temperatures resulted in large, unoriented pores, while low freezing temperatures resulted in lamellar, oriented pores. Two-step freezing combining high-temperature cryogelation and low-temperature freezing produced elongated pores with larger diameters than those made with low-temperature freezing alone. The incorporation of MNPs

affects pore morphology in several ways. An applied SMF has the potential to influence cryogelation by reducing the extent of freezing at high freezing temperatures, possibly due to the destabilization of hydrogen bonds. DAB fitting of the SAXS curves showed that CNC-MNPs have more tightly packed polymers inside their nanocrystal structure compared to their pure CNC counterpart. This compactness was found to correlate with lower BET surface area and lower EMC in the resulting cryogel scaffolds. Overall, incorporating MNPs by co-precipitation onto CNC surfaces changes the formation of pores in cryogels. The findings in our experiment will serve as a reference for future fabrication of emerging CNC and CNC-MNP based porous materials where the tuning of composition and pore morphology is needed.

3.5 Supporting materials

Definition of models for fitting the SAXS curves in SASView:

1. Surface Fractal model

$$I(q) = scale \times P(q)S(q) + background$$

$$P(q) = F(qR)^3$$

$$F(x) = \frac{3|\sin(x) - x\cos(x)|}{x^3}$$

$$S(q) = \Gamma(5 - D_s)\xi^{5-D_s}[1 + (q\xi)^2]^{-(5-D_s)/2}\sin [-(5 - D_s) \tan^{-1}(q\xi)]q^{-1}$$

$$scale = scale_factpr \times NV^1(\rho_{particle} - \rho_{solvent})^2$$

$$V = \frac{4}{3}\pi R^3$$

Where R is the radius of the building block, D_s is the surface fractal dimension, ξ is the cut-off length, $\rho_{solvent}$ and $\rho_{particle}$ are the scattering length density of the solvent and particles, respectively.

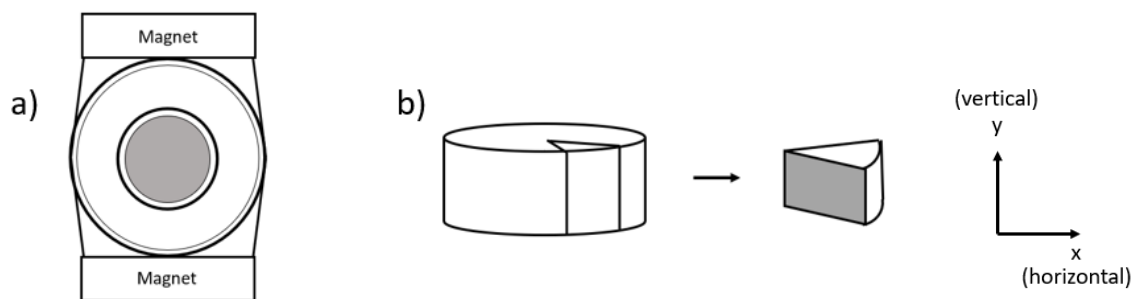
2. DAB (Debye Anderson Brumberger) Model

$$I(q) = scale \cdot \frac{L^3}{(1 + (q \cdot L)^2)^2} + background$$

Where:

$$scale = 8\pi\phi(1 - \phi)\Delta\rho^2$$

and the parameter L is the correlation length.



Scheme S3.1 (A) Top-down schematic diagram of the sample holder with two permanent magnets attached on opposite sides to generate an attractive magnetic field. The grey area is where the CNC and CNC-MNP samples were placed; (B) Schematic diagram of the resulting cryogel scaffold and the removal of one section for analysis. TEM images and subsequent graphical analysis were obtained on the cross-sectional area (grey). In this schematic diagram, the x-axis is the horizontal axis, the y-axis is the vertical axis.

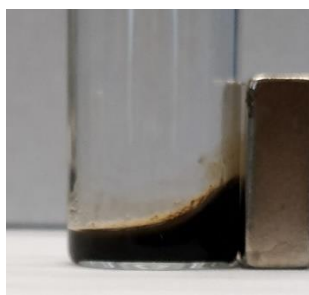
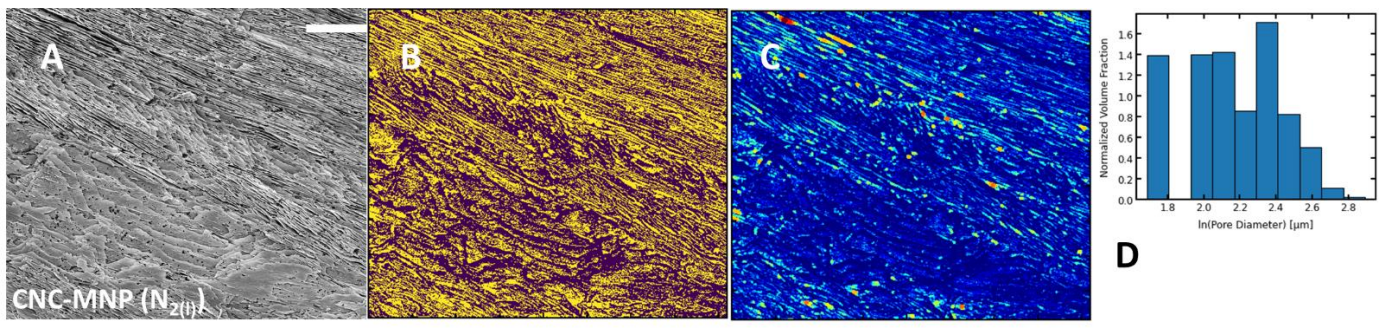
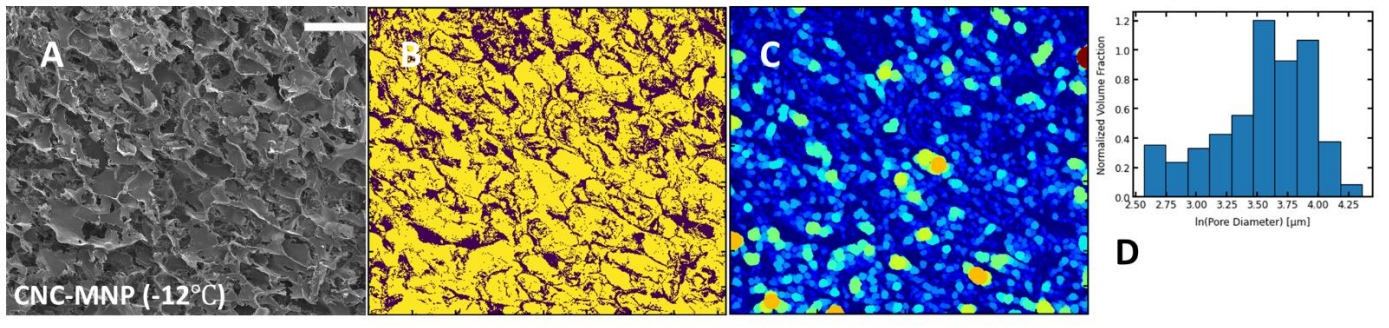
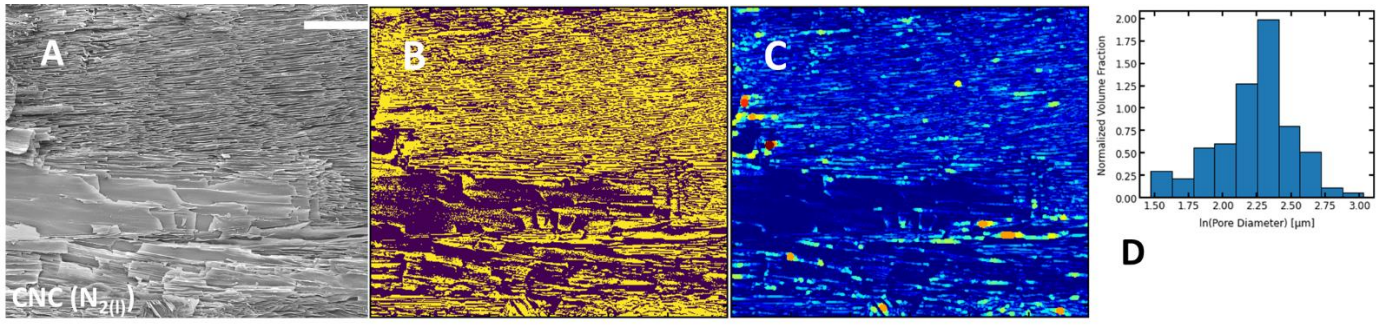
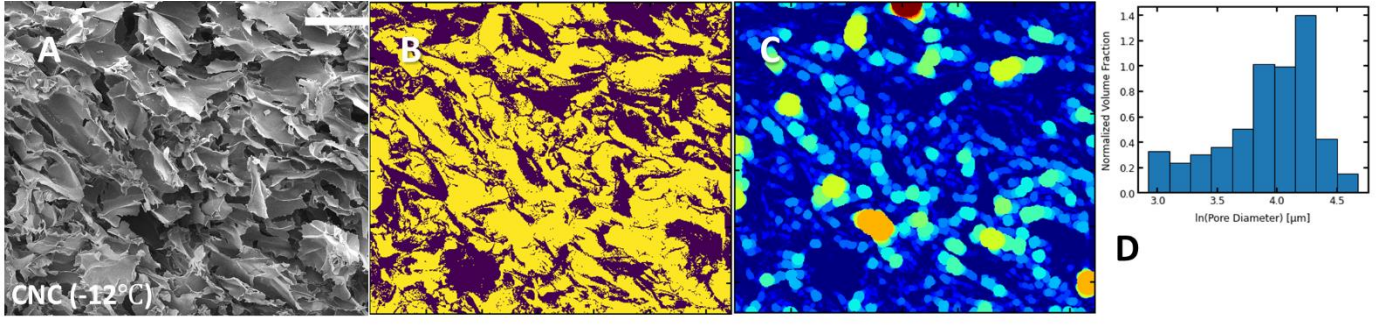


Figure S3.1 As-synthesized MNP decorated CNCs under the influence of a bar magnet.



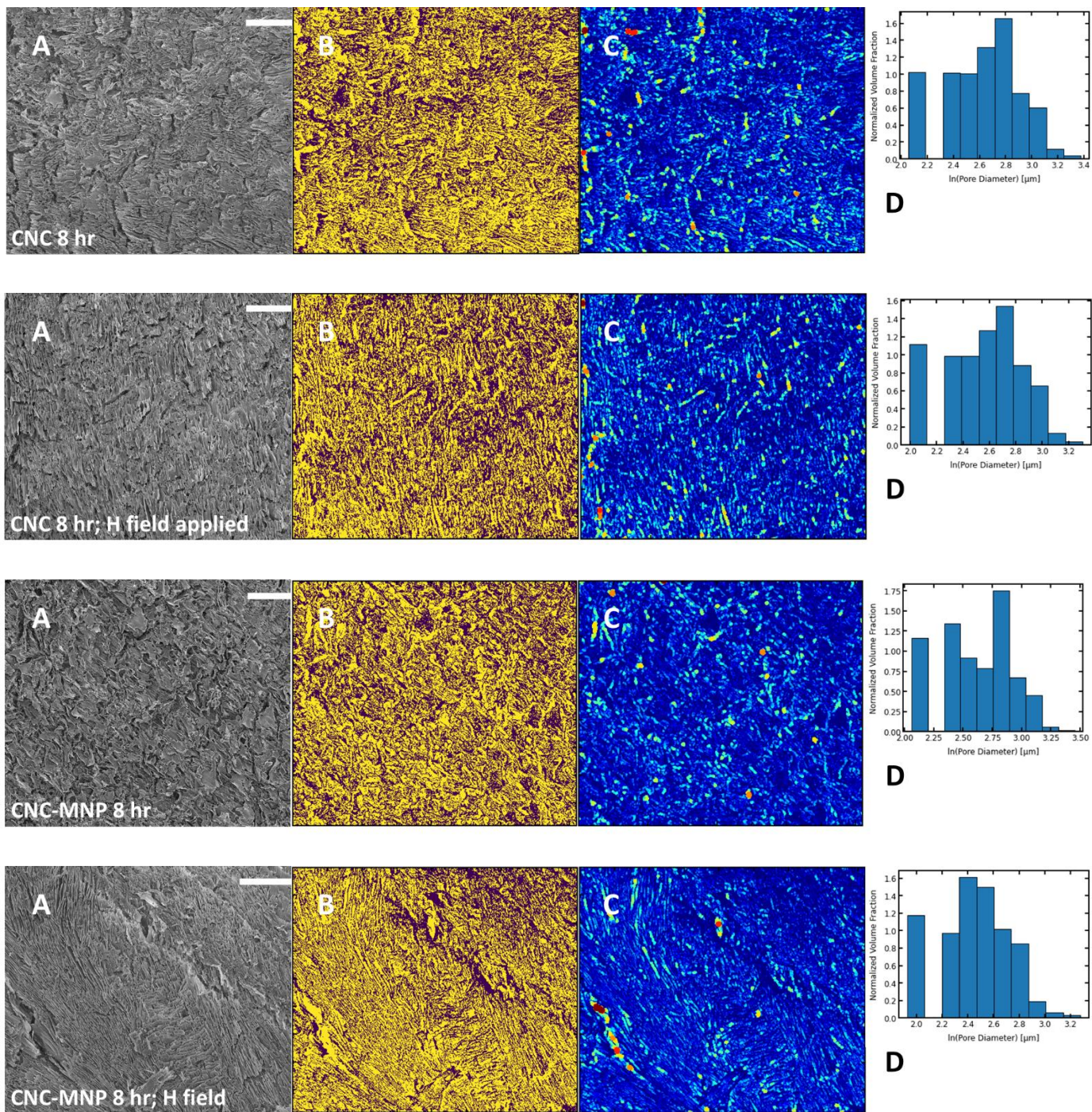
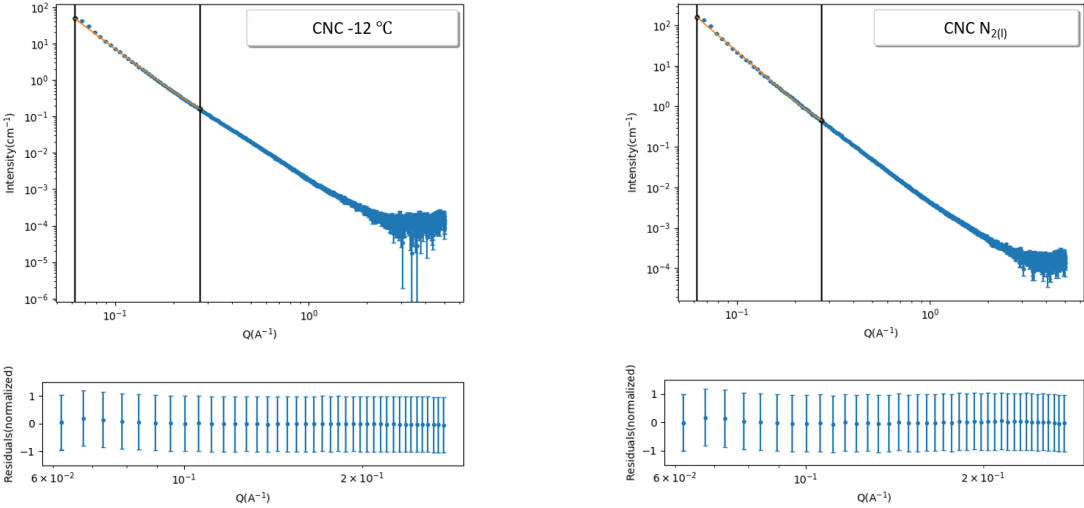
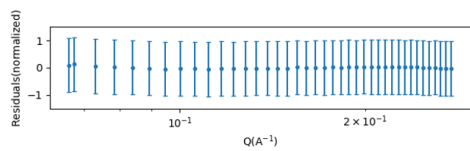
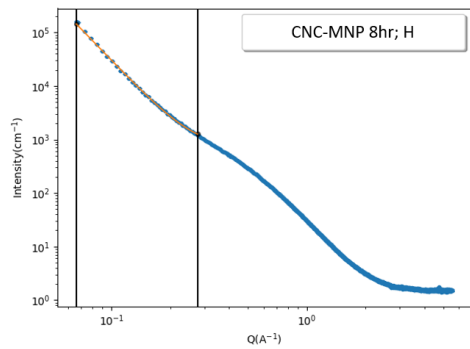
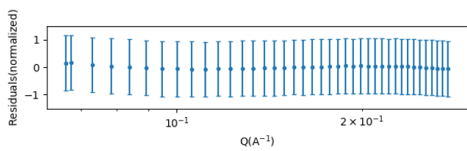
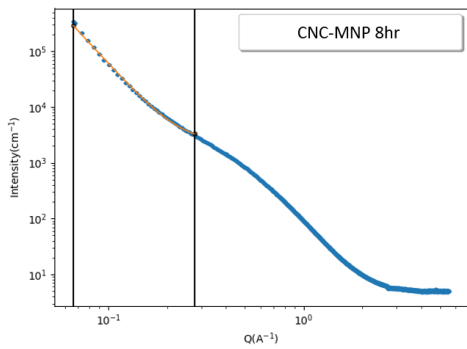
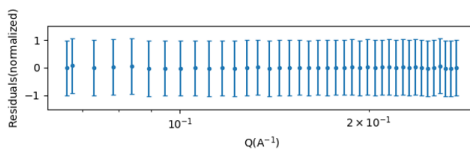
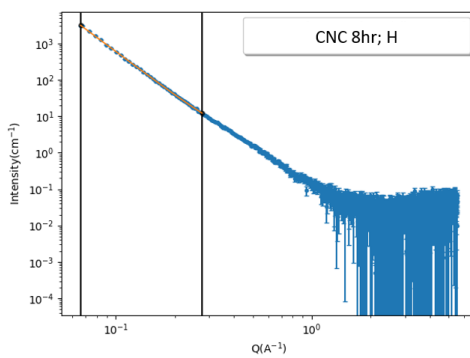
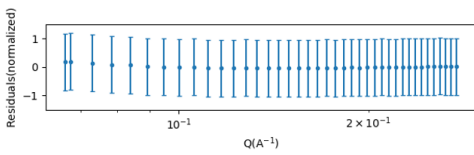
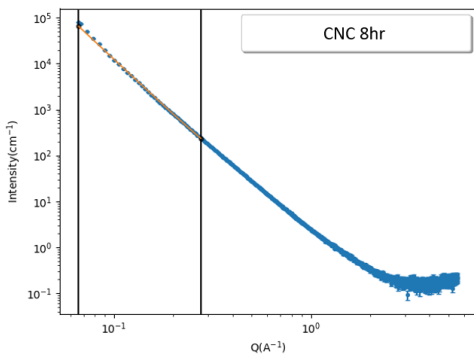
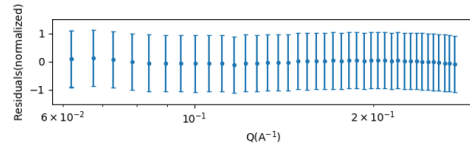
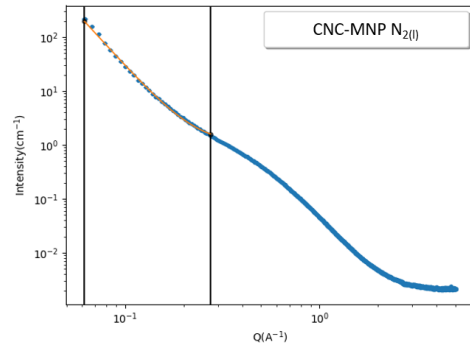
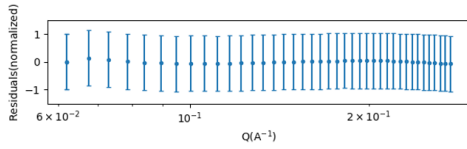
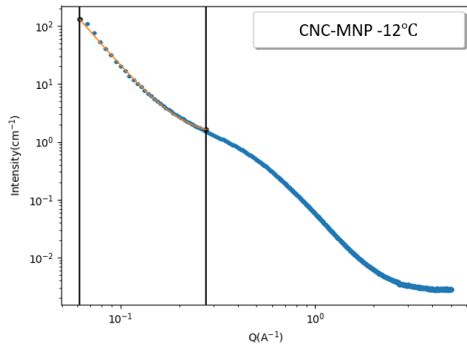


Figure S3.2 Summary of the SEM images and their subsequent processing using the "local thickness" method. Each row is devoted to one of the 8 cryogel scaffold samples, with the name of the sample indicated at the lower-left corner of each row. For each row, (A) shows the SEM image of the cryogel scaffold, (B)

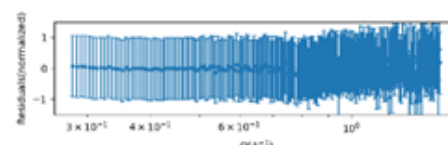
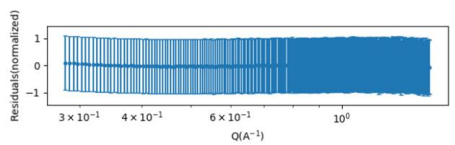
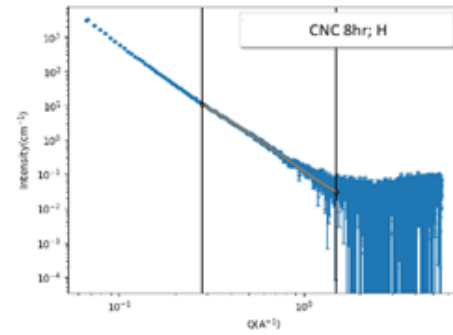
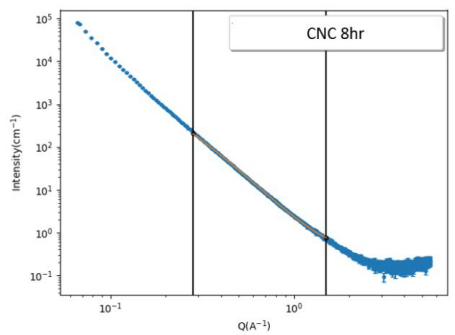
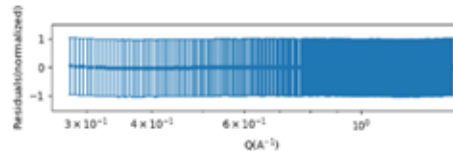
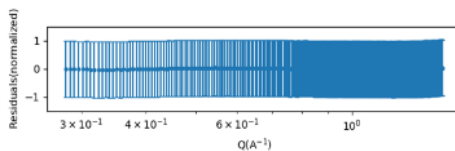
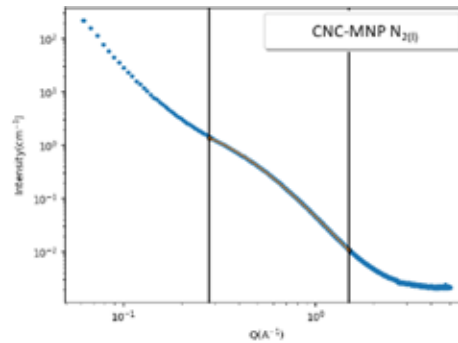
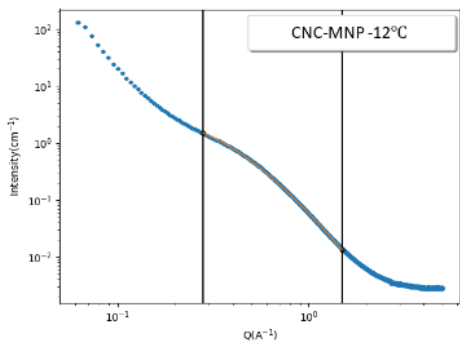
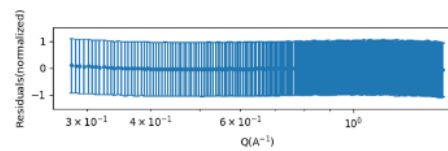
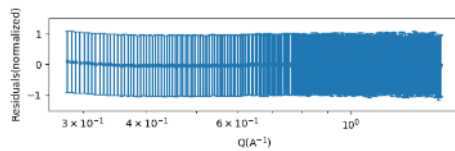
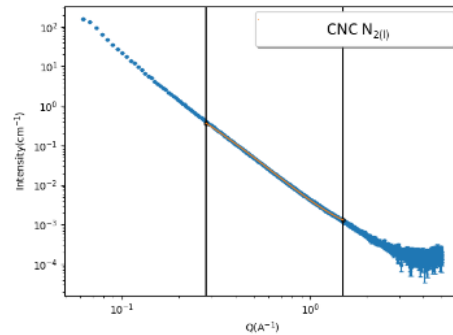
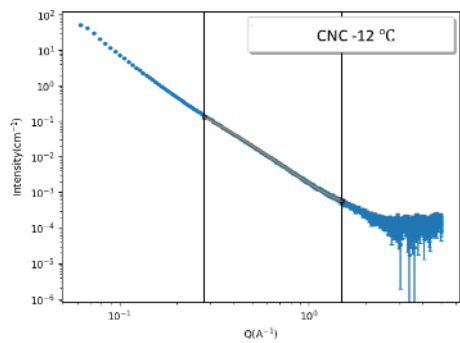
shows the inverted binary image achieved by Otsu thresholding, (C) shows the local thickness fitting, and (D) shows the histogram of the pore diameter distribution against normalized volume fraction for each. The scale bars on (A) represent $200 \mu m$. The yellow color in (B) indicates areas of emptiness, and the brown color indicates partitioning formed by the aggregation of CNC.

(A)





(B)



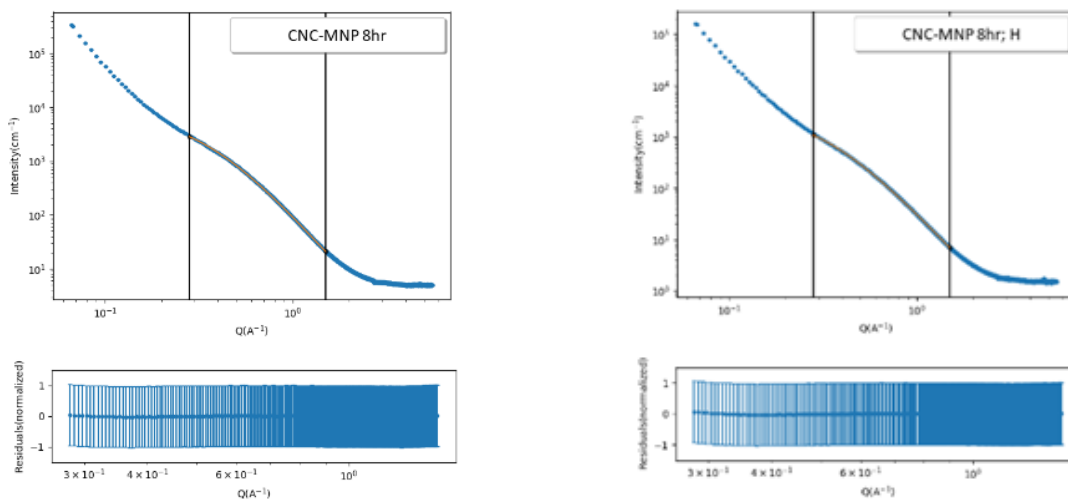


Figure S3.3 Fitting of the SAXS curves and corresponding residual graphs for each of 8 cryogel scaffolds. **(A)** The low end of the SAXS curve ($0.065 - 0.28 \text{ \AA}^{-1}$) was fitted using the surface fractal model. **(B)** The middle range of the SAXS curve ($0.28 - 1.5 \text{ \AA}^{-1}$) was fitted using the Debye-Anderson-Brumberger (DAB) model.

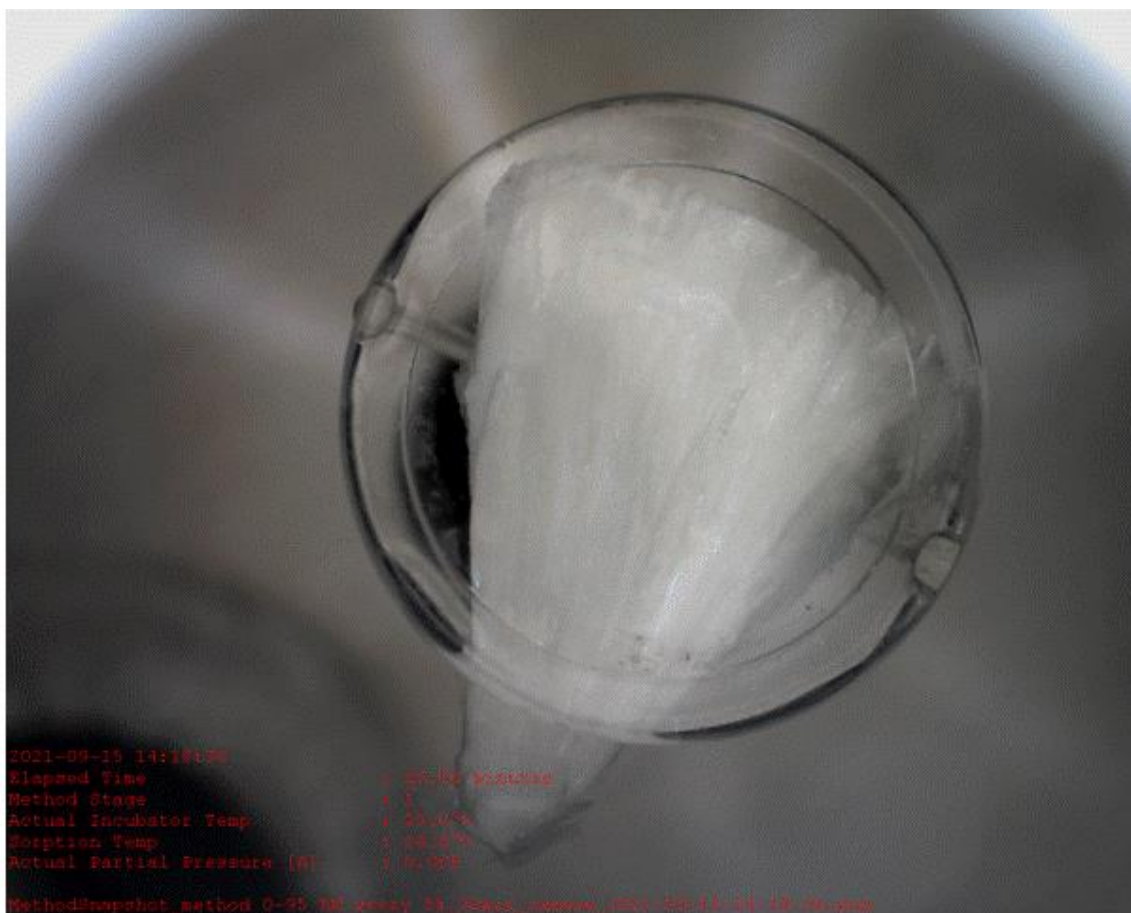


Figure S3.4 Cross-section of the CNC $N_{2(l)}$ cryogel scaffold. Structural expansion and contraction of the cryogel scaffold is observed with changing relative humidity in the environment.

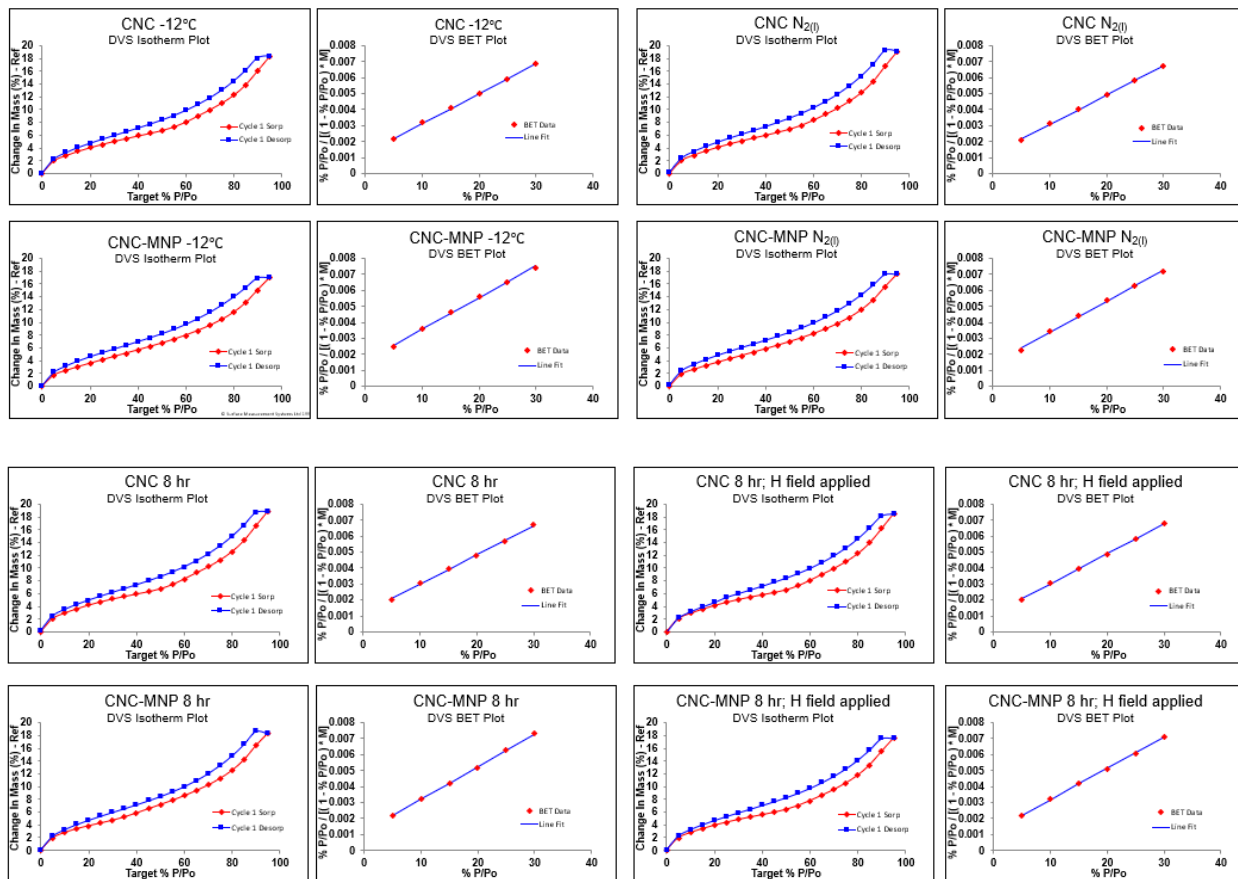


Figure S3.5 Adsorption isotherms for water vapor at 25°C for each of the cryogel scaffolds. Each adsorption cycle runs between 0 – 98% in actual % partial pressure.

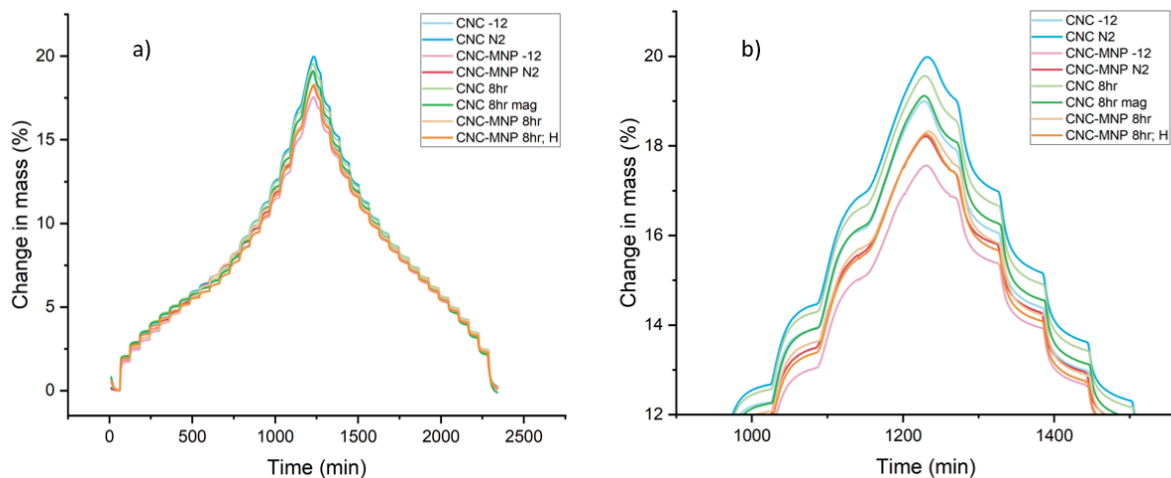


Figure S3.6 (A) Percent change in sample mass relative to reference mass versus running time in an adsorption and desorption cycle at 95% relative humidity (approximately between 0 – 98% in actual % partial pressure). **(B)** is a zoom-in view of the turning point from adsorption to desorption, where EMC of the cryogel scaffolds occurs.

3.6 References

1. Munier, P., Gordeyeva, K., Bergström, L. and Fall, A.B., 2016. Directional freezing of nanocellulose dispersions aligns the rod-like particles and produces low-density and robust particle networks. *Biomacromolecules*, 17(5), pp.1875-1881.
2. Börjesson, M. and Westman, G., 2015. Crystalline nanocellulose—preparation, modification, and properties. *Cellulose-Fundamental Aspects and Current Trends*, pp.159-191.
3. Lagerwall, J.P., Schütz, C., Salajkova, M., Noh, J., Park, J.H., Scalia, G. and Bergström, L., 2014. Cellulose nanocrystal-based materials: from liquid crystal self-assembly and glass formation to multifunctional thin films. *NPG Asia Materials*, 6(1), pp.e80.
4. Imlimthan, S., Correia, A., Figueiredo, P., Lintinen, K., Balasubramanian, V., Airaksinen, A.J., Kostianen, M.A., Santos, H.A. and Sarparanta, M., 2020. Systematic in vitro biocompatibility studies of multimodal cellulose nanocrystal and lignin nanoparticles. *Journal of Biomedical Materials Research Part A*, 108(3), pp.770-783.
5. Wang, D.C., Yu, H.Y., Qi, D., Ramasamy, M., Yao, J., Tang, F., Tam, K.M.C. and Ni, Q., 2019. Supramolecular self-assembly of 3D conductive cellulose nanofiber aerogels for flexible supercapacitors and ultrasensitive sensors. *ACS applied materials & interfaces*, 11(27), pp.24435-24446.
6. Sakai, K., Kobayashi, Y., Saito, T. and Isogai, A., 2016. Partitioned pores at microscale and nanoscale: thermal diffusivity in ultrahigh porosity solids of nanocellulose. *Scientific Reports*, 6(1), pp.1-7.

7. Song, K., Qian, X., Li, X., Zhao, Y. and Yu, Z., 2019. Fabrication of a novel functional CNC crosslinked and reinforced adsorbent from feather biomass for efficient metal removal. *Carbohydrate Polymers*, 222, p.115016.
8. Hees, T., Zhong, F., Rudolph, T., Walther, A. and Mülhaupt, R., 2017. Nanocellulose aerogels for supporting iron catalysts and in situ formation of polyethylene nanocomposites. *Advanced Functional Materials*, 27(11), p.1605586.
9. Akhlaghi, S.P., Tiong, D., Berry, R.M. and Tam, K.C., 2014. Comparative release studies of two cationic model drugs from different cellulose nanocrystal derivatives. *European Journal of Pharmaceutics and Biopharmaceutics*, 88(1), pp.207-215.
10. Ciolacu, D., Rudaz, C., Vasilescu, M. and Budtova, T., 2016. Physically and chemically crosslinked cellulose cryogels: Structure, properties and application for controlled release. *Carbohydrate Polymers*, 151, pp.392-400.
11. Or, T., Saem, S., Esteve, A., Osorio, D.A., De France, K.J., Vapaavuori, J., Hoare, T., Cerf, A., Cranston, E.D. and Moran-Mirabal, J.M., 2019. Patterned cellulose nanocrystal aerogel films with tunable dimensions and morphologies as ultra-porous scaffolds for cell culture. *ACS Applied Nano Materials*, 2(7), pp.4169-4179.
12. Camarero-Espinosa, S., Rothen-Rutishauser, B., Weder, C. and Foster, E.J., 2016. Directed cell growth in multi-zonal scaffolds for cartilage tissue engineering. *Biomaterials*, 74, pp.42-52.
13. Osorio, D.A., Lee, B.E., Kwiecien, J.M., Wang, X., Shahid, I., Hurley, A.L., Cranston, E.D. and Grandfield, K., 2019. Crosslinked cellulose nanocrystal aerogels as viable bone tissue scaffolds. *Acta Biomaterialia*, 87, pp.152-165.

14. Ferreira, F.V., Otoni, C.G., Kevin, J., Barud, H.S., Lona, L.M., Cranston, E.D. and Rojas, O.J., 2020. Porous nanocellulose gels and foams: Breakthrough status in the development of scaffolds for tissue engineering. *Materials Today*, 37, pp.126-141.
15. Sun, Y., Chu, Y., Wu, W. and Xiao, H., 2021. Nanocellulose-based lightweight porous materials: A review. *Carbohydrate Polymers*, 255, p.117489.
16. Islam, M.S., Chen, L., Sisler, J. and Tam, K.C., 2018. Cellulose nanocrystal (CNC)–inorganic hybrid systems: synthesis, properties and applications. *Journal of Materials Chemistry B*, 6(6), pp.864-883.
17. Torkashvand, N. and Sarlak, N., 2019. Fabrication of a dual T1 and T2 contrast agent for magnetic resonance imaging using cellulose nanocrystals/Fe₃O₄ nanocomposite. *European Polymer Journal*, 118, pp.128-136.
18. Anirudhan, T.S. and Shainy, F., 2015. Effective removal of mercury (II) ions from chlor-alkali industrial wastewater using 2-mercaptobenzamide modified itaconic acid-grafted-magnetite nanocellulose composite. *Journal of colloid and interface science*, 456, pp.22-31.
19. Hassan, A., Sorour, N.M., El-Baz, A. and Shetaia, Y., 2019. Simple synthesis of bacterial cellulose/magnetite nanoparticles composite for the removal of antimony from aqueous solution. *International Journal of Environmental Science and Technology*, 16(3), pp.1433-1448.
20. Tomás, A.R., Gonçalves, A.I., Paz, E., Freitas, P., Domingues, R.M. and Gomes, M.E., 2019. Magneto-mechanical actuation of magnetic responsive fibrous scaffolds boosts tenogenesis of human adipose stem cells. *Nanoscale*, 11(39), pp.18255-18271.

21. Echeverry-Rendon, M., Reece, L.M., Pastrana, F., Arias, S.L., Shetty, A.R., Pavón, J.J. and Allain, J.P., 2017. Bacterial Nanocellulose Magnetically Functionalized for Neuro-Endovascular Treatment. *Macromolecular Bioscience*, 17(6), p.1600382.
22. Jiang, F. and Hsieh, Y.L., 2014. Super water absorbing and shape memory nanocellulose aerogels from TEMPO-oxidized cellulose nanofibrils via cyclic freezing–thawing. *Journal of Materials Chemistry A*, 2(2), pp.350-359.
23. Martoia, F., Cochereau, T., Dumont, P.J., Orgéas, L., Terrien, M. and Belgacem, M.N., 2016. Cellulose nanofibril foams: Links between ice-templating conditions, microstructures and mechanical properties. *Materials & Design*, 104, pp.376-391.
24. Ciftci, D., Ubeyitogullari, A., Huerta, R.R., Ciftci, O.N., Flores, R.A. and Saldaña, M.D., 2017. Lupin hull cellulose nanofiber aerogel preparation by supercritical CO₂ and freeze drying. *The Journal of Supercritical Fluids*, 127, pp.137-145.
25. Michel, B., Bras, J., Dufresne, A., Heggset, E.B. and Syverud, K., 2020. Production and mechanical characterisation of TEMPO-oxidised cellulose nanofibrils/ β -cyclodextrin films and cryogels. *Molecules*, 25(10), p.2381.
26. Osorio, D.A., Seifried, B., Moquin, P., Grandfield, K. and Cranston, E.D., 2018. Morphology of crosslinked cellulose nanocrystal aerogels: cryo-templating versus pressurized gas expansion processing. *Journal of Materials Science*, 53(13), pp.9842-9860.
27. Yazawa, K., Ishida, K., Masunaga, H., Hikima, T. and Numata, K., 2016. Influence of water content on the β -sheet formation, thermal stability, water removal, and mechanical properties of silk materials. *Biomacromolecules*, 17(3), pp.1057-1066.

28. Bajpai, A.K. and Mishra, A., 2005. Preparation and characterization of tetracycline-loaded interpenetrating polymer networks of carboxymethyl cellulose and poly (acrylic acid): water sorption and drug release study. *Polymer International*, 54(10), pp.1347-1356.
29. López-Castejón, M.L., Bengoechea, C., García-Morales, M. and Martínez, I., 2016. Influence of tragacanth gum in egg white based bioplastics: Thermomechanical and water uptake properties. *Carbohydrate Polymers*, 152, pp.62-69.
30. Jiang, J., Zhang, Q., Zhan, X. and Chen, F., 2019. A multifunctional gelatin-based aerogel with superior pollutants adsorption, oil/water separation and photocatalytic properties. *Chemical Engineering Journal*, 358, pp.1539-1551.
31. Saini, R.K., Bagri, L.P. and Bajpai, A.K., 2019. Nano-silver hydroxyapatite based antibacterial 3D scaffolds of gelatin/alginate/poly (vinyl alcohol) for bone tissue engineering applications. *Colloids and Surfaces B: Biointerfaces*, 177, pp.211-218.
32. Volkova, N. and Berillo, D., 2021. Water uptake as a crucial factor on the properties of cryogels of gelatine crosslinked by dextran dialdehyde. *Gels*, 7(4), p.159.
33. Zografí, G., Kontny, M.J., Yang, A.Y.S. and Brenner, G.S., 1984. Surface area and water vapor sorption of macrocrystalline cellulose. *International Journal of Pharmaceutics*, 18(1-2), pp.99-116.
34. Strømme, M., Mihranyan, A., Ek, R. and Niklasson, G.A., 2003. Fractal dimension of cellulose powders analyzed by multilayer BET adsorption of water and nitrogen. *The Journal of Physical Chemistry B*, 107(51), pp.14378-14382.
35. Mihranyan, A., Llagostera, A.P., Karmhag, R., Strømme, M. and Ek, R., 2004. Moisture sorption by cellulose powders of varying crystallinity. *International Journal of Pharmaceutics*, 269(2), pp.433-442.

36. Guo, X., Wu, Y. and Xie, X., 2017. Water vapor sorption properties of cellulose nanocrystals and nanofibers using dynamic vapor sorption apparatus. *Scientific Reports*, 7(1), pp.1-12.
37. Cai, R., Yang, H., He, J. and Zhu, W., 2009. The effects of magnetic fields on water molecular hydrogen bonds. *Journal of Molecular Structure*, 938(1-3), pp.15-19.
38. Toledo, E.J., Ramalho, T.C. and Magriotis, Z.M., 2008. Influence of magnetic field on physical–chemical properties of the liquid water: Insights from experimental and theoretical models. *Journal of Molecular Structure*, 888(1-3), pp.409-415.
39. Zhang, G., Zhang, W. and Dong, H., 2010. Magnetic freezing of confined water. *The Journal of Chemical Physics*, 133(13), p.134703.
40. Wang, Y., Zhang, B., Gong, Z., Gao, K., Ou, Y. and Zhang, J., 2013. The effect of a static magnetic field on the hydrogen bonding in water using frictional experiments. *Journal of Molecular Structure*, 1052, pp.102-104.
41. Chang, K.T. and Weng, C.I., 2008. An investigation into the structure of aqueous NaCl electrolyte solutions under magnetic fields. *Computational Materials Science*, 43(4), pp.1048-1055.
42. Mok, J.H., Choi, W., Park, S.H., Lee, S.H. and Jun, S., 2015. Emerging pulsed electric field (PEF) and static magnetic field (SMF) combination technology for food freezing. *International Journal of Refrigeration*, 50, pp.137-145.
43. Zhao, H., Zhang, F., Hu, H., Liu, S. and Han, J., 2017. Experimental study on freezing of liquids under static magnetic field. *Chinese Journal of Chemical Engineering*, 25(9), pp.1288-1293.

44. Jin, S., Sun, S., Jiang, X., Zhao, Y., Wang, Y. and Deng, Y., 2020. Effect of static magnetic field on the freezing process of deionized water and 0.9% NaCl solution. *Journal of Food Processing and Preservation*, 44(9), p.e14663.
45. Tang, J., Shao, S. and Tian, C., 2019. Effects of the magnetic field on the freezing parameters of the pork. *International Journal of Refrigeration*, 107, pp.31-38.
46. Lin, H., Zhao, S., Han, X., Guan, W., Liu, B., Chen, A., Sun, Y. and Wang, J., 2022. Effect of static magnetic field extended supercooling preservation on beef quality. *Food Chemistry*, 370, p.131264.
47. Tang, J., Zhang, H., Tian, C. and Shao, S., 2020. Effects of different magnetic fields on the freezing parameters of cherry. *Journal of Food Engineering*, 278, p.109949.
48. Gostick, J.T., Khan, Z.A., Tranter, T.G., Kok, M.D., Agnaou, M., Sadeghi, M. and Jarvis, R., 2019. PoreSpy: A python toolkit for quantitative analysis of porous media images. *Journal of Open Source Software*, 4(37), p.1296.
49. Chiang, M.Y., Landis, F.A., Wang, X., Smith, J.R., Cicerone, M.T., Dunkers, J. and Luo, Y., 2009. Local thickness and anisotropy approaches to characterize pore size distribution of three-dimensional porous networks. *Tissue Engineering Part C: Methods*, 15(1), pp.65-76.
50. Youssef, A., Hrynevich, A., Fladeland, L., Balles, A., Groll, J., Dalton, P.D. and Zabler, S., 2019. The impact of melt electrowritten scaffold design on porosity determined by x-ray microtomography. *Tissue Engineering Part C: Methods*, 25(6), pp.367-379.
51. Mildner, D.F.R. and Hall, P.L., 1986. Small-angle scattering from porous solids with fractal geometry. *Journal of Physics D: Applied Physics*, 19(8), p.1535.

52. Debye, P., Anderson Jr, H.R. and Brumberger, H., 1957. Scattering by an inhomogeneous solid. II. The correlation function and its application. *Journal of Applied Physics*, 28(6), pp.679-683.
53. López, G.P., Castner, D.G. and Ratner, B.D., 1991. XPS O 1s binding energies for polymers containing hydroxyl, ether, ketone and ester groups. *Surface and Interface Analysis*, 17(5), pp.267-272.
54. Louette, P., Bodino, F. and Pireaux, J.J., 2005. Poly (ether ether ketone)(PEEK) XPS reference core level and energy loss spectra. *Surface Science Spectra*, 12(1), pp.149-153.
55. Geidobler, R. and Winter, G., 2013. Controlled ice nucleation in the field of freeze-drying: fundamentals and technology review. *European Journal of Pharmaceutics and Biopharmaceutics*, 85(2), pp.214-222.
56. Rambhatla, S., Ramot, R., Bhugra, C. and Pikal, M.J., 2004. Heat and mass transfer scale-up issues during freeze drying: II. Control and characterization of the degree of supercooling. *Aaps Pharmscitech*, 5(4), pp.54-62.
57. Qian, L., Ahmed, A., Foster, A., Rannard, S.P., Cooper, A.I. and Zhang, H., 2009. Systematic tuning of pore morphologies and pore volumes in macroporous materials by freezing. *Journal of Materials Chemistry*, 19(29), pp.5212-5219.
58. Zhang, H., Liu, C., Chen, L. and Dai, B., 2019. Control of ice crystal growth and its effect on porous structure of chitosan cryogels. *Chemical Engineering Science*, 201, pp.50-57.
59. Lewis, L., Hatzikiriakos, S.G., Hamad, W.Y. and MacLachlan, M.J., 2019. Freeze–Thaw gelation of cellulose nanocrystals. *ACS Macro Letters*, 8(5), pp.486-491.

60. Zhang, H., Hussain, I., Brust, M., Butler, M.F., Rannard, S.P. and Cooper, A.I., 2005. Aligned two- and three-dimensional structures by directional freezing of polymers and nanoparticles. *Nature Materials*, 4(10), pp.787-793.
61. Moscoso-Londoño, O., Gonzalez, J.S., Muraca, D., Hoppe, C.E., Alvarez, V.A., López-Quintela, A., Socolovsky, L.M. and Pirota, K.R., 2013. Structural and magnetic behavior of ferrogels obtained by freezing thawing of polyvinyl alcohol/poly (acrylic acid)(PAA)-coated iron oxide nanoparticles. *European Polymer Journal*, 49(2), pp.279-289.
62. Kobayashi, A., Golash, H.N. and Kirschvink, J.L., 2016. A first test of the hypothesis of biogenic magnetite-based heterogeneous ice-crystal nucleation in cryopreservation. *Cryobiology*, 72(3), pp.216-224.
63. Matsumoto, M., Saito, S. and Ohmine, I., 2002. Molecular dynamics simulation of the ice nucleation and growth process leading to water freezing. *Nature*, 416(6879), pp.409-413.
64. Cherny, A.Y., Anitas, E.M., Osipov, V.A. and Kuklin, A.I., 2019. The structure of deterministic mass and surface fractals: Theory and methods of analyzing small-angle scattering data. *Physical Chemistry Chemical Physics*, 21(24), pp.12748-12762.
65. Anitas, E.M., 2018. Small-angle scattering from mass and surface fractals. *Complexity in Biological and Physical Systems-Bifurcations, Solitons and Fractals*, pp.169-189.
66. Hossain, L., Raghuwanshi, V.S., Tanner, J., Wu, C.M., Kleinerman, O., Cohen, Y. and Garnier, G., 2020. Structure and swelling of cross-linked nanocellulose foams. *Journal of colloid and interface science*, 568, pp.234-244.
67. Kansara, A.M., Prajapati, P.K., Aswal, V.K. and Singh, P.S., 2019. Structure-property interplay of asymmetric membranes comprising of soft polydimethylsiloxane chains and hard silica nanomaterials. *Polymer*, 160, pp.30-42.

68. Thommes, M., Kaneko, K., Neimark, A.V., Olivier, J.P., Rodriguez-Reinoso, F., Rouquerol, J. and Sing, K.S., 2015. Physisorption of gases, with special reference to the evaluation of surface area and pore size distribution (IUPAC Technical Report). *Pure and Applied Chemistry*, 87(9-10), pp.1051-1069.
69. Kocherbitov, V., Ulvenlund, S., Kober, M., Jarring, K. and Arnebrant, T., 2008. Hydration of microcrystalline cellulose and milled cellulose studied by sorption calorimetry. *The Journal of Physical Chemistry B*, 112(12), pp.3728-3734.
70. Young, P.M., Edge, S., Staniforth, J.N., Steele, D.F. and Price, R., 2005. Dynamic vapor sorption properties of sodium starch glycolate disintegrants. *Pharmaceutical Development and Technology*, 10(2), pp.249-259.
71. Sheokand, S., Modi, S.R. and Bansal, A.K., 2014. Dynamic vapor sorption as a tool for characterization and quantification of amorphous content in predominantly crystalline materials. *Journal of Pharmaceutical Sciences*, 103(11), pp.3364-3376.
72. Agrawal, A.M., Manek, R.V., Kolling, W.M. and Neau, S.H., 2004. Water distribution studies within microcrystalline cellulose and chitosan using differential scanning calorimetry and dynamic vapor sorption analysis. *Journal of Pharmaceutical Sciences*, 93(7), pp.1766-1779.
73. Farrando-Pérez, J., López, C., Silvestre-Albero, J. and Gallego-Gómez, F., 2018. Direct Measurement of Microporosity and Molecular Accessibility in Stöber Spheres by Adsorption Isotherms. *The Journal of Physical Chemistry C*, 122(38), pp.22008-22017.
74. Gallego-Gómez, F., Farrando-Pérez, J., López, C. and Silvestre-Albero, J., 2020. Micropore Filling and Multilayer Formation in Stöber Spheres upon Water Adsorption. *The Journal of Physical Chemistry C*, 124(38), pp.20922-20930.

75. Schlumberger, C., Scherdel, C., Kriesten, M., Leicht, P., Keilbach, A., Ehmann, H., Kotnik, P., Reichenauer, G. and Thommes, M., 2022. Reliable surface area determination of powders and meso/macroporous materials: Small-angle X-ray scattering and gas physisorption. *Microporous and Mesoporous Materials*, 329, p.111554.
76. Raouf, A., Guilbaud, J.P., Van Damme, H., Porion, P. and Levitz, P., 1998. Analysis of the multilayer thickness relationship for water vapor and nitrogen adsorption. *Journal of Colloid and Interface Science*, 206(1), pp.1-9.

Chapter 4

Integrated Optics Techniques Combined with Surface-Enhanced Raman Spectroscopy

4.1 Introduction

Integrated optics with polarized Raman spectroscopy is the focus of the second half of this thesis. The present chapter offers a brief overview of Raman spectroscopy, integrated optics techniques such as waveguiding and prism coupling, and a description of the integrated optics spectrometer that was constructed for this research. Experimental considerations involving the assembly and operation of the integrated optics setup are discussed in detail in the following sections. This chapter should be considered a brief tutorial and an operations manual for the integrated optics polarized Raman studies discussed in Chapters 5 and 6.

The birth of integrated optics (IO) in the late 1960s created the potential for a new way to study and utilize Raman spectroscopy. The unique properties of *guided* electromagnetic fields as sources of spectroscopic excitation have the capacity to allow the study of molecular interactions at interfaces and the characterization of thin films. With the development of stable, compact and inexpensive multi-colored semiconductor lasers, polarization-specific *waveguide* Raman spectroscopy is positioned new insights into molecular vibrations at the nanoscale by interrogating the Raman polarizability tensor in polarization-specific ways.

4.2 Raman scattering

Raman scattering is a form of light-matter interaction where light is scattered inelastically by molecules or phonons.^{1,2} As shown in Figure 4.1, the wavelength of the scattered light is not equal to that of the incident light in inelastic scattering. This is unlike elastic scattering, such as Rayleigh scattering, where the wavelength of the light is unchanged prior to and post scattering. Another type of common light-matter interaction is fluorescence and phosphorescence, where the light is absorbed and subsequently emitted by matter.^{1,2}

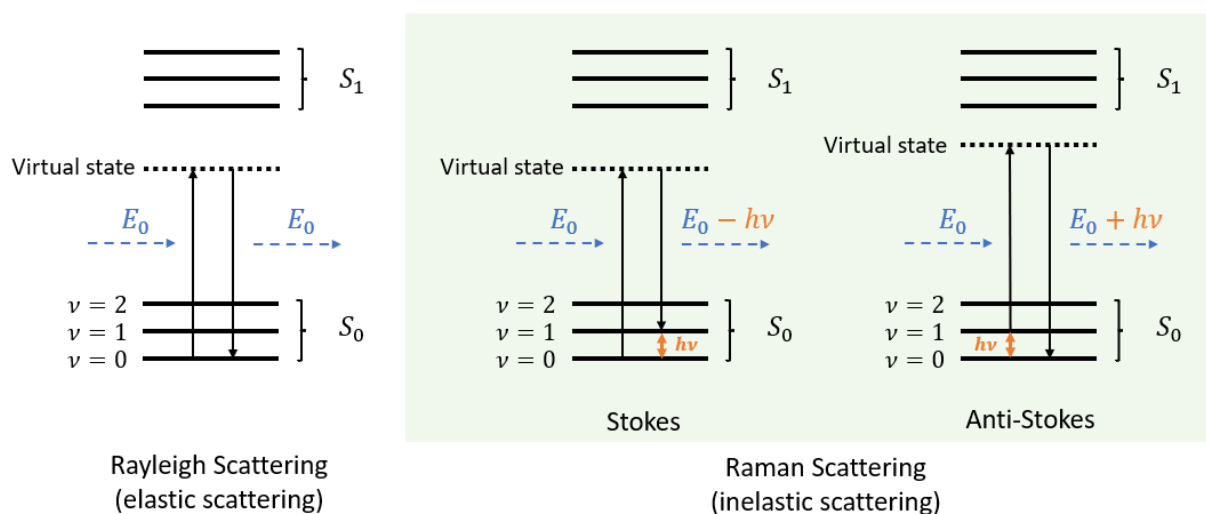


Figure 4.1 Inelastic Raman scattering versus elastic Rayleigh scattering. S_0 represents the electronic ground state. ν_0 , ν_1 and ν_2 represents the vibrational ground state (0) and level 1 and level 2 of the vibrationally excited states, respectively. Raman scattering can be categorized as Stokes Raman scattering or anti-Stokes Raman scattering, depending on whether the final vibrational state is higher (anti-Stokes) or lower (Stokes) than the initial state.

When light interacts with matter, the electromagnetic field perturbs the charge distribution. The classical approach to explaining Raman theorizes that the shift results from the modulation of the polarizability of molecules. In Raman spectroscopy, monochromatic light of optical frequency is employed to excite molecules to induce a change in the vibrational energy states. The Raman spectra, therefore, serve as molecular fingerprints that give information such as the structure, symmetry, and orientation of the probed molecules.^{1,3}

4.3 Surface-enhanced Raman spectroscopy (SERS)

The Raman effect is weak and, on the order of 10^{-8} to 10^{-12} of the incident light intensity because most of the scattering is elastic. Weak signal has hampered the use of conventional Raman spectroscopy for molecular sensing. Over the years, Surface-Enhanced Raman spectroscopy (SERS) has been elaborated as a technique to improve Raman signal intensity for routine sample analysis, sometimes to the point of single-molecule detection.^{3,4} SERS is commonly observed when Raman probe molecules are deposited on the surface of coinage metals such as silver and gold. In addition to traditional nearly-free electron metal substrates, enhanced SER activities have been reported recently for various categories of non-metal materials, including graphene, MXenes, transition-metal chalcogens/oxides, and conjugated organic molecules.⁴

The SER enhancement effects have been argued within the framework of two theories: electromagnetic enhancement and chemical enhancement. The electromagnetic mechanism is purely physical and invokes excitations of the surface plasmon modes of plasmonic metals.^{1,3} Surface plasmons are light-induced coherent oscillations of surface conduction electrons at the interface between a dielectric and a conducting material such as plasmonic metals. The excitation

of surface plasmon can be localized or propagating. The localized excitation, known as the local surface plasmon resonance (LSPR), occurs at fine structures such as surface roughening and nanoparticles much smaller than the wavelength of the incident light, and optimally on a 10 – 100 nm diameter scale.^{3,5} The LSPR wavelength depends on the size, shape, separation, material, and external dielectric properties of the fine structures.⁶ In any case, LSPR amplifies the incident electromagnetic wave by concentrating the local electric field near the surface of nanostructures, where local concentrations of charge carriers can be found. This field enhancement is associated with a strong potential gradient due to the curvature of a metallic interface and is commonly described as the "lightning rod effect".⁷

The propagating coupled electromagnetic-electron plasma excitation is known as the surface plasmon polariton (SPP).⁸ SPPs are electromagnetic waves trapped at the dielectric and metal interface due to their interactions with the nearly free electrons of the metal.⁹ For a planar dielectric-conducting interface, polaritons propagate in two-dimensional space at the interface of surfaces for length scales of tens to hundreds of micrometers.^{1,8} Both LSPR and SPPs contribute to the electromagnetic mechanism of SERS. The electromagnetic mechanism can increase Raman generation by a factor of 10^8 to 10^{11} .^{1,10}

The second theory to account for the SER enhancement invokes a charge transfer mechanism. The charge transfer mechanism is a chemical enhancement effect that shifts the Raman scattering from a non-resonant state to one in resonance with the laser light through the formation of charge-transfer complexes between the metal surface and the adsorbed molecules. The effect results in Raman scattering enhancement factors of approximately 10^2 to 10^3 .^{1,10,11} The mechanism of charge-transfer enhancement is still under study. Efforts now focus on the surprising discovery that different semiconducting materials can exhibit SERS activity. For example,

graphene and its analogs have an atomic-scale flat surface that serves as a platform for charge-transfer; some metal oxides can boost SERS activities by defect engineering; and conjugated organic compounds and their complexes have been shown to behave as highly tunable SERS substrates.⁴

In this thesis, we elaborate a multimode dielectric (glass) waveguide into a structure called an Optical Chemical Bench (OCB). The OCB is an autoscopic sensing element from which we excite the SER effect by coupling the evanescent field of the guided wave to produce a plasmonic response from surface-bound core-shell AuAg nanoparticles. The plasmonic nanoparticles are used to examine how small molecules bind to the metal surface via their polarized TE/TM SER response. Knowledge of the binding modes is then used to explore nanoparticle-nanoparticle binding mediated by ligands on the waveguide surface. We describe the OCB as a polarization mode filter where the waveguide surface is sparsely decorated with nanoparticles. The plasmonic nanoparticle regime is then used to construct a hierarchy of hybrid nanostructures that combine nanomagnetism with plasmonics. Accordingly, we examine the vibrational properties of ligand crosslinks among the AuAg and magnetite (Fe_3O_4) on the OCB. The next section introduces the concept of the OCB. We then provide background terminology to understand optical waveguiding and how waveguides can be used for Raman spectroscopy. We then describe the Integrated Optics Evanescent Wave SER spectrometer that was built for our studies.

4.4 Background to guided wave Raman spectroscopy

Since the development of Raman microscope, many techniques have been developed to harvest Raman signals. Here we first introduce the notion of a waveguide and then expand that

notion to the arena of nanoplasmonics. In general, waveguides are physical structures that confine and guide electromagnetic waves. By concentrating, say a 200 μm diameter laser beam within the small volume of 1 μm thick waveguide structure, the optical field intensity is significantly increased. Under this condition, the waveguide offers a photon bath sufficient to excite Raman scattering from molecules embedded in and even adsorbed near the surface of the waveguide. With slab waveguides, the opportunity arises to create integrated Raman lab-on-a-chip platforms.^{3, 12} Duperat's 1974 paper on Raman waveguide spectroscopy in thin polymer films can be considered groundbreaking in its adaptation of some of the simplest methods to make and characterize a passive integrated optics structure, namely the slab waveguide.¹³

In this thesis, two types of OCB are explored for guided wave Raman. The first is the evanescent wave-activated SERS waveguide with plasmonic nanostructures.^{3, 12, 14–16} This type of waveguide comprises transparent materials such as Si_3N_4 or SiO_2 . When light propagates in the waveguide, a SER response is elicited through evanescent wave excitation of plasmonic nanostructures located on the surface of the waveguide (Figure 4.2A). Compared with SERS from free-space confocal Raman microscopy, SERS integrated optics offers reduced signal-to-background noise and improved selectivity to study molecular orientations.¹² More discussion on integrated SERS waveguides with plasmonic nanostructures can be found in Chapter 5 of this thesis.

The second type of OCB is made by by sol-gel processing of hybrid organic-inorganic molecular precursors of the type $(R'O)_3\text{SiOR}$. Here, R' represents methyl or ethyl and R is an organic functional group with a Si-R covalent bond. Sol-gel is a wet-chemical process that uses acid or base-catalyzed hydrolysis and polycondensation of $(R'O)_3\text{SiOR}$ to make a colloidal suspension (sol), followed by solvent evaporation to yield a continuous liquid phase (gel).¹⁷ The

sol-gel process is a flexible way to make waveguides because it offers control over the optical properties of the slabs through variations in the number and type of R groups in the precursor $(R'O)_3SiOR$. This flexibility allows the local environment of sol-gel glasses to be adapted to accommodate different types of guest species (Figure 4.2B).¹⁸ In photonic applications, for example, the phonon density of states can be controlled in sol-gel derived glasses for Tb^{3+} , Pr^{3+} , Y^{3+} and Er^{3+} to make lasers and amplifiers.¹⁸ As a result, sol-gel-derived waveguides find applications in information and communication technology, photonic devices, and sensing. More discussion on sol-gel-derived waveguides can be found in Chapter 6 of this thesis.

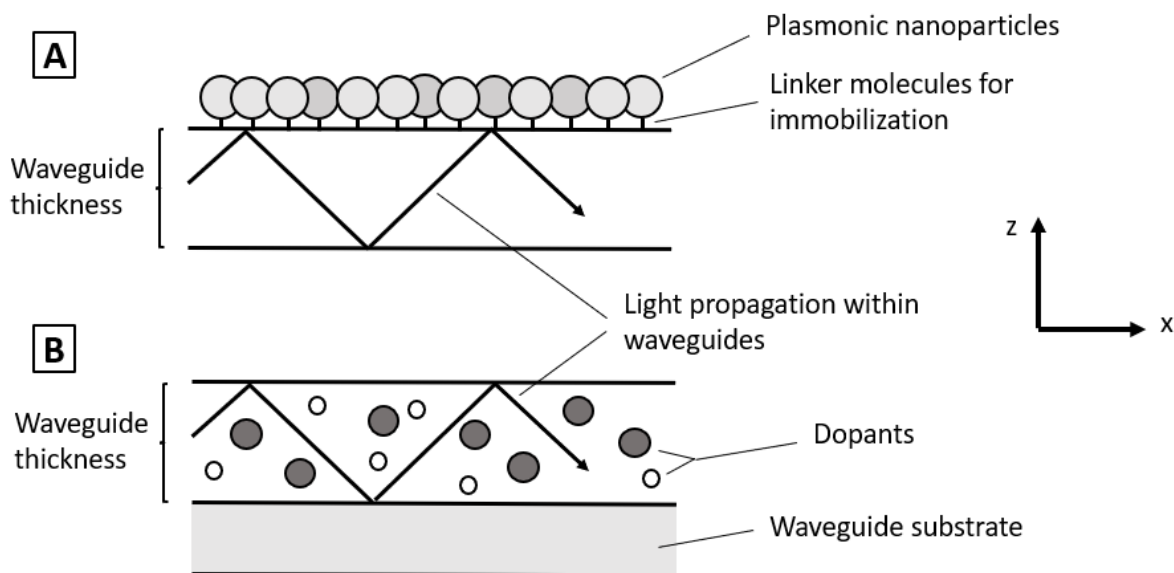


Figure 4.2 Schematics of two types of OCB for integrated optics Raman spectroscopy are explored in the thesis. Waveguide **A** consists of plasmonic nanoparticles chemically bound through the R-group ($-R-NH_2$ or $-R-SH$) of $(R'O)_3SiOR$ species to the surface of the waveguide. As light propagates in the waveguide, the evanescent field localized at the interface activates the SERS effect by exciting plasmonic response of the nanoparticles. Waveguide **B**

depicts a sol-gel-type waveguide supported on a substrate. This waveguide can accommodate different types of dopants to achieve desired optical effects. See text for details.

4.5 Waveguide Raman spectroscopy in planar slab waveguides

OCBs based on the plasmonic nanoparticle waveguide and the sol-gel derived waveguide described in this thesis are slab waveguide constructs. A slab waveguide with a planar geometry is the simplest waveguiding structure (Figure 4.3). It contains a layer of material (the core) that confines the propagating electromagnetic wave to the region of refractive index n_2 , which is larger than the surrounding medium (the cladding, n_1 , and n_3). This is a step-index structure because the core refractive index changes abruptly across the core-cladding interface. A slab waveguide can be made by depositing a layer of high refractive index film (the core) between layers of low refractive index substrate (cladding), or simply by using a low refractive index $n = 1.400 - 1.1420$ material like a silica glass surrounded by an air cladding ($n \cong 1.000$). The refractive index of the core can be real or complex, $n = n_1 + in_2$. In the latter case, the complex part of the refractive index is responsible for absorption or, equivalently, optical loss. Other sources of loss are in-plane and out-of-plane scattering by impurities that render the core layer inhomogeneous, surface roughness, core density fluctuations, and other core defects.

Waveguiding is governed by an eigenvalue equation that can be derived from the first principles of Maxwell's equations (electromagnetic wave representation) or given a physically intuitive representation through the geometric (ray) optics approximation.¹⁹ For the latter approximation, waveguiding is governed by the eigenvalue Equation 4.1, which can be derived from the geometry shown in Figure 4.3A:

$$2k_0 d \cos\theta = \varphi_1 + \varphi_2 + 2m\pi \quad (4.1)$$

In Eq 4.1 the quantities φ_1 and φ_2 are the phase shifts for total internal reflection at an angle θ at the top and bottom interface of the core. The quantity m is the mode number. The free space wavenumber is $k_0 = 2\pi/\lambda$. Polarization enters through Equation 4.1. Clearly, waveguiding is also governed by the thickness d of the core region. The number of eigenmodes supported by the waveguide increases with thickness.

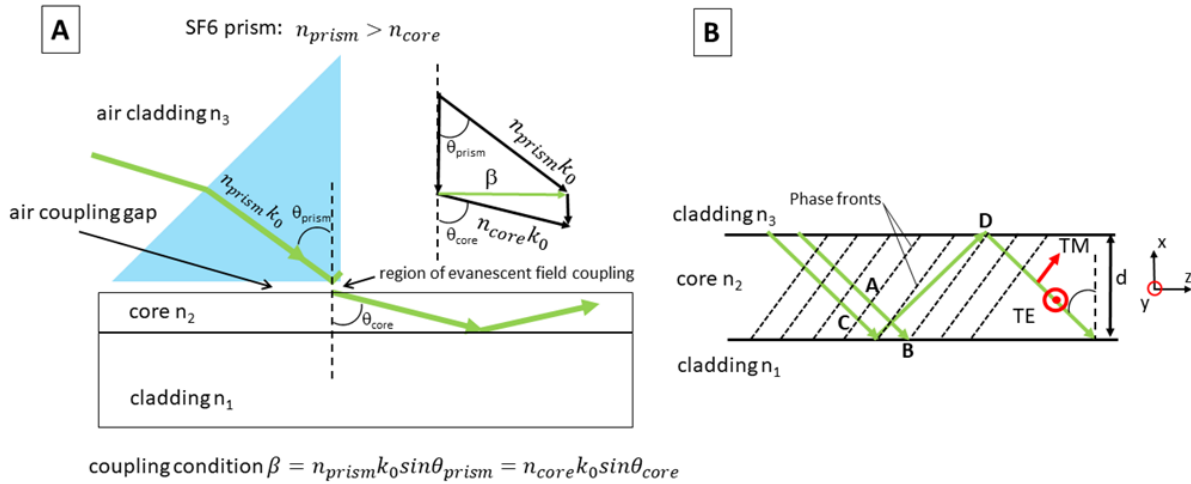


Figure 4.3. Schematics of ray optics as light is coupled by a prism into the core (n_2) of a slab waveguide (A). The evanescent field for coupling and the resulting propagating modes must travel with the same phase velocity and (TE/TM) polarization due to restrictions on resonant the eigenmodes (B).

In Figure 4.3A we show an incoming beam with a free space wave vector k_0 striking the hypotenuse of a high refractive index glass prism. The beam is refracted and propagates inside the prism with a wave vector $n_{prism}k_0$. The ray strikes the base of the prism near the bottom right

corner, where it is reflected, yielding an evanescent field that extends (tunnels) across an air gap of nanometers. The optimal air gap distance is about half the wavelength of the coupled beam.²⁰

²¹ When a light ray propagates, only certain reflection angles θ will constructively interfere in the waveguide. Light rays with reflection angles that fail to achieve total internal reflection lose a part of their energy upon each reflection at the film interfaces until the rays vanish. Only rays with allowed θ_m angles can survive propagation in the waveguide; therefore, only specific propagation modes (m) can exist. The refractive index n_{prism} and prism angle θ_{prism} determine the range of coupling angles and hence the propagation constant $\beta = n_{prism}k_0\sin\theta_{prism}$ (mode number) that is allowed for a given coupling angle. When the coupling angle corresponds to a mode of the waveguide, a standing wave is excited. This occurs when $\beta = n_{prism}k_0\sin\theta_{prism} = \beta = n_{core}k_0\sin\theta_{core}$. Each waveguide mode has a specific transverse field distribution pattern, revealing the oscillation pattern of the propagating light ray perpendicular to the direction of propagation. In the absence of perturbations, the amplitude and polarization profiles of a waveguide mode remain constant while propagating in the waveguide. Two types of waveguide modes can propagate in a waveguide: TE modes (transverse electric or s polarized modes; with electric vector E fixed and oriented perpendicular to the direction of propagation), and TM modes (transverse magnetic or p polarized modes; with the magnetic vector H fixed and oriented perpendicular both to the direction of propagation and the TE modes). For more information on the theory of dielectric planar waveguides, we refer the reader to the chapter by Marcuse.¹⁹

Restrictions on resonant eigenmodes mean that the evanescent field must travel with the same phase velocity and have the same TE/TM polarization as the mode that is excited in the film. This is depicted in Figure 4.3B. The dashed parallel lines depict the phase fronts of the propagating waves. Note the two points A and B in the diagram. The phase fronts are shown to move between

A and B, but they belong to the same plane wave. In the approximation, the ray AB is assumed to experience no reflection. There is a longer ray CD that belongs to the reflected wave. It has experienced two internal reflections while traveling through the phase front at A to the phase front at B. But all points on the same phase front of the plane wave must be in phase by assumption. This means that the optical path length of the ray AB can differ from that of the ray CD only by a multiple of 2π . Marcuse¹⁹ shows that the eigenvalue equation for TE polarization is:

$$\tan K = K(\gamma + \delta)/(K^2 - \gamma\delta) \quad (4.2)$$

Here,

$$K = (n_2^2 k_0^2 - \beta^2)^{\frac{1}{2}} = n_2 k_0 \sin \theta_2$$

$$\gamma = (\beta^2 - n_1^2 k^2)^{1/2} = [(n_2^2 - n_1^2)k^2 - K^2]^{1/2}$$

$$\delta = (\beta^2 - n_3^2 k^2)^{1/2} = [(n_2^2 - n_3^2)k^2 - K^2]^{1/2}$$

The eigenvalue equation for TM polarization is:

$$\tan Kd = n_2^2 K(n_3^2 \gamma + n_1^2 \delta)/(K^2 - \gamma\delta) \quad (4.3)$$

These equations can also be derived from the full electromagnetic treatment with Maxwell's equations.

The distance of the air gap between the prism base and the waveguide layer is critical. When coupling conditions are met, ripple-like "m-lines" (interference fringes) appear beneath the prism base lying parallel to the right-angle intersection of the two vertical planes.²² Their appearance indicates that the correct air gap for coupling has been achieved.

Prism coupling in the experiments described in this thesis was performed with a custom-designed SF6 prism, which has a refractive index of approximately 1.81 at 532 nm. A metal waveguide holder machined from thermally matched stainless steel alloy holds the prism and waveguide assembly in place. The prism gap is maintained by a top spring-loaded pressure bar where the "spring" comprises a column of convex Bell washers placed face to face in a clamshell-like configuration. Each clamshell was placed back to back to give the column stacking. Coupling pressure was adjusted by turning knurled knob thumbscrews whose length passed through the two Bell washer columns. The pressure was adjusted until m-lines (dark and light fringes) were observed under ambient light. This is an "artful" painstaking exercise and, when done correctly, allows the 532 nm laser ray to meet the coupling criteria and therefore excite a standing wave in the slab waveguide. Figure 4.4 depicts a waveguide and prism assembly on the waveguide holder. The waveguide holder is attached to an adjustable mount which allows linear movement in x, y, and z directions.

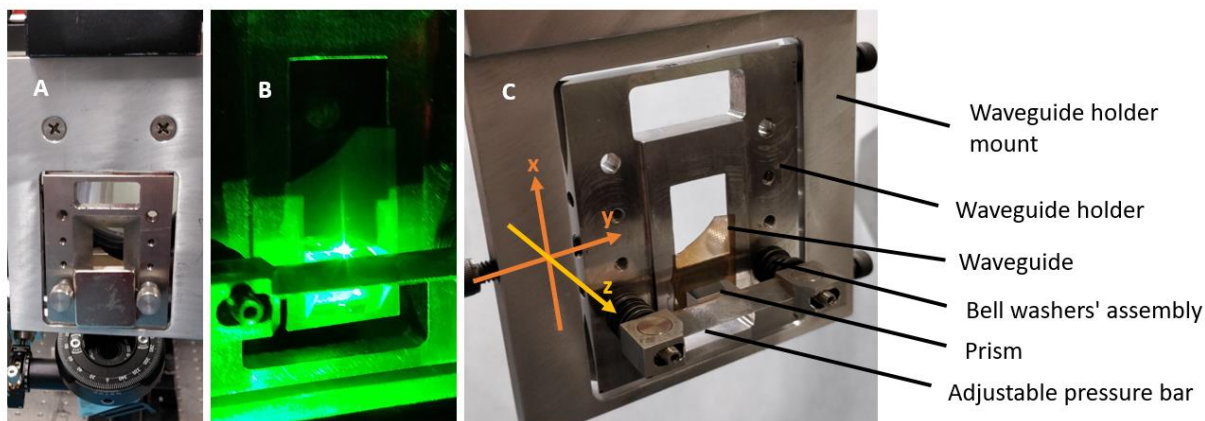


Figure 4.4 Waveguide coupling assembly. (A) reveals the backside of the assembly. The waveguide holder is positioned in a machined aluminum holder mount. The two knurled knobs to adjust the pressure on the pressure bar above the prism (not visible here) are shown. A flat square bar magnet for Chapter 6 experiments is shown attached between the knobs. A Glan-Thompson polarizer is visible as the labeled black rotatable optical component below the holder. (B) shows the front (top) view of the waveguide assembly. The prism coupler hypotenuse is visible below the bottom edge of the pressure bar. The bright white dot above the pressure bar is the coupling point of the prism. Emanating from the prism is the guided wave. TM polarization occurs in the z-direction. The TE wave is polarized in the x-y plane along the y-axis. The guided wave is attenuated and does not reach the top end of the glass slab waveguide because of optical loss associated with excitation (resonant absorption) of the surface plasmons from the AuAg core-shell nanoparticles on the waveguide surface (described further in Chapter 5). Raman intensity is collected orthogonal to the slab waveguide along the z-direction, as shown by the yellow-orange arrow of the axis system in panel (C). Panel (C) is the front view of the waveguide assembly. It faces the slit entrance to the Triax 550 spectrograph. More on this type of waveguide

and its application in integrated optics combining Polarized Raman and Evanescent Wave Surface-Enhanced Raman Scattering (IO-PEWSERS) is presented in Chapter 5.

4.6 Integrated optics spectrometer setup

The integrated optics (IO) spectrometer setup is a complete redesign of a previous version.²³ The current apparatus is shown schematically in Figure 4.5. The spectrometer combines a fast multi-channel Raman detection system with the optical waveguide prism-coupler. This spectrometer differs from similar systems described in the literature in the manner in which the laser is directed onto the coupling prism.^{24–31} In our system, the thin film waveguide remains fixed in space with respect to the Raman collection system. The entire IO setup is constructed on a Newport StabilizerTM I-2000 Series laminar flow table to suppress effects from ambient movements, air currents, and building vibrations.

The continuous wave light source is provided by a solid-state Laser Quantum Excel 532 nm compact laser. It produces a circular beam with a $1.5\text{mm} \pm 0.1\text{mm}$ diameter in transverse electromagnetic (TEM) modes. The laser beam is first directed into a precision beam-steering assembly by two reflecting mirrors. The beam-steering assembly is rotatable at the center by a goniometer. This controls the angle at which the laser beam is incident on the coupling prism hypotenuse. Upon entering the beam-steering assembly, the laser beam again encounters three $\lambda/2$ flatness reflecting mirrors. A Glan-Thompson polarizer (Thorlabs; calcite 5 mm x 5 mm) is situated on a rotational mount between mirrors 2 and 3.

The Glan-Thompson polarizer consists of two right-angled prisms cemented together at the intersection of their long faces. The interface of the two prisms creates birefringence for incident

light beams with mixed s and p polarization. The polarizer is designed such that the p-polarized (TM) incident ray experiences total internal reflection and is deflected. As a result, allowing only the s-polarized (TE) ray is transmitted. In the optical experiments conducted in this thesis, the Glan-Thompson polarizer was adjusted to optimize the intensity of the transmitted light.

After the third reflecting mirror, the now s-polarized laser beam encounters a focusing lens and a half-wave plate (Thorlabs, 532 nm). These are located in housings fixed to a rotatable mount at the exit of the beam-steerer. The focusing lens has a focal length of 62.90 mm, chosen so that its focal point lies near the axis of the rotation stage. This distance is approximately the distance to the right angle junction of the back prism edge in contact with the waveguide. This configuration ensures the maximum focus of the incident beam for coupling. The half-wave plate switches the polarization of the incident beam between TE and TM while maintaining the same coupling angle. Since the TE and TM polarizations are perpendicular to each other, the half-wave plate needs to be rotated by 45° to complete a 90° transition. The use of the rotation assembly in conjunction with a careful selection of polarizing optics provides a high degree of polarization purity in the incident laser beam and convenient switching between TE and TM polarizations while maintaining the same coupling spot. The waveguide setup acts as a beam shaper that converts the circular spot at the coupling point of the prism to a slit image (the waveguide streak) that is focused on the vertical entrance slit of the off-axis Horiba, Triax 550 spectrograph.

After coupling, the light ray travels in the waveguide along the x-direction, while Raman scattering in the z-direction is collected (Figure 4.4). The scattered Raman signal is re-focused at the entrance slit of the Raman monochromator by two planar convex collection lenses. The first lens 1 is a fast $f/2$ plano-convex achromatic. A polarization analyzer is placed between collection lenses 1 and 2 to further isolate the s- and p-polarized scattered light. Porto's notation is used to

assign the polarization states according to the laboratory Cartesian axis frame. This frame and the notation are described in Chapter 6 of this thesis.

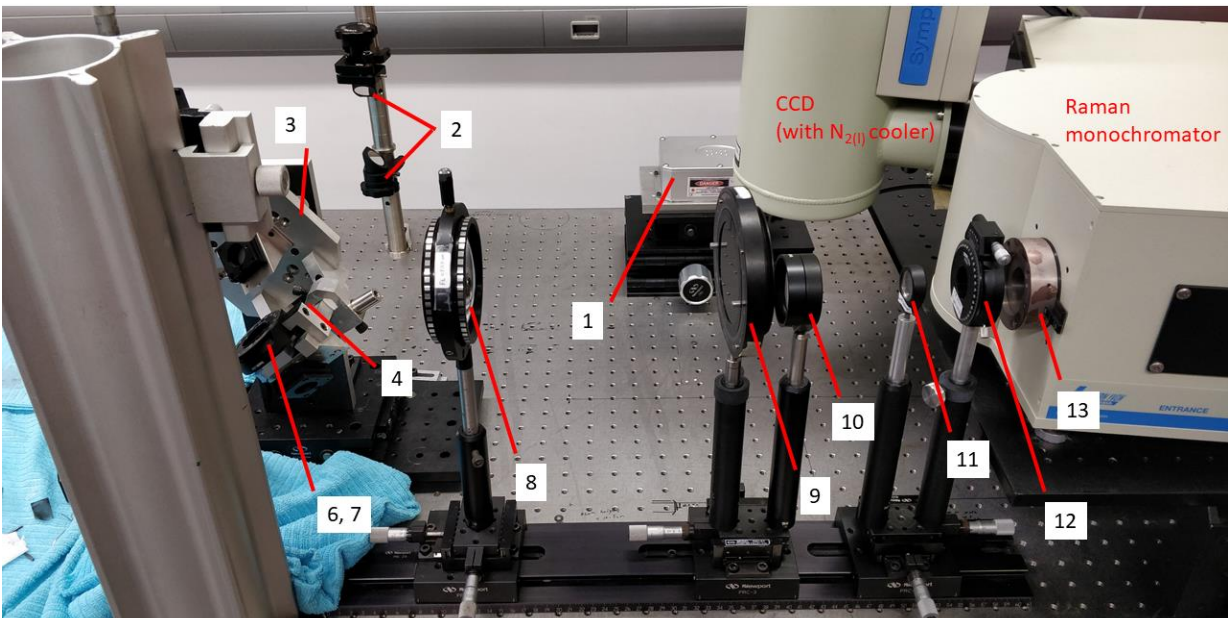
Immediately before entering the Raman monochromator through the knife-edge slit, the Raman scattering and the unfiltered 532 nm light encounter two more optical components: a quartz wedge depolarizer (Thorlabs, DPU-25) and a 532 nm holographic notch filter (Thorlabs, NF533-17). The depolarizer eliminates the polarization sensitivity of the gratings inside the Raman monochromator. The notch filter removes the unwanted 532 nm light within a small range of wavelengths while transmitting light outside of this range with little loss. The notch filter has passbands of 400 – 517 nm and 548 – 710 nm where light intensity transmission is greater than 90%. By attenuating the wavelengths between 518 – 547 nm, the notch filter effectively eliminated interference from the much stronger Rayleigh scattering and direct scattering of the 532 nm beam from defects in the waveguide. The optical bench is matched to the 550 mm focal length of the spectrograph (f number f/4.0).

The diverging Raman scatter is collected by a concave mirror in the Triax 550. The mirror directs the light onto an 1800 groove mm^{-1} holographic grating. The grating diffracts the light by creating wavelength-and-angle-dependent constructive and destructive interference. Consequently, each wavelength is reflected at a different angle onto the second concave mirror. This mirror re-focuses the light onto the liquid nitrogen-cooled coupled device detector (CCD) camera (Horiba, Symphony InGaAs Deep Cooled NIR Scientific Camera).

The Raman signals generated are directly transferred to a processing program, SynerJY V3.8 (Horiba). Typically, an acquisition time of 50 - 100 s is employed for each 500 cm^{-1} window in Raman acquisitions. Each spectrum was collected as the average of 3 acquisitions.

The Raman Imaging Mode allows one-dimensional spatial imaging up the long axis of the streak, with simultaneous collections of a complete Raman spectrum across the width of the streak at a well-defined longitudinal coordinate. In this way, one can obtain Raman spectra along the length of the waveguide streak. This is a powerful means to study the impact of polarization state mode conversion in the guided wave as it propagates away from the prism edge. A series of spectra that represent n different regions of the guided streak can be collected by binning together n groups of m adjacent CCD pixels along the vertical axis. The CCD detector was binned horizontally into groups of 2 pixels and vertically in groups of 20 pixels. Since individual pixel dimensions are 22 x 22 microns, each spectrum is collected from approximately 0.44 mm of the guided streak, assuming a 1:1 imaging by the collection optics.

Further processing of the Raman data was completed with Origin 2021b by OriginLab Corp.



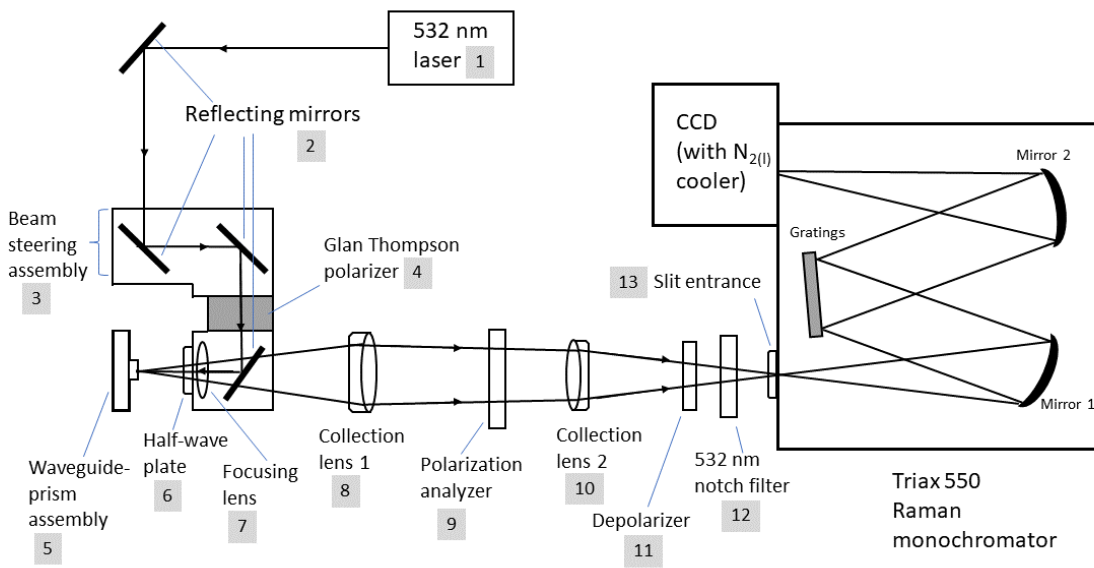
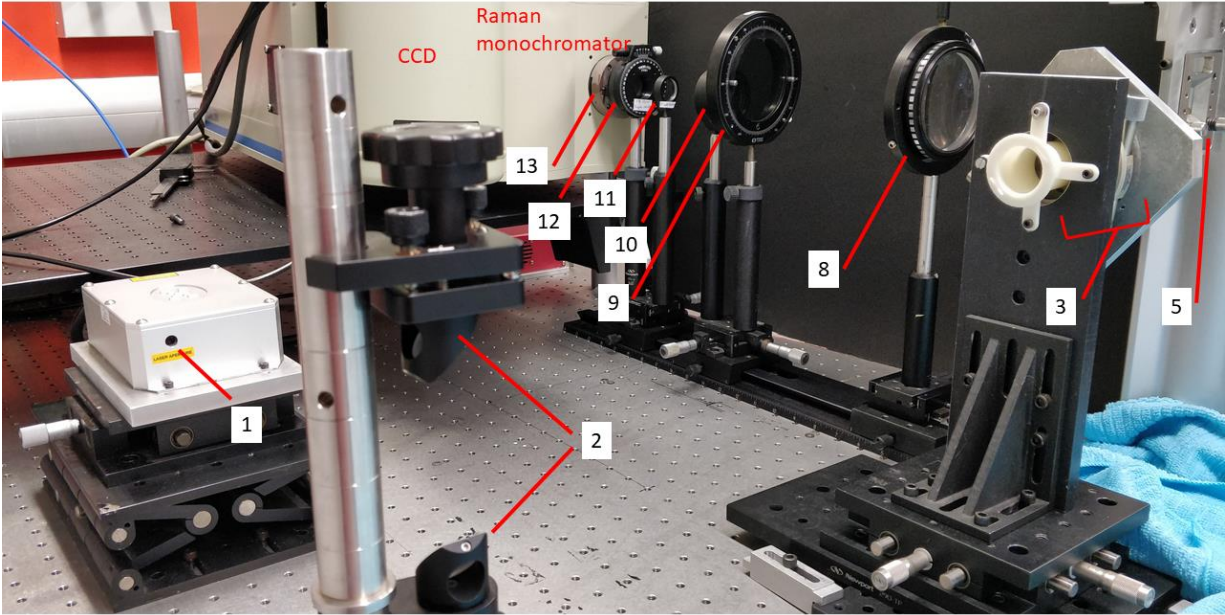


Figure 4.5 Photographs and schematic of the integrated optics spectroscopy setup. In this setup, light produced at the 532 nm laser source (1) is reflected by a mirror assembly (2) into the beam steering assembly (3). A Glan Thompson polarizer (4) is situated in the beam steering assembly to introduce TE polarization to the incident light. The light is focused by the focusing lens (7) and passes through the half-wave plate (6) for the final adjustment of TE/TM polarizations. The

light then reaches the waveguide-prism assembly (5), where it is coupled into the waveguide. Light scattered from the waveguide is collected, collimated, and re-focused by collection lenses 1 (8) and 2(10). A polarization analyzer (9) is placed between the two lenses to remove unwanted polarizations. The focused beam then passes through a depolarizer (11) and a 532 nm notch filter (12) before entering the Triax 550 Raman monochromator through the slit entrance (13).

4.7 References

1. Jones, R.R., Hooper, D.C., Zhang, L., Wolverson, D. and Valev, V.K., 2019. Raman techniques: fundamentals and frontiers. *Nanoscale Research Letters*, 14(1), pp.1-34.
2. Long, D.A. and Long, D.A., 2002. *The Raman effect: a unified treatment of the theory of Raman scattering by molecules* (Vol. 8, pp. 31-48). Chichester: Wiley.
3. Baldwin, J. A.1996. Surface enhanced Raman scattering of mercaptopyridine and pyrazinamide and the fabrication of a metal-ion sensor. PhD thesis. McGill University. Montreal.
4. Cong, S., Liu, X., Jiang, Y., Zhang, W. and Zhao, Z., 2020. Surface enhanced Raman scattering revealed by interfacial charge-transfer transitions. *The Innovation*, 1(3), p.100051.
5. Haes, A.J., Haynes, C.L., McFarland, A.D., Schatz, G.C., Van Duyne, R.P. and Zou, S., 2005. Plasmonic materials for surface-enhanced sensing and spectroscopy. *MRS Bulletin*, 30(5), pp.368-375.
6. Kelly, K.L., Coronado, E., Zhao, L.L. and Schatz, G.C., 2003. The optical properties of metal nanoparticles: the influence of size, shape, and dielectric environment. *The Journal of Physical Chemistry B*, 107(3), pp.668-677.
7. Liao, P.F. and Wokaun, A., 1982. Lightning rod effect in surface-enhanced Raman scattering. *The Journal of Chemical Physics*, 76(1), pp.751-752.
8. Van Duyne, R.P., 2004. Molecular plasmonics. *Science*, 306(5698), pp.985-986.

9. Barnes, W.L., Dereux, A. and Ebbesen, T.W., 2003. Surface plasmon subwavelength optics. *Nature*, 424(6950), pp.824-830.
10. Verma, P., 2017. Tip-enhanced Raman spectroscopy: technique and recent advances. *Chemical Reviews*, 117(9), pp.6447-6466.
11. Yamamoto, Y.S., Ozaki, Y. and Itoh, T., 2014. Recent progress and frontiers in the electromagnetic mechanism of surface-enhanced Raman scattering. *Journal of Photochemistry and Photobiology C: Photochemistry Reviews*, 21, pp.81-104.
12. Turk, N., Raza, A., Wuytens, P., Demol, H., Van Daele, M., Detavernier, C., Skirtach, A., Gevaert, K. and Baets, R., 2019. Comparison of free-space and waveguide-based SERS platforms. *Nanomaterials*, 9(10), p.1401.
13. Levy, Y., Imbert, C., Cipriani, J., Racine, S. and Dupeyrat, R., 1974. Raman scattering of thin films as a waveguide. *Optics Communications*, 11(1), pp.66-69.
14. Mak, J.S., Rutledge, S.A., Abu-Ghazalah, R.M., Eftekhari, F., Irizar, J., Tam, N.C., Zheng, G. and Helmy, A.S., 2013. Recent developments in optofluidic-assisted Raman spectroscopy. *Progress in Quantum Electronics*, 37(1), pp.1-50.
15. Gu, Y., Xu, S., Li, H., Wang, S., Cong, M., Lombardi, J.R. and Xu, W., 2013. Waveguide-enhanced surface plasmons for ultrasensitive SERS detection. *The Journal of Physical Chemistry Letters*, 4(18), pp.3153-3157.
16. Peyskens, F., Wuytens, P., Raza, A., Van Dorpe, P. and Baets, R., 2018. Waveguide excitation and collection of surface-enhanced Raman scattering from a single plasmonic antenna. *Nanophotonics*, 7(7), pp.1299-1306.

17. Asmatulu, R., 2012. Nanocoatings for corrosion protection of aerospace alloys. In *Corrosion Protection and Control Using Nanomaterials* (pp. 357-374). Woodhead Publishing.
18. Chiappini, A., Chiasera, A., Berneschi, S., Armellini, C., Carpentiero, A., Mazzola, M., Moser, E., Varas, S., Righini, G.C. and Ferrari, M., 2011. Sol-gel-derived photonic structures: fabrication, assessment, and application. *Journal of Sol-gel Science and Technology*, 60(3), pp.408-425.
19. Marcuse, D., 1991. *Theory of Dielectric Optical Waveguides* 2nd edn. San Diego, CA: Academic Press.
20. Tien, P.K., Ulrich, R. and Martin, R.J., 1969. Modes of propagating light waves in thin deposited semiconductor films. *Applied Physics Letters*, 14(9), pp.291-294.
21. Ulrich, R. and Torge, R., 1973. Measurement of thin film parameters with a prism coupler. *Applied Optics*, 12(12), pp.2901-2908.
22. Monneret, S., Huguet-Chantome, P. and Flory, F., 2000. m-Lines technique: Prism coupling measurement and discussion of accuracy for homogeneous waveguides. *Journal of Optics A: Pure and Applied Optics*, 2(3), p.188.
23. Kanigan, T. 1995. Integrated optics spectroscopy of polymer thin films. Ph.D. thesis. McGill University. Montreal.
24. Ives, J.T. and Reichert, W.M., 1988. Polymer thin film integrated optics: fabrication and characterization of polystyrene waveguides. *Journal of Applied Polymer Science*, 36(2), pp.429-443.

25. Lou, L., Mugnier, J., Bahtat, M., Brandel, V. and Genet, M., 1992, December. Polarized waveguide Raman spectroscopy of the thorium phosphate xerogel thin films. In *Sol-Gel Optics II* (Vol. 1758, pp. 83-91). International Society for Optics and Photonics.
26. Ramabadran, U.B., Jackson, H.E. and Boyd, J.T., 1993. Raman investigation of the nonlinear optical phenomenon of polarization rotation in Ti: LiNbO₃ channel waveguides. *Journal of Applied Physics*, 74(3), pp.1492-1500.
27. Ellahi, S. and Hester, R.E., 1994. Enhanced waveguide Raman spectroscopy with thin films. Plenary lecture. *Analyst*, 119(4), pp.491-495.
28. Miller, D.R., Han, O.H. and Bohn, P.W., 1987. Quantitative Raman spectroscopy of homogeneous molecular profiles in optical waveguides via direct measurement. *Applied Spectroscopy*, 41(2), pp.245-248.
29. Tait, J.K., Dixon, N.M., Everall, N., Davies, G., McIntyre, R. and Yarwood, J., 1993. Waveguide Raman spectroscopy of polymers and polymer laminates. *Journal of Raman Spectroscopy*, 24(8), pp.511-518.
30. Scherer, J.R. and Bailey, G.F., 1983. Water in polymer membranes. Part I: Water sorption and refractive index of cellulose acetate. *Journal of Membrane Science*, 13(1), pp.29-41.
31. Scherer, J.R. and Bailey, G.F., 1983. Water in polymer membranes. Part II: Raman scattering from guided laser beams. *Journal of Membrane Science*, 13(1), pp.43-52.

Chapter 5

Integrated Optics Polarized Light and Evanescent Wave Surface-Enhanced Raman Scattering (IO-PEWSERS) to detect ligand Interactions at nanoparticle surfaces

5.1 Introduction

This chapter applies the Optical Chemical Bench (OCB) spectroscopic construct and the custom-built guided wave Raman spectrometer that was introduced in Chapter 4. The applications focus on several areas. We calibrated the OCB against previous work that examined SERS from 4-mercaptopyridine. This is important because we developed a new nanoplasmonic particle into the OCB, namely core-shell AuAg. 3-Aminopropyltrimethoxysilane (APTES) replaced the mercapto analog as the molecular adhesive. The availability of very high-resolution SEM gives us a more reliable picture of the nanoparticles on the OCB surface, from which we were able to build a simple model to simulate polarized guided wave propagation in the multimode silica glass waveguide. The capacity of the 4MPy modified OCB to recognize cations in solution was examined by studying the time-dependent binding of Fe^{2+} . We used the OCB to study the ligand interface between magnetite nanoparticles decorated with 4-aminobenzoic acid (4ABA) and the nanoplasmonic AuAg particles on the OCB. These experiments make contact with the emerging research area that focuses on magnetoplasmonics. Overall, the experiments described in this chapter give insight into how the TE and TM polarization modes interact with adsorbates that are built up as hierarchical structures on the OCB.

5.1.1 Plasmon waveguide coupled with surface-enhanced Raman spectroscopy for near-field probing of molecules and molecular orientations

A persistent challenge to the study of nanomaterials is how to gather information at the nanoscale by interrogation with macroscale tools. In this regard, the optical near-field has been utilized to couple across the nano-macro interface. Among near-field methods, nanoparticle coinage metal resonators have been recruited to create enhanced field intensity through the well-known plasmonic response localized at the nanoparticle surface.¹ This, of course, is fundamental to the surface-enhanced Raman (SER) effect that underlies SER spectroscopy (SERS).^{2, 3} In addition to detection and assignment of vibrational modes, analysis of the polarization dependence of SERS is important to reveal details about the spatial orientation of molecules bound to the nanoparticles. Accordingly, arguments have been advanced that encourage the use of waveguide constructs to conduct polarized SERS, especially incorporating metal films that can be excited at their plasma frequency.⁴ Unlike roughed metal surfaces, waveguides that incorporate smooth metal films offer reproducible sampling configurations for SERS. Examples of these are the surface plasmon resonance (SPR) sensor chip and the plasmon waveguide (PW).⁴ The PW has been introduced as a configuration that has the potential to probe molecule orientation through its capacity to support both transverse electric (TE) and transverse magnetic (TM) polarizations. This contrasts with the SPR experiment that is confined to TM polarization. The PW bears some resemblance to a passive integrated optics component called a waveguide polarization mode stripper (TE-pass polarizer). This guided wave polarizer is an important device in integrated optics circuits that incorporate directional coupler switches and Y-junction intensity modulators. It offers high-differential TE (or quasi-TE) - TM (or quasi-TM) mode attenuation.⁵ In general, a metal overlayer on a dielectric waveguide behaves like a high-loss medium with a complex dielectric

function $\epsilon(\omega) = \epsilon(\omega)_1 - i\epsilon(\omega)_2$ over the frequency range ω of light. This is because the inertia of charge carriers inside a metal film dominates above the metal plasma frequency ω_p . As a result, a metal-clad waveguide has a complex propagation constant $k = \beta - j\alpha$ ($\alpha > 0$) along the propagation direction. Selective attenuation of the TM polarization is known to depend strongly on the thickness of a buffer (insulator) layer between the metal and the guiding layer.⁵ In the present study, we take advantage of the principle of a metal-clad resonance structure comprising a multimode dielectric waveguide that is sparsely decorated with a plasmonic bimetallic Au-Ag nanoparticle overlayer. Sparse coverage allows the TE and TM modes to propagate over sufficient distances that polarized SERS can be collected from the waveguide streak when imaged into a polychromator equipped with a cooled CCD detector. We refer to this integrated optics construct as an Optical Chemical Bench (OCB). Rather than selecting a uniform metal film, this plasmonic nanoparticle configuration was chosen because of our long-term interest in exploring the coupling between plasmonic nanoparticles and magnetite nanoparticles in the context of nanomagnetoplasmonics. Magnetoplasmonic nanostructures exhibit a rich phenomenology associated with their size, particle-particle interaction distance, surface functionalization, and differences between quasi-free electrons (for plasma response) and bound electrons (for magnetic response).⁶ Our current interest is in heterostructures in which the plasmonic and magnetic moieties are in close contact, with the separation governed by surface-bound ligands. In turn, the ligands can be selected to regulate the self-assembly of the magnetoplasmonic particles. To our knowledge, little is known about the nature of ligand couplings that mediate interactions between plasmonic and magnetite nanoparticles. The OCB was conceived as one method to explore such interactions through the SER effect.

Resonant coupling of polarized waveguide modes to surface plasmon excitations has been pursued in different experimental configurations. The purpose of doing so can be divided into experiments that focus on chemical sensing and those that probe nanoparticle-interfacial interactions and orientational details on plasmonic nanoparticles. Notable among the methods is the work of Smith et al.⁷ They showed that plasmon waveguide resonance spectroscopy could interrogate molecules on flat gold surfaces using both s- and p-polarization. Elsewhere, integrated optics evanescent wave SERS (IOEWSERS) has been used to explore enhanced Raman scattering from molecules attached to silver nanoparticles bound through a chemical spacer to a dielectric waveguide. In this case, the evanescent tail of a propagating TE wave elicited a SERS response that was used to examine proton-deprotonation and Cu^{2+} coordination to 4-mercaptopyridine.⁶

5.1.2 Design of the present study

In the present study, Au-Ag bimetallic nanoparticles with imperfect core-shell structure (AuAg NPs) were employed as the SERS agents. AuAg NPs were characterized according to shape morphology, composition, and optical extinction. The AuAg NPs were then bound to the surface of a multimode slab waveguide by adsorption onto 3-aminopropyltriethoxysilane that was covalently attached to the glass waveguide surface, yielding the foundation OCB sensor construct. The starting point for the OCB is shown in Figure 5.1 on the left. Hierarchies of molecular and magnetite nanoparticle assemblies were then constructed from the bimetallic particles on the OCB. These are shown in Figure 5.1 by adsorbing 4-aminobenzoic acid (bottom), 4-mercaptopyridine (middle) or 4-aminobenzoic acid-functionalized magnetite nanoparticles to the AuAg nanoparticles (top). The 4-mercaptopyridine construct can be used to bind Fe^{2+} . The nanoplasmonic AuAg cladding and its components were excited with TE or TM polarized light

that was injected into the waveguide by prism coupling. Finite-difference time-domain (FDTD) calculations were carried out to give additional insight into excitation by the TE/TM polarized waves, the influence of the polarized evanescent field on bimetallic plasmonic nanoparticles near the waveguide surface, and the impact of plasmonic particle-particle interactions on the localized field response.

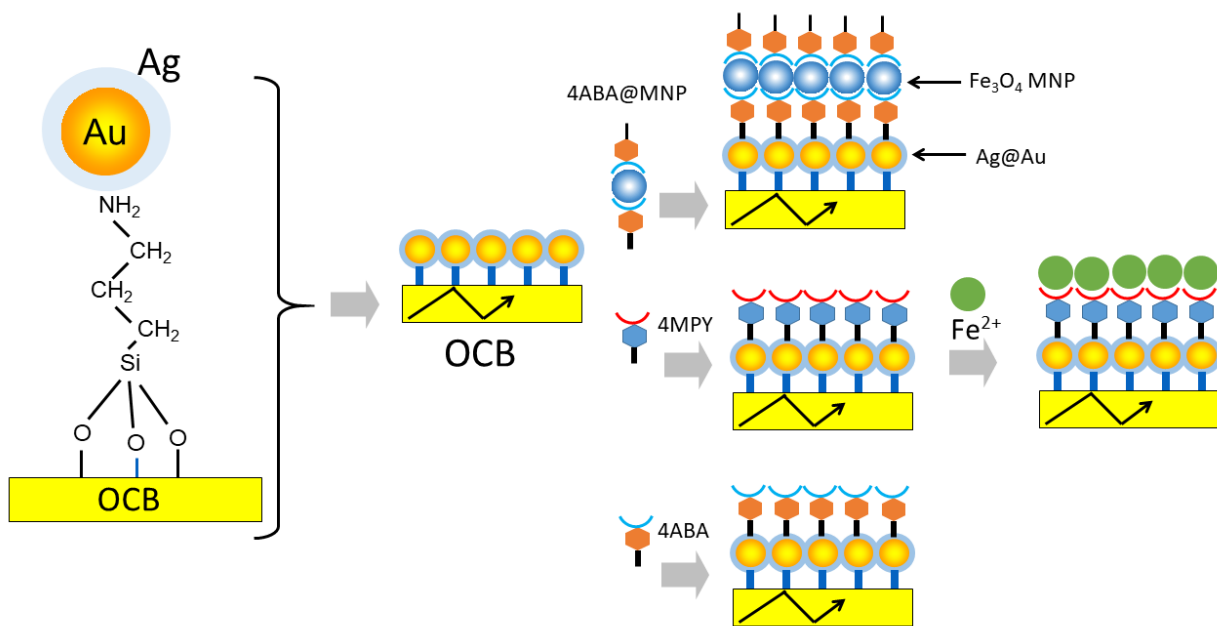


Figure 5.1 Hierarchies of assembly of species on a slab waveguide optical chemical bench (OCB). 3-aminopropyl trimethoxysilane grafted to the glass waveguide surface is used as a molecular adhesive to bind AuAg core-shell nanoparticles. This OCB is further modified by binding 4-aminobenzoic acid derivatized magnetite nanoparticles to the plasmonic AuAg nanoparticles (top center diagram). Alternatively, 4-mercaptopyridine is ligated to the AuAg nanoparticles (middle center diagram). The 4MPy ligands can recognize and bind Fe^{2+} ; or 4-aminobenzoic acid can bind to the AuAg nanoparticles (bottom center diagram).

5.2 Experimental

5.2.1 Synthesis of AuAg NPs

AuAg NPs were prepared by a seed-mediated method adapted from the procedure of Calagua et al.¹ Briefly, a gold seed solution was prepared by dissolving 0.04g of $\text{HAuCl}_4 \cdot 3\text{H}_2\text{O}$ (Sigma-Aldrich) in 100 mL of MiliQ water. The solution was constantly stirred and brought to a boil. A second solution of 0.114g of trisodium citrate dihydrate (Sigma-Aldrich) in 1 mL of MiliQ water was prepared. The citrate solution was added to the HAuCl_4 solution in one batch. The resulting solution was boiled for an additional 15 min and then cooled to room temperature in an ice bath.

To grow the gold core, 0.002g of $\text{HAuCl}_4 \cdot 3\text{H}_2\text{O}$ was dissolved in 20 mL of MiliQ water. 20 μL of 1N HCl, and then 200 μL of the previously prepared gold seed solution were added. The mixture was vigorously stirred until homogeneous before 100 μL of freshly prepared 0.1 M ascorbic acid solution (Sigma-Aldrich) was added. This was followed by the addition of 100 μL of 0.3 M sodium citrate.

To grow the silver shell, 200 μL of 0.1 M AgNO_3 solution was added to the 20 mL of the gold core suspension prepared in the previous step. A second solution was prepared by diluting 100 μL of 0.1 M ascorbic acid solution in 5 mL of MiliQ water. This ascorbic acid solution was added dropwise to the gold core solution. The reaction was allowed to proceed for 20 minutes. The resulting AuAg NPs were used immediately.

5.2.2 Hierarchies of assemblies on the waveguide optical chemical bench

5.2.2.1 Preparation of the nanoplasmonic OCB by functionalization with AuAg nanoparticles

All steps were carried out under anaerobic conditions with a Schlenk manifold. Multimode slab optical waveguides were prepared from HiQa™ glass coverslips (Sigma-Aldrich) cut to the appropriate size. The coverslips were cleaned with soapy water (Sparkleen™, Fisher Scientific) and ethanol before immersion in piranha solution for 1 hr (Caution! Piranha solution is strongly acidic and a strong oxidizer. It consists of 3 parts concentrated sulfuric acid and 1 part 30 wt. % hydrogen peroxide solution.) The cleaned waveguide was rinsed with a copious amount of deionized water until the pH of the rinse was neutral. The waveguide was then rinsed again with ethanol before being placed in a round bottom Schlenk flask equipped with a magnetic stir bar. The flask was evacuated, then backfilled with argon. Degassed anhydrous toluene (15 mL) and (3-aminopropyl)triethoxysilane (99%, Sigma-Aldrich, 0.5 mL) were injected by syringe into the flask. The reaction mixture was heated to 70 °C for 1 hr under argon. Afterward, the system was cooled to room temperature, and the liquid reaction medium was removed via syringe. Anhydrous toluene (Sigma-Aldrich) and then methanol (Sigma-Aldrich) were introduced via syringe to rinse the waveguide. The wash fluids were removed, and the system was evacuated to dryness. The functionalized waveguide was annealed under vacuum at 100 °C for 1 hr before it was immersed in a suspension of freshly synthesized AuAg NPs to provide sub-monolayer AuAg coverage.

5.2.2.2 Binding of 4MPy or 4ABA molecules onto the nanoplasmonic AuAg waveguide OCB

The binding of 4MPy molecules was achieved by submerging the as-prepared AuAg coated glass waveguide into a 4MPy solution in ethanol (6×10^{-3} M, 4MPy, Sigma-Aldrich) for 30

min with occasional agitations. Similarly, to bind 4ABA to the waveguide surface, the same procedure was followed with a 4ABA solution ethanol ($6 \times 10^{-3} \text{M}$, 4ABA, Sigma-Aldrich).

5.2.2.3 Binding of Fe^{2+} to 4MPy onto the nanoplasmonic AuAg waveguide OCB

0.5 mM of Fe^{2+} solution was prepared by dissolving 152 mg of FeSO_4 in deionized water. A 4MPy functionalized AuAg OCB was immersed in the Fe^{2+} solution and agitated lightly. Different samples were allowed to react for 0, 8, 20, 35, and 50 minutes.

5.2.2.4 Binding 4ABA functionalized magnetite nanoparticles (MNPs) onto the nanoplasmonic AuAg waveguide OCB

Magnetite nanoparticles (MNPs) were synthesized using a modified coprecipitation protocol for magnetite nanoparticles.⁹ Briefly, 1.5 g of $\text{FeCl}_2 \cdot 4\text{H}_2\text{O}$ (Sigma-Aldrich) and 4.1 g of $\text{FeCl}_3 \cdot 6\text{H}_2\text{O}$ (Sigma-Aldrich) were dissolved in 100 ml of vigorously stirred deionized water at 70 °C under a nitrogen gas flow. A 20 ml volume of 5 wt% NH_4OH was added dropwise until the solution color changed from orange to black. The product was collected by magnetic separation and washed with a copious amount of deionized water until the supernatant pH was neutral. Oxidation of the product is expected since no coating agent was added during synthesis.

MNPs were functionalized with 4ABA (Sigma-Aldrich) by incubating the MNPs in $2 \times 10^{-2} \text{M}$ of 4ABA solution in 95% ethanol. The surface-modified MNPs were extracted by a magnet and re-dispersed in fresh 95% ethanol. A nanoplasmonic AuAg waveguide OCB was then dipped into the ABA-MNPS suspension.

5.2.3 X-Ray photoelectron spectroscopy (XPS)

XPS was performed using a Thermo Scientific K-Alpha X-Ray Photoelectron Spectrometer. The X-ray source employed was an Al-K α X-ray of 1486.6 eV. The X-ray beam was directed at an incident angle of 60° from normal (30° from the horizontal plane of the sample) with a focal spot size of 400 μm . A flood gun was used alongside the X-ray gun to reduce peak shifting.

Samples were mounted onto conductive copper tape. The XPS vacuum chamber was maintained at $<2 \times 10^{-7}$ mbar throughout the experiments. N(1s), and O(1s) spectra were collected for magnetite nanoparticles as-synthesized or after incubation in 2×10^{-2} M of 4ABA solution in 95% ethanol.

5.2.4 Integrated Optics (IO) SERS Spectrometer

A custom-built IO-SERS instrument was used to acquire polarization-dependent enhanced Raman scattering from the nanoplasmonic OCBs. A diagram of the setup together with the scattering geometry is shown in Figure 5.2. A Laser Quantum Excel model 08542 diode laser provided 532 nm CW light. The 1.5 mm circular cross-section beam was directed by mirrors to the entrance port of a rotation stage that supported a precision beam-steering apparatus. The apparatus incorporated three 45° $\lambda/2$ flatness mirrors, a Glan-Thomson polarizer, a halfwave plate, and a plano-convex focusing lens. These components rotate simultaneously about the axis of the entrance hole for the incident beam that enters the beam-steering unit parallel to the plane of the optical table. The slab waveguide OCB was mounted on a stainless steel holder comprising thermally matched components, including an adjustable pressure bar that maintained a fixed

coupling gap between the prism and the OCB. The OCB holder was mounted on an xyz- θ stage bolted to the optical table through a dynamically damped optical post. A guided wave was launched by varying the rotation angle of the laser beam incident on the prism hypotenuse face with the beam point of focus at the prism bottom edge located on the rotation axis of the beam steering arm. Care was taken to ensure that the waveguide streak was oriented collinear with the slit of the spectrograph. In this manner, a selected wave polarization could be excited in the slab waveguide OCB. SERS was excited from the evanescent region of the standing guided wave. The laser power at the coupling prism was approximately 20 mW, except for the 4ABA@MNP@AuAg IO sample, which required \sim 50 mW to generate a sufficient Raman signal. The scattered light was collected by imaging the slit image of the glowing guided wave with a fast lens and diffraction-limited optics before focusing through a polarization analyzer, scrambler, and a super notch holographic Bragg filter onto the entrance slit of the spectrograph. The Horiba Triax 550 Raman spectrograph is equipped with a liquid nitrogen-cooled coupled device detector (CCD) camera. Raman signal was dispersed over the CCD chip by a holographic grating (1800 grooves mm^{-1}). A 100 s acquisition time was typically employed for each 500 cm^{-1} scan window. Spectra were plotted from the average of 3 acquisitions.

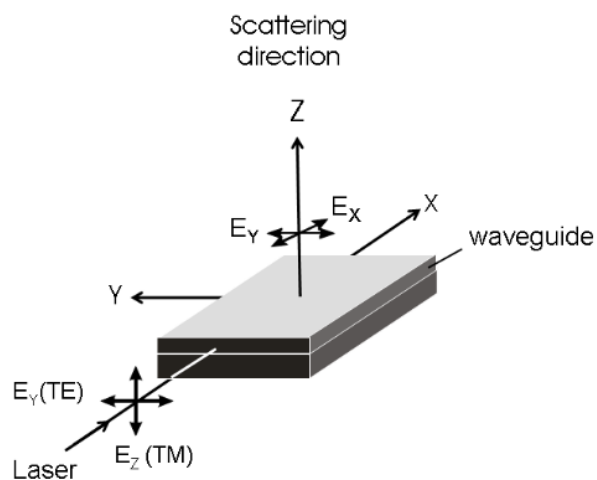
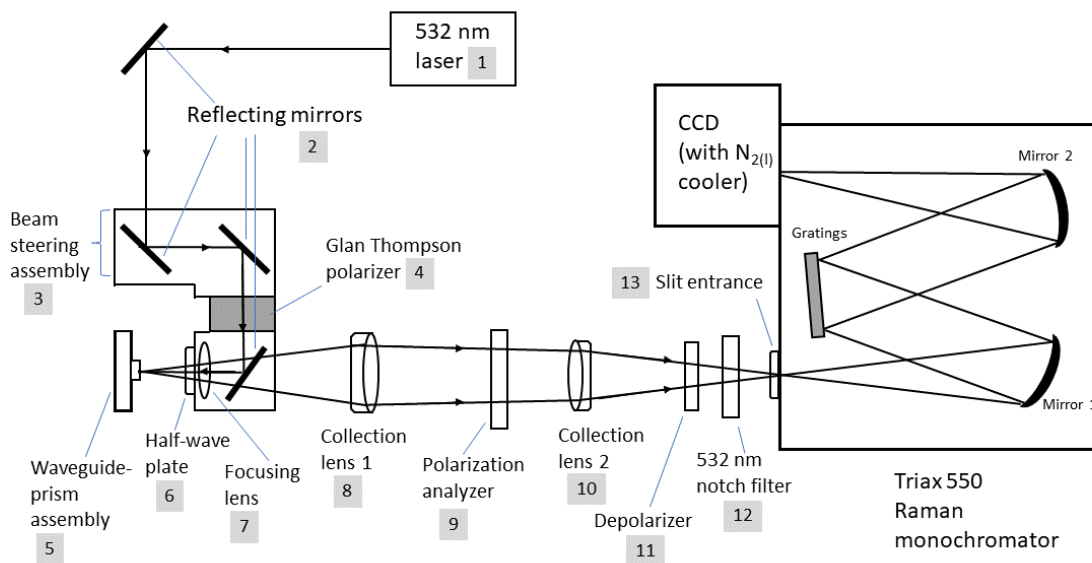


Figure 5.2 Schematic of the custom-built IO-SERS setup (top) and the scattering geometry as a laser beam is being guided into the nanoplasmonic OCB (bottom).

5.2.5 Scanning Electron Microscopy (SEM)

High-resolution SEM imaging and corresponding Energy-dispersive X-ray spectroscopy (EDX) were performed using a Helios NanoLab™ 660 instrument that combines field emission SEM (FESEM) and focused ion beam (FIB) capability. The Everhart-Thornley Detector (ETD) and a high voltage of 10.0 kV were selected.

5.2.6 Transmission Electron Microscopy (TEM)

Light-field and dark field TEM, as well as corresponding EDX were performed using FEI Titan Krios 300 kV Cryo-STEM.

5.2.7 Simulation of plasmonic electric field

The resonant optical response of AuAg nanoparticles was investigated using three-dimensional finite difference time domain (3D FDTD) simulations (Lumerical Solutions, Vancouver, BC, Canada). A miniature SiO₂ waveguide (1 μm in the x-direction and 0.35 μm in y- and z-directions) was created as a model for the real-life waveguide. The boundary conditions were PML (Perfectly Matched Layer) at y- and z-directions, which absorbs incident light with minimal reflections to respect the waveguide boundary, and periodic in the x-direction to show continuity. AuAg core-shell nanoparticles having a silver shell radius of 25 nm and a gold core radius of 10 nm were created as an idealized representation of the AuAg bimetallic nanoparticles. These core-shell nanoparticles were placed sparsely on the waveguide based on the pattern of nanoparticles observed by SEM in a randomly selected section of the real-life waveguide (Figure

5.3A, B). A pulse of light at 532 ± 10 nm was set to propagate through the center of the waveguide in either TE or TM polarization. The electric field distribution of a selected area on the waveguide model was simulated using 1 nm mesh size (Figure 5.3B). The yellow box in the xy plane indicates where the electric field intensity profiles were calculated and plotted (see text).

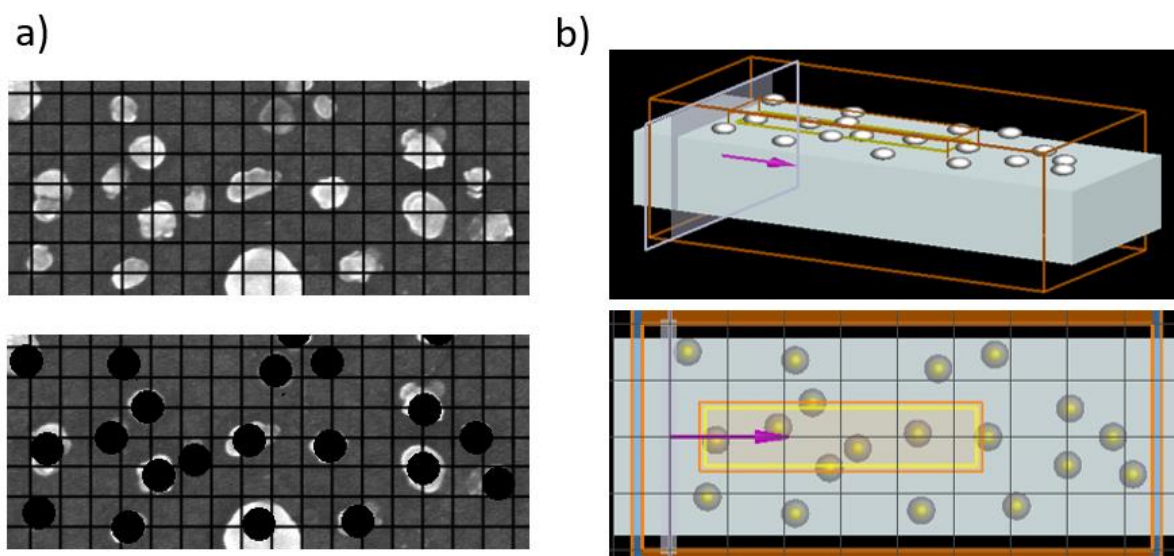


Figure 5.3 (A) An SEM image showing the sparsely distributed AuAg NPs on a section of the OCB (top) and the positioning of the particles using black discs (bottom). The side length of each square grid is 50 nm. (B) The 3D representation of the OCB structure with sparsely distributed AuAg core-shell nanoparticles mimicking that of the actual OCB calibrated from the SEM experiment.

5.3 Results and Discussion

5.3.1 OCB overlaid with AuAg nanoparticles- overlayer

TEM imaging (Figure 5.4A) reveals that the plasmonic NPs are faceted objects with an average size of 49.2 ± 14.4 nm. The light and dark color bands on the nanoparticles may correspond to stacking faults.¹⁰ Due to the similarity in contrast of silver and gold, these two components are difficult to distinguish with bright-field SEM imaging. The dark-field SEM, coupled with energy dispersive analysis by X-ray (EDX), is reported in Figure 5.4B. The SEM images showed evidence of core-shell particle structures, although particles made of homometallic silver or an ambiguous mix of silver and gold are also observed. The nanoparticles containing a mix of silver and gold may be attributed to AuAg alloy, as AuAg alloys are known to have more negative formation energy than their core-shell counterparts, indicating that the alloy phase is more stable.¹¹

Figure 5.4C shows the extinction spectrum of the nanoparticles in water. Lim et al. found core-shell NPs to have two distinct plasmon absorption bands whose relative intensities depend on the thickness of the shell.¹² A peak dominates the spectrum for AuAg NPs in aqueous suspension (Figure 5.4C) at 424 nm, consistent with a thicker Ag shell. The gold core contributes a weak shoulder to the spectral response, visible near 520 nm. Compared to homometallic gold or silver, core-shell nanoparticles exhibit a broader range of extinction. The extinction intensity in the high-energy end is on the blue side of the well-known 550 nm extinction band for Au NPs. The extinction intensity in the low-energy end extends well to the red that would not normally be observed for isolated Ag NPs. Overall, the spectrum is not that of a mixture of separate Ag and Au NPs, nor is it the result of significant contributions from alloy formation.^{13, 14}

Figure 5.5 shows an SEM image of the OCB waveguide featuring bimetallic AuAg NPs anchored by aminopropyl groups grafted to the glass substrate. Individual nanoparticles are dotted over the surface, which shows some evidence of aggregation among the particles. Overall, the waveguide surface is sparsely covered with AuAg NPs. Immobilization of the AuAg NPs on glass substrate led to further broadening of the plasmon absorption band (Figure 5.4C). These effects are likely due to the clustering of NPs on the substrate, mutual polarization among closely associated NPs, and multiple scattering from large aggregates.^{15, 16}

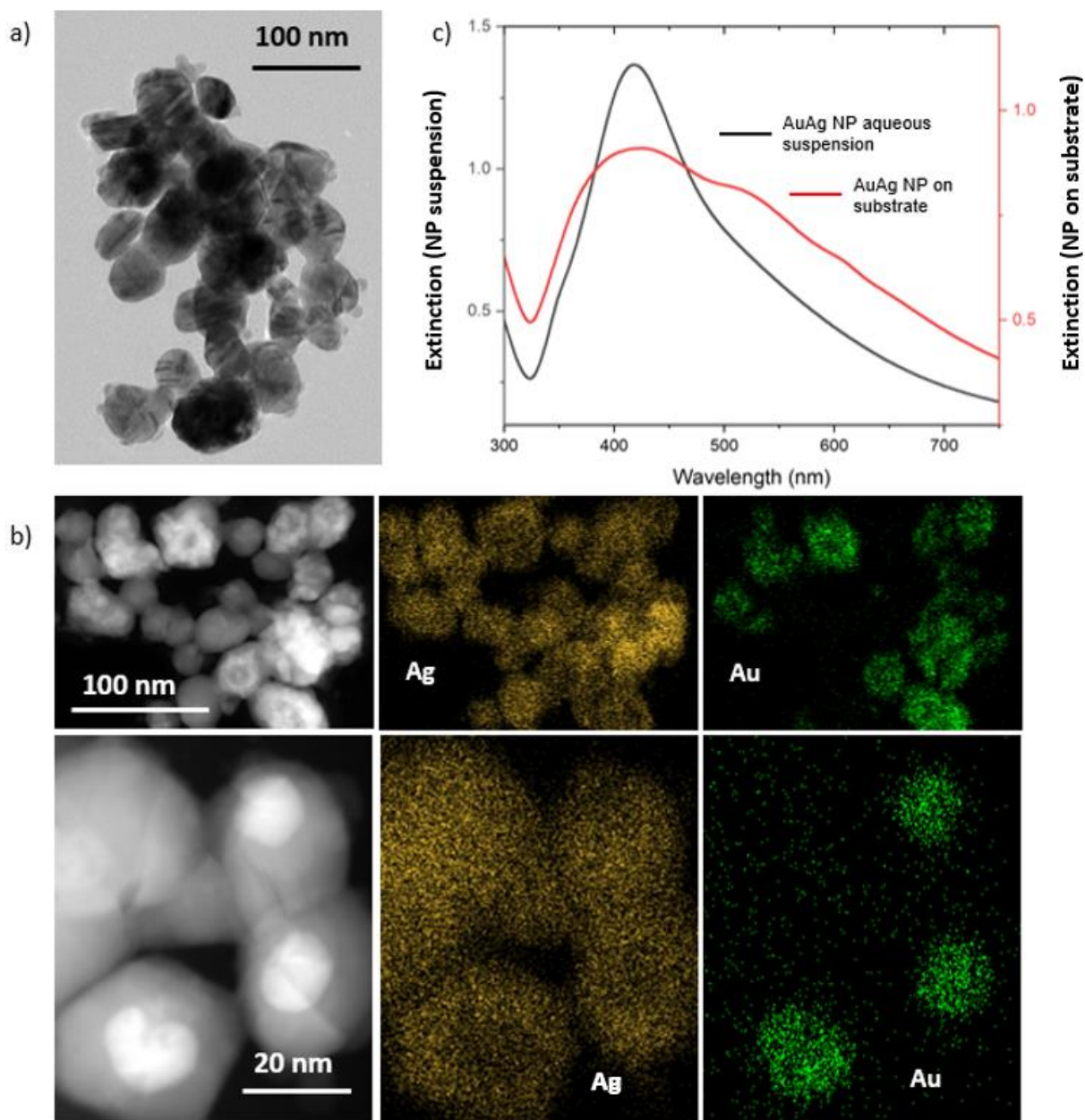


Figure 5.4 (A) Bright-field TEM image of the AuAg NPs; (B) Dark-field TEM images and EDX elemental analysis of Au and Ag components of the AuAg NPs; (C) UV-Vis extinction spectra of AuAg NPs suspended in water and after immobilization on a glass substrate.

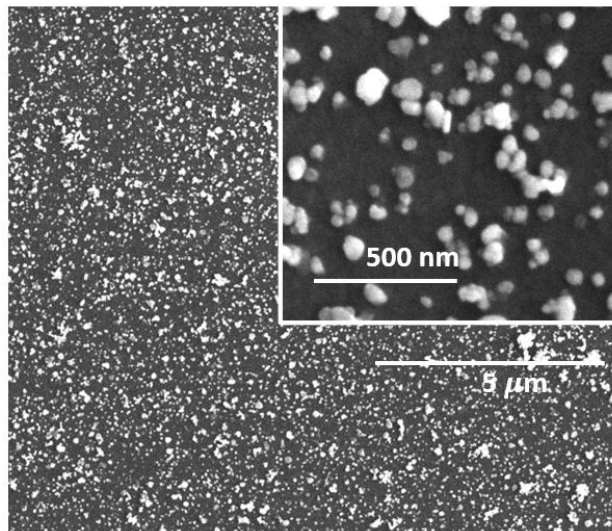


Figure 5.5 High-resolution SEM image of AuAg NPs immobilized on glass substrate using APTES.

5.3.2 Binding of 4-Mercaptopyridine (4MPy) on AgAu NP surface

5.3.2.1 Assignment of SER spectra

Prior to adsorbing 4MPy, polarization state-selected TE or TM 532 nm waves were excited in the waveguide in an attempt to detect the APTES grafting molecules.¹⁷ The APTES proved to be too weak a Raman scatterer, and its response was overwhelmed by Raman modes from the glass waveguide substrate.

The TE/TM polarized SER spectra obtained for 4MPy adsorbed on the AuAg NPs of the OCB are shown in Figure 5.6. Peak assignments for the SER spectra are based on previous studies where the Raman spectrum of 4MPy and its SER responses on different types of silver substrates

were examined.^{18–21} We focus on peak assignments derived from the TE polarized spectra in the following.

Raman peaks at 1061, 1191, and 1227 cm^{-1} belong respectively to the $18b_2$ $\beta(\text{CH})$, $9a_1$ $\beta(\text{CH})$, and $3b_2$ $\beta(\text{CH})$ in-plane bending modes of the pyridine ring. The peaks at 1587 and 1617 cm^{-1} originate in $8b_2$ and $8a_1$ νCC pyridine carbon stretching modes. There was no evidence of a peak assignable to $\nu(\text{SH})$ in any of the spectra. While it might be argued that thione/thiol tautomerism in 4MPy would make the $\nu(\text{SH})$ mode difficult to detect anyway, 4MPy exhibits what are referred to as X-sensitive vibrations.²² These are not precisely normal modes, i.e., they are mixed modes that result from the coupling of the $1a_1$ ring breathing mode with the vibration of the substituent (sulfur) of pyridine in the 4-position. With this reasoning, the $1a_1$ ring breathing mode at 1011 cm^{-1} is coupled with the $12a_1$ species at 1094 cm^{-1} , which is the most intense feature in this spectrum region. Thus, in 4MPy the sulfur substituent moves with significant amplitude when bound to Au (or Ag).

There is evidence that the 4MPy coexists as the neutral and the protonated species when bound to AuAg on the OCB, but not bound to the metal through the nitrogen atom. Protonation of 4MPy is known to weaken and shift the $9a_1$ $\beta(\text{CH})$ 1191 cm^{-1} peak to a higher wavenumber,^{19–21} where shifts have been recorded in the range between ~ 1200 and ~ 1225 cm^{-1} . This would place the $9a_1$ mode for non-protonated 4MPy under the $3b_2$ $\beta(\text{CH})$ band located at 1227 cm^{-1} , rendering this diagnostic equivocal for protonation. The *sine qua non* for the non-protonated nitrogen is the $8a_1$ νCC band that occurs at 1583 cm^{-1} . In Figure 5.6, the $8b_2\nu\text{CC}$ band in the SER spectrum is joined on the high wavenumber side by the $8a_1$ νCC peak at 1617 cm^{-1} . This is the spectroscopic signature for protonated nitrogen.^{20, 22} In other words, SERS detects both protonated and non-protonated 4MPy on the OCB.

Finally, our analysis assigns the peak at 1285 cm^{-1} to $\beta(\text{CH})/\delta(\text{NH})$, a coupling between ring in-plane bending and NH in-plane wag.²¹ The minor peaks below 900 cm^{-1} are likely pyridine ring deformation and aromatic CH out-of-plane bending modes.¹⁹

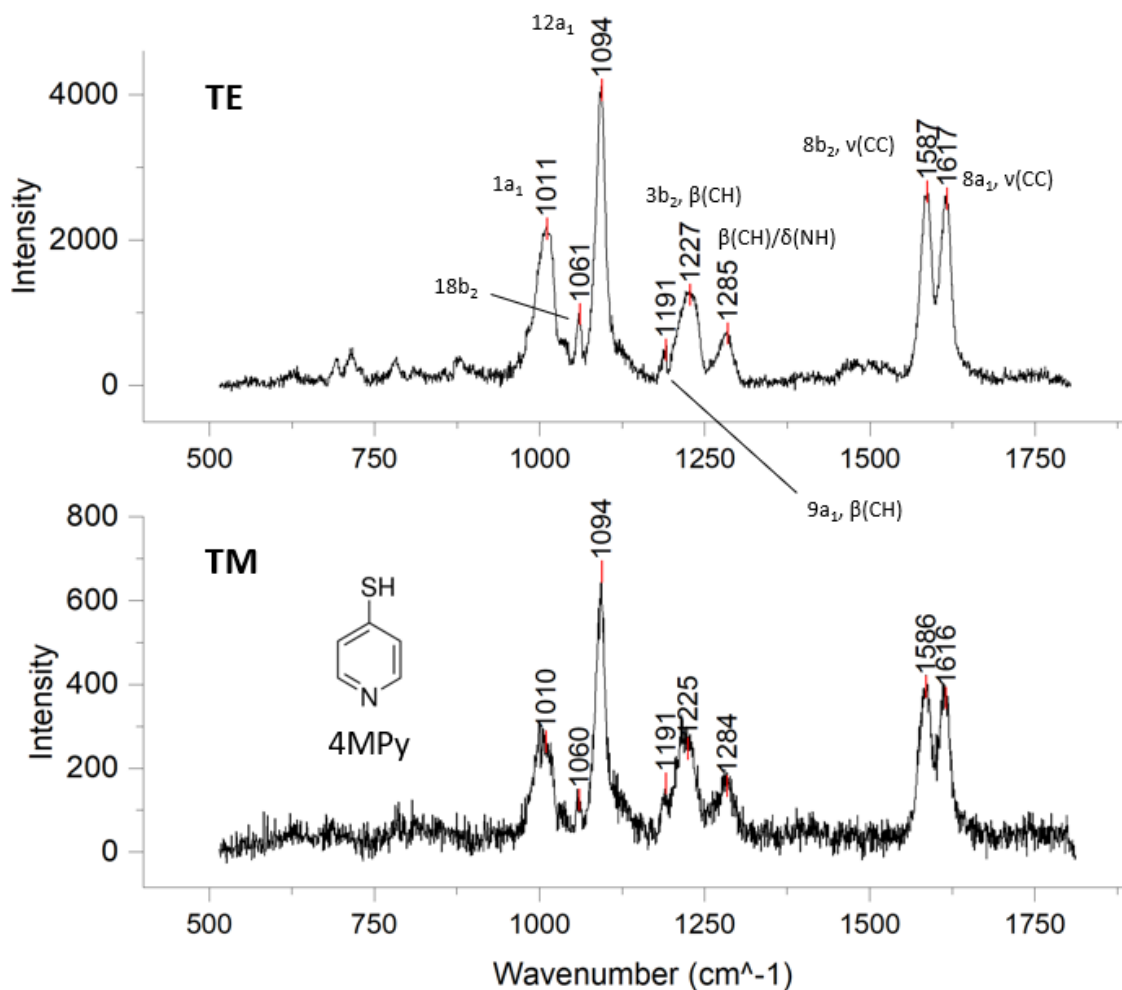


Figure 5.6 TE and TM SER spectra of 4MPy molecules adsorbed on AuAg NPs-glass integrated waveguide.

5.3.2.2 SER Response of 4MPy to TE and TM Polarization

Propagation of TE or TM waves did not produce significant differences in the number of peaks nor in the peak positions from the SER response of 4MPy over the 500 to 3200 cm^{-1} spectral range; however, the Raman counts for spectra obtained with TM polarization were uniformly diminished compared with those obtained with TE polarization. Despite differences in the waveguide scattering configurations, this observation also appears to conform to the theoretical predictions of Chen et al.,⁴ who found that the field enhancement factor for Raman scattering with the TE mode in a PW was larger than that compared with the TM mode in the same PW. This is consistent with the well-known fact that metal overlayers on dielectric waveguides behave as “mode strippers” (optical filters), preferentially removing TM polarization (intensity) from propagating waves comprising mixed TE/TM polarization.

5.3.2.3 Orientation of 4MPy on bimetallic AuAg nanoparticles on the OCB

Previous studies found that when 4MPy adsorbs onto silver NP and film surfaces, it assumes a roughly vertical orientation.^{18, 19} We find that 4MPy behaves similarly on our AuAg NP OCB. In section 2.1 above, we established that 4MPy binds to the surface of AuAg NPs through the sulfur atom. Figure 5.6 reveals that in the region 500-1800 cm^{-1} , the a_1 and b_2 modes of 4MPy are enhanced compared with the out-of-plane a_2 and b_1 vibrations. For an upright pyridine orientation, the a_1 and b_2 modes are normal to the surface. This is consistent with the evidence and interpretations that SER-responsive modes perpendicular to the surface receives the largest enhancement.^{18, 19, 23} In contrast, the out-of-plane a_2 and b_1 vibrations that are roughly parallel to the surface receive only minor enhancement.^{18, 19} Our SER spectra on bimetallic AuAg NPs are

consistent with an interpretation that 4MPy is bound through the sulfur atom and that it is oriented predominantly vertically. This assertion requires some qualifications and will be discussed in section 5.3.3.2.

5.3.2.4 Binding of Fe²⁺ to 4MPy

Anticipating our studies of binding MNPs to the AuAg OCB, we first examined the capacity of the OCB to detect binding Fe²⁺ as the OCB architecture evolves more complexity. Ferrous ions were provided by dissolved aqueous FeSO₄. Exposure of the OCB to solutions of Fe²⁺ caused some SER bands to increase in intensity relative to others. We observe in Figure 5.7 that exposure of 4MPy to Fe²⁺ cations over time is accompanied by diminished band intensity at 1617 cm⁻¹. This peak is associated with the 8a₁ ν(C=C) ring mode. In contrast, the β(CH)/δ(NH) and 8b₂ β(CH) modes located at the band positions 1285 and 1587 cm⁻¹ are enhanced. We note a small peak that emerges at 1039 cm⁻¹ after long exposure times. The increase in intensity of 8b₂ β(CH) (1587 cm⁻¹) band and the decrease in intensity of 8a₁ β(CH) 1617 cm⁻¹ band indicate binding of Fe²⁺ in some sort of nitrogen and/or arene-based coordination environment. Enhancement of the β(CH)/δ(NH) band at 1285 cm⁻¹ indicates a change in the pyridine nitrogen environment due to Lewis base donation of the nitrogen lone pair. The nitrogen lone pair directed outward from the ring skeleton is well oriented to overlap with a σ-symmetry and energy-adapted vacant Fe²⁺ orbital. The ring π-electrons can also supply additional π-bonding interactions with the iron d-orbitals.²⁴ Delocalized π* antibonding orbitals on the pyridyl ring can act as acceptors of Fe²⁺ d-orbital electron density.²⁴ This perturbation experienced by the delocalized π-electrons of the ring due to Fe²⁺ binding is the cause of changing intensity of these a₁ and b₂ modes.

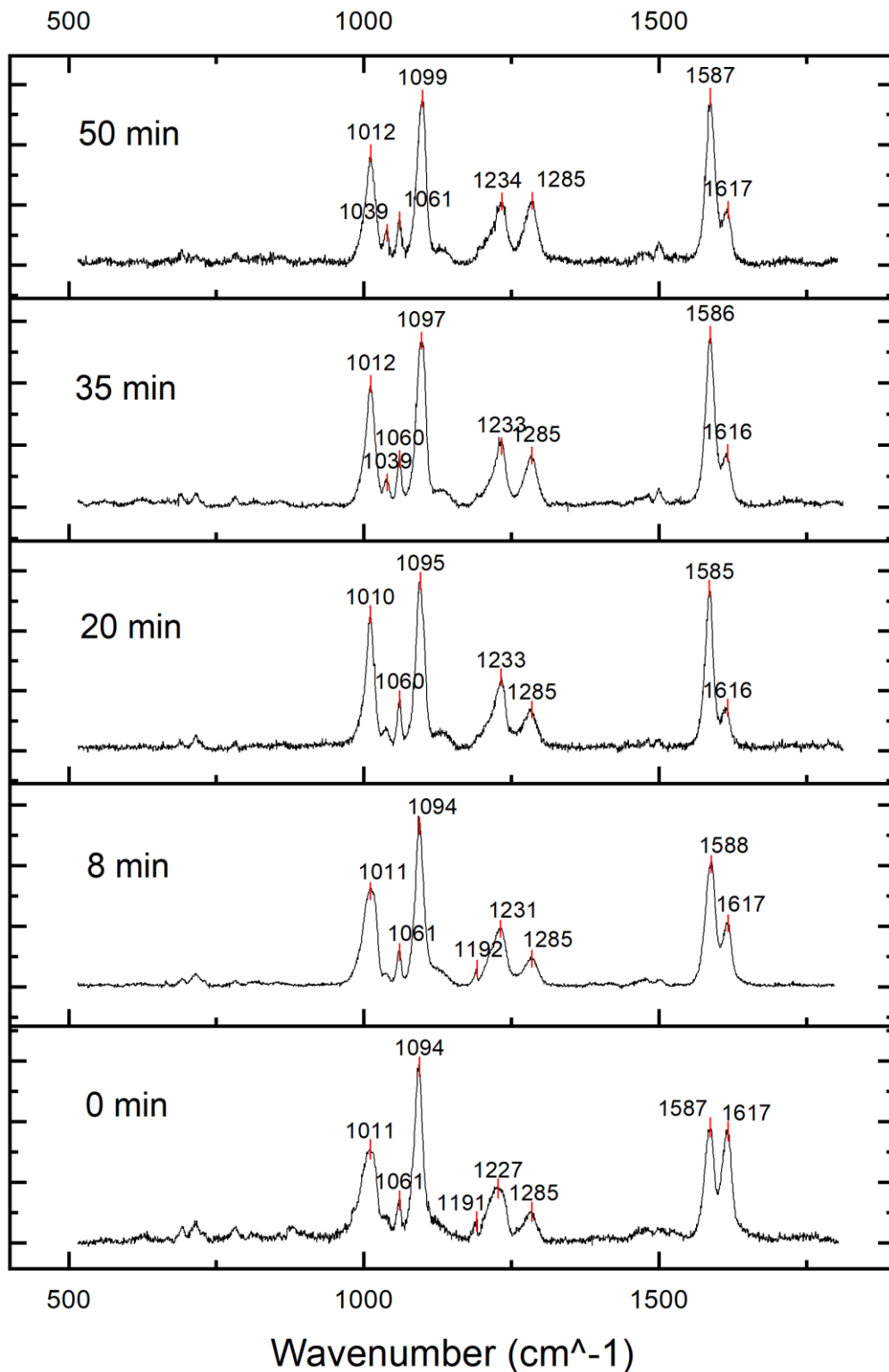


Figure 5.7 Guided wave TE polarized SER spectra of 4MPy molecules adsorbed on the AuAg OCB prior to and after different times of exposure to Fe^{2+} solution.

5.3.3 Binding of 4-aminobenzoic acid (4ABA) in comparison to that of 4MPy

5.3.3.1 SERS of 4ABA binding to AuAg NPs on the OCB

Figure 5.8 shows the TE/TM SER spectra of 4ABA molecules bound to AuAg NPs on the OCB. The unenhanced Raman spectrum of crystalline 4ABA is provided in Figure S5.1 for comparison. Focusing first on TE polarization, the most prominent peaks in the 4ABA SERS occur at 1126, 1386, and 1603 cm^{-1} . These are assigned to NH_2 bending (τNH_2), COO^- stretching (νCOO^-), and NH_2 deformation (δNH_2), respectively.^{25, 26} The τNH_2 mode is weak in the normal Raman spectrum of crystalline 4ABA (Figure S5.1), while the $\nu\text{C-OH}$ mode appears as a peak of medium strength at 1293 cm^{-1} .²⁷ The SERS of Figure 5.8 shows a significant enhancement in the τNH_2 mode and a blue-shift and moderate enhancement of the COO^- stretching mode. These features suggest that both the amine and carboxylic acid groups of 4ABA are involved in binding to the AuAg NPs. Although the literature on how 4ABA binds to silver surfaces is not fully resolved, there is agreement that the molecule can bind both through the amino and the carboxylic acid groups.²⁸ To assign the peaks in the TE spectra to bonding modes of 4ABA on the OCB, we can also turn to functional group analogs where recent data focuses on binding amino and aliphatic acids. Regarding the carboxylic acid terminus, Uznanski et al. presented evidence that this moiety in aliphatic molecules binds to Ag nanoparticle surfaces by symmetric chelation.²⁹ Al-Johani added precision to the notion of bidentate chelation by carrying out an exhaustive study of the binding of acetic acid and aliphatic di- and tri-carboxylic acid molecules on gold nanoparticle surfaces.³⁰ The monocarboxylic acid was shown to bind through both oxygen atoms to 2 adjacent atoms in a symmetric μ -bridging fashion at any of several crystal planes of Au. There is some theoretical evidence to suggest that amino acids bind to metal surfaces by donating the nitrogen lone pair to the antibonding orbitals of the metal, or by accepting the lone pair electrons of metal

to the antibonding orbitals of N–H bonds.³¹ The peak at 1603 cm^{-1} is assigned as an overlap of ν_{8a} ring stretching vibration and δNH_2 deformation. In crystalline 4ABA, the ν_{8a} band shows the strongest intensity among all Raman modes, while the δNH_2 band has a much weaker intensity and often appears as a shoulder to the ν_{8a} peak. Similar to the τNH_2 mode, the intensity of the δNH_2 mode is greatly enhanced upon metal binding. Past research has shown that the δNH_2 band gets strongly enhanced due to interaction with the silver surface, surpassing the ν_{8a} band in intensity.²⁶

The peaks at 1174 , 1197 , 1458 , and 1518 cm^{-1} are assigned to ring stretching modes ν_{9a} , ν_{13} , ν_{19b} , and ν_{19a} , respectively.²⁵ Past research has also suggested that 4ABA adsorbed on a metal surface can undergo dimerization, producing *p,p'*-azodibenzoate.²⁸ The signature of this surface product is a strong peak around 1460 cm^{-1} and a strong doublet around 1150 cm^{-1} .²⁸ The presence of *p,p'*-azodibenzoate is potentially observed in this experiment as the shoulder at 1144 cm^{-1} and an overlap with the ν_{19b} band.

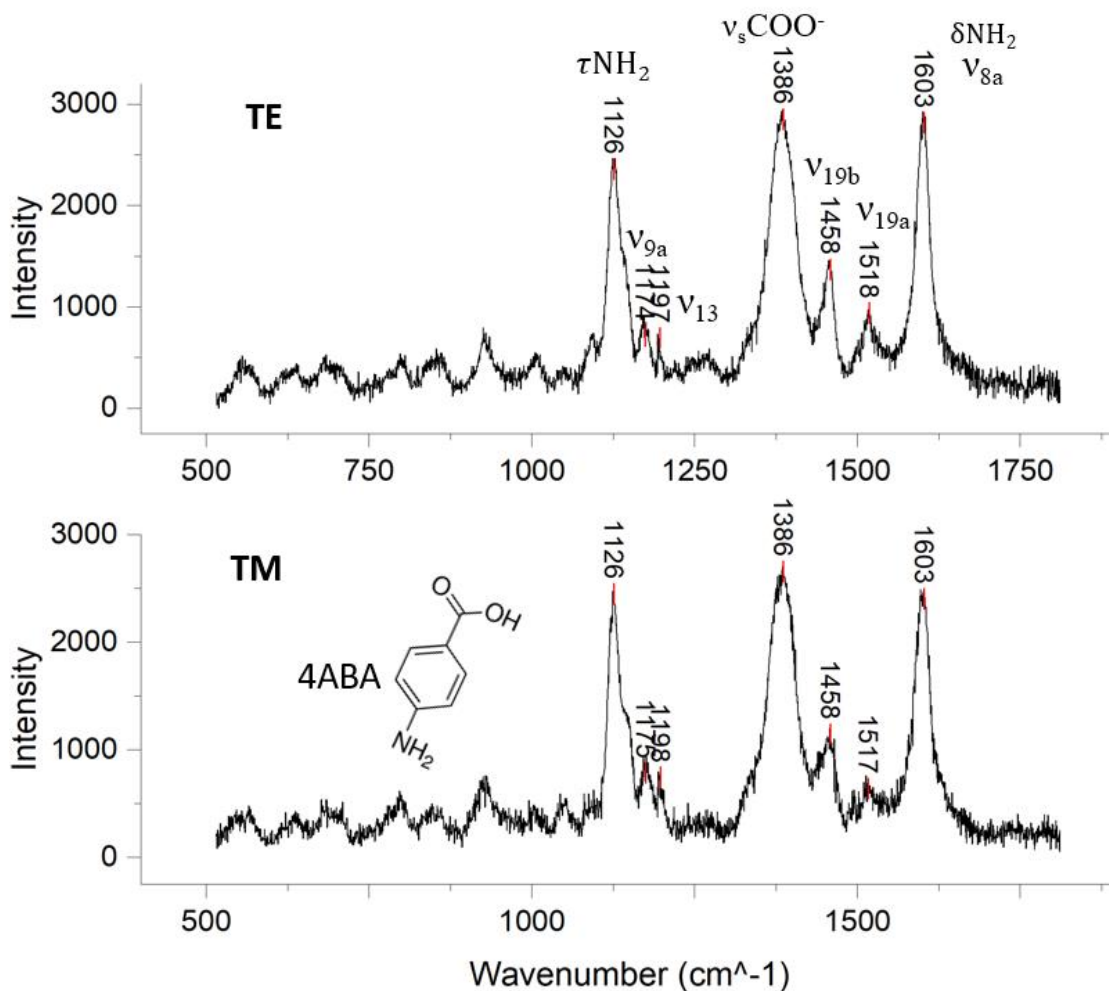


Figure 5.8 TE and TM SER spectra of 4ABA molecules adsorbed on the AuAg OCB.

5.3.3.2 Orientation of 4-aminobenzoic acid on nanoplasmonic AuAg on the OCB

Given the molecular structure of 4ABA and the Raman evidence we have provided, both the amino and carboxyl functional groups of a given 4ABA molecule appear to interact simultaneously with the metal surface. We conclude that the molecule lies horizontally on the AuAg NP surface.

Comparing the Raman responses from TE and TM guided waves, we did not observe significant differences in the SERS profiles of adsorbed 4ABA. Unlike the case for adsorbed 4MPy discussed previously, where the TM polarization produced a SER spectrum with significantly lower overall intensity than that produced by the TE polarization, such behavior was not observed for adsorbed 4ABA. The reason may be due to the “planar” orientation of adsorbed 4ABA compared to the upright orientation of adsorbed 4MPy.

At this point, it is helpful to qualify our discussion on the molecular orientation of 4MPy and 4ABA by framing the matter of molecular orientation a little more carefully in the language of the so-called Raman selection rules that have been developed for SERS. We know that for a fixed orientation of a molecule on a plasmonic surface, the SERS intensity for a given Raman mode depends on the symmetry of its tensor with respect to the surface, i.e., the intensity depends on molecular orientation. But knowledge of the Raman tensors of different modes is difficult to obtain, and the tensors can change on adsorption (i.e., as in the case of chemisorption). Moreover, it is difficult to describe local field polarization at the molecule and how that polarization connects with the Raman enhancement factor. Some advances have been made regarding these problems, especially for the case of a *flat metal surface*²³ and the research on the (flat) plasmonic waveguide published by Chen et al.⁴ Our analysis of the orientation of 4MPy and 4ABA presumes that the local field polarization is primarily perpendicular to the nanoparticle surface. Under this assumption, modes having a substantial Raman tensor component normal to the surface will be enhanced more than those whose normal components are weak or forbidden by symmetry. Qualitatively, one compares the SERS enhancement factor of the various modes, and relates these to the Raman tensors describing the unenhanced, unbound molecule. By this means, one can infer an approximate orientation - flat or upright on the surface. Underlying this approach are a number

of conditions that need to be met. The requirement that the polarization is perpendicular to the surface is difficult to justify in the case of rough metal surfaces, colloidal suspensions, and most likely, nanoplasmonic particles on the OCB. The enhancement factor for various Raman modes must be distinguishable from other effects, notably dispersion in the plasmon resonance which causes the enhancement factor to depend on the Raman shift.³² This information is often not readily available. It is the enhancement factor for a given mode and not the Raman intensity measured from the spectra that is the important parameter. Given the above remarks on the challenges faced in measuring enhancement factors, one has little recourse but to turn to qualitative arguments around the SER selection rules to assign molecular orientation. For this reason, our arguments for the different orientations of 4MPy and 4ABA remain qualitative.

5.3.3.3 4ABA-functionalized MNPs on nanoplasmonic AuAg on the OCB

To examine the ability of the OCB to detect 4ABA as a capping agent to bind deposited nanoparticles, instead of as a ligand directly binding to the surface of AuAg NPs, MNPs functionalized with 4ABA were deposited on the OCB. Our high-resolution SEM of MNPs deposited on the AuAg NP-covered waveguide is shown in Figure 5.9A. EDX reveals the composition of the major MNPs and AuAg NP clusters (Figure 5.9B). X-ray emissions from the Au and Ag overlap as expected, and in turn, we observe overlap with emissions from Fe. This indicates that the MNPs are in contact with, and probably ligated to the surface of the AuAg nanoparticles on the OCB. For more evidence, we turned to XPs.

XPS is used to examine the binding of 4ABA onto the MNPs (Figure 5.9C). Comparing the O1s spectra from pre-functionalized MNPs and after MNPs incubation in 4ABA solution, a

significant increase in O-C species (531.3 eV) is observed. This difference indicates the presence of COO^- species capable of monodentate or bidentate binding to the MNP surface through electrostatic or chemisorption.³³ Although the electron densities on the oxygen atoms are nonequivalent in the different carboxylate binding modes, the XPS cannot resolve the peaks.³³ The N1s spectra centered at 399.7 eV revealed an abundance of $-\text{NH}_2$ group on the surface of the MNPs after incubation in 4ABA solution. Prior to incubation, only a small amount of N-H was detected, likely remnants from the coprecipitation synthesis of MNPs, which employed ammonium hydroxide as a base. A small peak at 398.3 eV is also detected in the post-incubation N1s spectrum. It is assigned to N-Fe, suggesting possible covalent bonding between nitrogen and iron.^{34, 35} By XPS, the NH_2 and COO^- groups bind to the surface of MNPs.

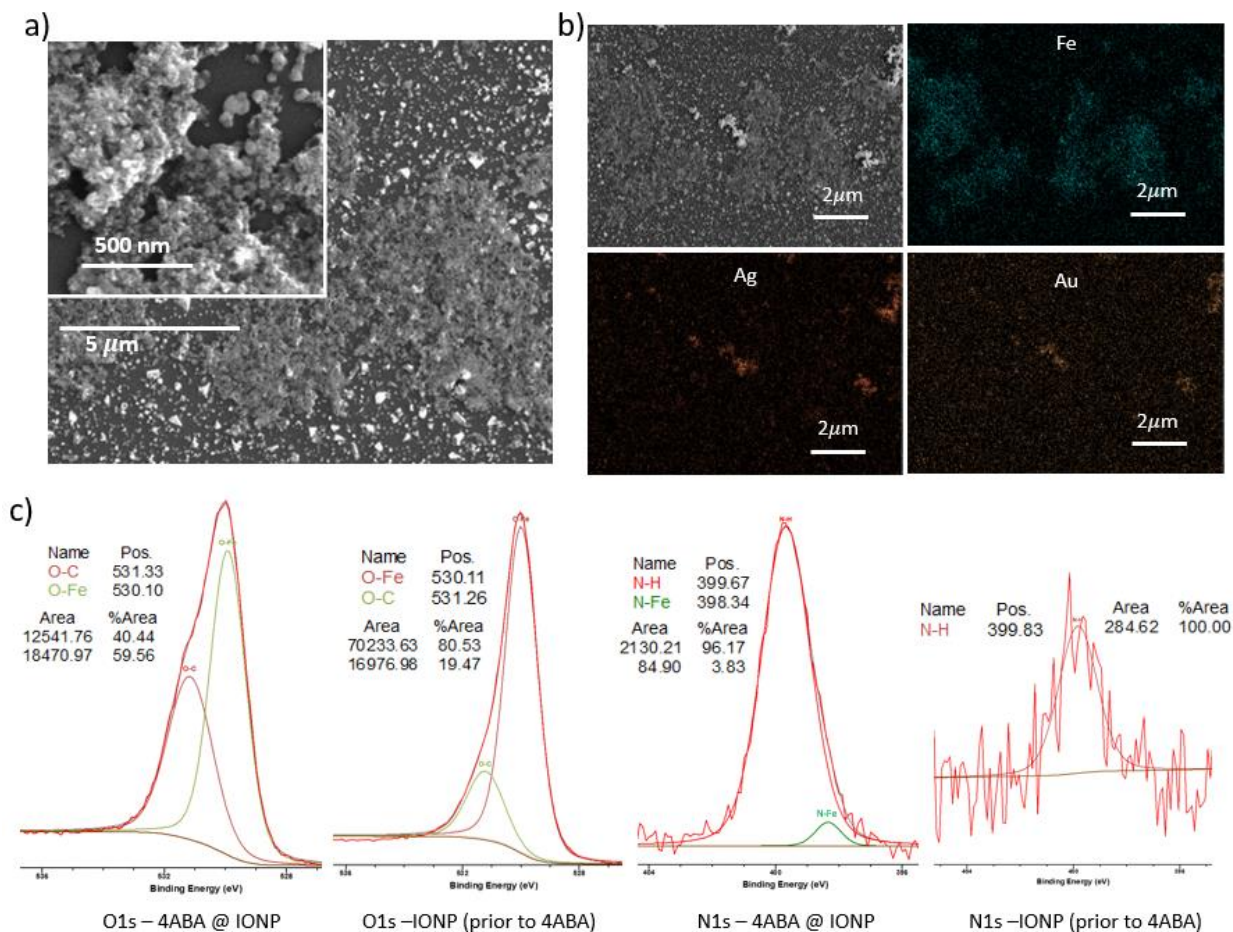


Figure 5.9 (A) High-resolution SEM image of 4ABA functionalized MNPs deposited on AuAg NPs immobilized on glass substrate using APTES; (B) Elemental mapping of Fe, Au, and Ag on a surface of 4ABA functionalized MNPs deposited on AuAg NPs integrated waveguide using SEM-EDX; (C) XPS analysis of O1s and N1s spectra of MNPs prior to and after incubation in 4ABA solution.

5.3.3.4 Detection of 4ABA-functionalized MNPs using OCB

MNPs decorated with 4ABA were deposited onto the AuAg NPs on the OCB. Raman spectra were gathered by scattering from TE and TM polarized guided waves. Peaks due to 4ABA

directly bonded to AuAg NPs (and not to MNPs) were identified in the SER spectra of Figure 5.8 in the previous section. In Figure 5.10, we see that these bands all have their counterparts when SERS is excited from the 4ABA-decorated MNPs bound to the AuAg NPs on the OCB. Nevertheless, a close comparison of Figures 5.7 and 5.9 reveals that the peak positions and relative intensities differ between the two types of bound 4ABA. We observe that from the 4ABA-decorated MNPs both the τNH_2 band and $\nu_s\text{COO}^-$ bands are blue-shifted and the bands are reduced in intensity. This outcome suggests a change in the binding environment of 4ABA. The ν_{19a} mode is also blue-shifted, but its relative intensity increases compared to the ν_{19b} and ν_{9a} ring modes. The peak at 1598 cm^{-1} dominates the spectra, and it is red-shifted from its original place at 1603 cm^{-1} .

We also note that propagating TE or TM guided waves yields slightly different SERS profiles. Compared to their TE counterparts, the τNH_2 , $\nu_s\text{COO}^-$ and ν_{19b} bands have slightly stronger intensities, while the peak at 1598 cm^{-1} is noticeably weaker. The $\nu_s\text{COO}^-$ band in TM polarization also appears to be broader and is slightly blue-shifted compared to that in TE. The SERS profile between $500 - 1050\text{ cm}^{-1}$ also shows Raman profiles that depend on the waveguide polarization.

The presence of bands attributable to τNH_2 and $\nu_s\text{COO}^-$ indicate that at least some NH_2 and COO^- groups have partially dissociated from the MNP surface and may have bonded with the AuAg surface. The fact that these two bands are no longer dominant suggests that, in this case, 4ABA does not assume the horizontal “planar” orientation it did when binding to AuAg NPs, in the absence of the MNPs.

Furthermore, the SERS from the OCB 4ABA-MNPs responds differently according to TE and TM polarizations. This contrasts with our studies of the polarization response of 4MPy or

4ABA on the AuAg NPs alone. In these cases, the molecules are orientated roughly upright (4MPy) or horizontally (4ABA). Note also that the TE and TM Raman spectral profiles for 45° angle Raman scattering from crystalline powders (pseudo-orthorhombic unit cell crystallites) are indistinguishable (Figure S5.1).³⁶ It can therefore be inferred that the 4ABA ligands deposited with the MNPs, now partially bound to the AuAg surface, exhibit orientations that are not upright, horizontal, or completely randomized. The different TE and TM SERS profiles suggest a complex environment for the surface ligands.

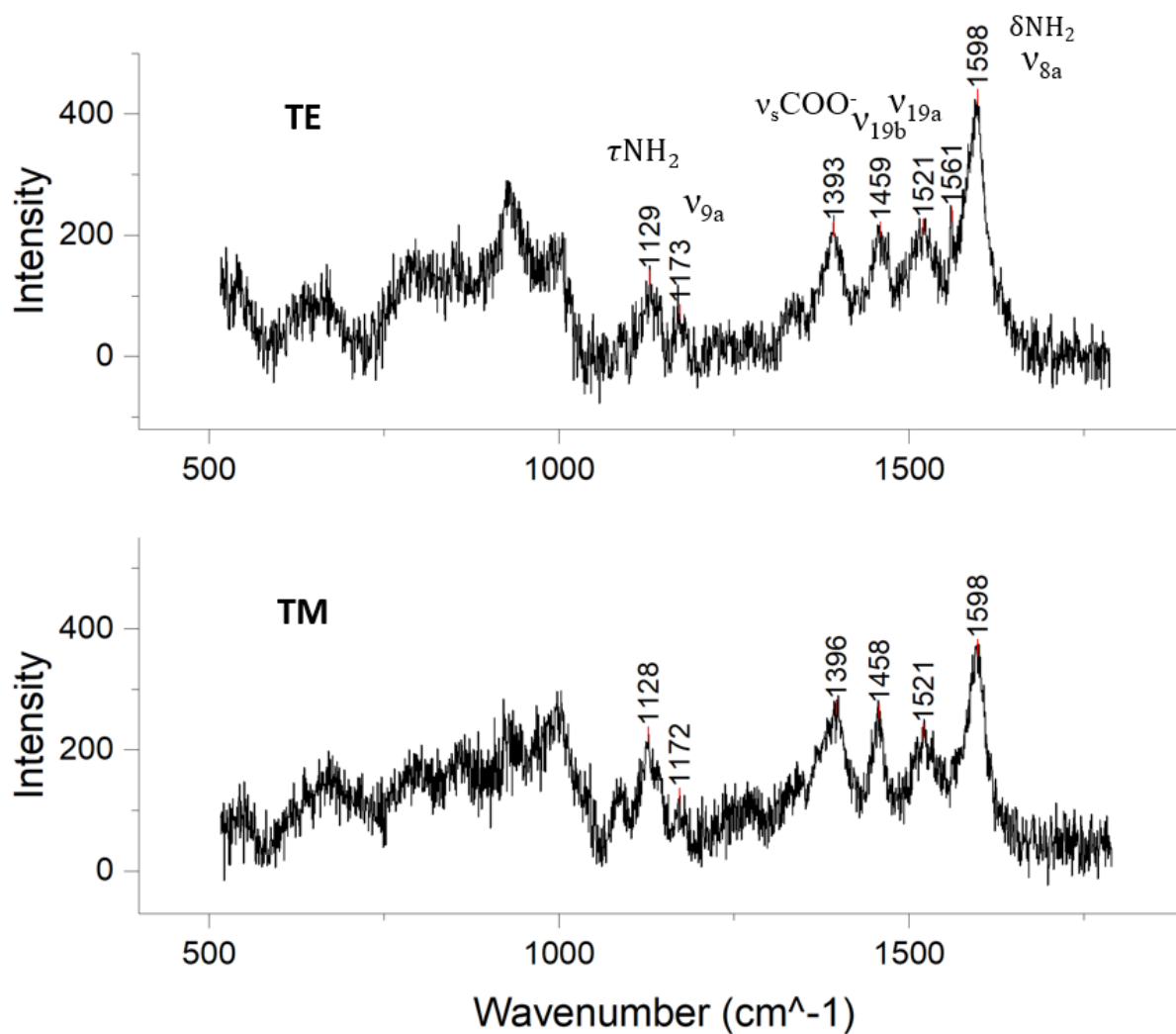


Figure 5.10 TE and TM SER spectra of 4ABA functionalized MNPS deposited on AuAg NPs-glass integrated waveguide.

5.3.4 FDTD simulation of electric fields of AuAg NPs excited by TE/TM polarized light

Since the Raman process is proportional to local electric field intensity,³⁷ it makes sense that methods of enhancing the local field may enhance the Raman response. It is well-known in SERS experiments that when plasmonic nanoparticles aggregate to the point where the individual particles are in close proximity, optical coupling between particles in the electromagnetic field

becomes very strong. Particle dimension, state of aggregation, and geometry play a large role in determining enhancements in plasmon resonance spectroscopy. Aggregates of plasmonic particles produce a stronger coupling of the electric field. As a result, the local field near the particle can be enhanced by many orders of magnitude over the incident field. The incident light around the plasmon resonance peak wavelength is scattered very strongly. With regards to the SER effect, Johnsson et al. have provided quantitative theoretical arguments that establish that the coupling between a molecule and the electromagnetic field is enhanced by placing the molecule between two silver nanoparticles.³⁸ In light of these remarks, Figures 5.3 and 5.5 encouraged us to examine how the TE and TM polarized evanescent waves might interact with the plasmonic nanoparticles attached to the OCB surface. Accordingly, we carried out FDTD calculations based on the simplification depicted in Figure 5.5. Figure 5.11A shows plots of the electric field intensity around AuAg NPs as they are excited by the evanescent field of TE or TM polarized light propagating in the waveguide beneath the nanoparticles. Excitation with the TE mode leads to symmetric field intensity concentrated at the north and south poles of the particles and nodes around the equator of particles. In Figure 5.11A, TE polarization lies in the xy plane oriented in the direction of the double-headed white arrow. For TM excitation, the electric field oscillates orthogonal to the xy plane. The field intensity concentrates around the equator of the nanoparticles and has lower intensity at the surface than that shown for the TE response. Particles isolated far enough apart show undistorted dipolar field intensity. For both polarizations, as the interparticle separation decreases, one observes distortions in the fields. This is evident left of center in the top part of the images in Figure 5.11A for both polarizations. With decreasing separation (bottom center, Figure 5.11A) one observes the high concentrations of field intensity that are the hallmark of the “hotspots” that are associated with enhanced SERS.^{37, 39}

TE and TM polarized light exhibit different transmission losses as the light propagates in asymmetric metal-clad thin-film-clad waveguides.⁴⁰ Attenuation experienced by the TM mode is greater than that of the TE mode because the TM mode interacts strongly with the metal surface, while the TE mode is repelled by the metal surface.⁴⁰ Figure 5.11B gives images of the waveguide streaks for the two polarizations. Like the metal-clad waveguide, the TM polarized wave in the OCB couples more strongly than does the TE polarization, and as a result, the TM wave suffers more loss. The plasmonic particles on the OCB behave somewhat similar to the polarization mode filter we presented in section 5.1.1. The discontinuous nature of the plasmonic AuAg NP overlayer allows us to propagate either polarization over distances larger than would be capable with a continuous metal film.

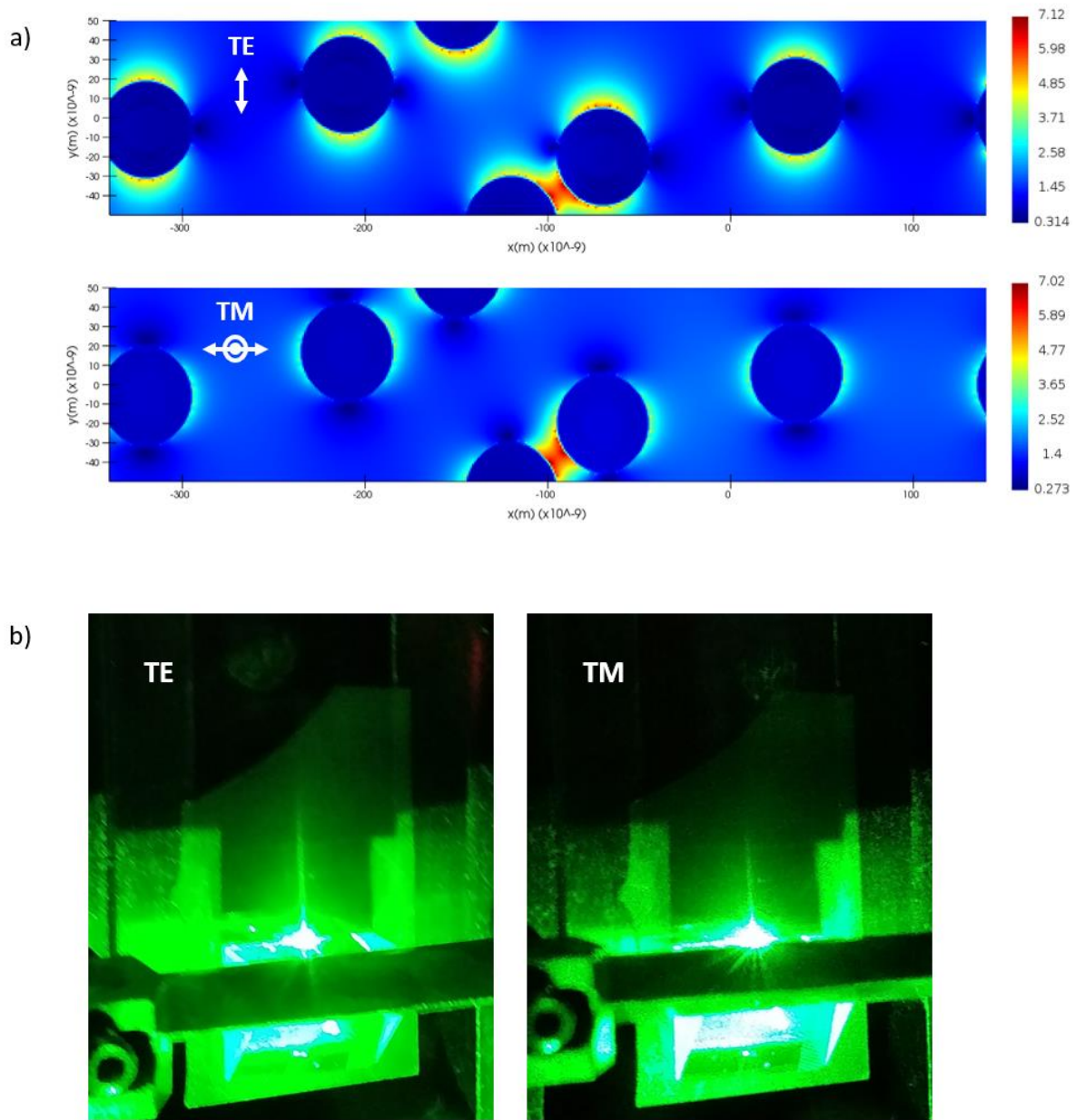


Figure 5.11 (A) FDTD electric field simulations of AuAg core-shell dimers. The color code on the right indicates the maximum and minimum electric field intensity is corresponding to TE and TM polarization. The vertical axis in each simulation is y , and the horizontal axis is x . The propagation direction is orthogonal to the xy plane. The double-headed arrow (TE) and the

arrow-and-dot (TM) indicate the direction of the exciting electric fields. **(B)** Waveguides streaks from prism coupling of the 532 nm laser polarized TE and TM orientation.

5.4 Conclusion

In this experiment, the integrated optics setup introduced in Chapter 4 is combined with an OCB prepared by immobilizing AuAg NPs on a glass substrate using 3-Aminopropyl trimethoxysilane (APTES). This IO-PEWSERS system operates by coupling TE or TM waves into the OCB waveguide and excites SERS using evanescent waves on the waveguide surface. The functionality of this ICB has been tested in several steps. In the first step, we verified the applicableness of the OCB by examining the SERS response from the binding of 4MPy molecules onto AuAg NPs. The TE-polarized SER spectrum of 4MPy is similar to that obtained in a previous experiment, also using TE polarization, but for different types of silver substrates. We further verified that 4MPy modified OCB has the ability to recognize cations in solution by carrying out a time-dependent binding study of Fe^{2+} . This demonstrated the availability of 4MPy pyridine nitrogen for cation binding.

Interestingly, we discovered that the TM-polarized SER spectrum for 4MPy has significantly lower peak intensity compared to its TE counterpart. To better understand the significance of this finding, we tested the binding of 4ABA on the OCB; however, the strong polarization-dependent SER intensity difference that is observed for 4MPy is not observed for 4ABA. We believe this difference in SER intensity is affected by molecular orientations.

Analyses of molecule binding modes using SER fingerprints suggested that 4MPy and 4ABA assumed a roughly upright (4MPy) or horizontal (4ABA) position on the AuAg NPs.

Furthermore, our electric field simulation using FDTD suggested that excitation by TE or TM polarized light resulted in different electric field profiles on the AuAg NPs. The TM mode showed greater attenuation compared to the TE mode, likely due to stronger interactions with plasmonic nanoparticles on the waveguide surface. Despite the fact that the precise Raman tensors of different vibrational modes are difficult to obtain and may change during the course of molecular binding, and that local field polarization and their Raman enhancement factors are hard to quantify, our SER results showed that molecules with different orientations interact differently with the electric field environment excited by different polarizations of light. Our OCB system, therefore, provides a qualitative system for differentiating molecular orientations.

To expand the application of our OCB system, we also tested the SER response of 4ABA functionalized MNPs depositing on the OCB. Some distinctions are observed comparing the TE and TM-induced SER spectra after nanoparticle deposition. We inferred that the polarization-dependent distinctions are produced by the partial binding of 4ABA ligands to the AuAg substrate upon deposition of the MNPs. However, the complexity of the OCB-nanoparticle interface environment warrants further investigations.

5.5 Supporting materials

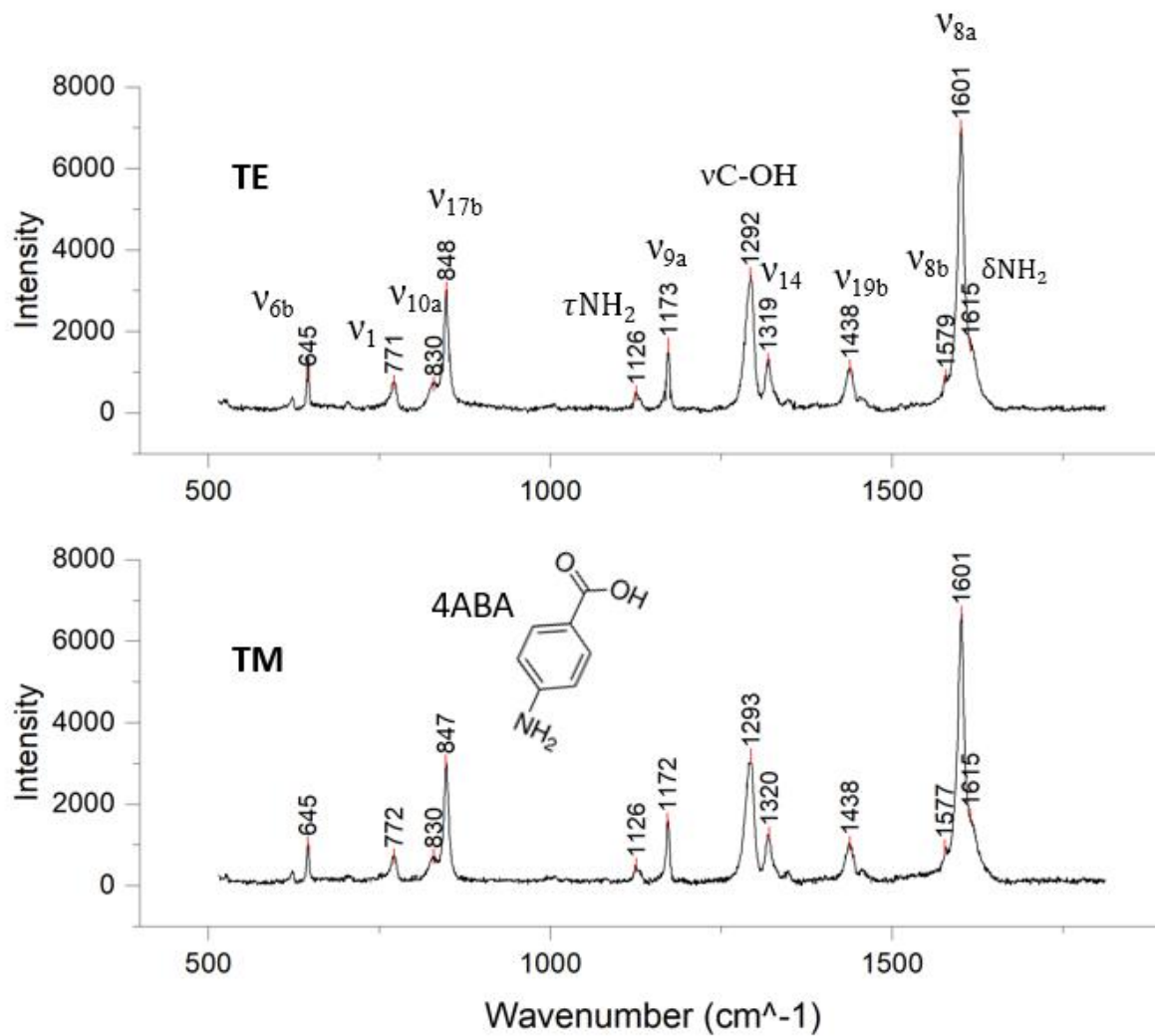


Figure S5.1 Raman spectra of crystalline 4ABA using either TE or TM polarized light.

5.6 References

1. Calagua, A., Alarcon, H., Paraguay, F. and Rodriguez, J., 2015. Synthesis and characterization of bimetallic gold-silver core-shell nanoparticles: a green approach. *Advances in Nanoparticles*, 4(04), p.116.
2. Futamata, M., Maruyama, Y. and Ishikawa, M., 2003. Local electric field and scattering cross section of Ag nanoparticles under surface plasmon resonance by finite difference time domain method. *The Journal of Physical Chemistry B*, 107(31), pp.7607-7617.
3. Mohammadpour, M., Khodabandeh, M.H., Visscher, L. and Jamshidi, Z., 2017. Elucidation of charge-transfer SERS selection rules by considering the excited state properties and the role of electrode potential. *Physical Chemistry Chemical Physics*, 19(11), pp.7833-7843.
4. Chen, C., Li, J.Y., Wang, L., Lu, D.F. and Qi, Z.M., 2015. Waveguide-coupled directional Raman radiation for surface analysis. *Physical Chemistry Chemical Physics*, 17(33), pp.21278-21287
5. Sun, L. and Yip, G.L., 1994. Analysis of metal-clad optical waveguide polarizers by the vector beam propagation method. *Applied Optics*, 33(6), pp.1047-1050.
6. Peddis, D., Laureti, S. and Fiorani, D. eds., 2021. *New Trends in Nanoparticle Magnetism* (Vol. 308). Berlin/Heidelberg, Germany: Springer.
7. McKee, K.J., Meyer, M.W. and Smith, E.A., 2012. Plasmon waveguide resonance Raman spectroscopy. *Analytical Chemistry*, 84(21), pp.9049-9055.
8. Baldwin, J. 1996. Surface enhanced Raman scattering of mercaptopyridine and pyrazinamide and the fabrication of a metal-ion sensor. Doctor of Philosophy. McGill University. Montreal, QC, Canada

9. Petcharoen, K. and Sirivat, A., 2012. Synthesis and characterization of magnetite nanoparticles via the chemical coprecipitation method. *Materials Science and Engineering: B*, 177(5), pp.421-427.
10. Kiani, M.T., Wang, Y., Bertin, N., Cai, W. and Gu, X.W., 2018. Strengthening mechanism of a single precipitate in a metallic nanocube. *Nano Letters*, 19(1), pp.255-260.
11. Qi, W.H. and Lee, S.T., 2010. Phase stability, melting, and alloy formation of Au– Ag bimetallic nanoparticles. *The Journal of Physical Chemistry C*, 114(21), pp.9580-9587.
12. Lim, D.K., Kim, I.J. and Nam, J.M., 2008. DNA-embedded Au/Ag core–shell nanoparticles. *Chemical communications*, (42), pp.5312-5314.
13. Okazaki, K.I., Kiyama, T., Hirahara, K., Tanaka, N., Kuwabata, S. and Torimoto, T., 2008. Single-step synthesis of gold–silver alloy nanoparticles in ionic liquids by a sputter deposition technique. *Chemical Communications*, (6), pp.691-693.
14. Rivas, L., Sanchez-Cortes, S., Garcia-Ramos, J.V. and Morcillo, G., 2000. Mixed silver/gold colloids: a study of their formation, morphology, and surface-enhanced Raman activity. *Langmuir*, 16(25), pp.9722-9728.
15. Ghosh, S.K. and Pal, T., 2007. Interparticle coupling effect on the surface plasmon resonance of gold nanoparticles: from theory to applications. *Chemical Reviews*, 107(11), pp.4797-4862.
16. He, R.X., Liang, R., Peng, P. and Zhou, Y.N., 2017. Effect of the size of silver nanoparticles on SERS signal enhancement. *Journal of Nanoparticle Research*, 19(8), pp.1-10.
17. Sun, Y., Yanagisawa, M., Kunimoto, M., Nakamura, M. and Homma, T., 2017. Depth profiling of APTES self-assembled monolayers using surface-enhanced confocal Raman

- microspectroscopy. *Spectrochimica Acta Part A: Molecular and Biomolecular Spectroscopy*, 184, pp.1-6.
18. Baldwin, J., Schühler, N., Butler, I.S. and Andrews, M.P., 1996. Integrated optics evanescent wave surface enhanced Raman scattering (IO-EWSERS) of mercaptopyrindines on a planar optical chemical bench: binding of hydrogen and copper ion. *Langmuir*, 12(26), pp.6389-6398.
19. Hu, J., Zhao, B., Xu, W., Li, B. and Fan, Y., 2002. Surface-enhanced Raman spectroscopy study on the structure changes of 4-mercaptopyridine adsorbed on silver substrates and silver colloids. *Spectrochimica Acta Part A: Molecular and Biomolecular Spectroscopy*, 58(13), pp.2827-2834.
20. Jung, H.S., Kim, K. and Kim, M.S., 1997. Raman spectroscopic investigation of the adsorption of 4-mercaptopyridine on a silver-sol surface. *Journal of Molecular Structure*, 407(2-3), pp.139-147.
21. Zhang, L., Bai, Y., Shang, Z., Zhang, Y. and Mo, Y., 2007. Experimental and theoretical studies of Raman spectroscopy on 4-mercaptopyridine aqueous solution and 4-mercaptopyridine/Ag complex system. *Journal of Raman Spectroscopy: An International Journal for Original Work in all Aspects of Raman Spectroscopy, Including Higher Order Processes, and also Brillouin and Rayleigh Scattering*, 38(9), pp.1106-1111.
22. Spinner, E., 1963. 717. The vibration spectra of some monosubstituted pyridines and pyridinium ions. *Journal of the Chemical Society (Resumed)*, pp.3860-3870.
23. Le Ru, E.C., Meyer, S.A., Artur, C., Etchegoin, P.G., Grand, J., Lang, P. and Maurel, F., 2011. Experimental demonstration of surface selection rules for SERS on flat metallic surfaces. *Chemical Communications*, 47(13), pp.3903-3905.

24. Pal, S., 2018. Pyridine: A useful ligand in transition metal complexes. *Pyridine*, 57.
25. Suh, J.S., DiLella, D.P. and Moskovits, M., 1983. Surface-enhanced Raman spectroscopy of colloidal metal systems: a two-dimensional phase equilibrium in p-aminobenzoic acid adsorbed on silver. *The Journal of Physical Chemistry*, 87(9), pp.1540-1544.
26. Liang, E.J., Engert, C. and Kiefer, W., 1993. Surface-enhanced Raman spectroscopy of p-aminobenzoic acid with excitation in the visible and near infrared spectral region. *Vibrational Spectroscopy*, 6(1), pp.79-85.
27. Samsonowicz, M., Hrynaszkiewicz, T., Świsłocka, R., Regulska, E. and Lewandowski, W., 2005. Experimental and theoretical IR, Raman, NMR spectra of 2-, 3- and 4-aminobenzoic acids. *Journal of Molecular Structure*, 744, pp.345-352.
28. Park, H., Lee, S.B., Kim, K. and Kim, M.S., 1990. Surface-enhanced Raman scattering of p-aminobenzoic acid at silver electrode. *Journal of Physical Chemistry*, 94(19), pp.7576-7580.
29. Uznanski, P., Zakrzewska, J., Favier, F., Kazmierski, S. and Bryszewska, E., 2017. Synthesis and characterization of silver nanoparticles from (bis) alkylamine silver carboxylate precursors. *Journal of Nanoparticle Research*, 19(3), pp.1-20.
30. Al-Johani, H., Abou-Hamad, E., Jedidi, A., Widdifield, C.M., Viger-Gravel, J., Sangaru, S.S., Gajan, D., Anjum, D.H., Ould-Chikh, S., Hedhili, M.N. and Gurinov, A., 2017. The structure and binding mode of citrate in the stabilization of gold nanoparticles. *Nature Chemistry*, 9(9), pp.890-895.
31. Pakiari, A.H. and Jamshidi, Z., 2007. Interaction of amino acids with gold and silver clusters. *The Journal of Physical Chemistry A*, 111(20), pp.4391-4396.

32. Buchanan, S., Le Ru, E.C. and Etchegoin, P.G., 2009. Plasmon-dispersion corrections and constraints for surface selection rules of single molecule SERS spectra. *Physical Chemistry Chemical Physics*, 11(34), pp.7406-7411.
33. Wilson, D. and Langell, M.A., 2014. XPS analysis of oleylamine/oleic acid capped Fe₃O₄ nanoparticles as a function of temperature. *Applied Surface Science*, 303, pp.6-13.
34. Wagner, A.J., Wolfe, G.M. and Fairbrother, D.H., 2003. Reactivity of vapor-deposited metal atoms with nitrogen-containing polymers and organic surfaces studied by in situ XPS. *Applied Surface Science*, 219(3-4), pp.317-328.
35. Degaga, G.D., Trought, M., Nemsak, S., Crumlin, E.J., Seel, M., Pandey, R. and Perrine, K.A., 2020. Investigation of N₂ adsorption on Fe₃O₄ (001) using ambient pressure X-ray photoelectron spectroscopy and density functional theory. *The Journal of Chemical Physics*, 152(5), p.054717.
36. Lai, T.F. and Marsh, R.E., 1967. The crystal structure of p-aminobenzoic acid. *Acta Crystallographica*, 22(6), pp.885-893.
37. Langer, J., Jimenez de Aberasturi, D., Aizpurua, J., Alvarez-Puebla, R.A., Auguie, B., Baumberg, J.J., Bazan, G.C., Bell, S.E., Boisen, A., Brolo, A.G. and Choo, J., 2019. Present and future of surface-enhanced Raman scattering. *ACS Nano*, 14(1), pp.28-117.
38. Johansson, P., Xu, H. and Käll, M., 2005. Surface-enhanced Raman scattering and fluorescence near metal nanoparticles. *Physical Review B*, 72(3), p.035427.
39. Sriram, S., Bhaskaran, M., Chen, S., Jayawardhana, S., Stoddart, P.R., Liu, J.Z., Medhekar, N.V., Kalantar-Zadeh, K. and Mitchell, A., 2012. Influence of electric field on SERS: frequency effects, intensity changes, and susceptible bonds. *Journal of the American Chemical Society*, 134(10), pp.4646-4653.

40. Suematsu, Y., Hakuta, M., Furuya, K., Chiba, K. and Hasumi, R., 1972. Fundamental transverse electric field (TE₀) mode selection for thin-film asymmetric light guides. *Applied Physics Letters*, 21(6), pp.291-293.

Chapter 6

Polarization mode conversion in sol-gel derived waveguides

6.1 Introduction

This chapter validates our design and implementation of our custom-built Raman Waveguide spectrometer for the case of wave propagation in a medium with an *anisotropic refractive index*. We then follow up with preliminary experiments to determine if an applied magnetic field can induce polarization mode conversion in a non-Faraday effect configuration optical chemical bench comprising core doped magnetite nanoparticles. In effect, doping the waveguide core with magnetic nanoparticles creates a gyrotropic medium.

6.1.1 Background to waveguide polarization state mode conversion and polarized waveguide Raman spectroscopy

Chapter 4 presented some background theories of propagation of electromagnetic waves in a dielectric waveguide. The analysis presumed propagation in a dielectric waveguide having an isotropic refractive index. In this case, for the waveguide depicted in Figure 4.3, the refractive index profile $n(z)$ is fixed and uniform along the longitudinal propagation x-direction of the waveguide, meaning that the electric (\mathbf{E}) and magnetic (\mathbf{H}) fields of the transverse wave satisfy the vector wave equations of a dielectric source-free medium:

$$\nabla^2 \mathbf{E} + k_0^2 n^2 \cdot \nabla(\nabla \cdot \mathbf{E}), \quad (6.1)$$

$$\nabla \times [n^{-2} \cdot (\nabla \times \mathbf{H})] = k_0^2 \mathbf{H} \quad (6.2)$$

Note that the refractive index n is a 3 x 3 tensor. In these equations, the wave vector for propagation in free space, k_0 , has the value $2\pi/\lambda_0$. For a dielectric waveguide with an isotropic refractive index, the \mathbf{E} and \mathbf{H} fields separate into x- and z-dependent terms as follows:

$$E(x, z) = e(z) \exp(i\beta x) \quad (6.3)$$

$$H(x, z) = h(z) \exp(i\beta x) \quad (6.4)$$

These equations describe a standing wave with fields $e(z)$ and $h(z)$ propagating along the x-direction with propagation constants $\beta = k_{1x} = k_{2x} = k_{3x}$. In this case, the vector wave equations yield analytical solutions. The modal fields separate into the well-known polarizations TE_m and TM_m , where m is the mode index that counts the number of nodes in the standing wave. The propagation constant β is also a function of the mode index, so we write this as β_m . The quantity, β_m/k_0 gives the ratio of the wave velocity in vacuum to that in the waveguide. We call this ratio the effective index, $n_{eff,m}$ of mode m . Within the guiding layer, the field intensity distributions are sinusoidal. In the substrate and superstrate regions, the field profiles decay exponentially. This portion of the field is called the evanescent wave. Values of $n_{eff,m}$ fall between the refractive indices of the film and substrate. TE and TM polarized modes of the same order, m , have different n_{eff} . Although the modes may be close together, orthogonality requires that they are never degenerate in an isotropic waveguide.

Let us now consider a waveguide with an *anisotropic* refractive index. We shall show, for a simple case, that this can lead to polarization mode conversion, ie, that a propagating TE polarized wave can acquire TM character and *vice versa*. Because we are interested in Raman vibrational spectroscopy, we take the unusual step of converting the waveguide “optical readout”

into polarized vibrational modes instead of the simple expedient of optical detection of rotation of the plane of polarization. The advantage here is that we can interpret changes in the molecular features of the waveguide that cause polarization mode conversion.

Now a non-absorptive dielectric waveguide medium can be described in terms of its dielectric tensor through,

$$\varepsilon = \varepsilon_0 n^2 = \varepsilon_0 \begin{bmatrix} n_{xx}^2 & n_{xy}^2 & n_{xz}^2 \\ n_{xy}^2 & n_{yy}^2 & n_{yz}^2 \\ n_{xz}^2 & n_{yz}^2 & n_{zz}^2 \end{bmatrix} \quad (6.5)$$

The tensor is symmetric and real. In this case, the waveguide modes now have a complicated polarization dependence. We call these hybrid modes, coupled TE-TM modes. However, when the dielectric tensor is diagonal, the TE and TM modes are uncoupled and they propagate just as they do in a medium with an isotropic refractive index. A complete analysis of coupled mode theories that have been developed to handle the complicated problem of mode conversion is beyond the scope of this chapter. Nevertheless, we note that hybrid modes are widely described in the framework of linear combinations of TE and TM modes. In turn, polarized Raman spectra are readily described in terms of these linearly polarized TE and TM fields, meaning that this type of coupled mode theory offers a framework for interpreting polarized Raman spectra collected from anisotropic films.

In the sol gel medium described below, the refractive index of the dielectric waveguide is initially isotropic. We will show that this implies that one will obtain three polarized Raman spectra that have roughly the same band profile, and one spectrum that differs from the other three and corresponds to strongly polarized Raman modes. By introducing anisotropy in the refractive index, mode mixing will occur. One must observe changes in the Raman spectra that reflect mode mixing

as a result. We first show that this is indeed the case when thermal energy is deposited in a waveguide by the highly spatially confined laser beam. This leads to thermally activated crosslinking of acrylate moieties in the glass. The result is that a polarized laser beam “writes” an anisotropic refractive index into the glass waveguide. The formation of C-C bonds from C=C olefin causes the matrix to densify and thus raises the local refractive index. This refractive index perturbation is highly localized. In fact, localization is accompanied by self-focusing of the laser beam so that diffractive losses are compensated by ongoing local increases in the refractive index. In effect, as it propagates the waveguide mode creates its own permanent internal “optical waveguide” whose shape and spatial dimensions are governed by the mode index and corresponding beam shape used to induce the refractive index change. This type of optical self-inscription can be conducted with polarized light so that one can intentionally write an anisotropy into the refractive index, but only in the highly localized region of the propagating wave. In effect, one can create an anisotropic waveguide-within-a-waveguide. The anisotropy in the refractive index can then be “read” by interrogating the self-written waveguide at reduced power. Thus, in our experiments, instead of measuring the rotation of the electric field vector, our optical “readout” will be the change in the polarization state of a vibrational C-H mode of a functional group component of a hybrid organic-inorganic sol-gel derived alkyl-substituted alkoxy silane

One can also induce mode conversion with magnetic media. When a propagating electromagnetic (EM) wave encounters a magnetic medium, the EM response depends on whether the light is transmitted, reflected, or absorbed by the medium. In the case of transmission, the plane of polarization is rotated when linearly polarized light travels through a magnetized sample. This is the Kerr effect. In micro-optics, Faraday’s rotation is the outcome of mode polarization in a dielectric medium when an external static magnetic field is applied along the direction of

propagation. The origin of this change in propagation mode is attributed to the Lorentz force $\mathbf{F} = q\mathbf{E} + q\mathbf{v} \times \mathbf{B}$ acting on the propagating light. Here, q is the electron charge, \mathbf{v} is the electron velocity and \mathbf{B} is the magnetic induction. Linearly polarized guided waves have two circularly polarized components in a magnetic medium. Each circularly polarized component interacts with the electrons in the waveguide medium. Two distinct and opposite oscillating electric dipoles are induced, each with its own corresponding electric and magnetic fields. The force exerted on an electron in the waveguide medium due to these electric and magnetic fields is the Lorentz force. With an external magnetic field applied to the waveguide, the external field interacts with the oscillating dipoles along the propagation path, whose orientation depends on the directions of the two circularly polarized light beams. The oscillating dipoles with different orientations, therefore, interact with the applied magnetic field differently. As a result, the two circularly polarized beams now experience different refractive indexes while propagating through the medium, changing the polarization plane of the overall propagating light.^{1,2}

The second part of this chapter documents our studies of how the local superparamagnetic field of magnetite (Fe_3O_4) doped in a hybrid sol-gel glass waveguide might influence guided wave propagation under the force of an applied magnetic field. An external magnetic field will induce the superparamagnetic spin vector to align with the film. In particular, we are interested in the interconversion of transverse electric (TE) and transverse magnetic (TM) waveguide eigenmodes. This interconversion is important to the phenomenon of phase matching. Phase matching between the fundamental TE and TM modes is an essential condition for complete polarization rotation in magneto-optical waveguides with longitudinally directed magnetization. Without phase matching between the TE and TM modes, the propagation constants for the different modes of polarization limit the maximum power transfer ratio. The result is that the form birefringence of a planar

waveguide limits optical isolation and the performance of the waveguide as a nonreciprocal device degrades. The incentive for our study is based on the possibility of using the magnetic field response of superparamagnetic nanoparticles to regulate TE-TM mode conversion. Although this phenomenon is documented through the Kerr effect in a series of papers published in the photonics literature,³⁻⁵ our interest is to gain more fundamental insight into how the vibrational properties of the nanocomposite waveguide might be readout as signatures of mode conversion. We note that the challenge to this experiment is formidable. For background, we note the theoretical treatment by Chung and Kim.⁶ These researchers treat the case of mode conversion in a lossless (non-absorbing) gyrotropic waveguide medium relevant to guided wave modulators, switches, and phase shifters. The assumption that the waveguide is lossless simplifies the mathematics because the gyrotropic medium can be treated as having a dielectric permittivity tensor that is Hermitian. Regrettably, we find no treatments of gyrotropic media that incorporate optical loss. Magnetite nanoparticles are lossy. They absorb light in the visible domain. Light absorption by magnetic NPs is associated with thermally induced electron delocalization between adjacent Fe²⁺ and Fe³⁺ ions, where the electronic transitions arise from intervalence charge transfer transitions that occur in the visible and out into the near-IR region. Simply put, we attempt to look for signs of mode conversion in a self inscribed gyrotropic “waveguide-within-a-waveguide” made from a hybrid sol gel glass and magnetite nanoparticles. Despite the lack of a resolved theoretical framework to understand mode conversion in such a lossy gyrotropic medium, we hypothesized that the NPs, under the influence of an external magnetic field, might induce mode conversion. Our intention was to "sense" the intervention of the magnetic medium by "reading out" polarization mode conversion as was done for the case of optical self inscription.

To understand the above-mentioned experiments in self inscribed waveguides, we first remind the reader of how the tensorial properties of the molecular polarizability can be exploited to measure mode conversion using guided wave polarized Raman spectroscopy.

6.1.2 Polarized Raman Spectroscopy

As discussed in Chapter 4, the Raman effect is directly related to the induced dipole of a probe molecule. The induced dipole results from a perturbation in the polarizability of a probe molecule due to its molecular vibrations. The relationship between the induced dipole of a probe molecule and the incident beam of excitation is:⁷

$$\vec{\mu} = \alpha \vec{E} \quad (6.6)$$

where $\vec{\mu}$ is the induced dipole and \vec{E} is the electric vector of the incident beam of excitation. Both $\vec{\mu}$ and \vec{E} are three-dimensional vectors, the polarizability tensor α is, therefore, a second-rank tensor, namely a matrix.

$$\begin{bmatrix} \mu_x \\ \mu_y \\ \mu_z \end{bmatrix} = \begin{bmatrix} \alpha_{xx} & \alpha_{xy} & \alpha_{xz} \\ \alpha_{yx} & \alpha_{yy} & \alpha_{yz} \\ \alpha_{zx} & \alpha_{zy} & \alpha_{zz} \end{bmatrix} \begin{bmatrix} E_x \\ E_y \\ E_z \end{bmatrix} \quad (6.7)$$

The polarizability tensor α describes the polarizability of individual vibration in the probe molecule. Each coefficient describes a directional specific change in polarizability due to interaction with a unit incident electric field with polarization along an axis. However, not every coefficient in the polarizability matrix leads to a different induced dipole moment. A few of the coefficients may be equal depending on the symmetry of the tensor. For example, a tensor with spherical symmetry has equal off-diagonal coefficients and equal diagonal coefficients.⁷ This

symmetry is affected by molecular structure, inter- or intramolecular interactions, and the three-dimensional packing of the probe molecules. Polarizability tensors can be visualized as polarizability ellipsoids with different shapes. The differential polarizability ellipsoids determine the mode of the vibrations. The directional information in the vibrational modes is lost if an incident ray with a non-specified electric vector is used to excite the probe molecules. In polarized Raman spectroscopy, the combination of a polarized incident beam with a polarization analyzer of the scattered light can extract precise directional information about the differential polarizability of molecules; hence, the orientation of the molecules can be determined.

Polarized waveguide Raman spectroscopy on thin films can be used to interpret the mode conversion.⁸ When a guided wave excites a Raman probe molecule, the induced dipole moment depends on the angle between the electric vector of the incident light and the magnitude of the polarizability. The tensorial character of the polarizability thus contains directional information about this excitation event. For a particular vibrational mode, the Raman intensity is proportional to:⁸

$$I_{FF'} \propto E_0^2 \alpha_{FF'}^2 \quad (6.8)$$

where F is the axis along which the Raman scattering occurs, F' is the axis of polarization of the incident radiation, E_0^2 is the intensity of the incident radiation, and $\alpha_{FF'}$ are components of the polarisability tensor α . Specifically, $\alpha_{FF'}$ are derivatives of the polarizability tensor with respect to the normal coordinate of vibrations, and each normal mode of vibration has a unique α .⁸

As shown in equation 6.8, the observed Raman intensity changes depending on the incident and scattering geometries. The symmetry properties of α_{ij} depend on both the symmetry properties of the molecular polarizability tensor and the orientation of molecules being probed.

The tensorial nature of the Raman response also reveals that the polarization of both the incident and the scattered radiation is essential to decipher the orientation of probe molecules or molecular subunits in the waveguide medium. Polarized Raman spectroscopy is, therefore, a suitable technique to study TE-TM mode conversion in guided waves. Polarized Raman can monitor the anisotropy of the waveguide due to intrinsic or induced birefringence or mode conversion caused by a magnetic field.

6.1.3 Porto notation

We adopt Porto notation to describe the spectral patterns in guided wave polarized Raman spectroscopy. The notation takes the following format:

$$A(BC)D$$

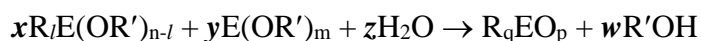
where A represents the direction of propagation of the incident light, B represents the direction of polarization of the incident light, C represents the direction of polarization of the scattered light, and D represents the direction of propagation of the scattered light.

Figure 6.1 illustrates how to interpret polarized Raman spectroscopy with planar waveguide using Porto notation. As shown in Chapter 4, the integrated optics configuration is oriented in a way such that the waveguide lies in the xy-plane. The incident laser beam propagates in the x-direction upon coupling into the waveguide, while Raman scattering is observed in the z-direction. Incident light with a TE propagation mode is polarized along the y-axis (E_y) and incident light to excite a TM propagation mode is polarized along the z-axis (E_z). The polarization of the collected Raman scattering can be controlled using a polarization analyzer orientated along either the x- or y-axis. The Porto notations for the four incident-and scattered Raman polarizations are:

X(YY)Z, X(YX)Z, X(ZX)Z, and X(ZY)Z. This underscores a unique benefit of guided wave Raman spectroscopy: one can obtain four output spectra in a given experiment. Indeed, a simple analysis of the polarizability tensor shows that it is diagonal for an isotropic medium (uniform refractive index). This is also true if the three principal axes of ϵ are oriented along the x-, y-, or z-axis or in the xz-plane. The off-axis components are identically zero. In this case, it can be shown that only the X(YY)Z leads to strongly polarized spectra; the other three configurations yield identical Raman spectra. Any birefringence that is induced in the medium will show up as mode conversion. Therefore, comparing Raman spectroscopic measurements from four polarizations reveals how to extract orientational information about probe molecules. For example, previous work in our lab has demonstrated that a waveguide fabricated from amorphous polystyrene is three-dimensionally isotropic, in which case three of the four Raman measurements, X(YX)Z, X(ZY)Z, and X(ZX)Z, produced the same scattering activities. For cases with uniaxial chain polymer orientation, the two-dimensionally isotropic alignment of the chains leads to pairs of equivalent Raman measurements with polarized waveguide Raman spectroscopy.⁸

6.1.4 Sol-gel derived waveguide and laser-induced anisotropy

The sol-gel process has been widely used to produce films, waveguides, photonic crystals, insulators, protective and functional coatings, bulk glasses, even cosmetic products.^{9, 10} Most generally, the sol-gel process is an acid- or base-catalyzed polycondensation reaction, often utilizing silicon alkoxides and similar metal alkoxides. These are prepared as represented by the generic reaction:



R can be a latently reactive functional group (vinyl or acrylate) covalently bound to an oxide-forming p-block element, E (usually Si). When R undergoes thermally or photoinitiated propagation, we obtain a hybrid organic-inorganic glass that is inscribed with an increased refractive index localized to the propagating beamwidth, or smaller, of a guided wave. A sol is produced in the early stages of reaction. The sol is a liquid phase with nanoparticles dispersed in the fluid. The nanoparticles can be branched (acid-catalyzed reaction) or roughly spherical (base-catalyzed reaction). The sol eventually converts to a gel phase during spin-coating in the event that one makes an amorphous waveguide. The gel phase is usually consolidated by heating to drive off excess liquid.⁹ The sol-gel process is versatile because it can be modified to create products with different properties. Some examples of tuning the properties of sol-gel derived glass include the introduction of an organic polymer into the sol-gel matrix to increase flexibility of the product, incorporation of gold nanoparticles to create a metallo-dielectric SERS biosensor, and tuning of refractive indexes with rare-earth dopant.^{9, 10}

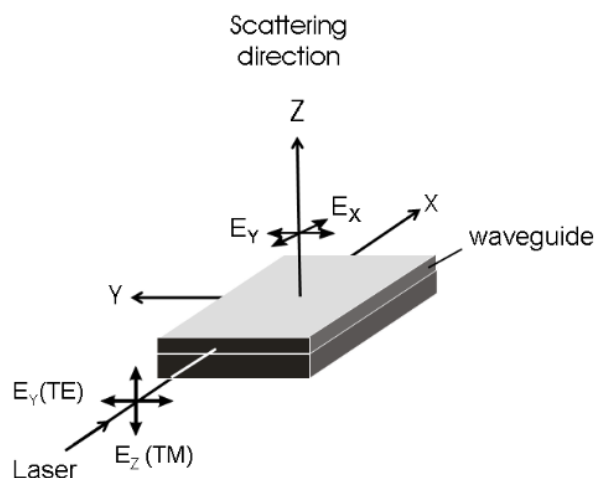


Figure 6.1 Raman scattering geometry illustrating Porto notation. Figure adapted from Kanigan Ph.D. thesis (1995)⁸ Figure 2.7.

Below, we describe our fabrication and guided wave spectroscopy of hybrid organic-inorganic sol-gel glass waveguides and our attempts to induce mode conversion by incorporating magnetite (Fe_3O_4) nanoparticles. Past research in our laboratory^{11 - 14} revealed that the methacrylate moiety of sol-gel polymerized methacryloxypropyl trimethoxysilane would undergo thermal or photo-initiated crosslinking in a guided wave configuration. In some cases, the effect would proceed with an induced anisotropy in the refractive index of the waveguide. With the new custom-built guided wave Raman spectrometer, we first identified mode conversion in our sol-gel films. This is a precondition to benchmark mode conversion in response to the coupling of waveguide modes with the induced magnetic field response on magnetite nanoparticle waveguides. Mode conversion within the waveguides was monitored by polarized Raman spectroscopy. Four incident-and scattered polarizations were examined: X(YY)Z, X(YX)Z, X(ZX)Z, and X(ZY)Z.

6.2 Experimental

6.2.1 MAPTMS sol-gel

With minor modifications, the sol-gel derived glass waveguide was fabricated according to reported procedures.^{8, 15} The starting materials were: 3-(Trimethoxy-silyl) propylmethacrylate (MAPTMS; 98%, 248.35 g/mol, Sigma), zirconium (IV) propoxide solution ($\text{Zr}(\text{OCH}_2\text{CH}_2\text{CH}_3)_4$, 70% in propanol; 327.57 g/mol, Sigma) and methacrylic acid (MAA; $\text{CH}_2\text{C}(\text{CH}_3)\text{COOH}$, 86.09 g/mol, >98%, Sigma). The overall molar ratio of the three chemicals in the sol was 5:2:2.

In one round bottom flask, MAA (1.39 g) was slowly added to zirconium propoxide (7.49 g) in a 1:1 molar ratio. An exothermic reaction occurred to form a zirconium alkoxide complex. In another round bottom flask, HCl solution (0.05 N, 0.54g) was added under vigorous stir into

MAPTMS (10.14 g). This mixture was cloudy at first due to the immiscibility of MAPTMS and water but was cleared in minutes as MAPTMS was hydrolyzed.

After approximately one hour of stirring, the hydrolyzed MAPTMS was added dropwise into the zirconium alkoxide complex. Deionized (DI) water was then added to hydrolyze the suspension further. The amount of water added was up to 0.97g; however, the actual amount differed due to the clumping, or “orange skin” texture, observed when casting the fully hydrolyzed sol into films. The “orange skin” texture was identified as excess hydrolysis by Dr. Oubaha through personal communications. Indeed, the “orange skin” texture was minimized when the water usage was reduced, but the appropriate amount of DI water depends on the moisture level of the ambient environment and must be tested through actual film casting. It was suspected that extra moisture had entered MAPTMS during storage.

The mixture was stirred (400 rpm) in a capped vial wrapped in aluminum foil for about 16 hours. Before film casting, the resulting clear and pale-yellow mixture was filtered through 0.2um syringe filters.

6.2.2 Synthesis of magnetite nanoparticles (MNPs)

MNPs with oleylamine capping agents were synthesized based on a procedure developed by Xu et al. with modifications.¹⁶ 1.095 g of iron(III) acetylacetonate ($\text{Fe}(\text{acac})_3$; 97%, 353.17 g/mol, Sigma) was added to 30 mL of oleylamine. Oleylamine served as the solvent, the reducing agent, and the stabilizing ligand. The reaction mixture was stirred and heated to 120 °C. At 120 °C, the mixture was subjected to at least three cycles of vacuum evacuation followed by an Argon flow. At the end of this process, the reaction mixture was immersed in an Argon atmosphere. The

mixture was further heated to 300 °C at a rate of 200 °C per hour. The mixture was maintained at 300 °C for 1 hour before being removed from the heat. The argon atmosphere was removed once the mixture had cooled to below 80°C. The MNPs were precipitated from the mixture by washing with ethyl acetate and ethanol. The precipitated particles were collected using a magnet bar and air-dried.

The oleylamine-capped nanoparticles underwent ligand exchange with APTES.¹⁷ Under ambient conditions, 0.25 mL of 3-Aminopropyltriethoxysilane (APTES, 99%, 221.37 g/mol, Sigma), 10 mg of the previously synthesized MNPs, and 0.005 mL of acetic acid were mixed in 40 mL of hexane. The mixture was shaken for at least 16 hours, during which the NPs precipitated. The black-brown precipitate was collected using a magnet bar and was washed three times with water by centrifugation.

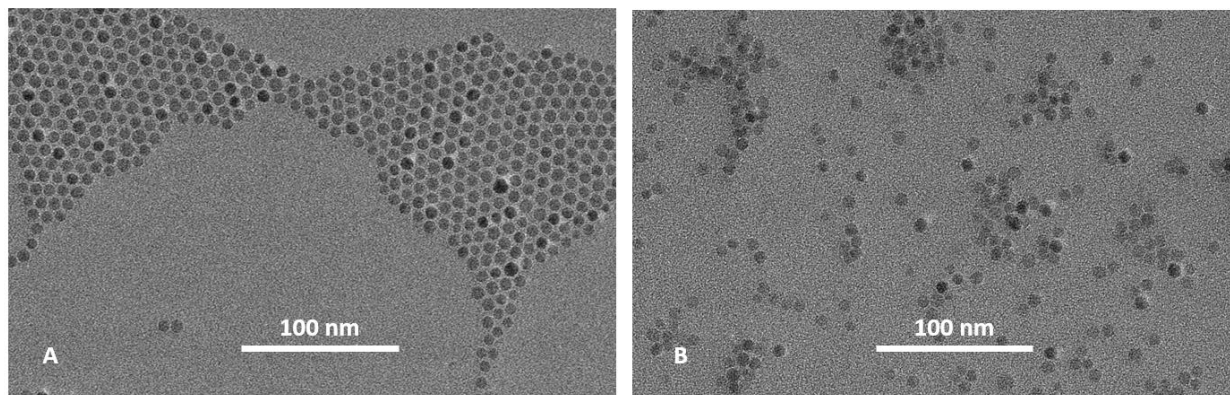


Figure 6.2 Iron oxide nanoparticles with oleylamine (A) and APTES (B) capping agents. The MNPs are approximately 9 nm in diameter.

6.2.3 Incorporation of magnetite nanoparticles (MNPs) into the sol

The as-synthesized MNPs were re-dispersed in a small amount of water (approximately 20 μL of water for 10 mg of MNPs) in order to mix with the acidic sol for sol-gel casting. Four MNP concentrations in the sol were tested: 3.07 mg/mL, 1.53 mg/mL, 1.18 mg/mL, and 0.7 mg/mL.

6.2.4 Fabrication of sol-gel derived (laser poled) waveguides

Spin coating was accomplished using a Laurell WS400-LITE spin coater. For each waveguide, an appropriate amount of the as-prepared sol was pipette-delivered onto an acid-cleaned fused silica microscope slide (Alfa Aesar, fused). The sol was spread across the surface of the fused silica slide before being spin-coated at 1200 rpm for 20 seconds. The wet film was subsequently baked at 100 °C for 30 minutes and then dried at room temperature in air for at least 4 hours. The film thickness was not measured due to imposed Covid-19 restrictions and limited instrument access during the time of the experiment. The approximate film thickness is 1 μm based on previous experiments in our lab.⁸

Each waveguide was poled by TE+TM polarization (turning of the half-wave plate by 22.5°) at approximately 55 mW for at least 2 hours. Polarized Raman spectra of the same coupling location were then collected, as described in Chapter 4.

6.2.5 Applied magnetic field

An applied magnetic field was achieved by inserting a NdFeB bar magnet (type BX8X84 1.5" x 1.5" x 0.25" thick nickel plated; K&J Magnet Inc.) directly behind the waveguide, between

the poles for the prism holder (Chapter 4, Figure 4.2). The magnetic field lines coming out of the permanent magnet are orthogonal to the plane of the waveguide at the center of the magnet. Towards the edges of the magnet, the field lines bend over into a circular shape to meet with the opposite pole.

6.2.6 Photographs of the coupling waveguides

Photographs of the coupling waveguides were taken during the collection of Raman measurements using a cellphone camera. Two sets of photographs were taken. One set was taken with just the cellphone camera, and the other set was taken using the cellphone camera through the protective lens of laser safety glasses (LG12; Thorlabs), which greatly reduced the transmission of light at 532 nm. The coupling and propagation of light within the waveguide have a high concentration of light. Reducing the transmission of light helps to differentiate between waveguide couplings from scattered light.

6.3 Results and Discussion

6.3.1 sol-gel derived waveguide with no incorporated MNPs: Sol-gel glass waveguide with isotropic refractive index

Figure 6.3 shows the Raman spectra of the as-derived hybrid sol-gel glass waveguide. The sample was thermally cured but had not been subjected to polarization-induced anisotropy (PIA, or “poling” as described in the previous work by our lab⁸) by the guided wave. The signature Raman band for the C-H vibrations in the range of 2800 – 3200 cm^{-1} shows different band profiles

when different combinations of input and output analyzer orientations (denoted by the Porto notation) are used. Specifically, the X(YY)Z spectrum is strongly polarized, having a substantially more intense signal than do the other three spectra, which show less intense peaks but self-similar Raman profiles. The sol gel comprising the waveguide in this case is an isotropic glass. By definition, the refractive index is isotropic. For an isotropic refractive index the scattering activities for the different combinations of polarizer and analyzer predict that the three spectra obtained from the combinations X(YX)Z, X(ZX)Z, and X(ZY)Z will be identical.⁸ This is what we observed.

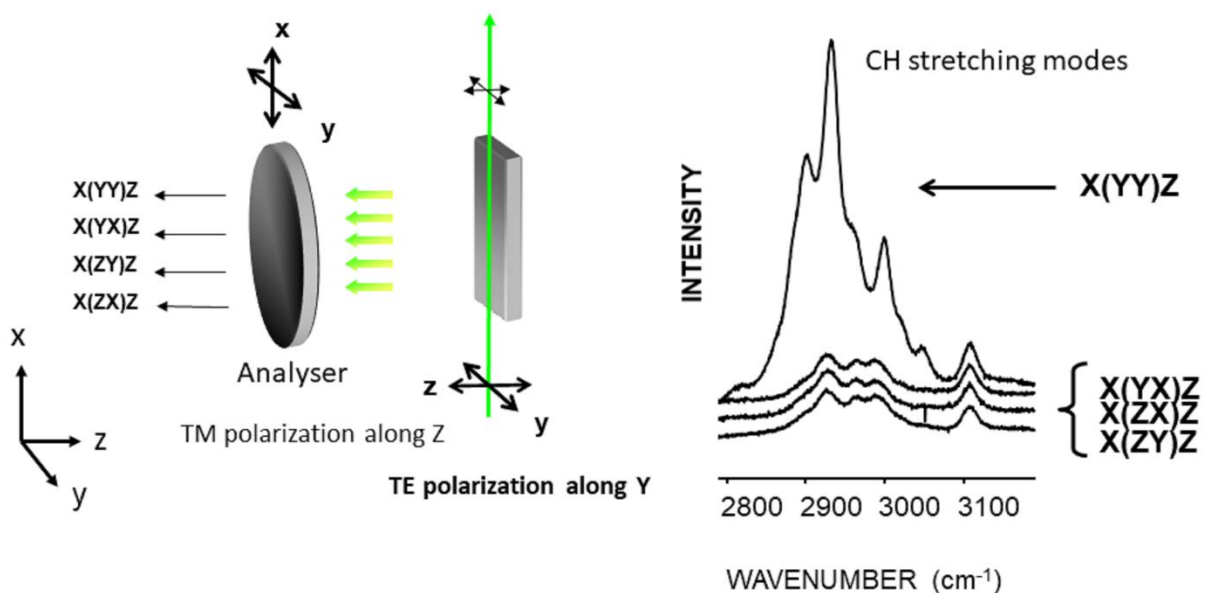


Figure 6.3 Right-hand image shows the guided wave Raman spectra in the C-H stretching region of the hybrid organic-inorganic waveguide (no MNPs) for four different acquisitions of polarizations according to the Porto notation. The left-hand image shows the waveguide, input polarization, and analyzer configurations in the laboratory frame of reference. The combinations of input and output analyzer orientations are given according to their corresponding Porto

notation. Note how the X(YY)Z spectrum is strongly polarized and that the remaining three spectra are similar, according to predictions from the scattering activities.

6.3.2 Sol-gel glass waveguide with polarization induced anisotropy

In this experiment, anisotropy was introduced to the hybrid sol-gel waveguide by “poling” with TE+TM polarization for approximately 2 hours with approximately 55 mW of external laser power (measured at the coupling prism hypotenuse), following a procedure described in previous work by Kanigan.⁸ In this case, the laser was polarized TE+TM by adjusting a half-wave plate to 22.5°. Note that this experiment “writes” a spatially localized poled waveguide inside the slab waveguide. The refractive index of the surrounding cladding is isotropic, but the index in the self-written waveguide is anisotropic. We then lowered the laser power to acquire the Raman spectrum of the poled self-written waveguide in the range of 700 – 3500 cm⁻¹. The result with unpolarized light is shown in Figure 6.4. The Raman modes in Figure 6.4 are assigned based on previous work.^{8, 18} We can observe that the deformation modes (δ) are located at 1458 cm⁻¹ or below, while the stretching modes (ν) are above 1600 cm⁻¹. The prominent “fingerprint” band at 2800 – 3200 cm⁻¹ has the highest CCD intensity count and is an area of interest for further analysis using input and output polarized Raman. This area contains several overlapping C-H symmetric and asymmetric stretching modes. The goal of using polarized Raman is to differentiate the behavior of these modes in different polarizations according to the Porto notation. Polarized Raman spectra were collected at the same coupling location, as described in Chapter 4.

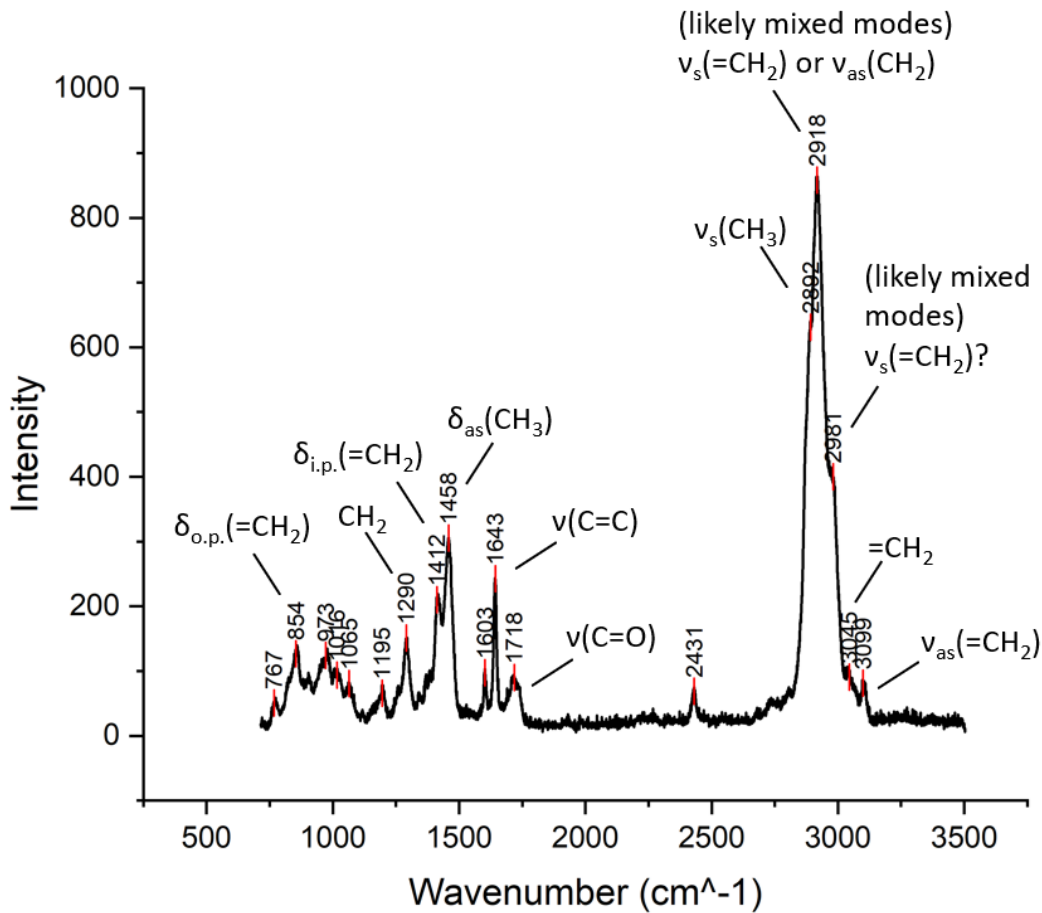


Figure 6.4 Raman spectrum of the uncured hybrid sol-gel waveguide after the introduction of anisotropy using the technique of TE+TM laser poling. The Raman spectrum is not polarized.

6.3.3 Raman optical “read” in C-H fingerprint region of induced anisotropy in the refractive index of the self-inscribed waveguide

Figure 6.5 (black line) reveals the CH-stretching “fingerprints” in the 2800-3200 cm^{-1} range for each of the X(YY)Z, X(YX)Z, X(ZY)Z, X(ZX)Z polarizations. Unlike the C-H fingerprint region for the “unpoled” waveguide shown Figure 6.3, the same Raman region of the

poled waveguide clearly shows different Raman profiles for the different combinations of input polarization and output analyzer. From Figure 6.5, the X(YY)Z spectrum arises from the highest CCD count intensity among the four polarized waveguide Raman spectra and is the most polarized. The $\nu_{as}(CH_2)$ mode at 2925 cm^{-1} is the most intense C-H stretching mode for X(YY)Z, and it remains the most prominent mode in X(ZY)Z spectrum. However, the $\nu_{as}(CH_2)$ mode becomes less intense in the X(YX)Z and X(ZX)Z spectra as the comparative intensities of the $\nu_{as}(CH_3)$ and $\nu_s(=CH_2)$ modes increase. Similarly, the $\nu_s(CH_3)$ mode at 2894 cm^{-1} , which has high intensity in the X(YY)Z and X(ZY)Z spectra, only appears as weak shoulders in the X(YX)Z and X(ZY)Z spectra with greatly diminished intensity. The X(YX)Z and X(ZX)Z spectra also express evidence of a more intense $\nu_{as}(=CH_2)$ mode at 3099 cm^{-1} than do the X(YY)Z and X(ZY)Z spectra.

The X(ZY)Z spectrum has acquired polarized character characteristic of the X(YY)Z orientation as a result of poling the sol-gel waveguide. Comparing the X(ZY)Z spectrum in the same region in Figure 6.3 with that in Figure 6.5, the presence of TE character in the X(ZY)Z spectrum confirms mode mixing caused by refractive index anisotropy “written” in the waveguide in the path of the laser beam.

The Raman spectral patterns of Figure 6.5 confirm mode mixing. By simultaneously exciting TE and TM modes, the waveguide film is exposed to a net electric field in the xz-plane at some angle to the y-axis. In this case, a refractive index change along the polarization direction generates off-diagonal dielectric tensor elements. When the laser power is reduced to collect the Raman spectra, these off-diagonal elements persist. They cause the TE-TM mode conversion that is observed in the Raman spectra.

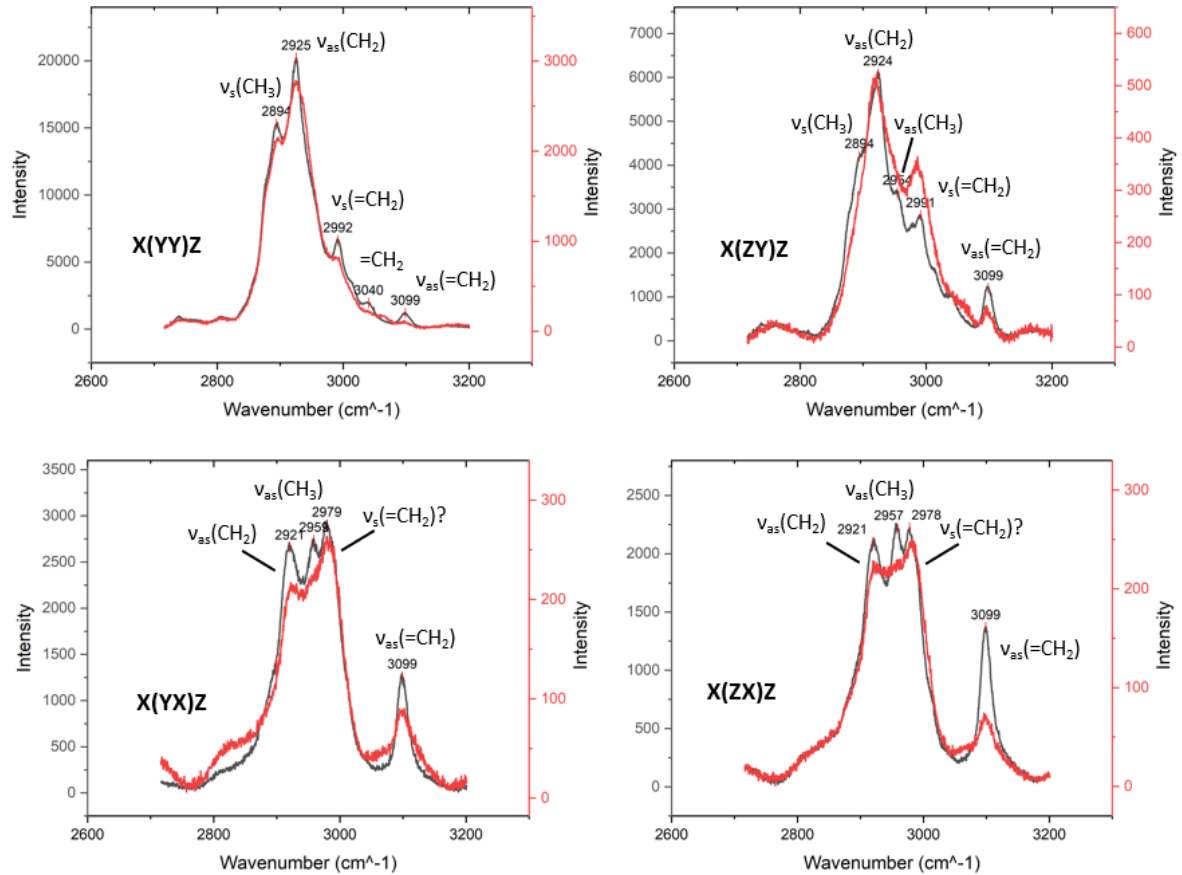


Figure 6.5 Polarized waveguide Raman spectra of the CH stretching region of a sol-gel derived waveguide, uncured and TE+TM poled. The Porto notation is indicative of the polarization of each spectrum. The black line shows spectra of the poled waveguide in the absence of MNPs, while the red line shows spectra of the poled waveguide with MNPs. Band position and mode assignment are labeled for the sol-gel waveguide without MNPs (black).

6.3.4 MNP doped sol-gel glass waveguide with polarization induced anisotropy

6.3.4.1 Problem of optical loss in gyrotropic sol-gel glass waveguides

Guided wave Raman spectra were gathered from a set of nanocomposite MNP waveguides comprising 0.7, 1.18, 1.53 and 3.07 mg/ml sol of Fe₃O₄ nanoparticles. Figure 6.6 shows a series

of photographs of the slab waveguides and the guided mode streaks in bright green that were imaged onto the detector. Though difficult to discern from these images, the streaks attenuate systematically from left to right in order of increasing loadings of the MNPs. Raman spectra were only obtainable for the waveguide made with 0.7 mg/ml sol of MNPs. This is because of the strong extinction of the laser beam caused by optical absorption and scattering by the absorbing (black) MNPs.¹⁹ In the language of optics, magnetite MNPs induce “optical limiting”, where the magnetite inclusions strongly attenuate the optical beam to a threshold level at high laser intensity whilst exhibiting linear transmittance at low intensity. Furthermore, the APTES ligands covering the surface of MNPs, despite providing adequate miscibility for MNPs to suspend in sol-gel, did not allow uniform dispersion of the MNPs. Aggregation of the MNPs in the sol-gel derived waveguide can result in greater light attenuation, not just by absorption but also by scattering. In our case, optical limiting clearly diminished our capacity to study mode conversion as a function of MNP loading.

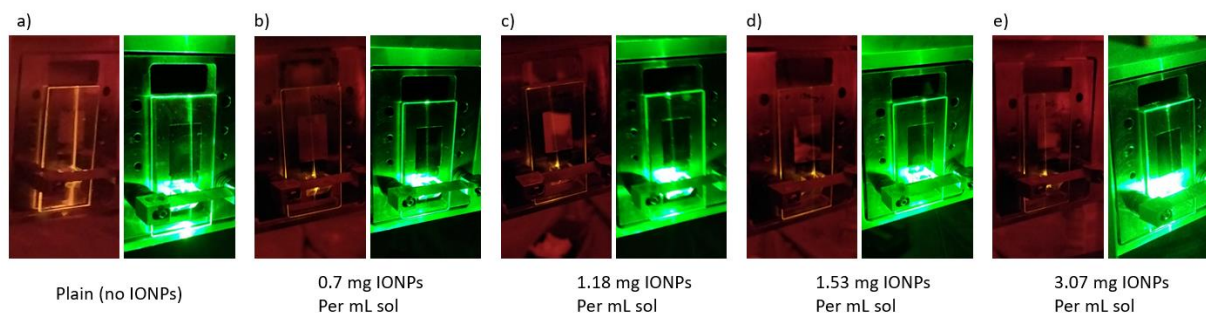


Figure 6.6 Photographs of light propagating in sol-gel waveguides. Two versions were taken for each waveguide. The red-tinted photos were taken through the lens of LG12 laser safety glasses, which filter green light that is scattered. It can be observed that doping with MNPs

significantly increases the attenuation of green light in the waveguide. The higher the concentration of incorporated MNPs, the higher the attenuation.

6.3.4.2 Poled gyrotropic MNP sol-gel waveguide

A hybrid organic-inorganic sol was doped with 0.7 mg of magnetite nanoparticles. The composite was spin-coated and thermally cured to produce a slab waveguide. The sample was then poled as described in the Experimental section. Poling created a permanent spatially localized self-written nanocomposite gyrotropic waveguide within the slab waveguide. We proceeded to gather four polarized waveguide Raman spectra in the 3000 cm^{-1} CH stretching region of the poled waveguide. The poled spectra from the nanocomposite are shown in Figure 6.5 overlaid in red on the black spectral features obtained from the poled waveguide without MNPs. Note that the Raman counts in red on the right-hand vertical axis are substantially lower due to waveguide absorption loss

The strongly polarized X(YY)Z spectrum is characteristically the most intense in both cases for the doped and undoped waveguides. The peak shape of the X(YY)Z spectrum for the MNP waveguide is similar to that of the waveguide without MNPs. Dissimilarities are more evident for the X(ZY)Z, X(ZX)Z, and X(YXZ) spectra. In the X(ZY)Z spectrum, the MNP waveguide yielded a less intense $\nu_s(\text{CH}_3)$ mode at 2894 cm^{-1} and a more intense $\nu_s(=\text{CH}_2)$ mode at 2991 cm^{-1} . For the X(ZX)Z and X(YX)Z polarizations, the MNP waveguide showed decreased intensities in the $\nu_{as}(\text{CH}_2)$, $\nu_{as}(\text{CH}_3)$, and $\nu_{as}(=\text{CH}_2)$ modes at 2921 cm^{-1} , 2957 cm^{-1} , and 3099 cm^{-1} , respectively. The reduction in intensities suggests that the asymmetric stretching modes of CH_2 , CH_3 , and $=\text{CH}_2$ are less active in the MNP incorporated waveguide.

6.3.4.3 Polarized Raman spectra after an applied magnetic field orthogonal to the waveguide plane

A bar magnet was attached to the back of the waveguide to try to induce mode mixing. The magnet generates a magnetic field orthogonal to the plane of the waveguide at the center of the magnet. Figure 6.7 (A) contains four polarized spectra, X(YY)Z, X(YX)Z, (XZY)Z, and X(ZX)Z of the CH stretching region of the poled nanocomposite MNP waveguide with an applied magnetic field (red line) and without the applied field (black line). These Raman spectra showed that an applied magnetic field does not result in mode conversion. However, these spectra are the average of all Raman signals over a propagation distance. To better examine whether changes have occurred during propagation, distance resolved Raman measurements (along the x-axis) were obtained for the X(YY)Z polarization, which offers the best signal-to-noise ratio, and focus on the CH stretching region.

The CCD was set in “camera” mode to gather Raman spectra from the waveguide streak with spatial resolution along the propagation x-axis, beginning at the coupling prism edge and evolving away from it. This strategy allows one to “watch” and map polarization mode conversion, should it occur along the path of the streak, beginning at the coupling edge. Accordingly, the detector pixel matrix was binned to achieve spatial resolution along the direction of the propagating guided wave. We gathered 10 spectra starting from the source (prism edge position 1) to the terminus (position 10). Figure 6.7 (B) shows the distance (spatially) resolved Raman spectra in the CH stretching region for the totally polarized X(YY)Z orientation of the nanocomposite MNP waveguide. In spectrum b), a magnetic field was then applied orthogonal to the plane of the waveguide. This setup differs from the conventional Faraday configuration, where the magnetic field is applied in the x (longitudinal) direction. Close examination of the spectra reveals small differences. Comparing positions 1 and 2 in Figure 6.7 (B-a) and (B-c), we can observe a shift in

the initial intensity of the propagation streak after the magnet is applied. Although both distance-resolved spectra show that propagation intensity quickly diminished, likely due to the attenuation of the MNPs, the spectrum with an applied magnetic field has slightly increased intensity compared to the spectrum without an applied magnetic field.

Figure 6.7 (C) is similar to Figure 6.7 (B), but for the distance (spatially) resolved Raman spectra in the X(YY)Z CH stretching region for the waveguide without MNPs. In the presence of the applied field, the number of counts drops from a maximum of ~2800 (no applied magnetic field) to less than 1750 counts when the magnetic field is applied. This might suggest that intensity for the fully polarized mode peaking at ν_s (CH₂) 2925 cm⁻¹ is “partially siphoned off” to the X(ZY)Z, perhaps representing some manifestation of mode conversion. As interesting as the finding is, we cannot at this stage rule out random errors, including in-plane and out-of-plane scattering by MNP aggregates, that might lead to a false reading for mode conversion.

There are two reasons why we might not see evidence of TE-TM mode conversion when focusing on the X(YY)Z polarization combination. In the first case, the ν_{as} (CH₂) 2925 cm⁻¹ mode overwhelms all other modes in intensity. Small changes in the intensity of this mode (parasitic losses to TM polarization) might go unnoticed. To remedy this problem, distance resolved Raman measurements should also be performed in the X(ZY)Z polarization. X(ZY)Z polarization is TM in origin and has demonstrated mode changes as the electric field vector rotates from TE to TM orientation via laser polarization poling.

Secondly, it is unlikely that there is a persistent (remanent) magnetic field in the nanocomposite waveguide. The total magnetic spin vector of the individual superparamagnetic nanoparticles can fluctuate through 2π radians because the barrier to spin rotation/randomization (Néel transition) is well below the mean thermal energy of the waveguide. This means there is not

likely to be any permanent (remnant) magnetic field inside the waveguide. Moreover, we would not expect a particular alignment of any residual magnetism since the nanoparticles were not oriented in a magnetic field during the curing of the waveguide (see future work below). At this point in time, we do not know if the nanoparticles have spontaneously aligned themselves in chains or other types of aggregates. If kinetically trapped in the glass, it is possible that some aggregates might manifest a persistent magnetism (remnant magnetism), much as occurs in magnetotactic bacteria.²⁰

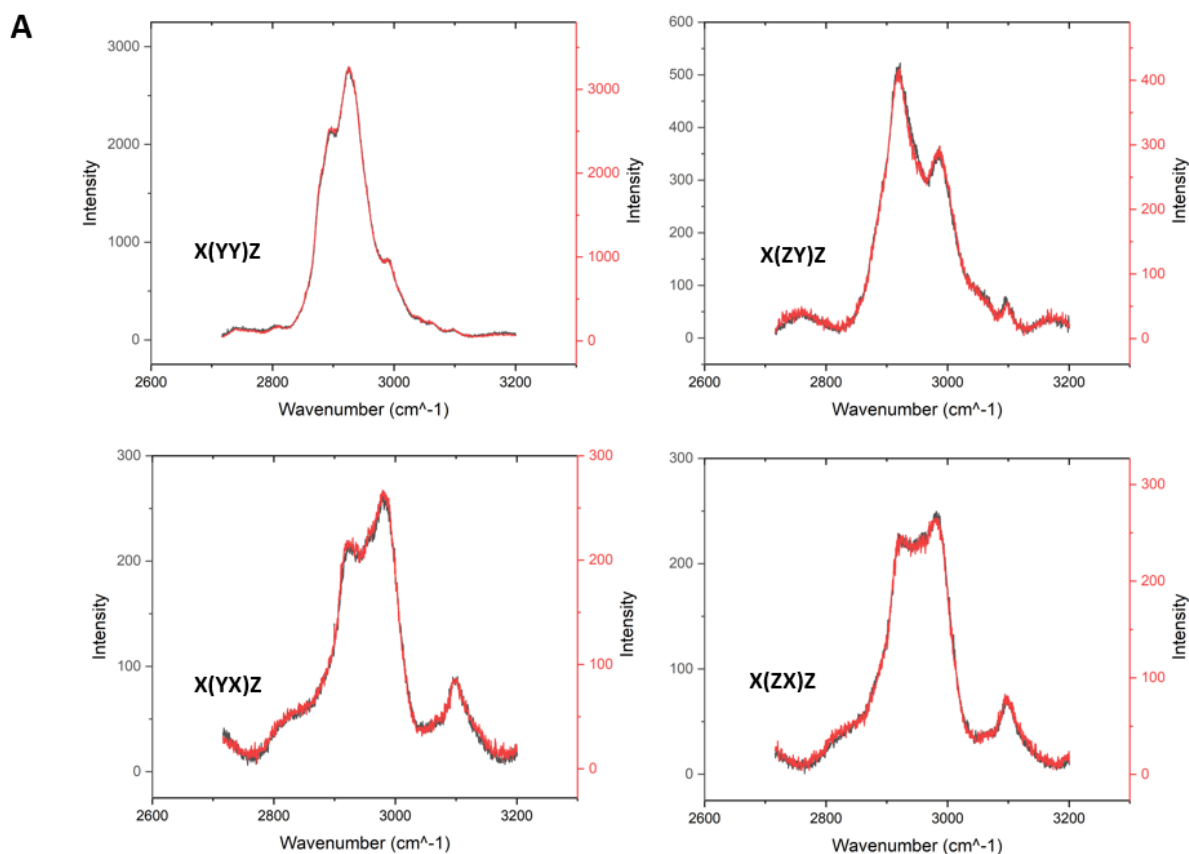


Figure 6.7 (A) The red line shows the four polarized spectra of the C-H stretching region of the MNP incorporated, uncured and TE+TM poled, sol-gel derived waveguide with an applied

magnetic field orthogonal to the waveguide plane. The red spectra are overlaid onto the polarized spectra of the same poled MNP waveguide without an applied magnetic field (black line).

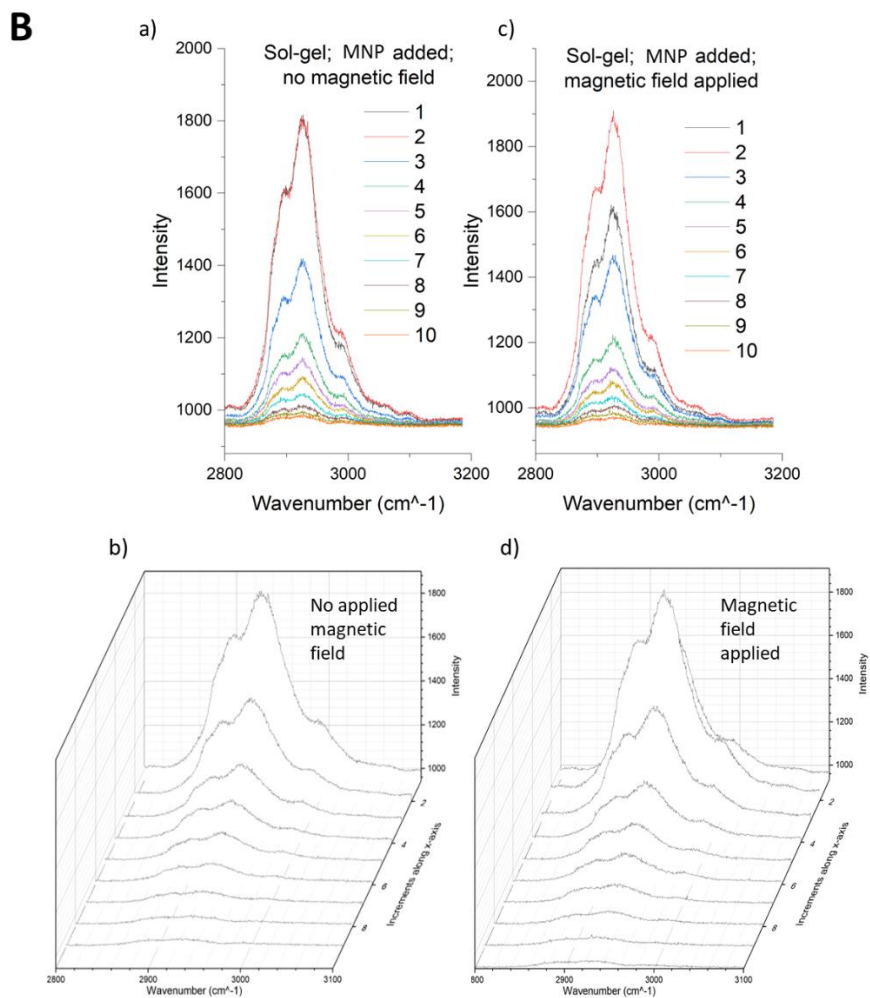


Figure 6.7 (B) Distance resolved Raman measurements (along the x-axis) of X(YY)Z focusing on the CH stretching region of the sol-gel derived waveguide, poled, with incorporated MNPs. No external magnetic field was applied for spectra **(B-a)** and **(B-b)**. An external magnetic field was applied by inserting a bar magnet for spectra **(B-c)** and **(B-d)**.

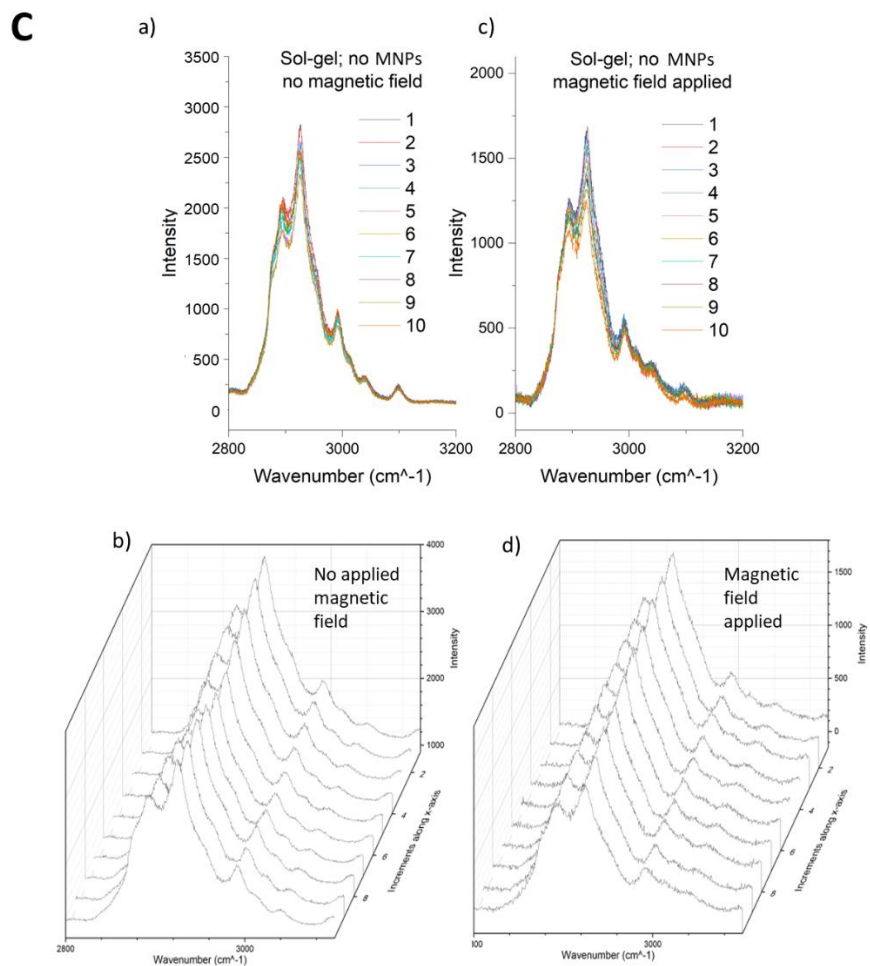


Figure 6.7 (C) Distance resolved Raman measurements (along the x-axis) of X(Y_Y)Z focusing on the CH stretching region of the sol-gel derived waveguide, poled, without incorporated MNPs. No external magnetic field was applied for spectra (C-a) and (C-b). An external magnetic field was applied by inserting a bar magnet for spectra (C-c) and (C-d).

6.3.5 Recommendations for future experiments

Here we suggest how to formulate new experiments that might clarify the possibility of mode-changing phenomena under the influence of an external magnetic field. The current limitations are:

- The magnetic field was applied by inserting a bar magnet directly adjacent to the waveguide holder, which was magnetically susceptible. The motion of inserting this magnet, as well as the attractive force imposed by the magnet, can induce small changes to the coupling of the waveguide, which could directly affect light propagation.
- The MNPs employed in this experiment were capped with APTES ligands. Although APTES ligands allowed MNPs to disperse in the sol-gel medium, the dispersion was ununiform, and aggregation was observed. Although MNPs are optically limiting as per their light attenuation property, reducing the aggregation of MNPs may help with lessening the light attenuation and provide a longer optical path for the propagating light. The possible mode change phenomenon due to an applied magnetic field can be minute in nature. Replacing the ligand can decrease light attenuation and increase the length of the propagating streak, and this can lead to better resolutions for polarized Raman spectra. In addition, replacing the ligand may allow for incorporating a higher concentration of MNPs. A high MNP concentration can also increase any possible magnetically-assisted effects.
- Mode conversion in a waveguide occurs when there is coupling between pairs of off-diagonal dielectric tensor elements (mode degeneracy) present simultaneously for both the TE and TM modes. Parameters such as the refractive index, the thickness of the waveguide film, and the chosen coupling angle (propagation constant) determine the

modes that are allowed in a waveguide, therefore also affecting mode degeneracy. The film thickness need to be accurately determined to achieve optimal waveguide design and quality control.

- A possible magnetically induced mode-changing event can be subtle. As a result, it may be the best to induce such as phenomenon using a waveguide containing no previously induced anisotropy. The reason is that preexisting anisotropies, such as those caused by laser poling, would also produce mode changes that may interfere with the potential magnetically-induced mode-changing effects.
- Spatially-resolved Raman spectroscopy should be performed with other polarizations as well as X(YY)Z. The dominant ν_{aS} (CH₂) mode at 2925 cm⁻¹ in X(YY)Z could mask the TE-to-TM conversion as TM polarizations result in lower intensity modes. The obscuring effect can be magnified when accompanied by the light attenuation effect by the incorporated MNPs, as both would lead to reducing mode intensities.

6.4 Conclusion and Future work

In this chapter, we confirmed the ability of polarized Raman spectroscopy to detect changes in light propagation mode. Our data from previous experiments showed that the uncured, unpoled sol-gel derived waveguide produced two distinct sets of polarized Raman spectral patterns, one for X(YY)Z polarization, another shared by X(YX)Z, X(ZX)Z, and X(ZY)Z polarizations. The two sets of polarized Raman spectral patterns are the signature of an isotropic waveguide. In this experiment, waveguide anisotropy was first induced by subjecting the waveguide to TE+TM laser poling. The poling led to thermally activated crosslinking of acrylate moieties in the glass, which

raised the local refractive index. This laser-induced anisotropy resulted in mode changes detectable by polarized Raman spectroscopy. Instead of producing two sets of spectral patterns typical of an isotropic medium, three distinct sets of spectral patterns are produced for the poled waveguide: one for X(YY)Z, one for X(ZY)Z, and one shared by X(YX)Z and X(ZX)Z.

In the next step, APTES-ligand-coated MNPs were incorporated into the uncured, laser-poled sol-gel waveguide. It was found that the incorporation of MNPs into waveguides indeed changed the propagation profile of guided waves. The presence of MNPs greatly attenuated light propagation due to absorption and scattering. In addition, the incorporation of MNPs seemingly disrupted the alignment of polymers inside the waveguide medium. The resulting polarized Raman spectra showed similar peak shapes as the spectra for waveguide without incorporated MNPs, with exceptions for some Raman modes, such as the $\nu_s(\text{CH}_3)$ and $\nu_s(=\text{CH}_2)$ modes for X(ZY)Z, and the $\nu_{as}(\text{CH}_2)$, $\nu_{as}(\text{CH}_3)$, and $\nu_{as}(=\text{CH}_2)$ modes for X(YX)Z and X(ZX)Z.

This chapter further explored the potential of inducing mode-changing behaviors by applying an external magnetic field to light propagating in an MNP-incorporated, TE+TM poled, sol-gel derived waveguide. The regular polarized Raman spectra, which averaged all signals across the span of light propagation, showed no difference in spectral patterns before and after applying an external magnetic field for all four polarizations. The distance-resolved Raman spectrum for X(YY)Z also produced similar spectral patterns before and after an applied magnetic field. Still, some fluctuations in the spectra may indicate underlying mode-changing activities. Limitations such as the physical placement of the magnet bar, light attenuation due to partly aggregated MNPs in the waveguide, interference due to preexisting anisotropy in the waveguide, and lack of data from other polarizations for distance-resolved polarized Raman, may have prevented us from

clarifying the possible magnetically-induced mode change phenomenon. Whether an applied magnetic field can induce mode changes in light propagation remains inconclusive.

For future experiments, the experimental apparatus should be redesigned in a way such that the magnetic field can be applied from an external structure to minimize its interference with waveguide coupling. The MNPs and their surface ligand can also be redesigned. Optimal materials for the MNPs should be highly magnetic to reduce the MNP concentration in the waveguide, while optimal ligands for the MNPs should opt to achieve uniform particle dispersion inside the waveguide medium. Accurately determining the film thickness helps to optimize the sol-gel waveguide design. In addition, the experiment on magnetically induced mode changing phenomenon should be performed on uncured, un-poled waveguides to minimize interference from preexisting anisotropies. The distance resolved polarized Raman spectra of different polarizations should be obtained to provide verifications to possible TE-TM conversions.

6.5 References

1. Tao, Z., 2004. Effect of magnetic field of light on refractive index. *Chinese Physics*, 13(8), p.1358.
2. Berman, P.R., 2010. Optical faraday rotation. *American Journal of Physics*, 78(3), pp.270-276.
3. Hocini, A., Boumaza, T., Bouchemat, M., Royer, F. and Rousseau, J.J., 2010. Phase matched magneto optical single mode rib waveguides based on geometrical adjustments. *AEU-International Journal of Electronics and Communications*, 64(11), pp.1042-1045.
4. Amata, H., Royer, F., Choueikani, F., Jamon, D., Parsy, F., Broquin, J.E., Neveu, S. and Jacques Rousseau, J., 2011. Hybrid magneto-optical mode converter made with a magnetic nanoparticles-doped SiO₂/ZrO₂ layer coated on an ion-exchanged glass waveguide. *Applied Physics Letters*, 99(25), p.251108.
5. Bouras, M. and Hocini, A., 2016. Mode conversion in magneto-optic rib waveguide made by silica matrix doped with magnetic nanoparticles. *Optics Communications*, 363, pp.138-144.
6. Chung, S.K. and Kim, S.S., 1988. An exact wave-optics analysis of optical waveguide with anisotropic and gyrotropic materials. *Journal of applied physics*, 63(12), pp.5654-5659.
7. Tanaka, M. and Young, R.J., 2006. Review Polarised Raman spectroscopy for the study of molecular orientation distributions in polymers. *Journal of Materials Science*, 41(3), pp.963-991.
8. Kanigan, T. 1995. *Integrated optics spectroscopy of polymer thin films*. Ph.D. thesis. McGill University. Montreal.

9. Gvishi, R., 2009. Fast sol–gel technology: from fabrication to applications. *Journal of Sol-Gel Science and Technology*, 50(2), pp.241-253.
10. Chiappini, A., Chiasera, A., Berneschi, S., Armellini, C., Carpentiero, A., Mazzola, M., Moser, E., Varas, S., Righini, G.C. and Ferrari, M., 2011. Sol–gel-derived photonic structures: fabrication, assessment, and application. *Journal of Sol-Gel Science and Technology*, 60(3), pp.408-425.
11. Saravanamuttu, K., Du, X.M., Najafi, S.I. and Andrews, M.P., 1998. Photoinduced structural relaxation and densification in sol-gel-derived nanocomposite thin films: implications for integrated optics device fabrication. *Canadian Journal of Chemistry*, 76(11), p.1717.
12. Saravanamuttu, K. and Andrews, M.P., 2000, May. Photo-oriented polymerization in hybrid glass waveguides. In *Sol-Gel Optics V* (Vol. 3943, pp. 53-57). SPIE.
13. Andrews, M.P., Belanger, N., Duxin, N., Maron, E., Lofgreen, J., Djeghelian, H., Shan, G., Manseau, M.P., van Veggel, F.C.J.M. and Fu, S.W., 2007, October. Light-induced self-inscription (LISI) in nanocomposite network glasses. In *Photonics North 2007* (Vol. 6796, pp. 529-537). SPIE.
14. Andrews, M.P., Belanger, N. and Fu, S.W., 2005, September. Optical self-inscription in waveguides and pattern formation in sol-gel derived nanophase organo-silica films. In *Complex Mediums VI: Light and Complexity* (Vol. 5924, pp. 131-137). SPIE.
15. Oubaha, M., Smahi, M., Etienne, P., Coudray, P. and Moreau, Y., 2003. Spectroscopic characterization of intrinsic losses in an organic–inorganic hybrid waveguide synthesized by the sol–gel process. *Journal of Non-Crystalline Solids*, 318(3), pp.305-313.

16. Xu, Z., Shen, C., Hou, Y., Gao, H. and Sun, S., 2009. Oleylamine as both reducing agent and stabilizer in a facile synthesis of magnetite nanoparticles. *Chemistry of Materials*, 21(9), pp.1778-1780.
17. De Palma, R., Peeters, S., Van Bael, M.J., Van den Rul, H., Bonroy, K., Laureyn, W., Mullens, J., Borghs, G. and Maes, G., 2007. Silane ligand exchange to make hydrophobic superparamagnetic nanoparticles water-dispersible. *Chemistry of Materials*, 19(7), pp.1821-1831.
18. Bersani, D., Lottici, P.P., Tosini, L. and Montenero, A., 1999. Raman study of the polymerization processes in trimethoxysilylpropyl methacrylate (TMSPM). *Journal of Raman spectroscopy*, 30(11), pp.1043-1047.
19. Singh, C.P., Bindra, K.S., Bhalerao, G.M. and Oak, S.M., 2008. Investigation of optical limiting in iron oxide nanoparticles. *Optics Express*, 16(12), pp.8440-8450.
20. Moskowitz, B.M., Frankel, R.B., Flanders, P.J., Blakemore, R.P. and Schwartz, B.B., 1988. Magnetic properties of magnetotactic bacteria. *Journal of Magnetism and Magnetic Materials*, 73(3), pp.273-288.

Chapter 7

Summary of findings and suggestions for future research

7.1 Summary of chapters

The research undertaken in this thesis explores interfaces of magnetic and plasmonic particles at the nanoscale. Part one of this thesis, Chapter 2, details physical and chemical changes to magnetic iron particles in two classes of “smart” magnetorheological fluids (MRFs) formulated from iron microparticles and hosted in different carrier fluids for use in a prototype avionic rotary clutch. Hydrocarbon and fluorocarbon fluids containing carbonyl iron microparticles were aligned in a magnetic field and subjected to shear forces under various operating conditions. Oxidation under shear was postulated to be an important feature of MRF failure in the clutch over time. We carried out a detailed analysis of the Fe(0) microparticle surfaces with TEM, SEM, surface XPS, and XPS depth profiling. Our studies revealed some key outcomes of frictional shear force interactions at the interface between the iron particles and the carrier fluids that contribute to degradation. In hydrocarbon MRFs, we detected iron oxide surface layers encapsulating the core Fe(0) microparticles. FeF₂ appeared as the predominant species at the surface of Fe(0) microparticles aged in perfluoro-polyethers. In both carrier fluids, surface coarsening was observed, together with evidence that collisions among iron particles under shear change the surface topography to produce nanoparticles through cracking and erosion of the surface layers. Accompanying these chemical changes at the surface iron particles, outgassing was observed during the shearing operation of the clutch. Magnetization measurements appear to be rather

insensitive to changes in the magnetic properties of the fluids, but oxidation at the nanoscale, and the physical consequences of microparticle wear, provide more sensitive insight and important evidence that nanoscale transformations are important components of MRF aging. Knowledge of the physical-chemical processes leading to oxidation at microparticle nanoscale surfaces can be used to design and improve the formulation of smart fluids beyond avionics and into the realms of automotive, medical prosthetics, robotics and body armor.

In part two of this thesis, in Chapter 3, we investigate the fabrication of cryogel porous scaffolds by unidirectional freezing of carboxylated cellulose nanocrystal (CNC) and magnetic iron oxide nanoparticle-grafted CNC (MNP-CNC). In some cases, we supplemented the hydrodynamic unidirectional flow field with a static magnetic field. Host factors influence the pore morphology of the cryogel scaffolds. These factors include the presence/absence of MNPs, freezing temperature, freezing mode, and an applied static magnetic field during freezing. Freezing temperatures caused the most notable changes to the macroscopic morphology of the scaffolds: high freezing temperatures resulted in large, unoriented pores, whereas low freezing temperatures resulted in lamellar, oriented pores. The combination of high-temperature cryogelation and low-temperature freezing produced intermediate scale elongated pore morphologies. Incorporation of MNPs affected freezing by reducing the extent of freezing at high freezing temperatures, possibly through destabilizing the hydrogen bonds in water. To study the nanoscopic structures and water sorption properties of the cryogel scaffolds, small-angle x-ray scattering (SAXS) and dynamic water sorption (DVS) were employed. Fitting of the SAXS data revealed that grafting of MNPs onto the CNC crystals led to a more compact arrangement of CNC polymer chain nanofibers which assemble to enhance the densification of the individual nanocrystals. DVS data indicated that this

densification correlates with lower BET surface area and lower water sorption in the resulting cryogel scaffolds.

The third part of this thesis introduces a nanoscale sensing technique that combines the rudiments of integrated optics with guided wave polarized Raman spectroscopy. Chapter 4 describes the integrated optics guided wave Raman spectrometer that was constructed for experiments detailed in Chapters 5 and 6. The setup allows quantitative mode selected polarized Raman spectroscopy in thin films and at interfaces. The selection of transverse magnetic (TM) or transverse electric (TE) waves allows one to interrogate components of the Raman polarizability tensor to reveal detailed information about chemical species in confined regions below the diffraction limit of conventional lens configurations and classic free-space Raman scattering geometries. Mode selection permits the experimentalist to excite discrete eigenmodes of the waveguide and thus to control the location of the field intensity. The use of the waveguide construct in combination with a CDD detector permits acquisition of spatially resolved Raman spectra without the need for moving parts like optical scanners or piezoelectric driven near field scanning probe optical fiber tips. We introduce the notion of an Optical Chemical Bench. The OCB is a slab waveguide circuit element that can be systematically modified to build up hierarchies of nanoscale matter. The OCB is therefore co-opted as a passive waveguide autoscopic element that reveals information about chemical and physical interactions within itself. In the simplest version of the OCB, we use thick film waveguides as multi-mode substrates for evanescent field Raman scattering.

In Chapter 5, we use polarized evanescent waves to excite surface-enhanced Raman Scattering (SERS) on a waveguide decorated with plasmonic gold-silver bimetallic nanoparticles (AuAg NPs). In effect, we make a nanoplasmonic waveguide, but one in which the guided wave

can propagate over larger distances than classical metal overlayer configurations like those used in the Kretschmann configurations. We show how our nanoplasmonic waveguide SERS setup can detect orientations of molecules binding to the AuAg NPs SER substrate. Our plasmonic SERS waveguide resembles a passive photonic device called a mode stripper. Accordingly, we investigate how the different boundary conditions associated with exciting plasmons with TE versus TM polarizations affect the SER spectra and provide at least qualitative evidence for molecular orientation at or near the nanoparticles. In our system, the TM mode was selectively attenuated and exhibited greater transmission losses. The lossy TM mode showed lower electric field intensity on the SER substrate, as demonstrated by FDTD simulations, and faster-diminishing SER signals compared to that of the TE mode. In view of research activity in the domain of magneto-nanoplasmonics, we provide the first evidence of ligand interactions that can be viewed as paradigms for ligand-mediated soft-soft transactions between nanoplasmonic particles and magnetic nanoparticles.

In Chapter 6 we describe a thin film OCB derived from a photo/thermal crosslinkable organic-inorganic sol-gel glass. The purpose of this study was first to establish that an anisotropy in the refractive index of the glass can be thermally written by the optical field of a laser propagating within the slab waveguide. The propagating wave causes thermal crosslinking of the glass and in effect, inscribes a waveguide-within-a-waveguide. In other words, one uses the guided wave to “write” a waveguide whose optical properties are differentiated from the host glass in both space and refractive index. The method was used to confirm that certain combinations of TE/TM polarization allow one to create an anisotropic refractive index. This anisotropy was shown to lead to polarization mode conversion, i.e., to changing TM polarization to TE. In this case, polarized light was coupled into sol-gel-derived waveguides, while the polarization of the scattered light was

also isolated using a polarization analyzer. Combining the polarization of the incoming and outgoing light we extract precise orientational information about the differential polarizability of molecules inside the waveguide. Our optical readout of mode conversion is a change in the C-H vibrational modes of the organic component of the host glass self-written waveguide. Returning to the theme of magnetism and magnetic nanoparticles, we formulated a magnetic nanoparticle composite waveguide. We then “wrote” a waveguide-within-a-waveguide with a polarized guided wave. The idea was to determine if we might stimulate mode conversion in a non-Faraday effect gyrotropic waveguide with a long term view to making a passive non-reciprocal optical device. The experiments are inconclusive, pointing out the need for new theory to understand wave propagation in lossy (absorbing) waveguides comprising gyrotropic media.

7.2 Contributions to original knowledge

1. The x-ray photoelectron spectroscopy (XPS) depth profiling of surface and sub-surface elements and their oxidation states for pristine and expired MRF particles is the first quantitative study to provide this type of knowledge on a degradation process relevant to smart magnetorheological fluids in shear operation. By combining XPS, SEM, and TEM, we identified key species that contribute to the degradation of MRFs. These include oxidation of Fe(0) particles, interfacial reactions between iron microparticles and the carrier fluid vehicles, nanoscale surface coarsening, and mixing of oxidation product species at the surface of iron particles due to shear-induced collisions.
2. For the first time, carboxylated cellulose nanocrystal (CNC) and magnetic particle-grafted cellulose nanocrystal (MNP-CNC) cryogel scaffolds were fabricated using a combination

of unidirectional high-temperature freezing in the presence and absence of a static magnetic field. This method is shown to tune pore morphologies of the resulting cryogel scaffolds.

3. Small-angle x-ray scattering (SAXS) and dynamic water sorption (DVS) were combined to reveal that the water sorption properties of CNC-based cryogel scaffolds correlate with the tightness of fiber-bundling inside a cellulose nanocrystal. According to the analysis of SAXS data using the Debye-Anderson-Brumberger (DAB) model, scaffolds made with MNP-CNC have smaller correlation lengths inside their crystals. This indicates that the MNP-CNC samples have more compact cellulose fibers within the CNC crystals. Such compactness correlates with reduced water sorption.
4. The capacity to propagate both TE and TM polarized guided waves for evanescent wave surface-enhanced Raman spectroscopy (SERS) was demonstrated experimentally for the first time. We introduce a nanoplasmonic waveguide construct called the Optical Chemical bench that allows one to build up hierarchies of nanoscale matter to probe vibrational properties and chemical interactions across the macroscale-nanoscale interface. We showed that the capacity to excite both TE and TM polarization states allows one to attribute the molecular orientation of small molecules on the surface of plasmonic core-shell AuAg nanoparticles on the surface of the waveguide. Finite-difference time-domain (FDTD) calculations shed light on the electric field interactions among bimetallic AuAg nanoparticles that contribute to SERS enhancements.
5. We introduce the first experiments that offer insight into inter-ligand soft-soft interactions at magnetic nanoparticle-nanoplasmonic particle interfaces. These constructs are relevant to the emerging area of magneto-nanoplasmonics, where it is very difficult to probe magneto-nanoplasmonic interfaces. We established how polarization mode dependent-

evanescent wave surface-enhanced Raman scattering could detect the ligand couplings between plasmonic and magnetic nanoscale particles in waveguide heterostructures.

6. We apply the method of optical wave self-inscription to write optical anisotropy in a photo/thermal responsive hybrid organic-inorganic glass waveguide. The method allows us to create a spatially resolved waveguide-within-a-waveguide. We establish how TE/TM polarization mode conversion can be a “readout” of the optical device by studying changes in the C-H stretching region of the photo-inscribed waveguide. These experiments are fundamental to the next stage of research, where we introduce for the first time, a method to make self-written magnetite nanoparticle waveguide gyrotropic composite media. Attempts to detect non-Faraday effect conversion were inconclusive, pointing in part to the need for new theories to examine the case of wave propagation in lossy gyrotropic media.

7.3 Future directions

This thesis lays the groundwork for taking interfacial studies further. This section outlines some directions for future research for each of the chemical systems involving iron oxides explored in this thesis.

7.3.1 Conduct targeted studies into factors that affect particle-fluid interfacial chemistry in magnetorheological fluids (MRF) systems

Chapter 2 explored the interfacial chemistry between carbonyl iron microparticles and commercial hydrocarbon and fluorocarbon carrier fluids. Carbonyl iron microparticles have been the standard magnetic component in most MRF applications, and they were the only magnetic

particles used in our MRF-related studies. We suggest expanding the repertoire of magnetic particles to include other magnetic elements and their oxides, magnetic alloys, and magnetic core-shell particles. Some examples include nickel, cobalt, and some types of manganese oxides, such as Mn_3O_4 .

The carrier fluids studied in this thesis were all commercially available fluids with largely undisclosed chemical compositions. The lack of knowledge in fluid composition significantly limited our ability to understand the evolution of chemical species in the degradation process. We propose to conduct controlled studies using carrier fluids with known chemical compositions. We may also diversify the type of applied stressors that contribute to the aging of the MRFs, such as studying the effects of temperature and mechanical compression, in addition to shear.

7.3.2 Effects of composition designs and fabrication techniques on the physicochemical properties of CNC-based composites

Despite its biocompatibility, biodegradability, and renewability, CNC alone may not offer the full range of chemical and mechanical properties required for different applications. One strategy is to alter the physicochemical properties of CNC by blending CNC with other natural or synthetic polymers to create nanocomposites.¹ Attractive physicochemical properties can also be added to CNC or CNC-based composites by incorporating inorganic nanoparticles, such as gold, silver, or iron oxides. Pertaining to cryogel scaffolds, changing the composition of the initial polymer gel may lead to different freezing processes. Different conditions for cryogel fabrication, such as precisely controlled freezing time, freezing temperature, and freezing rate, may produce different morphologies in the resulting scaffolds. Fabrication of the CNC and MNP-CNC cryogel

scaffolds studied in this thesis are but two examples of a vast plethora of CNC-based composites. Despite the rising interest in creating various CNC composites, however, studies examining their nanoscopic and interfacial chemical properties are not abundant. For future studies, we propose to design CNC-based composites targeting specific applications. The potential of examining the morphologies and interfacial chemistry for different CNC-based composites using techniques explored in this thesis is very exciting.

7.3.3 Improving the optical chemical bench (OCB) for nanoparticles detection

The optical chemical bench (OCB) combining polarized light and evanescent wave surface-enhanced Raman (SER) allows one to distinguish molecular orientations depending on the SER response of the molecules towards TE and TM polarized light. Comparing the SER spectra induced by TE and TM modes also showed a new way to explore the binding of nanoparticles on SERS-active substrates via surface functional groups. In the future, experiments can be performed to improve OCB's detection of nanoparticles. One suggestion would be to redesign the linkage between the SER-active substrates and the magnetic particles using DNA linkages or DNA templated-click chemistry. DNA has been shown to bind with nanoparticles to produce origami composites with precise structures.² In addition, past research has shown that polarized Raman spectroscopy can be used to detect the orientations of DNA oligonucleotide single crystals and oriented nucleic acid fibers.³ There is an enormous capacity to advance the OCB construct into other areas of chemical sensing for the purpose of acquiring knowledge of chemical interactions at thin films and interfaces. For example, one might study hyper-Rayleigh scattering from quadrupolar molecules like crystal violet absorbed on gold nanoparticle arrays on the OCB. There is a need to develop systematic methods that allow one to create well-defined periodic arrays of

plasmonic nanoparticles on the OCB. The physics literature offers abundant approaches based on nanolithography, and there is ample opportunity to recruit the methods of self-assembly in this service.

7.3.4 Optical anisotropy induced by magnetic particles and/or applied magnetic field

There is a need for new theories in the area of wave propagation in lossy gyrotropic waveguides. This would assist the design of waveguides in examining the potential for new non-reciprocal devices and their application not only in photonics but also in fields of study where magnetic forces are at play over nanometer length scales. We demonstrated in this thesis that photoinduced anisotropy in photo/thermally sensitive sol-gel derived waveguides can be detected using polarized Raman spectroscopy. The purpose was to calibrate mode conversion that would assist the detection of polarization mode conversion in spatially localized self-inscribed magnetic nanoparticle composite waveguides. The use of longer wavelength NIR lasers like a solid-state 1054 nm laser coupled with a NIR detector would likely reduce optical loss in the self-written waveguide. Alternatively, coupling scattered light into a NIR FT-Raman spectrometer might be of use. Studies should begin with self-written “isotropic” waveguides so that polarization mode conversion might be more easily detected and distinguished from the anisotropic case. Although results were obtained in the current experiment, we encourage the design of new experiments that address the problems we identified in Chapter 6. Improvements in sample preparation for gyrotropic medium waveguides are recommended. MNPs be made from high magnetic saturation materials and capped with suitable ligands that allow for uniform dispersion inside the sol-gel. Redesigning the ways of creating uniform magnetic fields (Helmholtz coils, for example) is recommended for these studies. Lithographic techniques can be used to make magnetic strips over

layers with an isolating buffer layer to control the transverse magnetic field in the vicinity of the waveguide. In this way, one might “watch mode conversion as it occurs in an active waveguide configuration. Other waveguide multilayer architectures can be constructed based on designs extant in the photonics literature.

7.4 References

1. Younas, M., Noreen, A., Sharif, A., Majeed, A., Hassan, A., Tabasum, S., Mohammadi, A. and Zia, K.M., 2019. A review on versatile applications of blends and composites of CNC with natural and synthetic polymers with mathematical modeling. *International Journal of Biological Macromolecules*, 124, pp.591-626.
2. Johnson, J.A., Dehankar, A., Robbins, A., Kabtiyal, P., Jergens, E., Lee, K.H., Johnston-Halperin, E., Poirier, M., Castro, C.E. and Winter, J.O., 2019. The path towards functional nanoparticle-DNA origami composites. *Materials Science and Engineering: R: Reports*, 138, pp.153-209.
3. Benevides, J.M., Overman, S.A. and Thomas Jr, G.J., 2005. Raman, polarized Raman and ultraviolet resonance Raman spectroscopy of nucleic acids and their complexes. *Journal of Raman Spectroscopy: An International Journal for Original Work in all Aspects of Raman Spectroscopy, Including Higher Order Processes, and also Brillouin and Rayleigh Scattering*, 36(4), pp.279-299.